Central University of Technology, Free State

Non-destructive testing of the parts manufactured by Direct Metal Laser Sintering

-Dean-Paul Riethmüller Kouprianoff-

Dissertation submitted in fulfilment of the requirements for the degree

MASTER of ENGINEERING in MECHANICAL ENGINEERING

Supervisor:	Prof. Ihar Yadroitsau, D. Eng.
Co-supervisors:	Dr. Ina Yadroitsava, Ph.D.
	Dr. Anton du Plessis, Ph.D.

Bloemfontein

August 2017

"Look deep into nature, and then you will understand everything better."

Albert Einstein

DECLARATION WITH REGARD TO INDEPENDENT WORK

I, *Dean-Paul Riethmüller Kouprianoff*, identity number and student number , do hereby declare that this research project submitted to the Central University of Technology, Free State (CUT, FS) for the Master of Engineering in Mechanical Engineering, is my own independent work; and complies with the code of academic integrity, as well as other relevant policies, procedures, rules and regulations of the Central University of Technology, Free State; and has not been submitted previously to any institution by myself or any other person in fulfilment of the requirements for the attainment of any qualification.

Signature of student... Paul ....

Date 20 October 2107

ACKNOWLEDGEMENTS

Thanks be to God that led me through this study and most of all for making it possible for me to learn about the physical principles He has created. I learnt that we can use these principles to create machines, tools and art; in a sense be like Him, creating and building. All of this seemed out of reach to me as a child. "*The heart of man plans his way, but the Lord establishes his steps.*" - Proverbs 16:9.

I acknowledge that God has provided for me according to His grace and His plan.

"*For my thoughts are not your thoughts, neither are your ways my ways, declares the Lord. For as the heavens are higher than the earth, so are my ways higher than your ways and my thoughts than your thoughts*."-Isaiah 55:8-9

During my study, I have come to know that there are great minds with great hearts in the science field. To my dismay I have also learnt that a great many of these do not believe in God. I was confronted with personal struggles based on "Science" and learnt in the end that these arguments are very much human opinions. "*The goal of this command is love, which comes from a pure heart and a good conscience and sincere faith. Some have wandered away from these and turned to meaningless talk*" - 1 Timothy 1:5-6. Praise God for his mercy towards me, which is available to all.

"*For God has bound all men over to disobedience so that he may have mercy on them all.*" - Romans 11:32

I would like to thank my supervisors, Prof. Ihar Yadroitsau (Igor Yadroitsev), and Dr. Ina Yadroitsava, for their constant guidance and involvement as well as their optimistic support and encouragement. I would also like to thank; Dr. Anton du Plessis, as well as the Central Analytical Facility (CAF) at Stellenbosch University for assisting and carrying out the X-ray Computed Tomography, IMCE for doing acoustic emission testing with their RFDA BASIC, PAUT which was carried out with the aid of Dr. Manfred Johannes from the CSIR, who assisted in giving advice and in making available their equipment; and the Electrical Engineering Department at CUT for their assistance.

This work is based on the research supported by the South African Research Chairs Initiative of the Department of Science and Technology and National Research Foundation of South Africa (Grant №97994) and the Collaborative Program in Additive Manufacturing (Contract № CSIR-NLC-CPAM-15-MOA-CUT-01).

ABSTRACT

Interest in Additive Manufacturing (AM) has grown considerably in the past decades and industry has gained great benefits from this type of technology. The main advantages are: geometrical freedom that allows the design of parts with complex shape, which are difficult or impossible to produce by conventional technology; shortened design-to-product time; customization and the possibility to use several materials in one process. Direct Metal Laser Sintering (DMLS) is one of the most promising AM technologies that utilizes metal powders. Due to the layer-by-layer nature of powder delivery used in DMLS, the drawbacks are: surface quality and accuracy, high residual stress in as-built parts and porosity – all of which depend on the powder material, process-parameters, scanning and building strategies. This can result in a substantial deterioration of the mechanical properties of the products and their performance characteristics. For this reason, it is very important to identify defective parts before enrolling into service.

Non-destructive testing (NDT) is effective for detection of internal defects without causing damage. NDT also covers a wide group of methods of analysis used to evaluate the properties of a material. NDT techniques like visual, acoustic, ultrasonic, thermal, X-ray and 3D-computed tomography (CT) inspections are now widely used for various industrial applications. For the analysis of material properties and the detection of defects, each of these methods uses different physical principles that have their advantages and disadvantages.

In this study, some of the NDT techniques are evaluated in terms of their applicability to the inspection of parts manufactured by DMLS technology: Visual, Ultrasonic, Computed Tomography and Acoustic Emission inspection.

Artificial defects were used to determine the feasibility of each NDT method. DMLS samples were produced containing a range of artificial defects. These samples were than subjected to each method and the results compared. A comparison between the amount of defect information obtained is made.

It was shown that the nature of the sample; shape, size, material and the type of defects present plays a vital role in the selection of testing methods. Ultrasonic-Total Focus Method indicated that some defects are present upon testing relatively big samples with simple geometry. X-ray Computed Tomography showed some limitations with regard to the possibilities and the amount of defect detail, the only drawback being the cost and time involved. Acoustic Emission showed to be a promising method for production parts although it requires an initial time investment; thereafter it is a simple and easy way of detecting defective samples.

Table of Contents

ABSTRACT V

LIST OF FIGURES VIII

LIST OF TABLES XV

GLOSSARY XVI

CHAPTER 1: INTRODUCTION 1

1.1-BACKGROUND 1
1.2 THE AIM OF THE PROJECT 1
1.3 THESIS STATEMENT 2
1.4 THE SCOPE OF THE PROJECT 2
1.5 RESEARCH METHODOLOGY 2
1.6 OBJECTIVES 3
1.7 AN OVERVIEW OF THE DISSERTATION 4
1.8 EXPECTED CONTRIBUTION 4
1.9 PUBLICATIONS AND PRESENTATIONS TO DATE 4

CHAPTER 2: LITERATURE REVIEW 6

2.1 ADDITIVE MANUFACTURING 6
2.2 DIRECT METAL LASER SINTERING 6
2.2.1 DMLS process 10
2.2.2 Single track formation 14
2.2.3 Single layer formation 20
2.2.4 Three-dimensional objects 24
2.2.5 Summary 26
2.3 PROPERTIES OF DMLS OBJECTS 26
2.3.1 DMLS microstructure 26
2.3.2 Residual stress 29
2.3.3 Porosity 32
2.3.3 Mechanical properties 34
2.3.5 DMLS Ti6Al4V alloy 34
2.3.6 Summary 39
2.4 DESTRUCTIVE TESTING 39
2.5 NON-DESTRUCTIVE TESTING 40
2.5.1 Introduction 40
2.5.2 Visual testing 42
2.5.3 Radiographic testing 43
2.5.4 Ultrasonic testing 51
2.5.5 Acoustic testing 74
2.5.6 Summary 80
2.6 NDT EVALUATION OF AM OBJECTS 80
2.6.1 CT scans 81
2.6.2 Ultrasound Testing 90
2.6.3 Acoustic Emission 93
2.6.4 Summary 96

CHAPTER 3: MATERIALS AND METHODS 98

3.1 EOSINT M280 98
3.2 DMLS TI6AL4V (ELI) SAMPLES 99

3.2.1 Rectangular samples ____ *99*
3.2.2 Samples with fine inner structure ____ *100*
Summary ____ *104*
3.3 METHODS ____ 104
3.3.1 Visual testing ____ *104*
3.3.2 Micro computed tomography ____ *105*
3.3.3 Phased array ultrasonic testing ____ *106*
3.3.4 Acoustic emission ____ *107*
3.3.5 Surface roughness testing ____ *108*
Summary ____ *108*

CHAPTER 4: RESULTS AND DISCUSSION ____ 109

4.1 TESTING THE SAMPLES WITH FINE INTERNAL STRUCTURE ____ 109
4.1.1 Pins with cubed cavities ____ *109*
4.1.2 Blocks with horizontal semi-cylinder channels ____ *114*
4.1.2 Step samples with horizontal cavities ____ *118*
4.2 TESTING OF ARTIFICIAL POROSITY IN LARGE RECTANGULAR SAMPLES ____ 120
4.3 NON-DESTRUCTIVE TESTING DMLS COMPONENTS USING AE ____ 127
4.3.1 AE testing of the rectangular blocks with artificial porosity ____ *129*
4.3.2 AE testing of the blocks with pins ____ *130*
4.3.4 Planned work ____ *131*

CHAPTER 5: CONCLUSIONS ____ 133

REFERENCES ____ 136

APPENDIX 1: BRIEF HISTORY OF AM ____ 143

LIST OF FIGURES

Figure 1: Flow chart of research methodology 3

Figure 2: Analysis of the application market for AM: in 2012 (a) and in 2014 (b) (Wohlers, 2014–2015) 7

Figure 3: Metal AM categories (Lewandowski and Seifi, 2016) 9

Figure 4: Functional principle of the DMLS (EOS GMBH, 2016) 10

Figure 5: Basic machine components (Kruth et al., 2010) 11

Figure 6: Fibre laser pumping (a) and fibre core light interaction (b) (Hecht, 2012) 12

Figure 7: Galvano mirrors and lenses used to produce a laser spot on a focal plane (OptoSigma, 2016) 13

Figure 8: Track from AISI 420 powder on the substrate (top view): laser power P = 50 W; laser spot diameter 70 m; scanning speed V = 0.10 m/s; powder layer thickness h = 50 m (Yadroitsev et al., 2010) 14

Figure 9: Results of numerical simulation of laser melting of Ti6Al4V substrate showing isothermal contours for different laser power and scanning speeds (Yadroitsev et al., 2015) 15

Figure 10: Instability of laser sintered tracks from SS grade 316L (−25 μm) powder on steel substrate. Thickness of the deposited powder layer is 50 μm, scanning speed V = 0.02 m/s: (a) P = 25W, (b) P = 12.5 W (Yadroitsev et al., 2010) 16

Figure 11: Cross-sections of laser sintered tracks from SS grade 904L powder on steel substrate (Yadroitsev et al., 2010) 17

Figure 12: Illustration of the simulation laser-powder-substrate interaction: non-uniform melting of particle (a), balling effect due to surface tension (b) Marangoni effects (c), recoil with Marangoni effects (d). The red colour corresponds to temperature scale capped at 4000K, blue is 293K. The red contour line is the melt line. The powder particle is illuminated by a laser moving to the right for 10 μs. The melt tracks are 2D slices of 3D simulations (Khairallah et al., 2016) 18

Figure 13: Time snapshots of the melt flow showing spattering and denudation. The melt has a large backward flow (blue colour; Vx<0) due to Marangoni effect and recoil, compared to forward flow (Vx> 0; red colour). The backward net flow breaks up later in time at the necking. The velocity scale is capped at +-1m/s for better visualization. The right panel magnified view at 270μs (flow rotated by +90º) shows the velocity components (Vx, Vy, Vz) and the temperature (with contour lines) at the depression. The white letter O shows that the laser centre is not at the bottom of the depression. (Khairallah et al., 2016) 19

Figure 14: Lateral 2D slices showing the temperature and velocity field of the melt as the laser scans (direction out of page) by a fixed location. They show the events before the arrival of the laser centre (45-76 μs), the indentation formation (76-82 μs), the indentation collapse and formation of a pore (92-103 μs) and the asymmetrical flow pattern due to an asymmetrical cooling as the melt solidifies (142-400 μs). (Khairallah et al., 2016) 20

Figure 15: Schematic showing how denudation affects track height (Yadroitsev & Smurov., 2011) 21

Figure 16: Different scanning strategies (Manfredi et al., 2014) 21

Figure 17: Top view of single layer produced by one-zone (a) and two-zone strategy (b) of laser scanning. P = 50 W; powder layer thickness h = 50 μm; scanning speed V = 0.12 m/s and hatch distance s = 120 μm (Yadroitsev et al., 2015) 22

Figure 18: Example of scan pattern for island scanning with revealed islands with the rotation angle beta (Kruth et al, 2010) 22

Figure 19: The exposure track (vector) is shown by a solid line (1). The dashed line represents the skywriting. In this area the laser beam is switched off (3). At the beginning of the part (4), the laser power is switched on with a sized value and the laser beam is run with a constant velocity (Manfredi et al. 2014) 23

Figure 20: Exposure strategy (EOS Training Manual, 2012) 23

Figure 21: Up-skin, down-skin and core regions (EOS Training Manual, 2012) 24

Figure 22: DMLS parameters (Yadroitsev, 2009) 24

Figure 23: Algorithm for finding optimal DMLS/SLM process-parameters (Yadroitsev et al., 2015) 25

Figure 24: CAD model of sphere (1) and effect of STL resolution on sphere geometry, increasing from left to right (2-4) (SolidWorks, 2015) 26

Figure 25: Microstructure (a) and microhardness profile (b) of AISI 420 steel at P = 60 W, V = 0.12 m/s, h = 40 µm, s = 120 µm (Yadroitsev et al., 2015) 27

Figure 26: Temperature evolution during laser scanning Ti6Al4V alloy at depths from the surface: 30, 60, 90 and 120 µm in depth. Laser power is 150 W; scanning speed is 1.2 m/s (Yadroitsava et al., 2015b) 28

Figure 27: Top surface of a DMLS part from AISI 316L stainless steel (polished and etched) (Kruth et al, 2010) 29

Figure 28: Compressive and tensile stresses during heating and cooling (a), long and short scanning vectors (b) (Kruth et al., 2004) 30

Figure 29 : Delamination of DMLS part during manufacturing (a) and macrocrack of Ti6Al4V part attached to substrate, SEM image(b) and top surface of TiAl part with microcracks (c) (Yadroitsava & Yadroitsev, 2015) 31

Figure 30: Pores in DMLS samples produced with two-zone strategy and scanning speed 0.12 m/s, hatch distance 120µm, powder layer thickness 50 µm and laser power P = 50 W (a); P = 70 W (b) (Yadroitsev et al., 2015) 32

Figure 31: Effect of scan speed on the relative density of AISI 316L stainless steel processed on a Concept Laser M3 machine (Kruth et al, 2010) 33

Figure 32: Material property comparison of different Ti6Al4V production methods (Lewandowski and Seifi, 2016) 34

Figure 33: Microstructure of an alpha-beta titanium alloy (Ti6Al4V) in representative metallurgical conditions. (a) Equiaxed α and a small amount of intergranular β. (b) Equiaxed and acicular α and a small amount of intergranular β. (c) Equiaxed α in an acicular α (transformed β) matrix. (d) Small amount of equiaxed α in an acicular α (transformed β) matrix. (e) Plate-like acicular α (transformed β); α at prior β grain boundaries. (f) Blocky and plate-like acicular α (transformed β); α at prior β grain boundaries (Donachie, 2000) 36

Figure 34: Microstructure of Ti6Al4V: (a) after DMLS process; (b) annealing 4 h at 800 °C; (c) WQ/840 °C; (d) WQ/840 °C + tempering/600 °C/4 h; (e) WQ/960 °C and (f) WQ/ 960 °C + tempering/600 °C/4 h. (Yadroitsev et al., 2014) 37

Figure 35: Delamination during DMLS process causing powder to vibrate and forming valleys in the powder bed (Van Zyl et al., 2016) 38

Figure 36: Example of an old boiler & Boiler explosion (Hellier, 2012) 41

Figure 37: Different NDT techniques 41

Figure 38: 2D flat panel detector with cone beam and 1D line detector with fan beam: a grey value profile along one pixel line is shown. (Kruth et al., 2011) 44

Figure 39: Photoelectric absorption (a) and Compton scattering (b). (Kruth et al., 2011) 45

Figure 40: Pair production (Hellier, 2012) 45

Figure 41: Linear attenuation coefficient for different photon energies. (Kruth et al., 2011) 46

Figure 42: Schematics of pencil, fan and cone beam CT methods, respectively. In this diagram, the fan beam image depicts a curved detector while the cone beam image depicts a flat panel detector, it should be noted that curved and flat panel detector arrays can be used in each instance (Maskery et al., 2016) 47

Figure 43: Image magnification and blurring by moving the object towards the source which has a finite X-ray spot (Kruth et al., 2011). 48

Figure 44: Effect of sample diameter on voxel size, when using a 2000 x 2000 pixel detector (Du Plessis et al., 2016) 48

Figure 45: Example of back-projection reconstruction (Kruth et al., 2011) 49

Figure 46: Effect of beam hardening without and with a physical filtering of the X-ray beam. Hollow cylinder: outer ø 6, inner ø 0.6 mm (Kruth et al., 2011) 50

Figure 47: X-ray CT 'cause of death' investigation on a mummified bird (Ikram et al., 2015) 50

Figure 48: Ultrasonic industry application (Ensminger & Bond, 2011) 53

Figure 49: Pulse-echo principle of operation (Ensminger and Bond, 2011) 54

Figure 50: Longitudinal wave (Hellier, 2012) 55

Figure 51: Depiction of Snell's law (Hellier, 2012) 57

Figure 52: Mode conversion of compression wave at steel-to-air interface (Hellier, 2012) 58

Figure 53: Decay of a propagating wave through material 59

Figure 54: 2 Dimensional illustrations of constructive (a) and destructive (b) interference (NDT Resource Centre, 2016) 59

Figure 55: Multiple points of sound origination along the face of the transducer (NDT Resource Centre, 2016) 60

Figure 56: Beam spread of near- and far-field (Hellier, 2012) 61

Figure 57: Amplitude over distance away from transducer (Hellier, 2012) 61

Figure 58: Unfavourable discontinuity orientation; reflecting away from the transducer (a) sound passing along crack (b) (Hellier, 2012) 62

Figure 59: UT equipment principle diagram 62

Figure 60: A- and B-scan of inspection block (NDT Resource Centre, 2016) 63

Figure 61: B-scan instrument (Hellier, 2012) 63

Figure 62: C-scan of test piece with defect (NDT Resource Centre, 2016) 64

Figure 63: Schematic of a single transducer (NDT Resource Centre, 2016) 65

Figure 64: Immersion bath with (a) bubbler (b) and squirter systems (c) (Hellier, 2012) 65

Figure 65:IIW type reference block (NDT Resource Centre, 2016) 66

Figure 66: Half skip method: no defect and no reflection (a); defect and reflection (b) (Hellier, 2012) 67

Figure 67: Angle beam on bar (Hellier, 2012) 68

Figure 68: Tandem setup on a plate for defect in the centre of test piece (Hellier, 2012) 68

Figure 69: Immersion technique (Hellier, 2012) 69

Figure 70: Tip diffraction echo (Hellier, 2012) 70

Figure 71: Time of flight diffraction (Hellier, 2012) 70

Figure 72: Two-point source interference pattern (Olympus, 2016) 71

Figure 73: Linear straight beam scan from left to right using a phased array transducer (Olympus, 2016) 72

Figure 74: Dimensional parameters of PAUT transducer (Olympus, 2016) 73

Figure 75: PAUT focused beam (Hellier, 2012) 73

Figure 76: PAUT A- and linear scan result (a) on a test piece with holes (b) (Olympus, 2016) 74

Figure 77: Single degree-of-freedom mass model (Schiefer and Sjoeberg., 2005) 76

Figure 78: RAM-NDT equipment from the Modal Shop and their process flow (Bono et al., 2010) 77

Figure 79: RAM-NDT software interface after an acoustic measurement of a component (top). An indication of a typical peak frequency shift of a defective component (bottom) (Bono et al., 2010) 79

Figure 80: RFDA-basic modulus of elasticity calculation for rectangular bar (IMCE, 2016) 79

Figure 81: RFDA-basic internal friction calculation characterized by the material and defects (IMCE, 2016) 80

Figure 82: Deviation of height of steps measured on CMM and CT scans (Gapinski et al., 2016) 82

Figure 83: Nylon SLS components glued together; the right picture is a section through the CT model, showing the nylon parts (grey colour), interlayer porosity (dark spots), small particle inclusions and the glue in white (de Chiffre et al., 2014) 82

Figure 84: Water in a glass container surrounded with air atmosphere (above) grey value cross-section (below) (du Plessis et al., 2014) 83

Figure 85: CAD dimensions of SLS and FDM dimensional samples Note: for better visibility, sample 1 is represented with a 1:2 scale, whereas samples 2 and 3 are represented with a 1:1 scale (Aloisi and Carmignato., 2016) ________ 84

Figure 86: Deviations between CT and CMM measurements for external diameters of SLS l sample. Vertical columns represent the deviations for each measure,, while the horizontal axis represents the measure and number. The dashed line shows the value corresponding to Rz/2of the external surface. (Left) Deviations between CT and CMM measurements for the internal diameters of the same sample. Vertical columns represent the deviations for each measure , while the horizontal axis represents the measure and number. The dashed line shows the value corresponding to Rz/2of the internal surface. (Right) (Aloisi and Carmignato., 2016) ________ 84

Figure 87: FV (a) and CT (b) height maps of the DMLS AlSi10Mg surface (Townsend et al., 2016) ________ 85

Figure 88: Design of internal features of samples (a) CT of internal features of samples (b) (Kim et al., 2016) 86

Figure 89: Tubular sample (a) AM research equipment (b) used by Karme et al. (2015) ________ 87

Figure 90: Porosity of tube specimen 3 (Karme et al., 2015) ________ 87

Figure 91: Surface reconstruction of specimen 3 overlaid with the CAD model pipe, showing volume decrease. Higher inner surface relief penetrated the original model in places where the polygon edges are located (4° intervals), otherwise the specimen surfaces are inside the model extents (Karme et al., 2015) ________ 87

Figure 92: Cross-sectional comparison of specimen built in X-plane; (a) X-ray CT (b) Confocal Microscope (Ziółkowski et al., 2014) ________ 88

Figure 93: Histogram of pore size in X (RED), Y (BLUE) and 45 ° to X,Y and Z bono(GREEN) directions (Ziółkowski et al., 2014) ________ 88

Figure 94: Sphericity distribution for specimens built in X (red), Y (blue) and 45 ° to X,Y and Z (green) directions (Ziółkowski et al., 2014) ________ 89

Figure 95: 3D view of Ti6Al4V DMLS sample showing the surface (left) and the internal defects (right) (du Plessis et al., 2015) ________ 89

Figure 96: Transparent view of DMLS cylinders before (left) and after (right) HIP treatment (du Plessis et al., 2015) ________ 90

Figure 97: Ultrasonic wave speed vs. X-ray CT porosity (Slotwinski et al., 2014) ________ 91

Figure 98: Laser-ultrasonic equipment (Popovich et al., 2016) ________ 91

Figure 99: EBM part scanned via ultrasonic; area (a)and A- and B- scans (b) (Waller et al., 2014) ________ 92

Figure 100: Eddy current testing of DMLS component (Waller et al., 2014) ________ 92

Figure 101: AE system for a FDM machine (Wu et al. 2016) ________ 93

Figure 102:DMLS sample with internal sinusoidal cavity; tested with AE in combination with pressure sensors (Strantza et al., 2015) ________ 94

Figure 103: Small MIM parts used during AE case study by Bono et al., 2010 ________ 95

Figure 104: AE drop test equipment from Modal Shop (Bono et al., 2010) ________ 95

Figure 105: MIM AE drop test results with (a) and without (b) traces – red indicating failed parts (Bono et al., 2010.) 96

Figure 106: EOSINT M280 machine 98

Figure 107: Outline of CAD drawing of samples without (left) and with defect (right) 100

Figure 108: CAD model for pins with cubed built cavities 101

Figure 109: Schema for DMLS scanning parameters of the pins with gaps (top view) 102

Figure 110: CAD model for horizontal block with semi-cylinder channels 102

Figure 111: CAD of step samples with cavities 103

Figure 112: SmartZoom5 (a) and Scope A1 (b) optical microscopes; NeoScope JCM 5000 scanning electron microscope (c) 104

Figure 113: CitoPress 1 (a) and polishing machine Tegramin-25 (b) 105

Figure 114: phoenix v|tome|x L 240 X-ray CT scanner (GE Oil & Gas, 2016) 105

Figure 115: M2M Gekko phased array flaw detector (M2M, 2016) 106

Figure 116: PAUT test procedure: 1– sample, 2–couplant on surface, 3- PAUT transducer, 4- transducer and wedge, 5-PAUT scanning on block, 6- experimental setup/equipment 107

Figure 117: RFDA Basic: testing equipment (a) and software (b) 108

Figure 118 Surface roughness tester Surftest SJ-210 measuring the flat specimen 108

Figure 119: Transparent 3D image of pins and cubed defect pore volumes from CT reconstruction 110

Figure 120: Cross-sections of internal cavities in pins 111

Figure 121: Cross-sections of internal cavities in pins at higher magnification. 112

Figure 122: The pin samples with induced cubed defects. CT slice images from side (a) and top (b) views (du Plessis et al., 2016) 113

Figure 123: CT image of cavity-P9. 113

Figure 124: Difference between prescribed CAD cavities and cavities estimated by CT scans in DMLS pins P1–P9 114

Figure 125: A transparent CT defect analysis view of CT reconstruction of the rectangular sample with induced line/track defects of varying thicknesses perpendicular to the build direction (du Plessis et al., 2016) 115

Figure 126: Cross-sections of Ti6Al4V ELI rectangular block with hemispherical cylinders with prescribed CAD radius indicated 116

Figure 127: Illustration of hemisphere-C1 build limitations 116

Figure 128: Illustration of hemisphere-C2 build limitations 117

Figure 129: CT reconstruction of semi-cylinder horizontal pore C3 with prescribed CAD diameter of 180 µm 117

Figure 130: SEM image of cross-sections of prescribed semi-spherical cylinders with intended diameter of 150 µm 118

Figure 131: 3D image of step samples with horizontal pore volumes from CT reconstruction (a) and transparent image with pores (b) 118

Figure 132: The stepped sample with defects. CT slice images from side view 119

Figure 133: Optical microscope photos of cross-sections of step samples 119

Figure 134: SEM image of S7 sample 120

Figure 135 Optical images of top (a) and side surface (b) and 3D reconstruction of top (c) and side surface (d) of DMLS Ti6Al4V sample 121

Figure 136: DMLS samples without defects and with artificial defects upon micro CT inspection (top view) 122

Figure 137: 3D distribution of the pores in the sub-volume near defects from a close-up 15 µm resolution at micro CT inspection: AB5 (a) and SR5 (b) samples 123

Figure 138: TFM result of AB 2;screen shot with descriptions: red arrows indicate the first back wall echo, thereafter the echo repeats, horizontal orange line/cursor could be set to investigate at certain depths; in this case 3.4mm 124

Figure 139: Defect position of samples AB5 (left) and SR5 (right) as indicated in Figure 140; measurements taken were made from edge to the centre of the wedge 124

Figure 140: TFM results of AB 5(top) and SR 5(bottom) 125

Figure 141: Flexural (a) and torsional (b) frequencies of the different specimens versus the mass 127

Figure 142: Flow diagram of post manufacturing AE NDT 128

Figure 143: AE testing setup with DIY electret microphone (a) and ICP microphone method (b) 128

Figure 144: PicoScope software interface on a personal computer. Fast FourierTransform(FFT) is shown with the cursor pointing towards peak frequency. 129

Figure 145: Discrete Fourier transform of all four sample traces overlaid 130

Figure 146: Amplitude of AE signals versus frequency for solid (samples 1–3) and “defect” block 131

LIST OF TABLES

Table 1: The AM categorization (Bikas et al., 2016) 8

Table 2: The tensile properties of conventional Ti6Al4V (Donachie, 2000). 35

Table 3: The tensile properties of horizontal DMLS Ti6Al4V (ELI) samples 38

Table 4: The VT advantages and limitations 43

Table 5: The advantages and limitations of RT 43

Table 6: Advantages and limitations of UT 52

Table 7: The acoustic properties of various mediums adapted from Hellier, (2012) 56

Table 8: The AE advantages and limitations 75

Table 10: The Ra values of Rubert values compared to Sa values of CT and FV (Townsend et al., 2016) 85

Table 11: The EOS technical data for EOSINT M280 machine (EOS GmbH, 2016) 98

Table 13: The sample identification for rectangular blocks 100

Table 14: Sample identification for pins with fine structure 101

Table 15: The sample identification for steps with rectangular defects 103

Table 17: The acoustic emission testing data, sizes and mass of the samples 126

Table 18: The comparison of flexural frequencies (Hz) between RFDA and the DIY –ICP microphone methods for as-built and stress-relieved blocks 129

GLOSSARY

AE	Acoustic Emission
AM	Additive Manufacturing
BW	Back Wall
CAD	Computer Aided Design
CMM	Coordinate Measuring Machine
CRPM	Centre for Rapid Prototyping and Manufacturing
CSIR	Council for Scientific and Industrial Research
CT	Computed Tomography
CUT, FS	Central University of Technology, Free State
DMD	Direct Metal Deposition
DMLS	Direct Metal Laser Sintering
EBM	Electron Beam Melting
EDM	Electric discharge machining
ET	Eddy Current Testing
ELI	Extra Low Interstitial
EMAT	Electromagnetic Acoustic Transducer
FEM	Finite Element Method
FFT	Fast Fourier Transform
FV	Focus Variation
HIP	Hot Isostatic Pressing
HT	Heat Treatment
IP	Initial Pulse
LENS	Laser-Engineered Net Shaping
MIM	Metal Injection Moulding
MRI	Magnetic Resonance Imaging
NIST	National Institute of Standards and Technology
NDT	Non-Destructive Testing
PAUT	Phased Array Ultrasonic Testing
PoD	Probability of Detection
RFDA	Resonant Frequency and Damping Analysis
RT	Radiographic Testing
SDK	Software Development Kit

SDOF	Single Degree-of-freedom
SLM	Selective Laser Melting
STL	Standard Triangle Language
TOFD	Time of Flight Diffraction
VT	Visual Testing
UT	Ultrasonic Testing
UTS	Ultimate Tensile Strength
XRD	X-ray diffractometer
YS	Yield Strength

Chapter 1: INTRODUCTION

1.1-Background

Additive Manufacturing (AM) is a technique used to manufacture components from a Computer Aided Drawing (CAD). Once a design has been developed using CAD, the machine will manufacture the part by depositing layers of material, on top of each other, to build up the part, as opposed to subtractive manufacturing methods. Direct Metal Laser Sintering (DMLS) is one such technology. Fine powder material is deposited onto a substrate/sintered part making a thin layer. A laser beam then melts the areas forming a cross-section where the material is solidified; the process is repeated until the entire three-dimensional (3D) component has been formed layer by layer. The nature of this manufacturing technique is sensitive to parameters such as powder morphology, powder size distribution and powder layer thickness, laser power density, scanning speed, scanning strategy, and so forth. These parameters influence the quality of a part as it is being produced and some defects arise when there are deviations. Therefore, it is absolutely necessary to be sure of the integrity of the part before commissioning it into service. In other manufacturing processes, integrity of the component is confirmed using a variety of tests, two of the methods being: destructive- and non-destructive testing. Destructive methods include cutting open the part to inspect it and tensile testing. Non-destructive methods do not compromise the integrity of the part, thus the part can be used in service once testing has been completed.

The main approach in this study is to investigate the existing non-destructive testing (NDT) methods used in industry and obtain the knowledge to apply and verify the applicability of these NDT methods for DMLS components. Therefore, it was decided to produce samples with and without defects and then to carry out the different NDT testing methods on them so as to be able to compare the results. The results will indicate whether these NDT testing methods could detect the defects and identify defect characteristics, such as position, shape and the smallest detectable size. Furthermore, it was also decided to focus on Ti6Al4V and to investigate how material post processing (stress-relief heat treatment) will influence the results. Ti6Al4V alloy is the most commonly used alloy for biomedical and aerospace applications.

1.2 The Aim of the Project

To investigate the existing NDT methods used in modern industry and gain knowledge on how to apply and verify the applicability of these NDT methods, taking into account the specificities of the DMLS technology which produces components, track by track, layer by layer from metal powders. Furthermore, to estimate the typical size of the pores at standard process-parameters and to identify appropriate methods of NDT for the DMLS objects.

1.3 Thesis Statement

As it is clearly seen from the literature review, powder materials are very sensitive to the manufacturing process-parameters. Non-destructive testing can be applied for the comprehensive analysis of the DMLS Ti6Al4V (ELI) material and to identify porosity and internal structures in DMLS parts.

1.4 The Scope of the Project

This research study is concerned with creating an understanding of the applicability of non-destructive methods for Ti6Al4V (ELI) objects manufactured by DMLS; it can be applied not only for the Ti6Al4V alloy, but also for other metallic powders used in DMLS.

1.5 Research Methodology

The methodology and research design of the proposed project flows logically from the main purpose of this study, which is to study the applicability of different NDT techniques. These techniques are compared in terms of the probability of detecting: porosity, accuracy and residual stress in Ti6Al4V ELI DMLS parts. Furthermore, features of the DMLS process, NDT methods, powder handling and characterization, EOSINT M280 machine, metallographic methods, microscopy, micro-hardness and tensile tests were studied and used. The following flow diagram presents the research methodology used in this study as a whole.

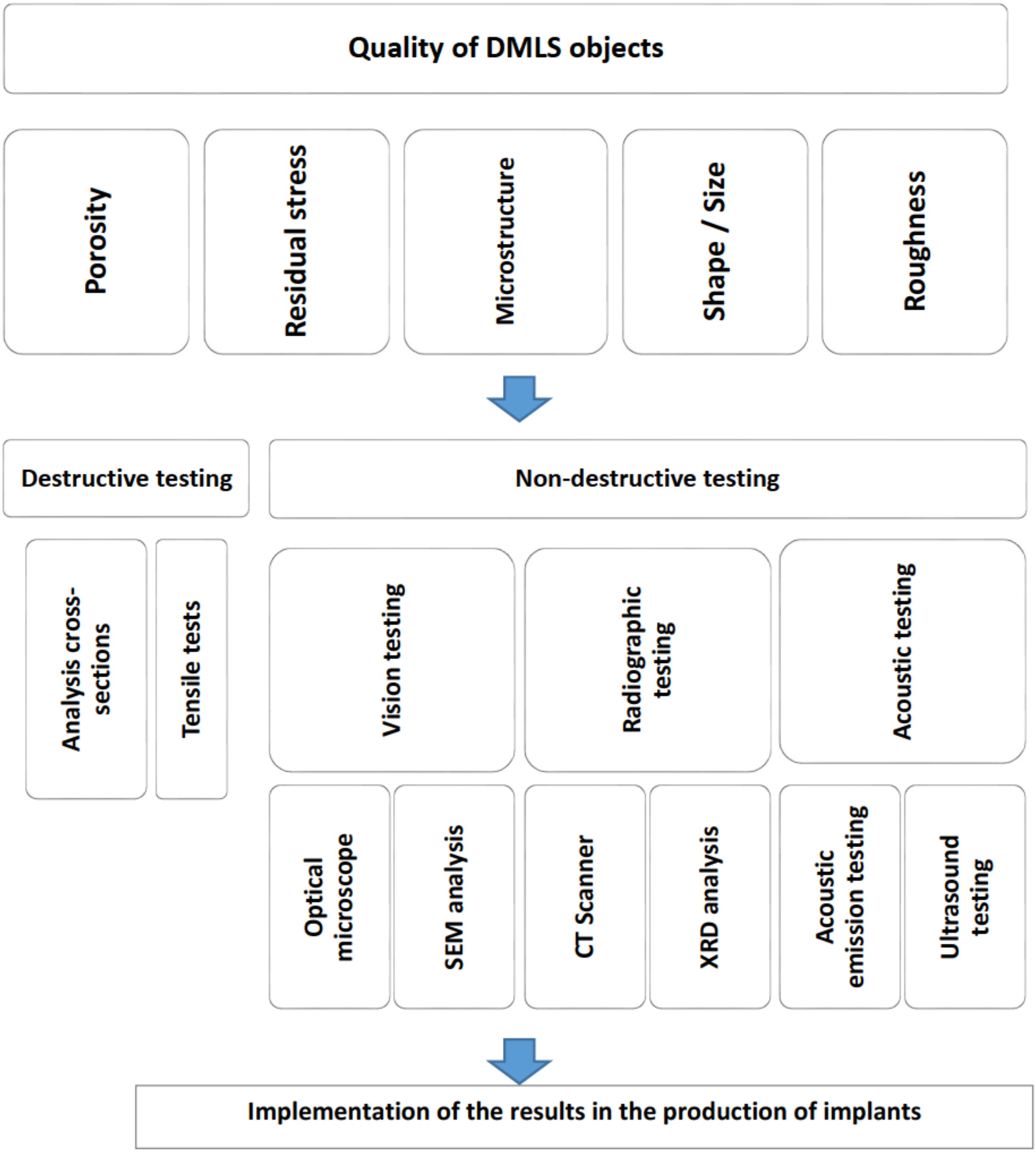
Quality of DMLS objects
Porosity
Residual stress
Microstructure
Shape / Size
Roughness
Destructive testing
Non-destructive testing
Analysis cross-sections
Tensile tests
Vision testing
Radiographic testing
Acoustic testing
Optical microscope
SEM analysis
CT Scanner
XRD analysis
Acoustic emission testing
Ultrasound testing
Implementation of the results in the production of implants

Figure 1: Flow chart of research methodology

1.6 Objectives

1. Investigate the DMLS process.
2. Investigate NDT methods for quality control.
3. Investigate the porosity, microstructure and residual stress of as-built DMLS parts.
4. Determine the most applicable method for DMLS.

5. Determine whether NDT could be applied in-house to investigate the porosity of DMLS parts.
6. Apply NDT for Ti6Al4V DMLS objects with different shapes, microstructure, porosity and residual stress.

1.7 An Overview of the Dissertation

The following outline defines the dissertations structure:

- Chapter 1 – Introduction: An introduction and background to the study. In this chapter the aim, the statement and the methodology of the study are described.
- Chapter 2 – Literature review: AM technology principles and state-of-the-art manufacturing methods are investigated. An in-depth study of the DMLS process and the nature of defect formation is presented. Component testing methods and the principle of operation are discussed.
- Chapter 3 – Materials and methods: Equipment selected for the research and the scientific approach to produce DMLS parts are presented. The NDT method and equipment to be used are described.
- Chapter 4 – Results and discussion: Results of the chosen methods and an image comparison between microscopy of physical sectioning and X-ray computed tomography are explained.
- Chapter 5 – Conclusion: Conclusions drawn from the study are defined.

1.8 Expected Contribution

The detrimental effect of porosity on the mechanical properties of Ti6Al4V (ELI) DMLS alloy limits the effectiveness in the application and qualification of DMLS implants. Consequently, in this work different approaches of NDT are utilized to implement the results in the production of the DMLS implants.

1.9 Publications and presentations to date

- D. Kouprianoff, A. du Plessis, I. Yadroitsava, I. Yadroitsev. Non-Destructive Testing of the Parts Manufactured by Direct Metal Laser Sintering. *In Proc. RAPDASA 17th International Conference "Building on the Foundations - Consolidating Impact into Products to Enhance Quality of Life for All South Africans"*, Vaal University of Technology, November 2- 4, 2016.

- D. Kouprianoff, A. du Plessis, I. Yadroitsava, I. Yadroitsev. Destructive and nondestructive testing on small and intricate DMLS components. *In Proc. RAPDASA 18th International Conference*, Durban, Inkosi Albert Luthuli International Convention Centre, November 8- 10, 2017.
- D. Kouprianoff, N. Luwes, I. Yadroitsava, I. Yadroitsev, E. Newby. On-line monitoring of laser powder bed fusion by acoustic emission. *In Proc. PRASA-RobMech International Conference incorporating the 28th Annual Symposium of the Pattern Recognition Association of South Africa and the 10th robotics and mechatronics conference of South Africa*, Bloemfontein, Central University of Technology, 29 November- 1 December, 2017.

Chapter 2: LITERATURE REVIEW

2.1 Additive Manufacturing

The term "Additive Manufacturing" (AM) sometimes is referred to as "3D printing" (Stratasys, 2015). "Additive Manufacturing" is defined by ASTM as "*a process of joining materials to make objects from 3D model data, usually layer upon layer, as opposed to subtractive manufacturing methodologies*", whereas 3D printing is just one AM method and defined as "*fabrication of objects through deposition of material through a print head, nozzle or another technology*" (ASTM F2792-12a).

AM creates 3D objects from a 3D model designed by CAD software. The computer software creates virtual cuts to the model (cross-sections), generating a sequence of layers. These layers represent the material that would be added by stacking them on to each other layer by layer which in turn forms the model. The machine superimposes the layers onto each other until the entire part has been formed.

Research on AM has been ongoing for over 50 years; the first commercial systems were released in the late 1980's. A brief history of some important events in AM can be found in Appendix A. Interest in AM has grown considerably in the past decades. This is due to the great benefits the manufacturing industry has gained from the technology. The AM benefits are: geometrical freedom, shortened design-to-product time, fewer processes, mass customization and a wide range of materials that can be used. This technology is not only restricted to prototyping, but various other fields such as modelling, tool making and the production of end-use parts. Customised medical implants, tooling inserts with conformal cooling channels and functional components with high geometrical complexity are good examples of the scope of application areas of this process (Kruth *et al.*, 2010). AM can produce parts that are intricate and which have complex geometries with minimal post processing required. When engineers and designers use AM, they are able to obtain more "design freedom" because of the limitations of conventional manufacturing methods; unique products can be manufactured at low volumes in an economical way (Bikas *et al.*, 2016). AM is used for modelling, prototyping, tooling and production. The pie chart in Figure 2 shows the percentage of use of AM in the different industries. According to the Wohlers Report 2013, in 2012 the largest application in AM was the consumer products/electronics market, occupying 21.8% of the overall market. Second on the list was the motor vehicles market (18.6%) and in the third place, medical/dental applications. Whereas in 2014 industrial/business machines took first place for the largest application in the AM market, adding up to 17.5%, the consumer products/electronics and motor vehicles sectors came in at second and third at 16.6% and 16.1% respectively.

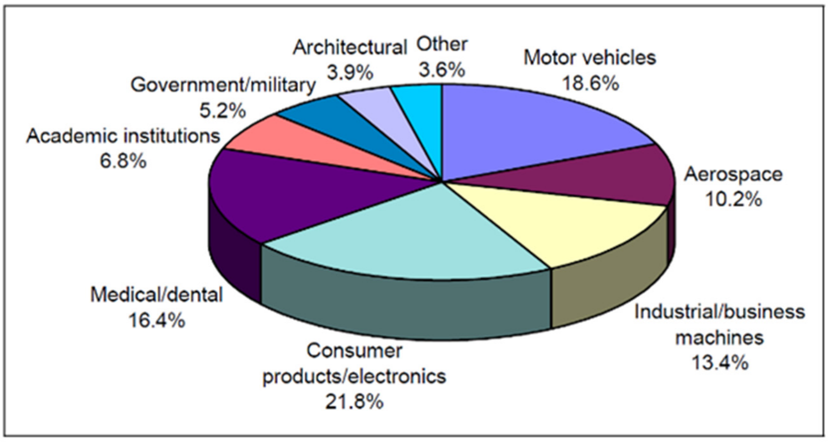

(a)

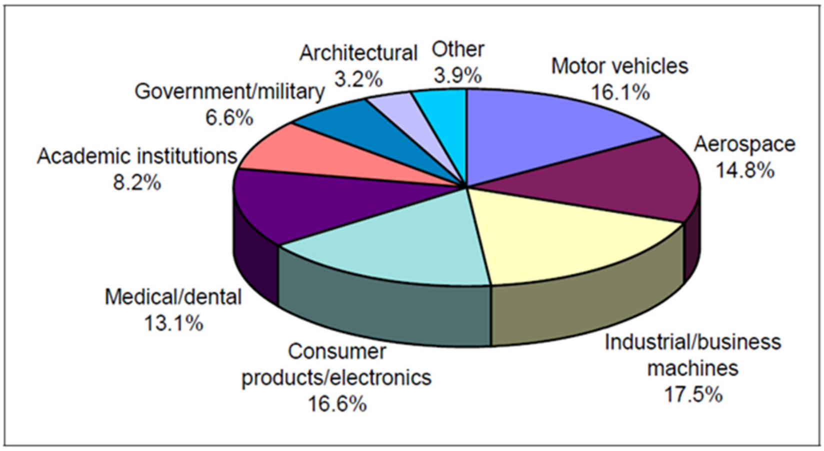

(b)

Figure 2: Analysis of the application market for AM: in 2012 (a) and in 2014 (b) (Wohlers, 2014–2015)

A large number of AM methods are available; they differ in the way the layers are deposited to create parts, the materials used and the operating principle. DMLS, makes use of powder sintering, while others, such as Stereolithography (SLA), cure a liquid material to form a solid. Each method has its advantages and disadvantages. A summary of the AM processes can be found in Table 1.

Table 1: The AM categorization (Bikas *et al.*, 2016)

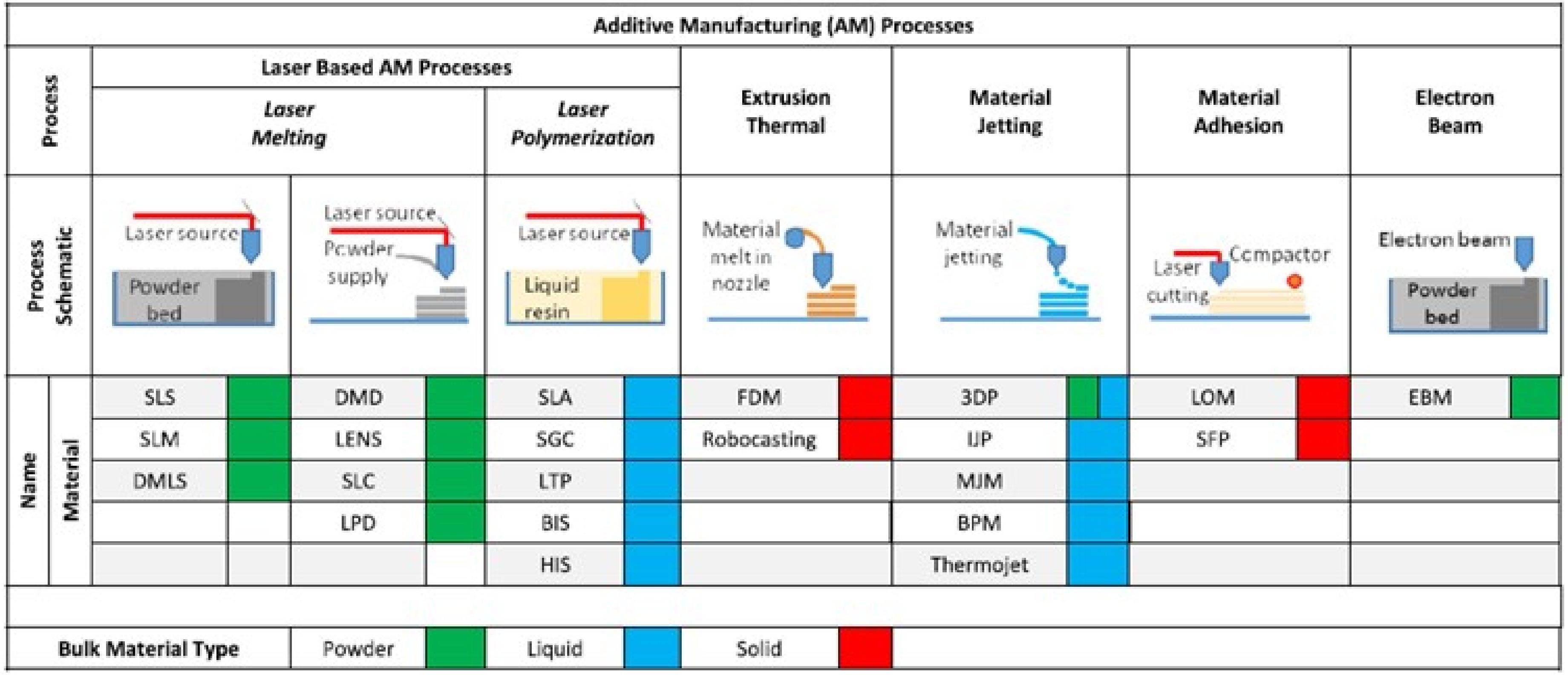

Additive Manufacturing (AM) Processes														
Process	**Laser Based AM Processes**						**Extrusion Thermal**		**Material Jetting**		**Material Adhesion**		**Electron Beam**	
	Laser Melting				***Laser Polymerization***									
Process Schematic	Laser source Powder bed		Laser source Powder supply		Laser source Liquid resin		Material melt in nozzle		Material jetting		Laser cutting Compactor		Electron beam Powder bed	
Name / **Material**	SLS	🟩	DMD	🟩	SLA	🟦	FDM	🟥	3DP	🟩🟦	LOM	🟥	EBM	🟩
	SLM	🟩	LENS	🟩	SGC	🟦	Robocasting	🟥	IJP	🟦	SFP	🟥		
	DMLS	🟩	SLC	🟩	LTP	🟦			MJM	🟦				
			LPD	🟩	BIS	🟦			BPM	🟦				
					HIS	🟦			Thermojet	🟦				
Bulk Material Type			Powder	🟩	Liquid	🟦	Solid	🟥						

A number of metal sintering methods are available depending on the heat source, these include laser, electron beam melting (EBM), arc, etc. Nickels (2016) affirms that it is hard to keep track of the differences in technologies in the growing metal AM industry, and the three most important aspects to consider when selecting a metal AM machine are: size, speed and part quality. Bikas *et al.* (2016) indicate that speed, cost of prototype, and, cost and range of materials are important considerations when choosing an AM machine. In Figure 3, the main metal AM categories are shown with their industry names, as presented by Lewandowski and Seifi in 2016. However, they indicated that most metal AM machine suppliers make use of the same principle of manufacturing from a pre-deposited metal powder and laser heat source. Some of these processes are: Direct Metal Laser Sintering (DMLS), Selective Laser Melting (SLM), LaserCusing, Laser Melting (LM), Laser Metal Fusion (LMF) and Selective Laser Sintering (SLS).

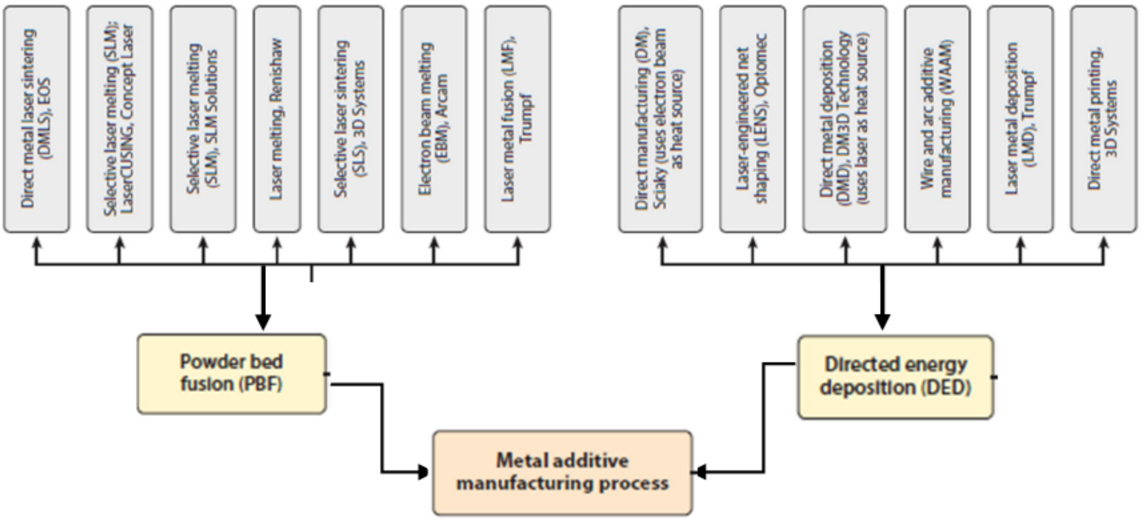
Direct metal laser sintering (DMLS), EOS
Selective laser melting (SLM); LaserCUSING, Concept Laser
Selective laser melting (SLM), SLM Solutions
Laser melting, Renishaw
Selective laser sintering (SLS), 3D Systems
Electron beam melting (EBM), Arcam
Laser metal fusion (LMF), Trumpf
Direct manufacturing (DM), Sciaky (uses electron beam as heat source)
Laser-engineered net shaping (LENS), Optomec
Direct metal deposition (DMD), DM3D Technology (uses laser as heat source)
Wire and arc additive manufacturing (WAAM)
Laser metal deposition (LMD), Trumpf
Direct metal printing, 3D Systems
Powder bed fusion (PBF)
Directed energy deposition (DED)
Metal additive manufacturing process

Figure 3: Metal AM categories (Lewandowski and Seifi, 2016)

Two other metal AM methods that are not included in Figure 2 are Binder Jetting and Sheet Lamination from Exone and Fabrasonic respectively.

2.2 Direct Metal Laser Sintering

Powder Bed Fusion (PBF) is a process by which regions in the powder bed are fused together by thermal energy as opposed to Direct Energy Deposition (DED), where the material is melted by a thermal source as the material is being deposited, as shown in Table 1. Direct Metal Laser Sintering (DMLS) is a PBF process "*used to make metal parts directly from metal powders*" (Figure 4) "*without intermediate 'green' or 'brown' parts; term denotes* *metal-based laser sintering systems from EOS GmbH - Electro Optical Systems*" (ASTM F2792, 2012).

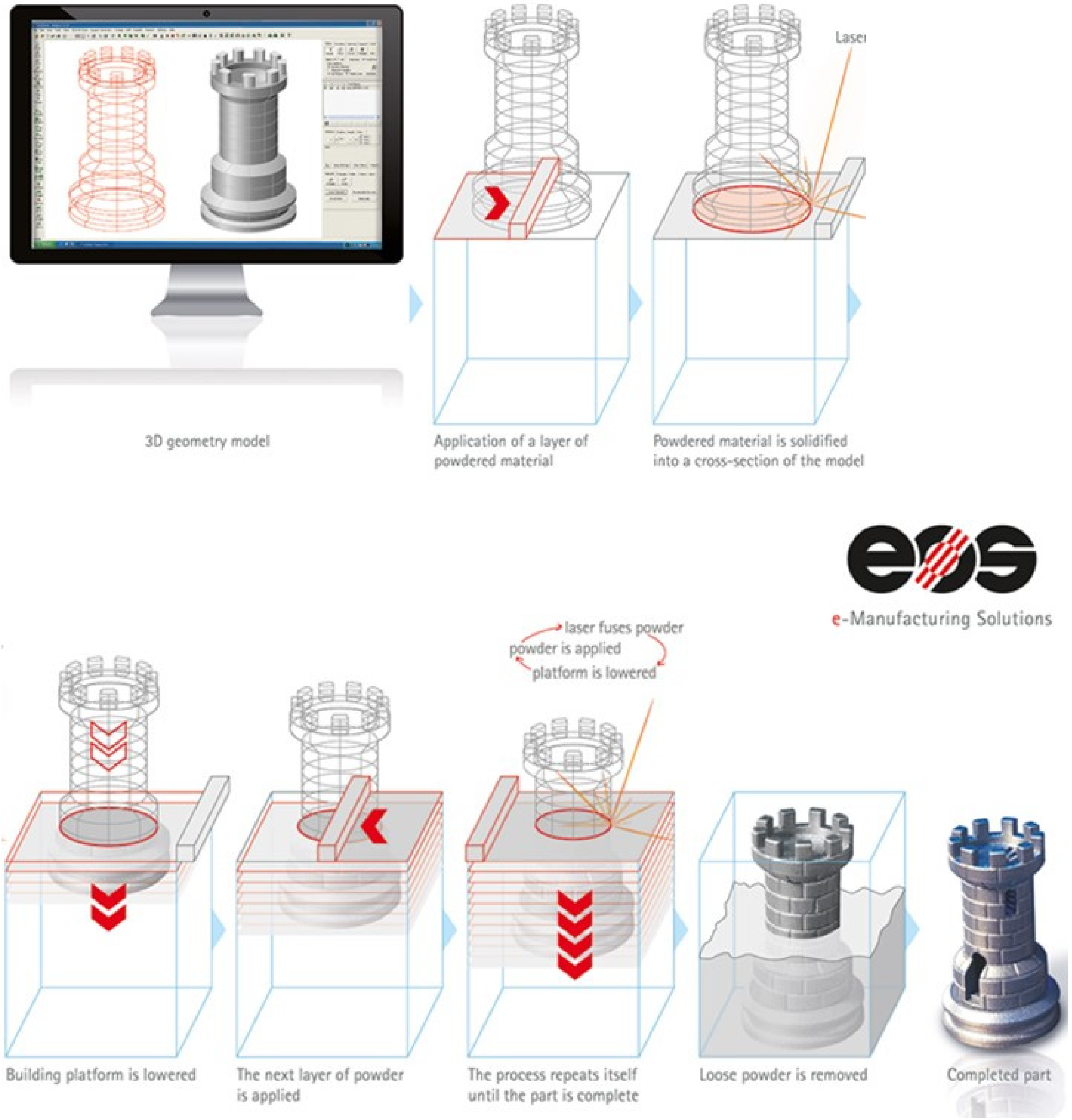
Laser
3D geometry model
Application of a layer of powdered material
Powdered material is solidified into a cross-section of the model
eos
e-Manufacturing Solutions
laser fuses powder
powder is applied
platform is lowered
Building platform is lowered
The next layer of powder is applied
The process repeats itself until the part is complete
Loose powder is removed
Completed part

Figure 4: Functional principle of the DMLS (EOS GMBH, 2016)

2.2.1 DMLS process

DMLS uses a fine powder that is melted by a laser beam which causes the material to fuse together. Firstly, a 3D model of the object is designed by CAD software. Then the software creates virtual cuts to the model, generating a sequence of layers. These layers represent the material that would be added by stacking them on to each other, layer by layer, which in turn forms the model. The parts are produced from powders that are fused by the energy of the laser beam. The laser beam scans the area of each virtual cross-section until the entire cross-section has been completed. Thereafter, another layer of powder is superimposed on the part and the beam once again scans the desired areas according to the virtual cut and also fuses the layer onto the previous one. This is repeated until the entire part has been formed (Fogannolo *et al.*, 2012; Bikas *et al.*, 2016).

DMLS is a multi-disciplinary technology based on electronics, optics, laser physics, heat transfer, metallurgy, mechanics of solids and fluid flows, etc. Figure 5 shows a schematic of basic DMLS machine components.

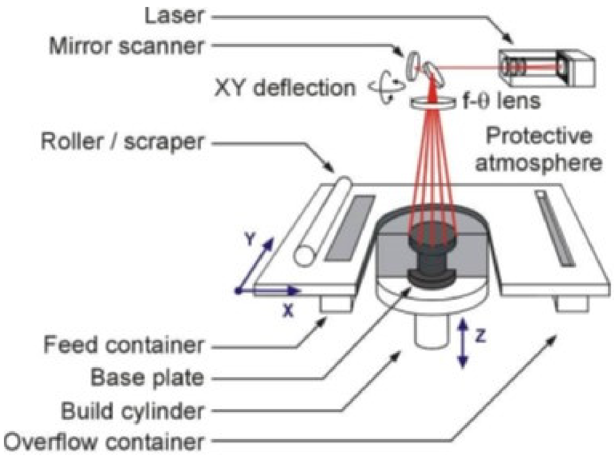

Figure 5: Basic machine components (Kruth et al., 2010)

Laser sources

Laser-powder interaction plays an important role in the DMLS manufacturing process. The word “laser” is an acronym for Light Amplification by Stimulated Emission of Radiation. In 1960, the first laser was announced by Theodore Maiman and for the past half century the technology has grown with many different techniques developed to produce laser emission. Laser is a unique source of light with unique properties. There are three properties that separate lasers from normal light sources: monochromaticity, directionality and coherence. The laser makes use of optical pumping to amplify and release photons; the way in which the amplification is generated defines the type of lasing technology – some of them being: ruby, CO_2 and fibre. In 1985, David Payne began to make fibre laser by using special-purpose optical fibres and doping them with rare earth elements.

Today, fibre lasers are very attractive for high power applications. Ytterbium fibre lasers have small photon-energy defect and high efficiency of diode pumping combined with energy dissipation advantages of the fibre geometry which allows the laser to be easily moved during lasing. The US Navy has developed a 33 kW laser weapon system (LaWS), a very powerful fibre laser using six individual fibre lasers. The most common geometry used is a dual-core structure. The outer core is undoped and collects the pumped light and guides it along the fibre. Stimulated emission generated in the fibre passes through the inner core which is monochromatic. The inner core contains the dopant that emits radiation once it is stimulated by the incoming light. The laser can be end- or side-pumped (Figure 6). The core can have various degrees of gain depending on the doping and the length of fibre used (Hecht, 2010; CSIR, 2016; Laser Focus World, 2012).

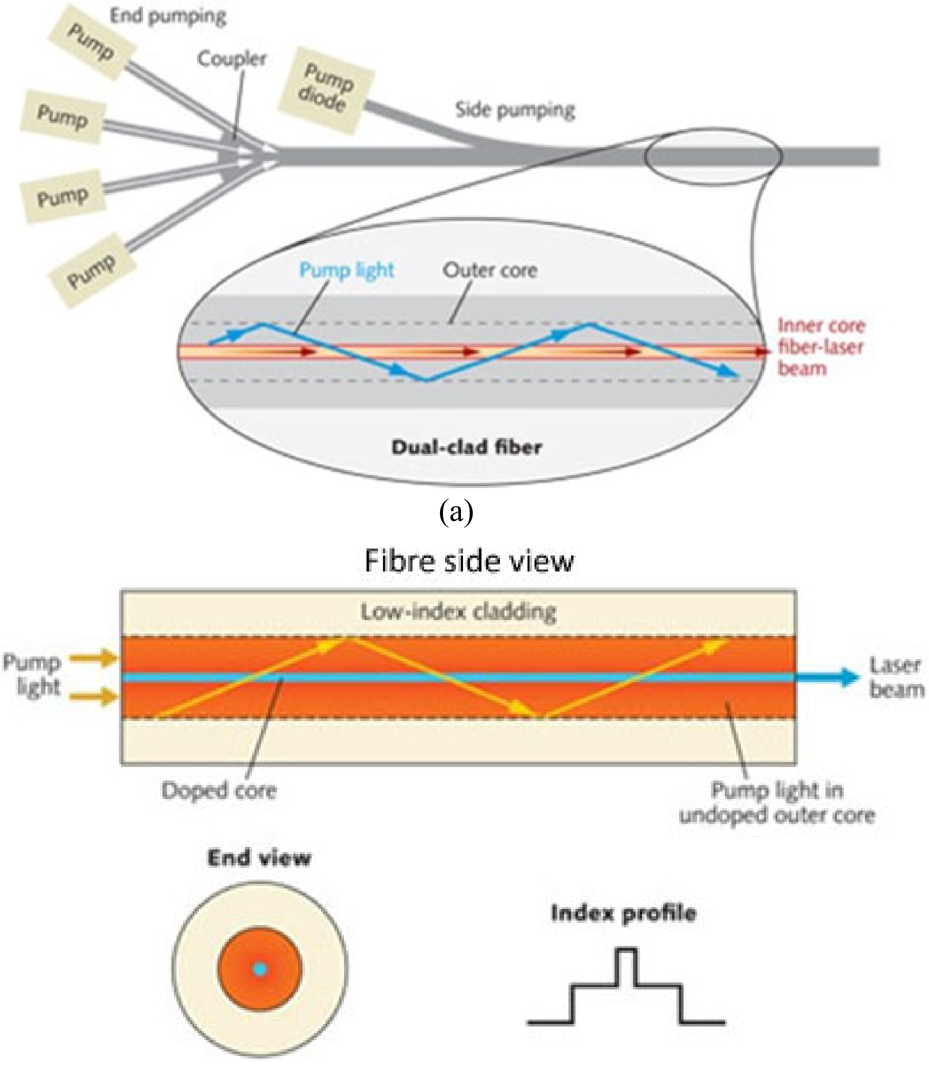
End pumping
Pump
Coupler
Pump diode
Side pumping
Pump
Pump
Pump
Pump light
Outer core
Inner core fiber-laser beam
Dual-clad fiber
Fibre side view
Low-index cladding
Pump light
Laser beam
Doped core
Pump light in undoped outer core
End view
Index profile

(a)

(b)

Figure 6: Fibre laser pumping (a) and fibre core light interaction (b) (Hecht, 2012)

The laser beam from the fibre laser passes through a series of Galvano mirrors and lenses. In Laser processing, F-Theta ($f\ \theta$) lenses are used as the laser spot can be moved on the same focal plane without distortion, as shown in Figure 7 (OptoSigma, 2016).

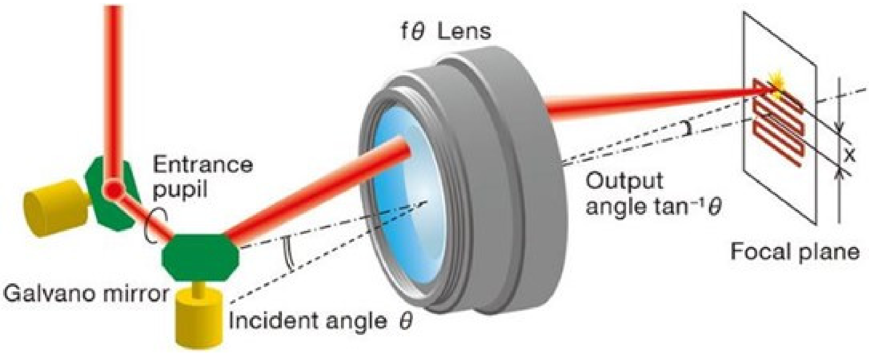

Figure 7: Galvano mirrors and lenses used to produce a laser spot on a focal plane (OptoSigma, 2016)

Laser beam – powder interaction

The laser-powder bed interaction can be divided into three stages: preheating, melting with shrinkage and re-solidification. The laser-matter interaction is dependent on several physical parameters such as wavelength, power density, time of interaction, the thermodynamic and physiochemical properties of the material, etc. The energy of the laser radiation is absorbed by the free electrons of the metal; the photons from the electro-magnetic field will oscillate the free electrons, the energy will then be transmitted to the other electrons and later to the lattice (Yadroitsev, 2009). In metals, the absorption occurs in a very thin layer on the surface of the metal and the laser radiation is predominately absorbed by the free electrons in the "electron gas". These electrons oscillate and reradiate within the metal without disturbing the solid atomic structure. The reflectivity and absorption of metals are greatly dependent on the wavelength and the photon energy. It was found that absorptivity of polished surfaces (A) is proportional to the electrical resistivity (ξr) (Yadroitsev, 2009), and agrees with:

$$A = 112.2\sqrt{\xi r}$$

The incidence angle has a great influence on the absorption of a smooth surface in relation with polarization. When the incidence angle increases, the absorption is reduced and where the angle is parallel, the absorption tends to zero. Therefore, circular polarization is preferred in DMLS because the surface of the powder bed creates various incident angles.

In DMLS, the powder bed has high absorptivity; the powder surface creates conditions for high absorption because of scattering and penetration of laser radiation into the powder layer, multiple reflections and wave guiding. The particle size determines the scattering regimes and the sensitivity to incident energy. The effective heat that can be obtained through laser irradiation on metallic powder differs from that of an opaque metallic body. Energy balance from laser radiation onto an opaque metallic body can be described by the relationship between the amount of heat that will be absorbed and the amount of heat that the material will conduct. The amount of laser absorption of the powder does not only depend on the amount of energy absorbed through the physiochemical properties, but also on the granulomorphometry and apparent density of the powder. Because of the above-mentioned, the absorption can differ greatly from powders to bulk materials. (e.g. $A_{Cu\ bulk} = 0.02$, $A_{Fe\ bulk} = 0.36$ and $A_{Cu\ powder} = 0.6$, $A_{Fe\ powder} = 0.7$ for wavelength= 1.06 µm) (Yadroitsev *et al.*, 2010; Yadroitsev, 2009).

2.2.2 Single track formation

In DMLS, a thin layer of powder is deposited onto a substrate or on a previously melted layer, thereafter the laser beam scans over the surface of the powder. After scanning, the substrate is lowered and another layer is deposited, keeping the surface of the powder in the focal plane of the laser. Due to surface tension, the molten material forms a cylinder-like track (Figure 8). Penetration into the substrate or previous layer has an additional stabilizing affect for continuous track formation. Each metallic powder material has its own set of process-parameters that yield stable or unstable tracks (Yadroitsev, 2009).

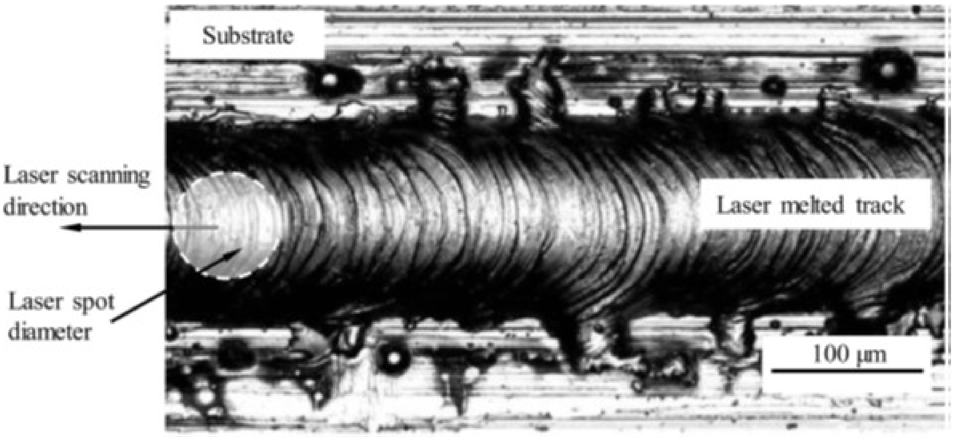

Figure 8: Track from AISI 420 powder on the substrate (top view): laser power P = 50 W; laser spot diameter 70 µm; scanning speed V = 0.10 m/s; powder layer thickness h = 50 µm (Yadroitsev et al., 2010)

The geometry of the single track is strongly dependent on the amount of material involved. Laser power density is the ratio of laser power to laser spot size, and scanning speed determines the geometric characteristics (width and depth of penetration) of the track, while the height of the track is determined by the powder layer thickness (Figure 9). If the layer thickness is too high, optimal adhesion to the substrate or previous layers will not be observed because of inadequate melting depth.

Not only the material under the laser spot is used to form the track but also the adjacent powder is melted due to scattering of the radiation and conduction through the solid material, neighbouring particles and capillary phenomena. After laser scanning, an adjacent area on the sides of the track is left without powder, known as the “denudation zone”, which can be twice that of the track width. The denudation zone defines the geometrical characteristics of the tracks and the morphology of the layers. It was found that inhomogeneity of the deposited layer and melt hydrodynamics makes the height of the tracks vary greatly (Manfredi *et al.*, 2014; Yadroitsev *et al.*, 2015; Yadroitsev and Yadroitsava, 2015).

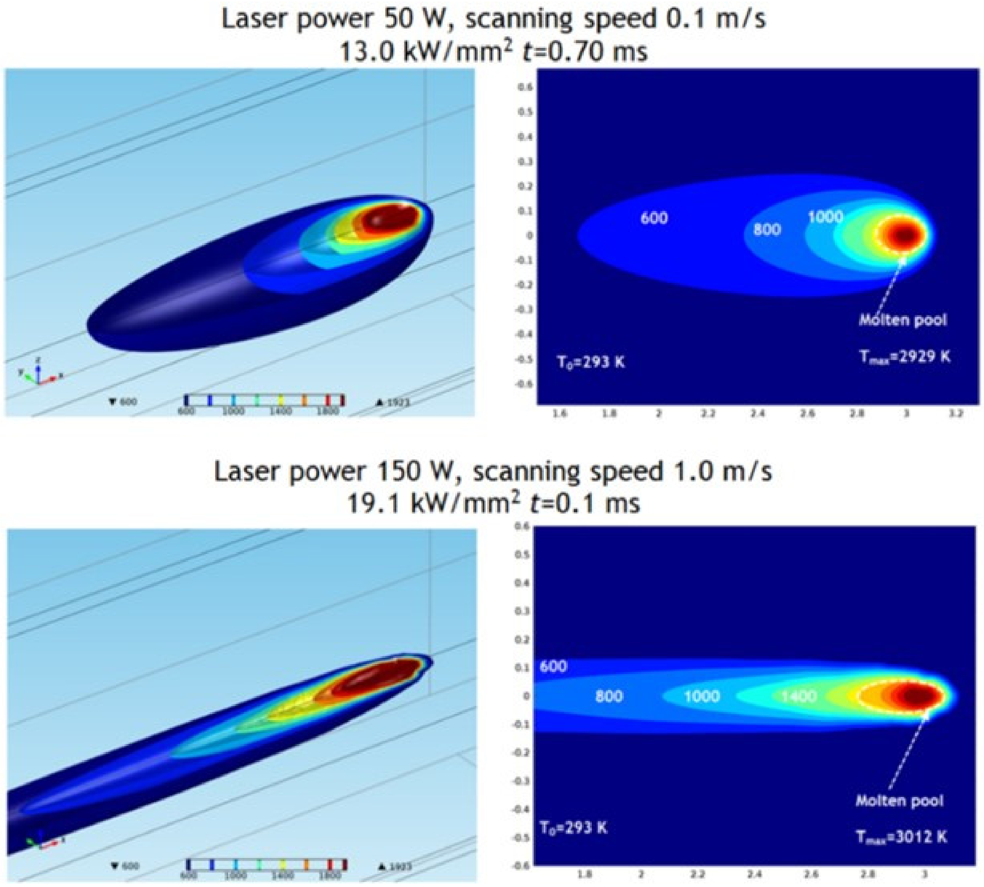

Figure 9: Results of numerical simulation of laser melting of Ti6Al4V substrate showing isothermal contours for different laser power and scanning speeds (Yadroitsev et al., 2015)

Yadroitsev *et al.* (2010) state that at low scanning speed, instability of the molten pool is caused due to an increase in melt volume and decrease in melt viscosity. Reducing laser power at low speeds influences the penetration and thus reduces the stabilizing effect that penetration gives to the molten pool. Instabilities such as distortions and irregularities of the track occur at low scanning speeds whilst at high scanning speeds it gives rise to a balling effect. If the energy is sufficient to maintain boiling and evaporation of the melt pool, the vapour recoil pressure causes distortion of the tracks. If the laser power is insufficient, the track could form a sequence of drops.

Balling is a disadvantageous phenomenon in DMLS (Figure 10). It occurs when the molten material does not wet the underlying substrate due to surface tension, which tends to spheroidise the liquid. Balling leads to rough surfaces, obstructing smooth layer deposition and decreasing the density of the part. Since liquid metals do not wet oxide films in the absence of chemical reactions, it is important to avoid oxidation and have sufficient re-melting of previous layers to break down oxide films and provide a solid-liquid interface (Kruth *et al.*, 2004). Thus, protective inert gas is used to prevent oxidation.

Vaporization occurs once the melt exceeds the melting temperature, causing some of the material to evaporate. The evaporated material will expand and cause a recoil pressure on the melt. A low recoil pressure could contribute to flattening of the melt pool, but too high pressures could push molten material out of the pool. A strict comparison between these findings cannot be made as the observations were made with laser melting experiments that were under vacuum (10^2 Pa). A further increase in temperature can even cause the material to interact with the laser beam resulting in the formation of plasma (Kruth *et al.*, 2004).

Yadroitsev *et al.* (2015) stated that distortion, irregularities and balling effect may be associated with the thermo-physical properties of the materials: granulomorphometric characteristics of the powder and inhomogeneity in powder layer thickness; energy input parameters including laser power, spot size and scanning speed; melt hydrodynamics, etc.

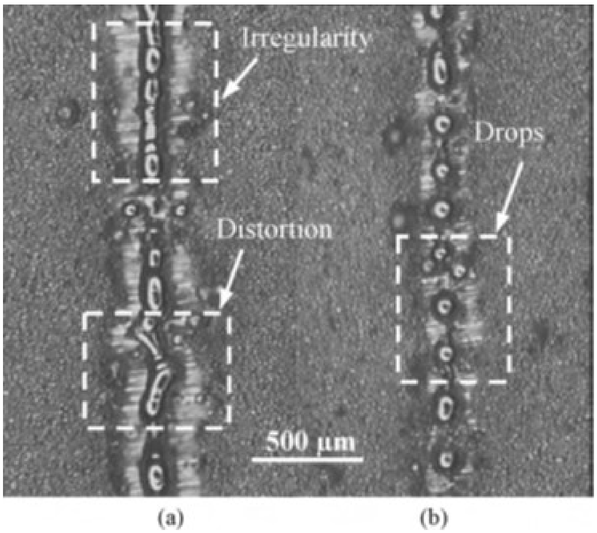

Figure 10: Instability of laser sintered tracks from SS grade 316L (−25 µm) powder on steel substrate. Thickness of the deposited powder layer is 50 µm, scanning speed V = 0.02 m/s: (a) P = 25W, (b) P = 12.5 W (Yadroitsev et al., 2010)

At low scanning speed with high laser power, there is an increase in melt volume and a decrease in melt viscosity and irregularities appear. At lower laser powers with low scanning speeds, insufficient melting and penetration occurs, and if there is sufficient energy to maintain melting, vapour recoil pressures would cause distortion of sintered tracks. With a further reduction of laser power, balling occurs, Figure 11 (Yadroitsev *et al.*, 2010).

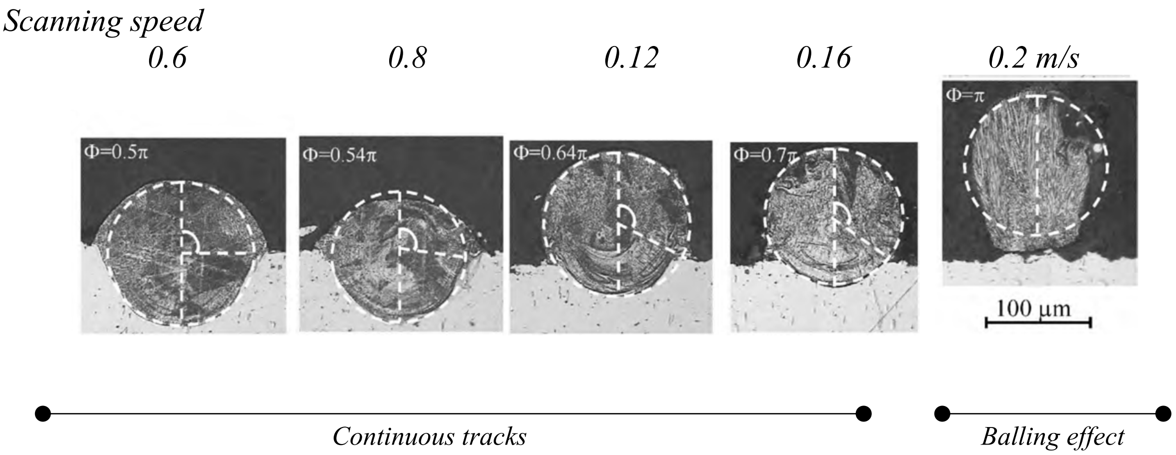

Figure 11: Cross-sections of laser sintered tracks from SS grade 904L powder on steel substrate (Yadroitsev et al., 2010)

As was indicated, short interaction of the powder and heat source caused by the high scanning speed of the laser beam leads to rapid heating, melting and circulation of molten metal, driven by surface tension and temperature gradients. During melting, drastic shrinkage occurs – the density increases from about 50% (apparent density of powder material) to 100% density once melted. The resulting heat flow will determine the geometry of the melt pool, the cooling rate and the transformation reaction in the melt pool and heat-affected zone (Kruth *et al.*, 2010).

Mesoscopic simulation of single tracks

Khairallah *et al.* (2016) takes a different experimental approach to that of the Finite Element Method (FEM) to model sparking, spattering and denudation effects during DMLS. A new high-fidelity mesoscopic simulation capability was used to study physical mechanisms without making physical assumptions; this model uses a laser ray tracing energy source and gives a 3D account of fluid flow effects due to recoil pressure, Marangoni flow and evaporative cooling with radiating surface cooling. Marangoni flow exists in a fluid due to a difference in surface tension – this causes a mass transfer between two fluids, in this case driven by temperature difference.

In Figure 12, the heat from the 150 W laser collides with the surface of the particle and diffuses inward. The laser is initially centred above the 27 μm particle and moves to the right at 1000 mm/s, the heat releases slowly to the substrate through a small contact point (Figure 12a).

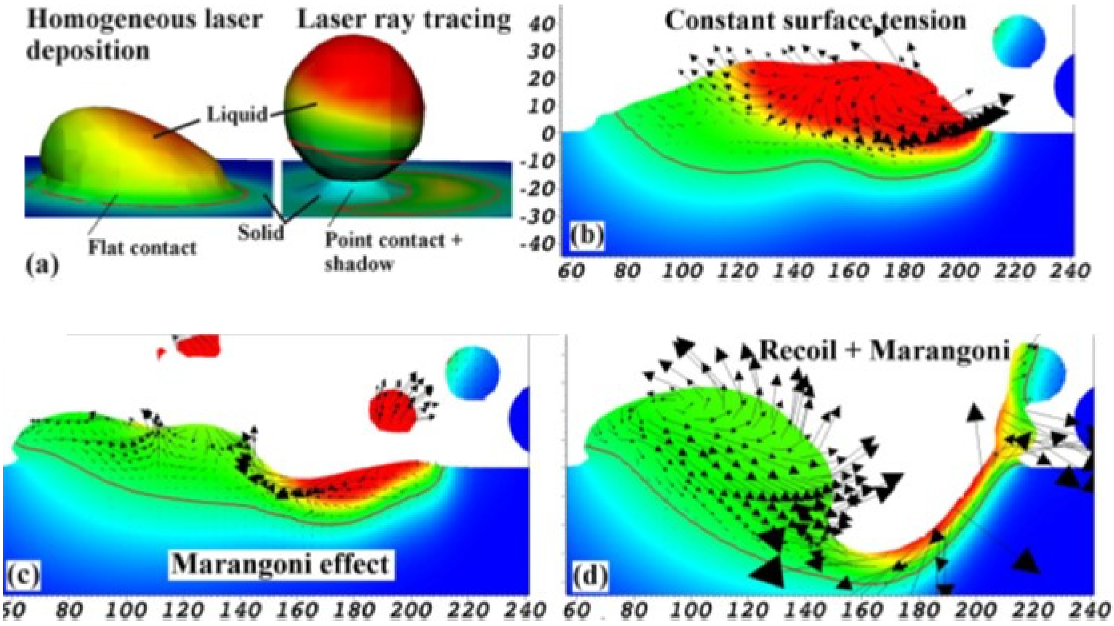

Figure 12: Illustration of the simulation laser-powder-substrate interaction: non-uniform melting of particle (a), balling effect due to surface tension (b) Marangoni effects (c), recoil with Marangoni effects (d). The red colour corresponds to temperature scale capped at 4000K, blue is 293K. The red contour line is the melt line. The powder particle is illuminated by a laser moving to the right for 10 µs. The melt tracks are 2D slices of 3D simulations (Khairallah et al., 2016)

If there is not sufficient energy, the particle will be partially melted and contribute to surface and pore defects (Figure 12b). The surface tension causes a balling effect creating liquid spheres. The melt pool is driven by buoyancy. A steep temperature gradient occurs beneath the laser which create Marangoni effects that drive the melt flow from the laser spot to the cold rear – this increases the melt depth, recirculating the flow which cools the location of the laser spot and creates spattering of melt with low viscosity that ejects away from the surface (Figure 12 c). Figure 12 d shows depression of the melt pool surface due to the vapour recoil pressures. In the area below the laser spot, the material could easily reach boiling point which causes recoil pressures and melt pool surface depression. By combining the Marangoni effect with the vapour recoil pressures, the melt depth increases significantly. This also leads to an increase in surface area of the melt pool which results in additional evaporative and radiated cooling (Khairallah *et al.*, 2016).

Thus, the track can be subdivided into three differentiable regions: 1) a depression zone located at the laser spot, 2) a tail end region of the melt track located near the end, and 3) a transition region inbetween, as shown in Figure 13. The depression has a complex flow and can be seen as the source of fluid. The transition zone has a surface velocity component (*Vx*) in the flow to the rear. At the tail, the backward flow starts to break up.

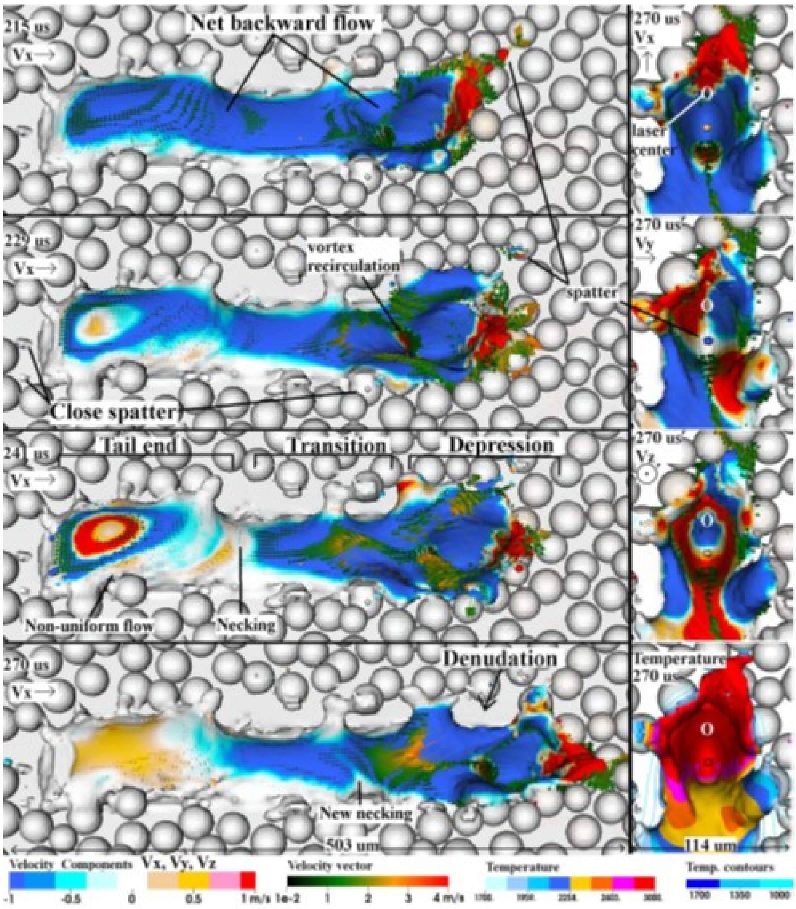
215 us
Vx
Net backward flow
270 us
Vx
laser center
225 us
Vx
vortex recirculation
spatter
270 us
Vy
Close spatter
241 us
Vx
Tail end
Transition
Depression
270 us
Vz
Non-uniform flow
Necking
270 us
Vx
Denudation
Temperature 270 us
New necking
503 um
114 um
Velocity Components Vx, Vy, Vz
-1
-0.5
0
0.5
1 m/s
Velocity vector
1e-2
1
2
3
4 m/s
Temperature
Temp. contours
1700
1350
1000

Figure 13: Time snapshots of the melt flow showing spattering and denudation. The melt has a large backward flow (blue colour; Vx<0) due to Marangoni effect and recoil, compared to forward flow (Vx> 0; red colour). The backward net flow breaks up later in time at the necking. The velocity scale is capped at +-1m/s for better visualization. The right panel magnified view at 270µs (flow rotated by +90°) shows the velocity components (Vx, Vy, Vz) and the temperature (with contour lines) at the depression. The white letter O shows that the laser centre is not at the bottom of the depression. (Khairallah et al., 2016)

Depression collapse and pore formation mechanism can be seen in Figure 14. A decrease in temperature and recoil pressure as surface tension increases causes the depression to close. The melt initially moves outwards but then abruptly changes direction; this fast flow can trap gas bubbles and form pores at the bottom of the track. The melt on the sides of the track will attract adjacent particles creating a denudation zone; this is as a result of the melt rising up, catching onto particles due to surface tension, whereafter they are melted and dragged back in the melt due to recirculating flow of the surface tension. Liquid build-up develops in front of the laser in the scanning direction. This build-up is similar to that of a boat moving in water. The liquid runs up the front wall of the depression and spills over onto particles ahead of the laser beam. Lateral shallow pores occur in the transition zone if a particle does not melt completely and merges with the melt pool – voids between particles may contribute to pores. End process pores arise at the end of scanning vectors when the laser is switched off; these pores form when the large pool collapses due to sudden heat removal. As a solution, it is suggested to ramp down the power of the laser at the end of scanning tracks (Khairallah *et al.*, 2016).

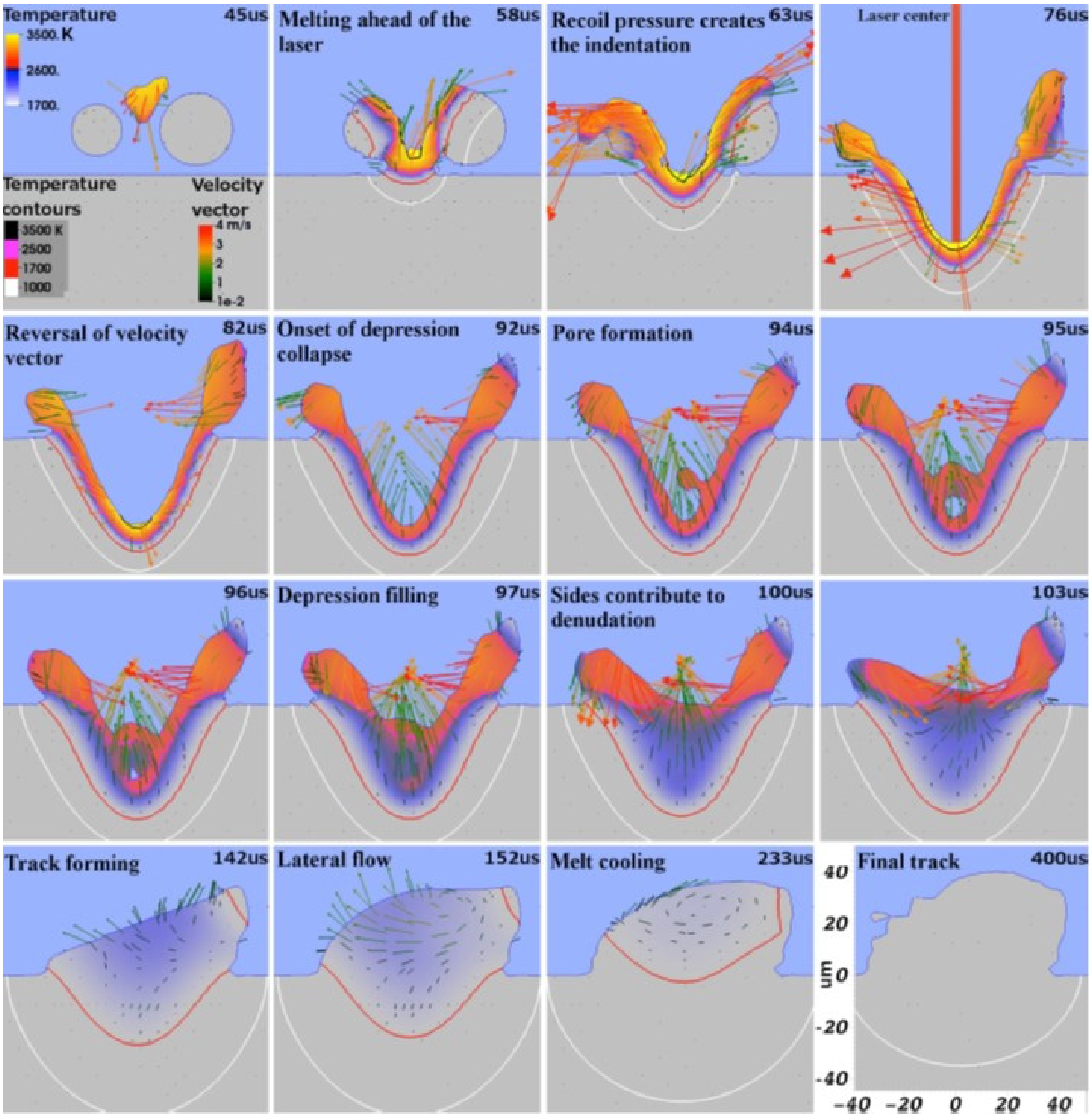

Figure 14: Lateral 2D slices showing the temperature and velocity field of the melt as the laser scans (direction out of page) by a fixed location. They show the events before the arrival of the laser centre (45-76 µs), the indentation formation (76-82 µs), the indentation collapse and formation of a pore (92-103 µs) and the asymmetrical flow pattern due to an asymmetrical cooling as the melt solidifies (142-400 µs). (Khairallah et al., 2016)

2.2.3 Single layer formation

As mentioned above, a single layer is formed from a sequence of tracks. Because of the creation of the denudation zone near the first track, powder material available for the second track would be less, thus the laser melting process of the second track will be different to the first, see Figure 15. Yadroitsev (2009) confirms that for consecutive tracks, the amount of melted material decreases with a decrease in hatch distance. The previously melted track can absorb fewer incidents of light than powder and acts as a heat sink for laser energy, reducing the amount of material melted. Non-uniform thickness of the next powder layer could be crucial, as a defective part with a porous structure would be produced. The denudation zone can be up to twice the width of the track (Yadroitsev *et al.*, 2015).

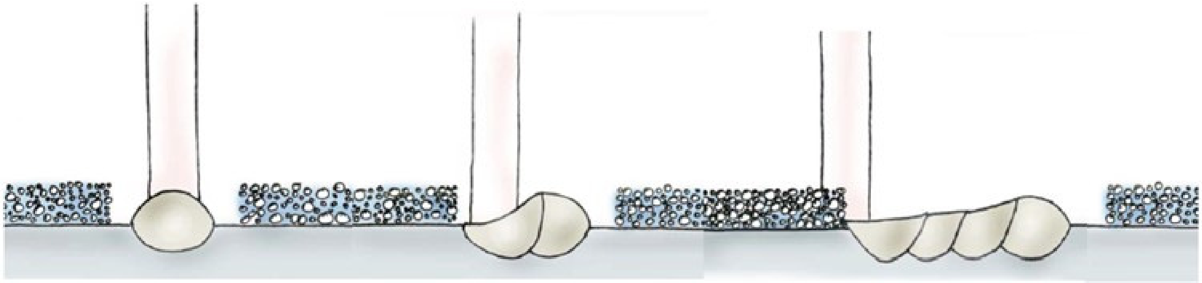

Figure 15: Schematic showing how denudation affects track height (Yadroitsev & Smurov., 2011)

Surface morphology of single layers is dependent on: the geometrical characteristics of single tracks, scanning strategy and hatch distance. The scanning strategy will have a direct influence on density, residuals stresses and microstructure formed during DMLS. Re-melting of entire layers during DMLS may result in higher densities, but also cause an increase in production time. If the layer thickness is too high, no optimal adhesion to the substrate or previous layers is able to occur because of inadequate melting depth.

Scanning strategies

For DMLS, different scanning strategies can be used: one-zone strategies, i.e. one-direction or zig-zag scanning, two-zone strategies, stripe and island strategy, spiral strategy, changing direction of the scanning for next layer, etc. (Figure 16). In a one-zone strategy, tracks overlap each other. In a two-zone strategy, each layer is processed twice; a certain hatch distance is selected for the first scan, once the first scan is completed, the laser scans in between the tracks and re-melts each of the two neighbouring tracks in the same direction or alternative directions. The default pattern of EOS DMLS machines makes use of stripes with zig-zag scanning and rotating the scanning direction by 67° between consecutive layers.

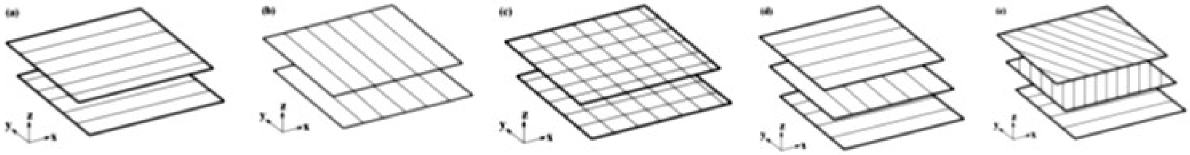

Figure 16: Different scanning strategies (Manfredi et al., 2014)

In Figure 17, the top surface of one-zone- and two-zone strategies are compared. The two-zone strategy has an increased surface quality and a reduction of droplets. In the two-zone strategy, different process-parameters can be used for the second scan as solidified material (not powder) is processed during rescanning.

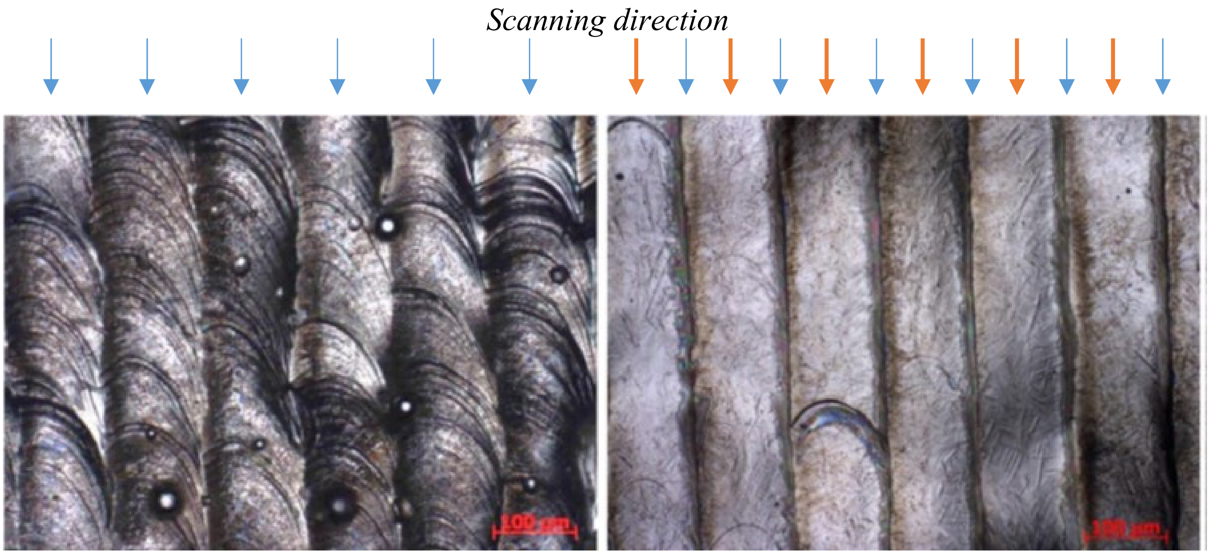

(a) (b)

Figure 17: Top view of single layer produced by one-zone (a) and two-zone strategy (b) of laser scanning. P = 50 W; powder layer thickness h = 50 µm; scanning speed V = 0.12 m/s and hatch distance s = 120 µm (Yadroitsev et al., 2015)

Figure 18 shows an example of an island scanning strategy; the area is divided into small square islands. The scanning sequence then selects the different squares to be scanned at random. The size and orientation in between layers can be different.

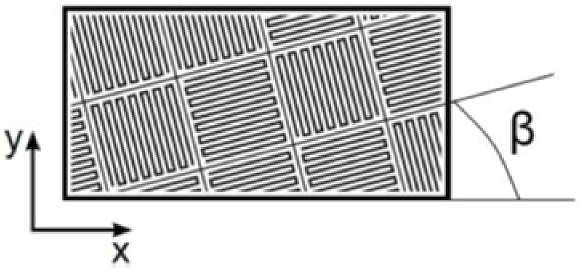

Figure 18: Example of scan pattern for island scanning with revealed islands with the rotation angle beta (Kruth et al, 2010)

The thermophysical conditions of the different strategies vary because the absorptivity, reflectivity, thermal conductivity and heat transfer of powder and solid material differ from one another.

During scanning, the galvano mirrors experience accelerations as they move to scan the different tracks. The inertia of these mirrors results in them taking some time to accelerate to the desired scanning speeds as they move to and fro. To avoid variations in scanning speeds at the edges of the part, DMLS software makes use of a technique called Skywriting (Figure

19). Skywriting solves this problem by moving the scanning track formed by the movement of the mirror past the desired point of scanning, but only switching the laser on when it is at the areas that are to be scanned (Manfredi *et al.*, 2014).

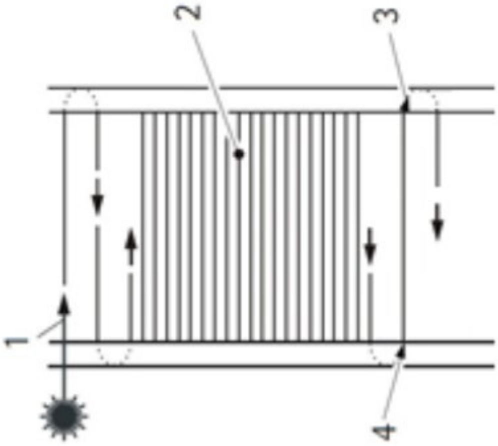

Figure 19: The exposure track (vector) is shown by a solid line (1). The dashed line represents the skywriting. In this area the laser beam is switched off (3). At the beginning of the part (4), the laser power is switched on with a sized value and the laser beam is run with a constant velocity (Manfredi et al. 2014)

As the melted zone is usually greater than the laser diameter, it is necessary to compensate for the dimensional error. This compensation takes place by shifting the beam path to the inside of the original CAD slice; this is called beam offset (BO) – Figure 20 shows these exposure strategies. The distance between the tracks is referred to as the hatch distance and in DMLS it is usually set to be equal to the laser beam diameter (Manfredi *et al.*, 2014; Yadroitsev, 2009; Kruth *et al.*, 2010).

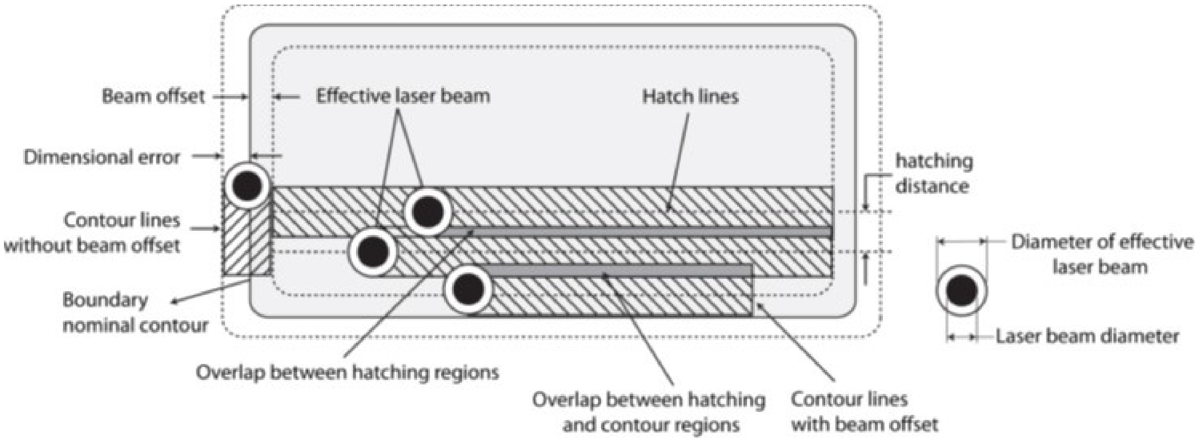
Beam offset
Effective laser beam
Hatch lines
Dimensional error
hatching distance
Contour lines without beam offset
Diameter of effective laser beam
Boundary nominal contour
Laser beam diameter
Overlap between hatching regions
Overlap between hatching and contour regions
Contour lines with beam offset

Figure 20: Exposure strategy (EOS Training Manual, 2012)

In DMLS, an object can be produced with different process-parameters for different parts of the 3D object. Different parameters can be assigned for up-skin, down-skin and core as well as for overlapping areas of the object for improved metallurgical contact with the substrate, surface quality, joining among overlapping zones or just in-situ treatment to change material properties. Down-skin is an important factor as it directly influences the capability of producing features such as overhangs.

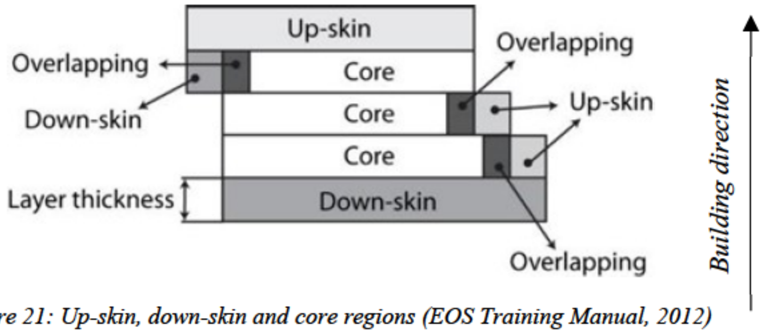
Up-skin
Overlapping
Overlapping
Core
Down-skin
Core
Up-skin
Core
Layer thickness
Down-skin
Overlapping
Building direction

Figure 21: Up-skin, down-skin and core regions (EOS Training Manual, 2012)

2.2.4 Three-dimensional objects

DMLS objects consist of a set of individual single layers and tracks. The primary units are single tracks; their combination creates a single layer, and from a sequence of layers a 3D object is formed. To produce fully dense objects from the powder material, optimal process-parameters and a specific strategy of manufacturing should be used.

Post processing of DMLS components includes polishing and heat treatment to change material properties and reduce stresses; HIP is used for reducing porosity and also for changing the material properties. To produce a metal product that is dense with good mechanical properties, three main categories with their sub-categories need to be addressed, as shown in Figure 22.

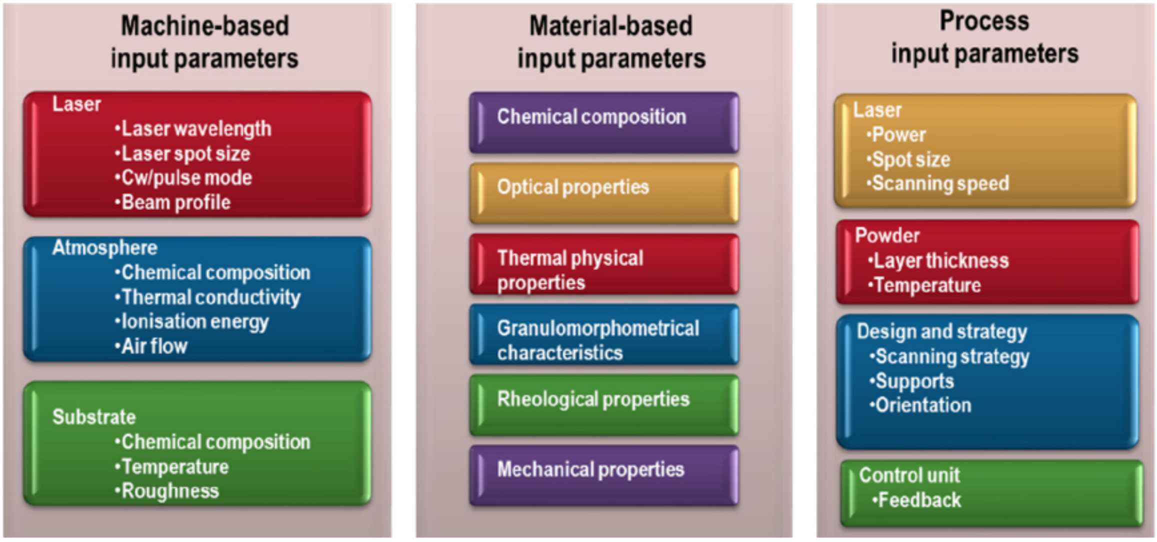
Machine-based input parameters
Laser
•Laser wavelength
•Laser spot size
•Cw/pulse mode
•Beam profile
Atmosphere
•Chemical composition
•Thermal conductivity
•Ionisation energy
•Air flow
Substrate
•Chemical composition
•Temperature
•Roughness
Material-based input parameters
Chemical composition
Optical properties
Thermal physical properties
Granulomorphometrical characteristics
Rheological properties
Mechanical properties
Process input parameters
Laser
•Power
•Spot size
•Scanning speed
Powder
•Layer thickness
•Temperature
Design and strategy
•Scanning strategy
•Supports
•Orientation
Control unit
•Feedback

Figure 22: DMLS parameters (Yadroitsev, 2009)

The properties of parts produced by this technology depend on the geometrical characteristics of each single track, the morphology of each layer, and the cohesion of tracks and layers. Changing only one process parameter or powder property (for example, particle size distribution or chemical composition) may cause porosity or cracks in the 3D object. Since temperature gradient and heat transfer determine the microstructure and final mechanical properties of the part, studies of temperature distribution during DMLS/SLM are of primary importance. Yadroitsev *et al.* (2015) suggested a parametric algorithm to produce high-quality DMLS 3D objects as shown in Figure 23.

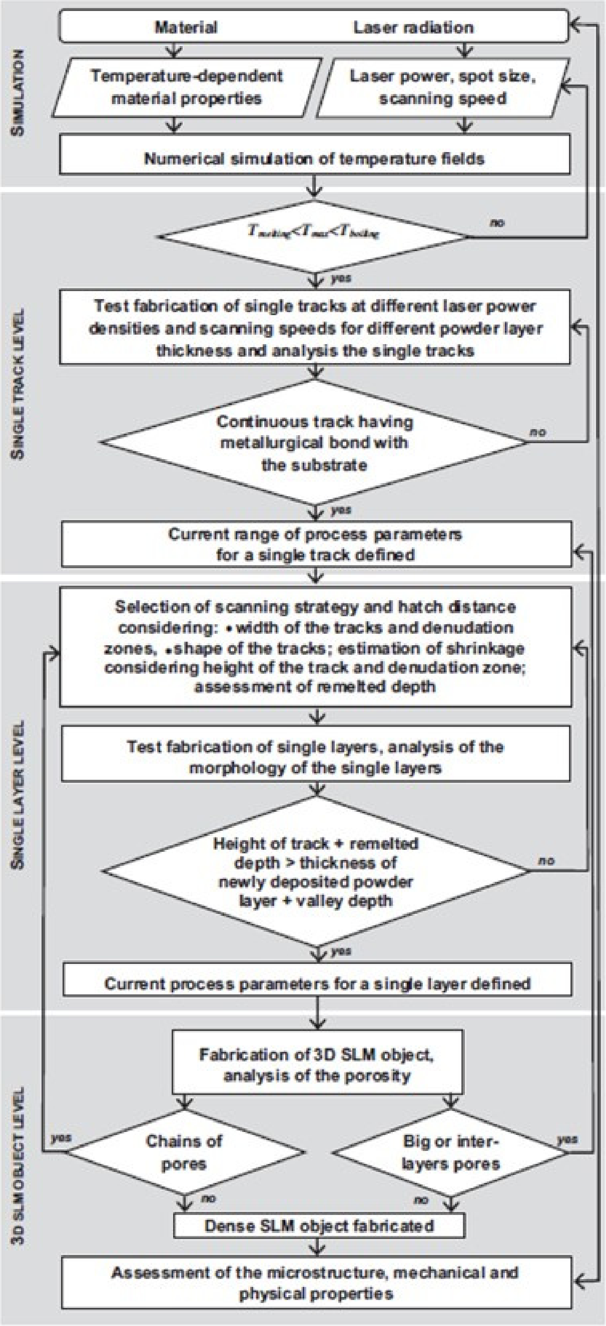
SIMULATION
Material
Laser radiation
Temperature-dependent material properties
Laser power, spot size, scanning speed
Numerical simulation of temperature fields
SINGLE TRACK LEVEL
$T_{melting}<T_{max}<T_{boiling}$
no
yes
Test fabrication of single tracks at different laser power densities and scanning speeds for different powder layer thickness and analysis the single tracks
Continuous track having metallurgical bond with the substrate
no
yes
Current range of process parameters for a single track defined
SINGLE LAYER LEVEL
Selection of scanning strategy and hatch distance considering: • width of the tracks and denudation zones, • shape of the tracks; estimation of shrinkage considering height of the track and denudation zone; assessment of remelted depth
Test fabrication of single layers, analysis of the morphology of the single layers
Height of track + remelted depth > thickness of newly deposited powder layer + valley depth
no
yes
Current process parameters for a single layer defined
3D SLM OBJECT LEVEL
Fabrication of 3D SLM object, analysis of the porosity
yes
Chains of pores
Big or inter-layers pores
yes
no
no
Dense SLM object fabricated
Assessment of the microstructure, mechanical and physical properties

Figure 23: Algorithm for finding optimal DMLS/SLM process-parameters (Yadroitsev et al., 2015)

Another factor that can influence the quality of the final 3D object is the resolution of the standard triangle language (STL) file. STL files are accepted as the industry standard when it comes to rapid prototyping (Materialise, 2015; SolidWorks, 2015). An STL file creates surface data from the 3D CAD model that is translated into triangles in a 3D space. The physical resolution of the STL file determines the size of the STL file; finer resolution leads to smoother surfaces (often depending on machine capabilities) and creates larger files, while smaller resolutions might affect the geometry of the part, as shown in Figure 24.

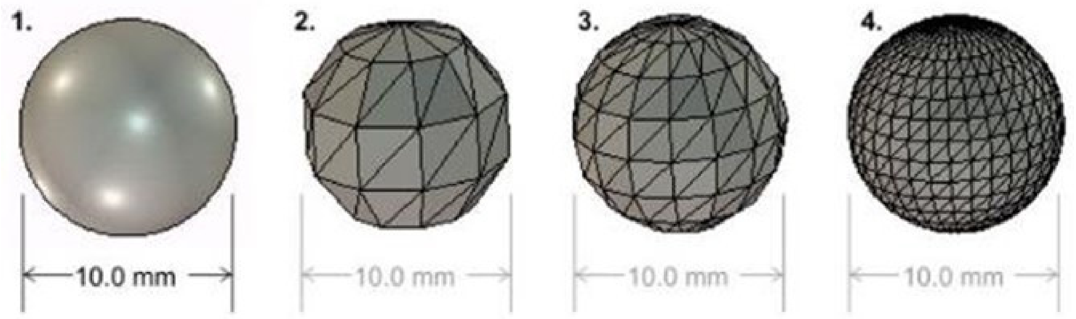

Figure 24: CAD model of sphere (1) and effect of STL resolution on sphere geometry, increasing from left to right (2-4) (SolidWorks, 2015)

2.2.5 Summary

The DMLS process is a parameter-sensitive process – a slight change in one parameter could have a great influence on the outcome. DMLS involves a multi-step process for building a part. To produce a 3D object, the primary tracks of each layer need to be created at optimum laser power, scanning speed, hatch distance, etc. The scanning strategy used affects the layer morphology and also temperature gradients. The sensitivity of the DMLS process makes testing and quality control all the more necessary.

2.3 Properties of DMLS objects

2.3.1 DMLS microstructure

The power density of the laser determines the temperature gradient and the scanning speed determines how long the heat source will interact with the material. A Gaussian laser beam has spatial intensity distribution, and the resulting temperature fields across the molten pool are not uniform. Figure 25 shows the etched DMLS AISI 240 steel cross-sectional microstructure of layers. It can be seen how the hemispheres of the tracks overlap, meaning that each track penetrated into the adjacent tracks. The melt pool geometry influences the grain growth and the resulting microstructure of the parts. A high temperature gradient causes non-equilibrium of solid/liquid interface leading to rapid solidification of the melt. Due to this rapid solidification, various effects arise – among these are changes in general microstructure and non-equilibrium phases (Yadroitsev *et al.*, 2015). The grain structure is also influenced by the previous solidified layer. Since the material's mechanical properties are dependent on the microstructure, DMLS part properties will differ from materials produced by conventional methods (Kruth *et al.*, 2010; Yadroitsev *et al.*, 2015).

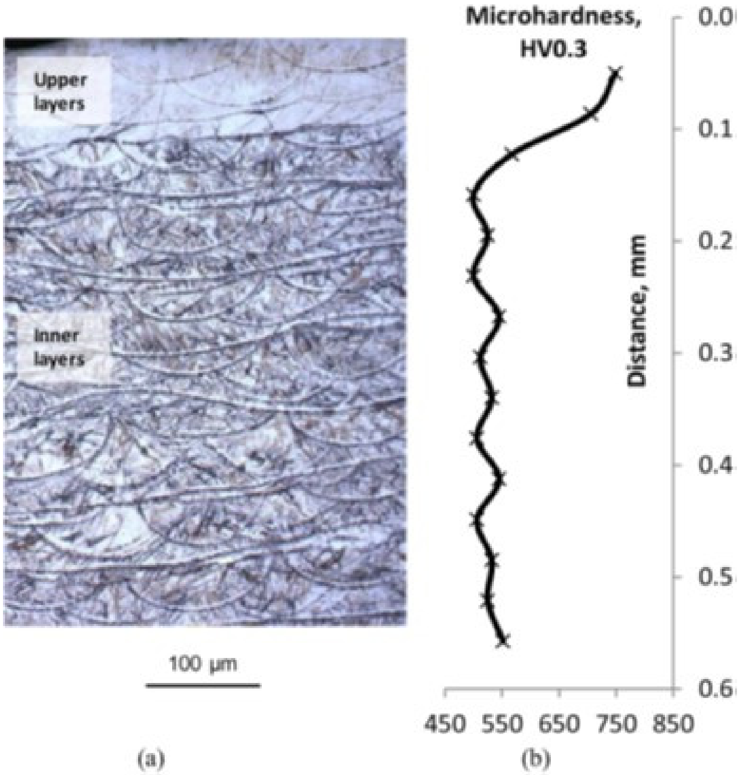

Figure 25: Microstructure (a) and microhardness profile (b) of AISI 420 steel at P = 60 W, V = 0.12 m/s, h = 40 µm, s = 120 µm (Yadroitsev et al., 2015)

Broderick *et al.* (1985) showed that the microstructure of rapidly solidified Ti6Al4V is greatly influenced by the cooling rate. Yadroitsava *et al.* (2015b) measured and simulated the thermal fields of Ti6Al4V alloy during DMLS. The inner solidified layer was subjected to several heating and cooling cycles. Figure 26 shows how the temperature of Ti6Al4V alloy varies at 30, 60, 90, 120 µm in depth, with laser power at 150 W and scanning speed at 1.2 m /s. It was found that the maximum temperature was below 3000 K. The depth of the heat-affected zone is dependent on the material properties and process-parameters.

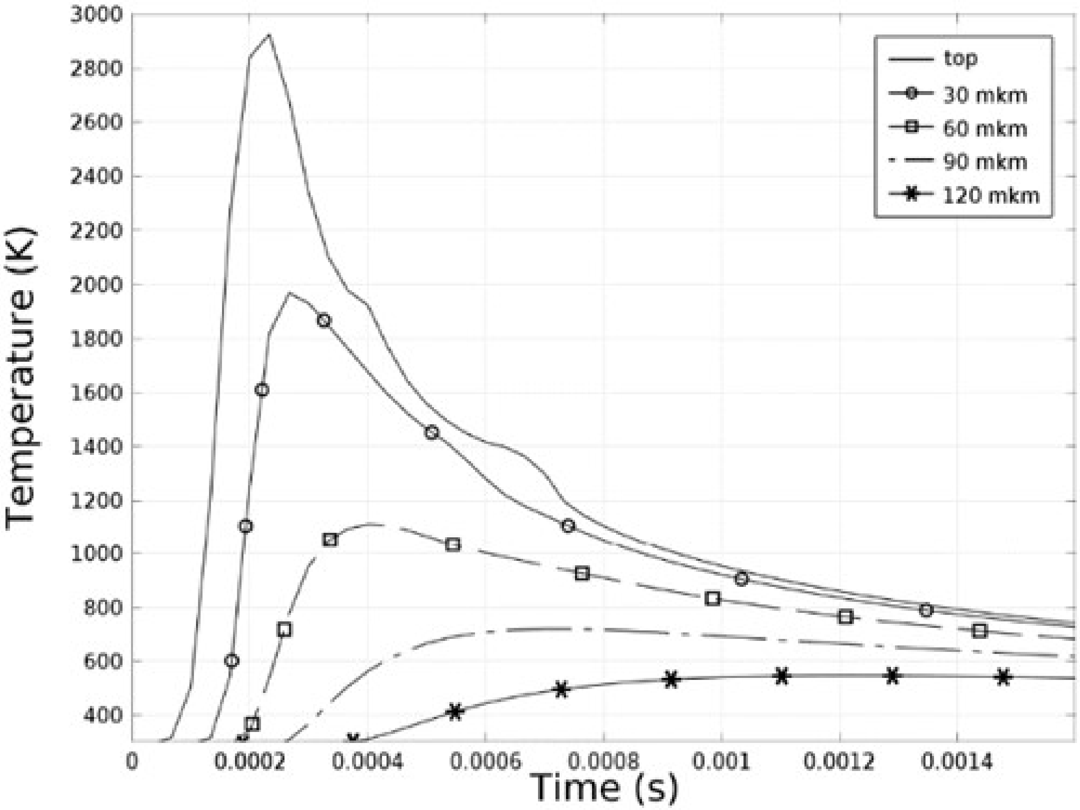

Figure 26: Temperature evolution during laser scanning Ti6Al4V alloy at depths from the surface: 30, 60, 90 and 120 μm in depth. Laser power is 150 W; scanning speed is 1.2 m/s (Yadroitsava et al., 2015b)

In Figure 25, a clear distinction between the upper and lower layers of DMLS AISI 420 stainless steel can be seen. The upper layers have a different microstructure and microhardness to that of the inner layers due to the in-situ tempering from the heat of the scanning cycles. This shows that in DMLS, an object with different microstructure and material properties can be generated by changing the process-parameters.

The scanning strategy used, can be recognized in the microstructure of the part. In Figure 27, the microstructure of AISI 316L stainless steel produced with DMLS is observed with an optical microscope, where the tracks and direction of scanning are clearly distinguishable. In Figure 25, a cross-section of AISI 420 part is shown where the solidified zones can be identified by the curved edges where the track bonded onto the previous tracks. In DMLS, the microstructure is a result of rapid solidification and its features correlate with the conducting direction. The melt pool boundaries of the track may cause anisotropy of the mechanical properties of the materials.

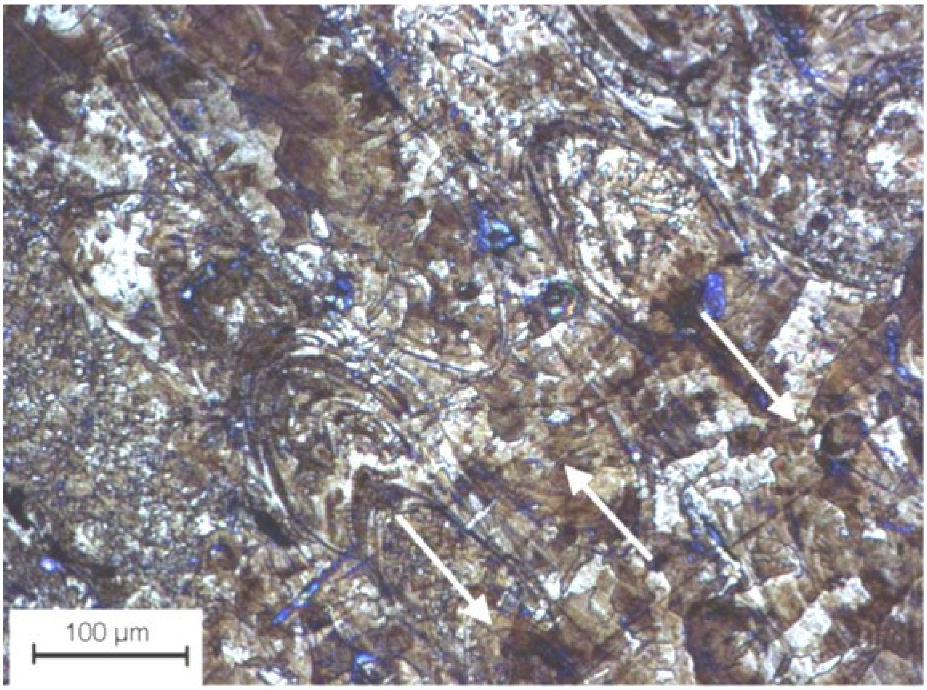

Figure 27: Top surface of a DMLS part from AISI 316L stainless steel (polished and etched) (Kruth et al, 2010)

2.3.2 Residual stress

Residual stress is the internal stress of a material after it has been through plastic deformation; in other words, the internal stresses that keep the materials microstructure in its deformed shape. Residual stress can have both undesirable and desirable effects on the material properties. It is a known fact that residual stress occurs in every existing material. The amount of residual stress formation in a material varies due to the following three factors: the type of material, material processing and the material loads (Hauk, 1997).

In DMLS parts, residual stress is a concern because it could cause part distortion fracture to initiate and reduce the strength of the part (Kruth *et al.*, 2010). Where specimens are exposed to thermal stresses, the rapid heating of the upper surface accompanied with slow heat conduction causes a steep temperature gradient. This results in compressive strains occurring in the bottom layers, because the surrounding material restricts free expansion of the top layers during heating. (Figure 28a). During cooling, the tensile upper layers become shorter than the bottom layers causing bending towards the laser (Figure 28a). The way in which these stresses are generated, cause the consolidated layers to bend towards the laser beam, which in turn could result in distortion and part failure by delamination or cracking. The cooling of layers below the top layers also adds to the tensile stress in the part as the layers shrink while their temperature decreases (Kruth *et al.*, 2004).

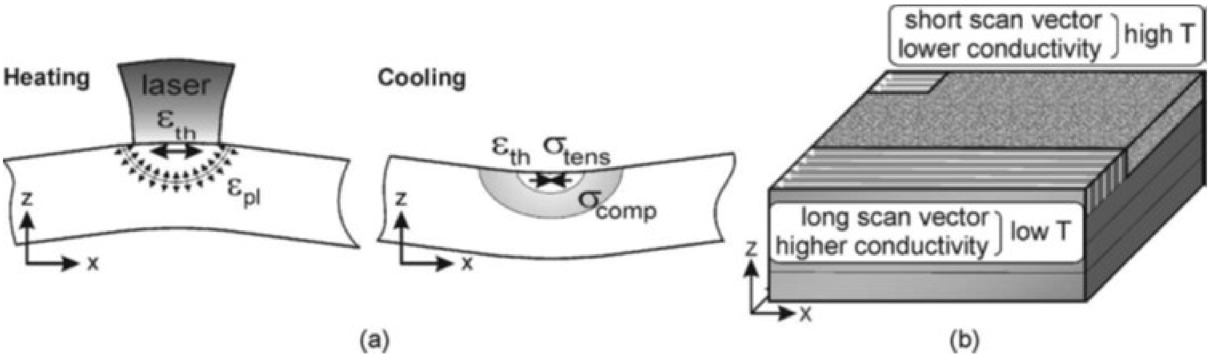

Figure 28: Compressive and tensile stresses during heating and cooling (a), long and short scanning vectors (b) (Kruth et al., 2004)

The material properties, part geometry and scanning strategy influence the internal stresses induced. It was suggested that if the scanning area is smaller, short scanning tracks can cause shorter cooling time for adjacent tracks resulting in higher temperatures. For larger scanning tracks, adjacent tracks have more cooling time leading to lower temperature of the scanned area (Figure 28b). Low temperatures could cause worse wetting conditions leading to density issues. When scanning small zones such as corners, less heat sink is available with the powder acting as isolation, resulting in higher temperatures in these areas (Kruth *et al.*, 2004).

In DMLS, a high temperature gradient is present due to the locally concentrated energy input which leads to high residual stresses. Residual stress in DMLS parts are caused by the deformation in various sections of the object due to different thermal gradients and temperature-dependent properties of the material; volumetric changes arising during heating and solidification, or due to phase transformation. In multi-material DMLS objects, a difference in material properties could cause residual stress to arise. These stresses could cause deformation of the part during manufacturing, as shown in Figure 29, and distortion and cracks can occur when removing the component from the substrate on which it was produced (Yadroitsava & Yadroitsev, 2015).

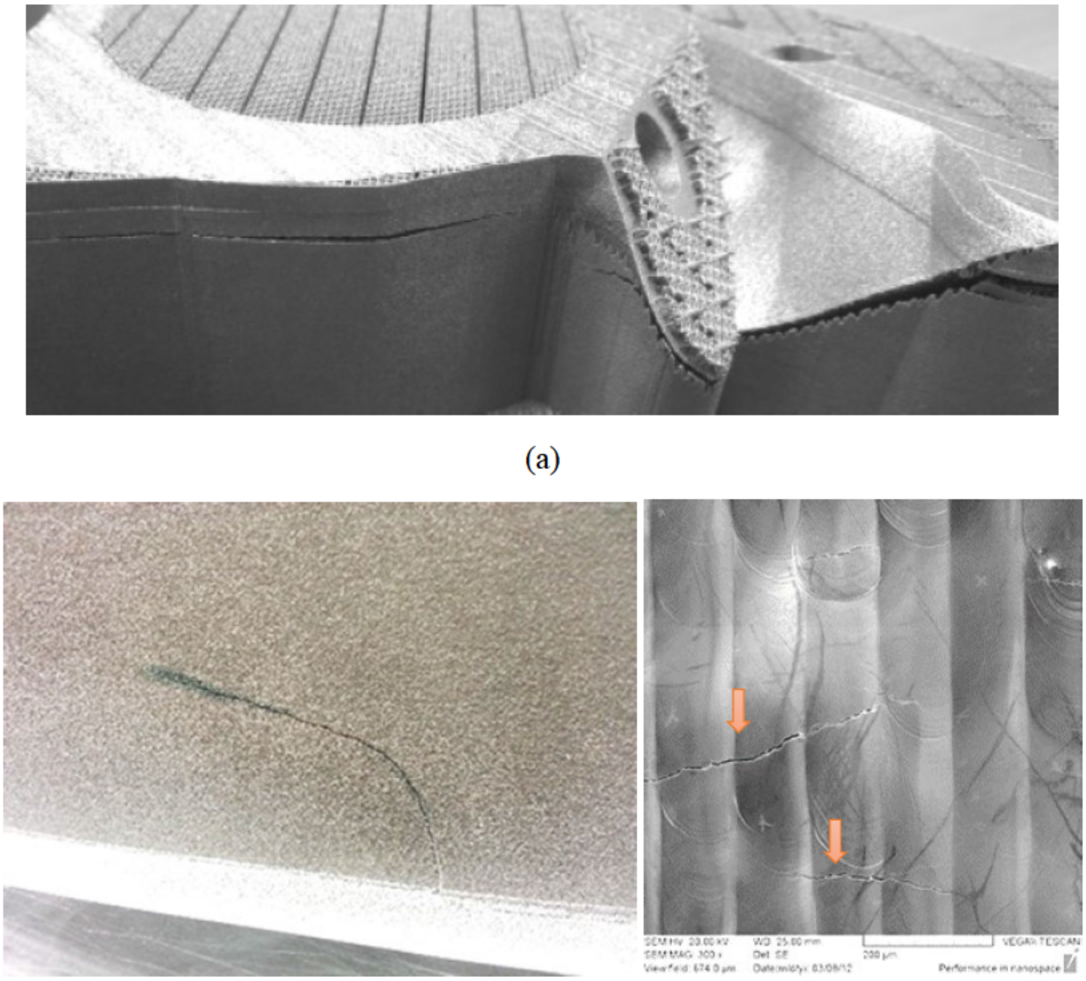

(a)

(b)

(c)

Figure 29 : Delamination of DMLS part during manufacturing (a) and macrocrack of Ti6Al4V part attached to substrate, SEM image(b) and top surface of TiAl part with microcracks (c) (Yadroitsava & Yadroitsev, 2015)

Tensile stresses occur for various reasons during the DMLS process. "*When the laser beam melts powder material and the substrate, stress in the liquid molten pool is zero. The temperature of surrounding solid material near the molten pool (heat-affected zone) increases. During laser melting, high compressive and tensile stresses are present under the front of the molten pool*" (Yadroitsev *et al.*, 2015). "*Thermal conductivity defines the heat dissipation and temperature-equalization in solids. When the laser beam leaves the irradiated zone, the track begins to solidify and cool down. Various layers of material cool at different rates, therefore contraction also occurs at different speeds. Deformations in surrounding material and solidifying track occur as a result of lowered yield strength at elevated temperature of the material. Non uniform deformation of the surrounding solid material results in residual stress being present in the DMLS objects.*"- (Yadroitsava & Yadroitsev., 2015)

Yadroitsev and Yadroitsava (2015) reported that the residual stress in 316L steel parallel to scanning direction often exceeds the yield stress of the wrought material. However, due to a very fine microstructure, the DMLS 316L stainless steel material properties exceed that of the wrought sibling. Heat treatment is seen as the most effective way to reduce residual stresses created during the DMLS manufacturing process. Heat treatment should be applied before removing the DMLS parts from the substrate. Vrancken *et al.* (2015) showed that residual stress can be reduced and ductility increased if the base plate is pre-heated during manufacturing of Ti6Al4V.

2.3.3 Porosity

Porosity remains a huge concern as it directly influences the material properties which, in turn, influence the component's performance. It is not only a concern for DMLS but for conventional production methods such as casting. As indicated by Kruth *et al.* (2010), the goal of DMLS is to obtain 100% dense parts – this is difficult due to lack of mechanical pressure and the fact that DMLS is only dependent on gravity, temperature and capillary effects. The processing strategies as well as process-parameters influence the attainable density.

If the molten pool exceeds the boiling point of the material during laser scanning, a keyhole regime, and finally a porosity regime, could initiate. To avoid pore formation, process-parameters should be adapted to avoid temperatures above the boiling point of the material. Although penetration into the substrate and/or adjacent tracks are necessary for cohesion, too deep penetration (keyhole) could cause gas bubbles to be locked in the material if the molten material collapses over it (Yadroitsev *et al.*, 2015).

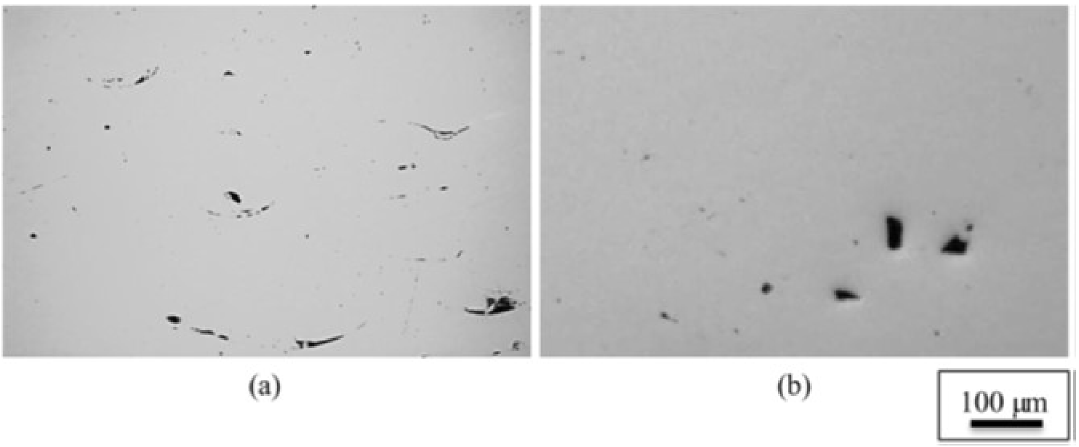

Figure 30: Pores in DMLS samples produced with two-zone strategy and scanning speed 0.12 m/s, hatch distance 120µm, powder layer thickness 50 µm and laser power P = 50 W (a); P = 70 W (b) (Yadroitsev et al., 2015)

In Figure 30a, the sample had elongated pores which were formed between the layers, i.e. inter-layers pores. The deposited layer was too thick for the chosen energy input, and porosity resulted from the lack of fusion at the layer boundaries. With the increase in power, inter-layer pores disappeared and the shapes of the residuary pores changed (Figure 30b). An increase in laser power may also result in undesirable effects. Higher energy input can cause high temperatures, overheating, boiling and evaporation of material in the laser interaction zone and irregular track formation (Figure 30). Non-optimal hatch distance can result in formation of gaps between tracks in a single layer, which causes a chain of pores in the final object (Yadroitsev *et al.*, 2015).

Figure 31 shows how the scanning speed influences the relative density at three different layer thicknesses of AISI 316L stainless steel processed on the Concept Laser M3 machine. A simple parameter such as scanning speed could vary slightly and cause a decrease in the density of the part. Different scanning speeds could produce desirable densities if the layer thickness is adjusted to the scanning speed of a specific power density (Kruth *et al.*, 2010).

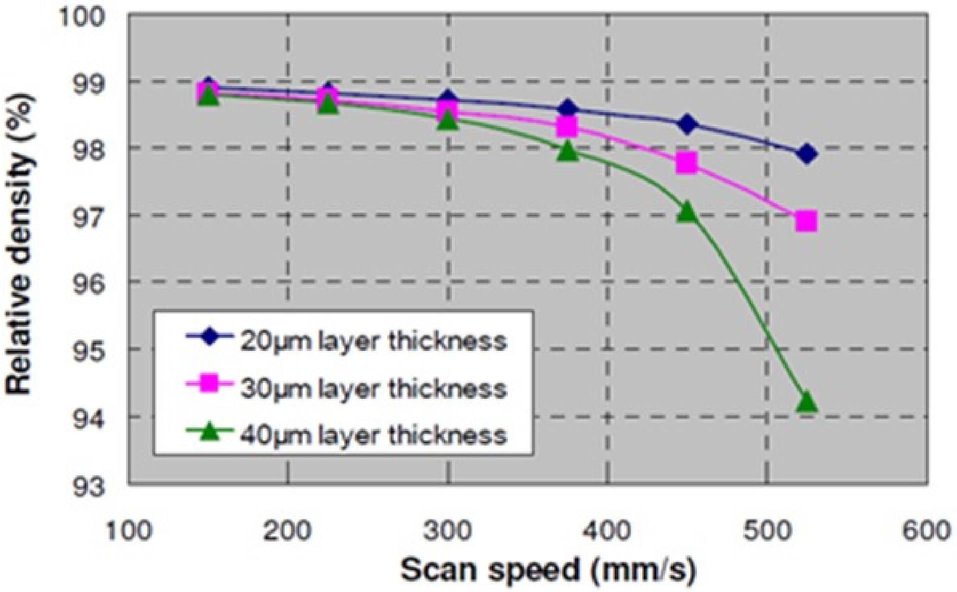

Figure 31: Effect of scan speed on the relative density of AISI 316L stainless steel processed on a Concept Laser M3 machine (Kruth et al, 2010)

As was indicated, laser surface re-melting or “two-zone” strategy is a promising technique to reduce the porosity even further by improving the surface quality of single layers. In section 2.2.3 above, the scanning strategy was discussed and it showed that methods such as remelting can produce a smoother layer surface without droplets (Figure 17). These strategies all contribute to produce objects with minimal pores. Surface quality of DMLS parts remains a huge drawback of this technology. However, re-melting improves the surface quality of production components (Kruth *et al.*, 2010; Yadroitsev *et al.*, 2015).

2.3.3 Mechanical properties

Xu *et al.* (2015) indicated that an important performance benchmark for AM metallic structural components is to achieve mechanical properties comparable or superior to their wrought counterparts, Figure 32 shows how the major metal AM processes of Ti6Al4V compare to wrought and cast alloy.

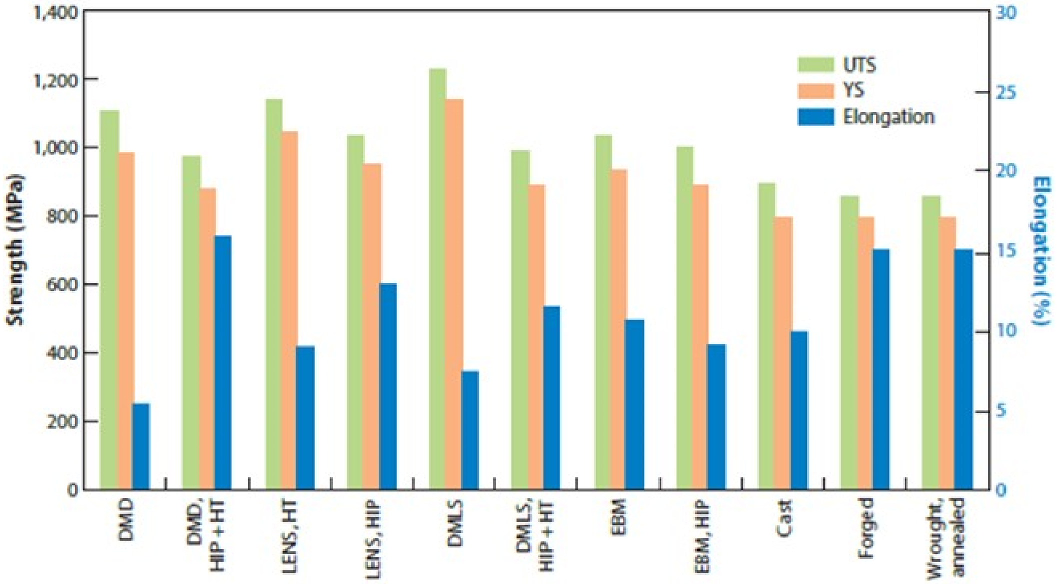

Figure 32: Material property comparison of different Ti6Al4V production methods (Lewandowski and Seifi, 2016)

To produce 3D objects that are fully dense and without defects with DMLS tends to be more complicated as it involves various components. Material properties such as yield strength, elongation, ductility and hardness are greatly affected by the microstructural features. Therefore, the mechanical properties obtained with DMLS differ from conventional production techniques (Kruth *et al.*, 2010).

2.3.5 DMLS Ti6Al4V alloy

Ti6Al4V is the most widely used titanium alloy, accounting for 50% of all titanium alloys produced with 80% of these used in the aerospace industry. The second largest use for Ti6Al4V is for medical prostheses, and this amounts to a mere 3% of the market (Boyer *et al.*, 2007). Titanium alloys are very sensitive to their processing conditions. Processing denotes the wrought, cast or powder methods used to produce the part as well as the heat treatments applied to the alloy (Donachie, 2000). As titanium is sensitive to processing, the properties obtained during the various processes differ (Table 2).

Table 2: The tensile properties of conventional Ti6Al4V (Donachie, 2000).

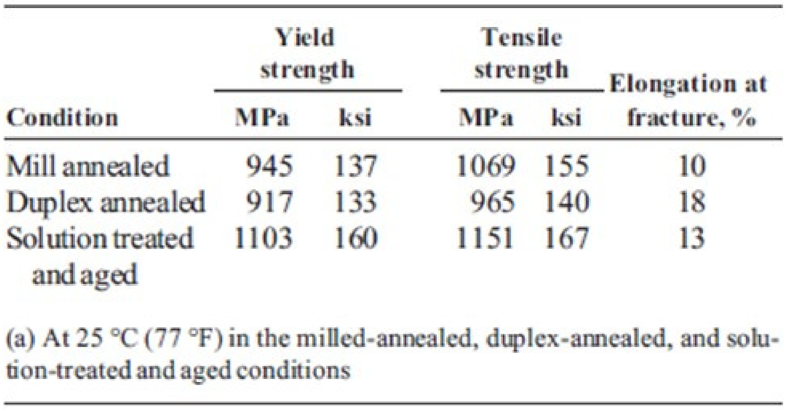

	Yield strength		Tensile strength		
Condition	MPa	ksi	MPa	ksi	Elongation at fracture, %
Mill annealed	945	137	1069	155	10
Duplex annealed	917	133	965	140	18
Solution treated and aged	1103	160	1151	167	13

(a) At 25 °C (77 °F) in the milled-annealed, duplex-annealed, and solution-treated and aged conditions

The microstructure of Ti6Al4V consists of alpha- (hexagonal closed-packed) and beta- (body-centred cubic) phase and therefore is referred to as an alpha-beta alloy. The formation of these phases is dependent on: the amount of prior work, the temperature from which cooled and the rate of cooling. Figure 33 shows how the microstructure could vary in conventional Ti6Al4V alloy (Donachie, 2000). "*The amount of equiaxed alpha and the coarseness or fineness of the transformed beta products affect the alloy properties of titanium*", as indicated by Donachie (2000).

In rapid solidified Ti6Al4V, both the prior beta grain size and the morphology of the alpha phase are strongly influenced by the cooling rate (Broderick *et al*., 1985). DMLS fabricated Ti6Al4V achieves yield strengths of over 1300 MPa with a tensile elongation well below the minimum threshold of 10% suggested for critical structural applications. The mechanical properties of Ti6Al4V depend largely on the constituent phases: their morphology, characteristic length scales, and the size and orientation of the prior-beta grains. Therefore, the DMLS process-parameters have an influence on the microstructures that are formed (Xu *et al*., 2015; Yadroitsev *et al*., 2014).

DMLS Ti6Al4V parts usually consist of columnar prior-beta grains filled with acicular alpha prime martensite (Figure 34). The alpha prime microstructure is due to rapid cooling, which has a high yield strength but with limited ductility. Alpha-beta microstructure can be achieved by post heat treatment.

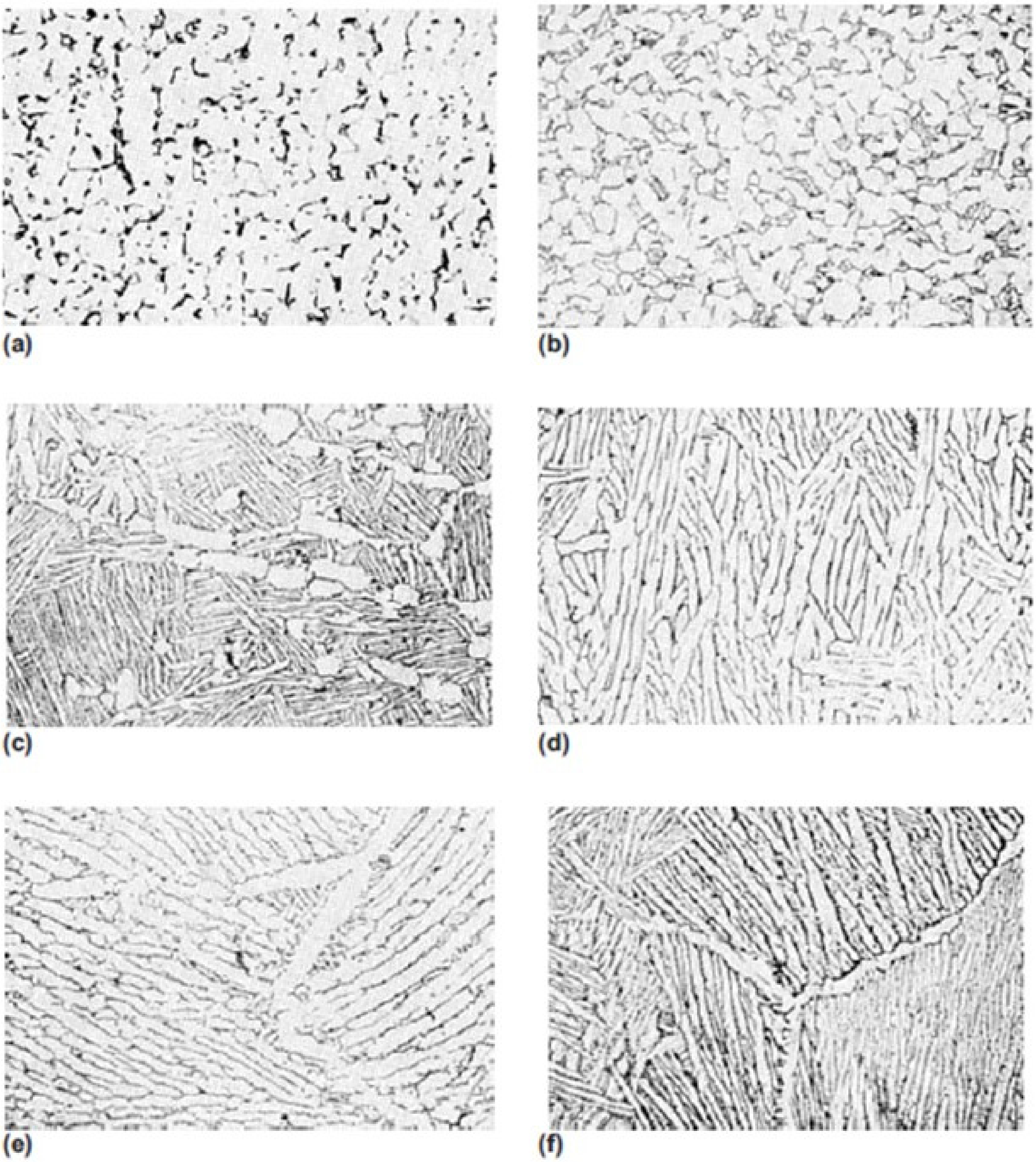

Figure 33: Microstructure of an alpha-beta titanium alloy (Ti6Al4V) in representative metallurgical conditions. (a) Equiaxed α and a small amount of intergranular β. (b) Equiaxed and acicular α and a small amount of intergranular β. (c) Equiaxed α in an acicular α (transformed β) matrix. (d) Small amount of equiaxed α in an acicular α (transformed β) matrix. (e) Plate-like acicular α (transformed β); α at prior β grain boundaries. (f) Blocky and plate-like acicular α (transformed β); α at prior β grain boundaries (Donachie, 2000)

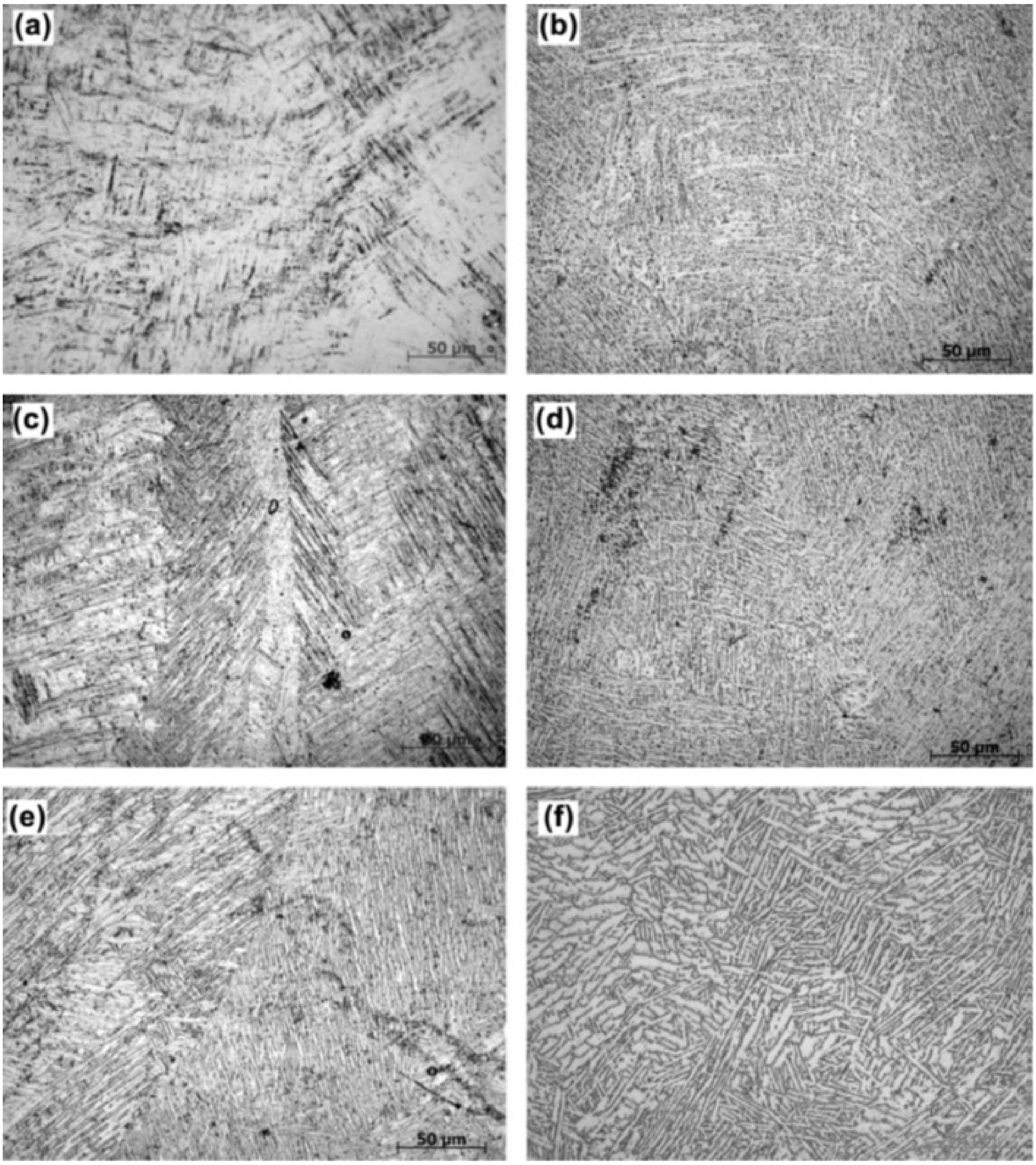

Figure 34: Microstructure of Ti6Al4V: (a) after DMLS process; (b) annealing 4 h at 800 °C; (c) WQ/840 °C; (d) WQ/840 °C + tempering/600 °C/4 h; (e) WQ/960 °C and (f) WQ/ 960 °C + tempering/600 °C/4 h. (Yadroitsev et al., 2014)

Van Zyl *et el.* (2016) found that residual stress near the top surface of DMLS Ti6Al4V as-built samples attached to the substrate were tensile and in the range of 200MPa–800MPa, with the major component being in the direction of scanning. These results were obtained using EOSINT M280 and standard Ti6Al4V parameter set. Analysis of stresses was carried out using an X-ray diffractometer (XRD). The concentrated heat from the laser causes high thermal gradients which induce high residual stresses.

Generally, slight deformation will not cause much concern during manufacturing; however, deformations that disturb the building process are undesirable. This happens by means of delamination or warping, which causes powder to vibrate and move in an undesirable fashion, as shown in Figure 35, or the component to move in the way of the recoating mechanism.

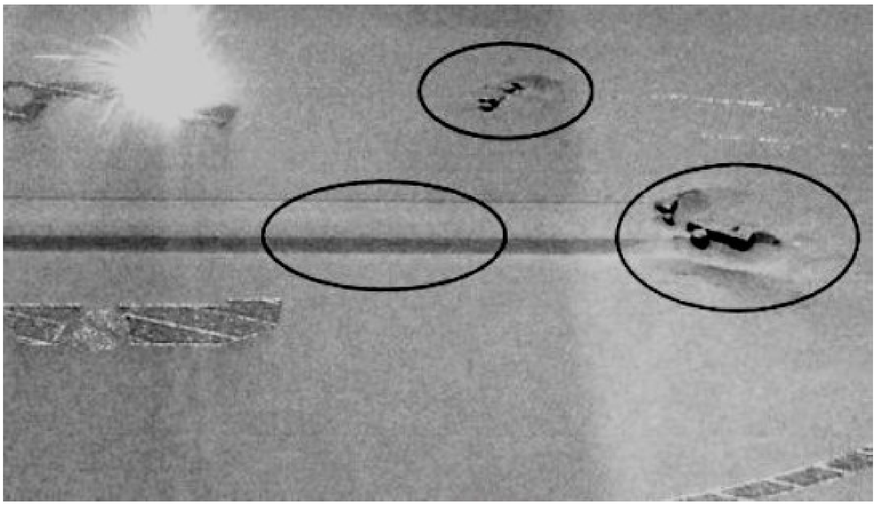

Figure 35: Delamination during DMLS process causing powder to vibrate and forming valleys in the powder bed (Van Zyl et al., 2016)

Residual stress and microstructure has a great influence on the fatigue and crack growth of titanium alloys and is no different for DMLS Ti6Al4V. A study by Leuders *et al.* (2013) showed that residual stress in Ti6Al4V drastically increases the crack growth rate. Pores remain the main cause of crack initiation.

Moletsane *et al.* (2016) state that in the case of optimal process-parameters being used during DMLS of Ti6Al4V (ELI), the only post processing needed to obtain material properties that meet ASTM standards is stress relieving. It was shown that great differences arise in the measured tensile properties of DMLS Ti6Al4V samples due to the anisotropic nature of the α′ martensitic microstructure. These tensile properties correlated with that of other published work and are shown in Table 3.

Table 3: The tensile properties of horizontal DMLS Ti6Al4V (ELI) samples

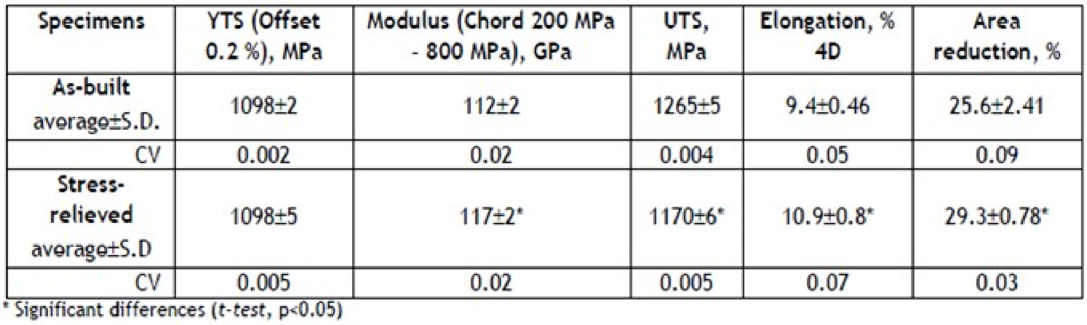

Specimens	YTS (Offset 0.2 %), MPa	Modulus (Chord 200 MPa - 800 MPa), GPa	UTS, MPa	Elongation, % 4D	Area reduction, %
As-built average±S.D.	1098±2	112±2	1265±5	9.4±0.46	25.6±2.41
CV	0.002	0.02	0.004	0.05	0.09
Stress-relieved average±S.D	1098±5	117±2*	1170±6*	10.9±0.8*	29.3±0.78*
CV	0.005	0.02	0.005	0.07	0.03

* Significant differences (*t-test*, $p<0.05$)

It is important to keep in mind how the building direction and process-parameters will influence the tensile properties during DMLS manufacturing. Pore size and morphology was measured before tensile testing; thereafter the specimens were subject to some elongation to cause micro-deformation. The pores were once again inspected followed by tensile testing until the point of fracture. It was found that pore growth and coalescence is the main crack formation mechanism in as-built and stress-relieved DMLS samples under quasi-static tensile loading (Krakhmalev *et al*., 2016).

2.3.6 Summary

Properties of DMLS components are directly drawn from the process-parameters involved during manufacturing. It is shown that one parameter can cause significant changes; one such change is scanning speed, which was shown to directly influence the density of the part. The material properties of DMLS Ti6Al4V compares well to that of wrought and other manufacturing methods.

Residual stress and porosity are the main concerns in the production of components, not only for quality control but also for production. Residual stress must be taken into consideration as delamination of components can interrupt a process or cause other problematic occurrences.

2.4 Destructive testing

Destructive testing, as the name suggests, involves the physical destruction of the object in order to evaluate its characteristics. Destructive testing is defined as a mechanical test (primarily destructive) of a material whereby certain specific characteristics of the material can be quantitatively evaluated. Destructive testing sometimes simulates service conditions. Destructive testing gives accurate results but it only applies to the specific specimen being tested, although it is assumed to be a good representative of the material or part being tested. Two destructive mechanical testing methods often used are: the “tensile test” – the machine applies a tensile force to a specimen and measures material properties such as yield point, elongation, and ultimate tensile strength; the “Charpy test” – the machine uses a pendulum to impact a specimen that is notched to determine the materials resistance to impact (notch toughness) (Hellier, 2012). Other destructive testing methods are: cross-sectioning of the parts in different directions, evaluating various mechanical and/or physical characteristics.

2.5 Non-destructive testing

2.5.1 Introduction

Non-destructive testing (NDT) refers to the various techniques used to monitor the health of a material, component, or system in a structure without causing damage. NDT can detect potential failures as well as inform users of the appropriate time to replace their components to increase the safety and performance. Therefore, NDT became a valuable and critical technique in many industries, as it can save both time and money in product evaluation, troubleshooting and research (Chen, 2014).

Regarding the nature and the characteristics of the part being examined with the aid of NDT, "*It is essential that as much information as possible be known and understood as a prerequisite to establishing test techniques*." Referring to the defects, Heiller mentions, "*An understanding of the origin of discontinuities is useful in determining the types and features of discontinuities that may be expected in the examination of a component. Awareness of the characteristics, locations, and orientations of discontinuities is most helpful and sometimes critical in defect detection and evaluation*." (Hellier, 2012)

Hellier (2012) remarks that for those who wonder where NDT began, there are some who would answer by referring to the creation of the heavens and earth in Genesis: "*In the beginning, God created the heavens and the earth and He saw that it was good*". This has been identified as the first non-destructive test – a visual test!

Some of the inspection practices may be attributed to the catastrophic failures of steam boilers. In Hartford, Connecticut, in March 1854 a steam boiler exploded killing 21 people with another 50 severely injured. Figure 36 shows a typical boiler of this time. The boiler was made by a reputable manufacturer and it was fairly new. At this time, boilers were manufactured with high safety factors. Based on a hearing, the jury offered suggestions to prevent this from happening again. This was an important moment for NDT. Ten years later, in 1864, the State of Connecticut passed a Boiler Inspection Law. The law required annual inspection of each boiler which would result in the issuance of a certificate if passed, and if not, the boiler would be retired from service (Hellier, 2012).

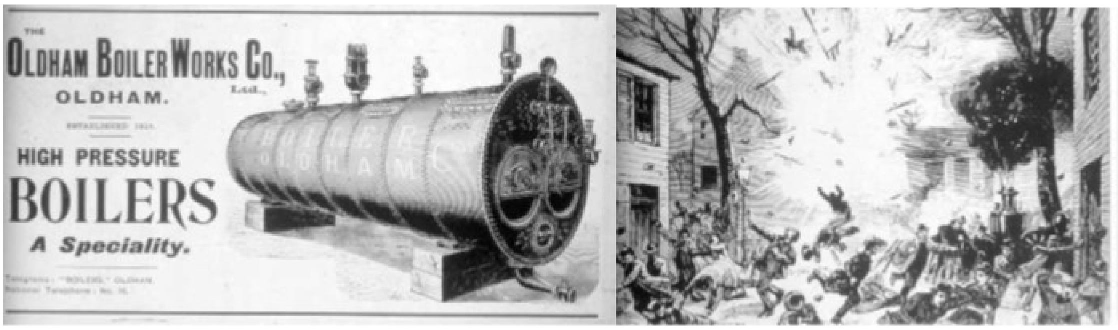
Oldham Boiler Works Co., Ltd.
OLDHAM.
HIGH PRESSURE
BOILERS
A Speciality.

Figure 36: Example of an old boiler & Boiler explosion (Hellier, 2012)

From the 1950s to the present, NDT has grown considerably due to innovation and development of new materials and instrumentation. NDT covers a wide range of methods of analysis used to evaluate the properties of a material and these are now widely used for various industrial applications. Some of the different NDT techniques are shown in Figure 37.

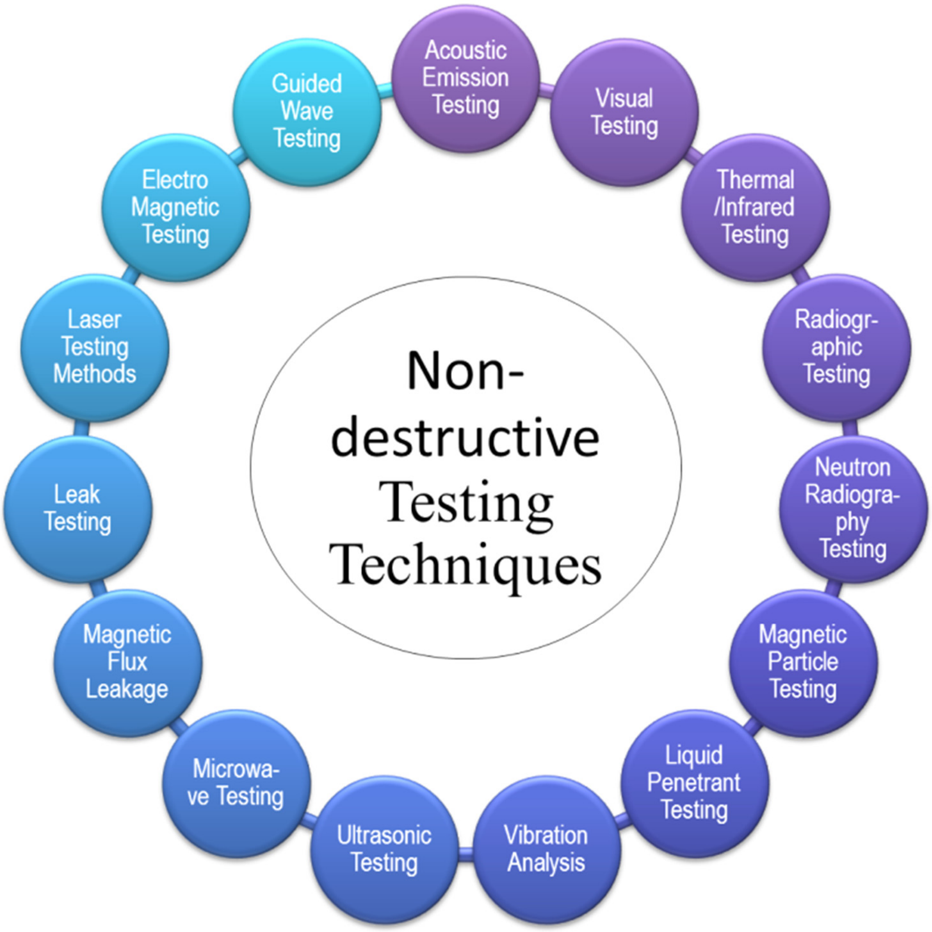
Non-destructive Testing Techniques
Acoustic Emission Testing
Visual Testing
Thermal /Infrared Testing
Radiogr-aphic Testing
Neutron Radiogra-phy Testing
Magnetic Particle Testing
Liquid Penetrant Testing
Vibration Analysis
Ultrasonic Testing
Microwa-ve Testing
Magnetic Flux Leakage
Leak Testing
Laser Testing Methods
Electro Magnetic Testing
Guided Wave Testing

Figure 37: Different NDT techniques

The key ingredient in the NDT process is the practitioner. "*There should always be that desire to 'do it right.' Think of the consequences if a serious discontinuity is missed and some* *type of failure results. Conscientious examiners are concerned and caring individuals. In NDT, there is no room for those who are 'just doing their job.' It takes a special kind of dedicated person, but the rewards are great! The thought of helping mankind by being involved in a technology that is devoted to making this world a safer place is motivation for many. NDT is an honourable profession for those who are honourable. When NDT practitioners lose their ethics, they have lost everything!*" - (Hellier, 2012).

The discontinuities can be categorized by the stage wherein they are generated:

- Inherent discontinuities: generated in the original production of an alloy stock material.
- Primary processing discontinuities: occurring in the first forming stages from a primary alloy.
- Secondary processing discontinuities: occurring in subsequent forming and finishing steps.
- Service discontinuities: created during the use of a component (Hellier, 2012).

Additionally, discontinuities may be categorized in terms of the forming process that caused them. For instance, discontinuities generated during casting are called "casting discontinuities."

When considering the applicability of NDT methods to be used on DMLS components, it is of great importance to understand the nature of the parts, formation of defects and NDT equipment. Failure to acquire the necessary background knowledge exposes the engineer to misinterpreting the results obtained (Carino, 2013; Hellier, 2012). Therefore, a thorough study of the DMLS process and the formation of defects are necessary to select a DMLS NDT method, as reported below. Only principles that are applicable to this study are investigated and reported.

2.5.2 Visual testing

Visual testing (VT) was the first method used in NDT history. As the name implies, this method makes use of an image to detect defects with the eye or a light-sensing device. VT has many applications in almost all industries. VT can be applied during production, on finished parts and during service (Hellier, 2012).

VT equipment makes use of visual aids, such as microscopes, to investigate the surface of a component. Table 4 shows the advantages and limitations of VT.

Table 4: The VT advantages and limitations

Advantages	Limitations
Inexpensive	Only surface can be inspected
Minimal training required	Access necessary

2.5.3 Radiographic testing

Radiographic testing (RT) is categorized in two ways: firstly, the way in which the data is extracted and secondly, according to the type of radiation used. Conventional RT makes use of a radiographic film or digital detectors to record data, whereas computed radiography (CR) makes use of an electronic sensing device and computer software to interpret the data. The three types of radiation used in the different methods are: neutron-, X-ray- and gamma radiation. X-ray machines are categorized by energy groups (Hellier, 2012; Raj *et al.*, 2007). RT can be applied to most materials, shapes and structures. Table 5 shows the advantages and limitations of RT.

Table 5: The advantages and limitations of RT

Advantages	Limitations
Provides a permanent record	Limited thickness based on material density
High sensitivity	Orientation of planar discontinuities is crucial
Most widely used and accepted volumetric examination	Radiation hazard

Innovations such as computed tomography (CT) make radiographic testing applications ever expanding. In CT, an object is exposed to collimated X-rays and the absorbed radiation is measured with a sensor on the opposite side, any discontinuities will affect the exposure absorbed by the sensor. The procedure is repeated from different angles around the object until a 3D image can be reconstructed. Colour synthesis or binary slicing can be performed which allows volumetric data to be extracted. A particular advantage of this CT is the ability to view cross-sections at various depths in the sample (du Plessis *et al.*, 2016; Hellier, 2012).

Ginzel (2002) defines CT as a procedure by which an image of the detail in a chosen plane, perpendicular to the axis of the specimen, is computed from a large number of X-ray absorption measurements made from many directions perpendicular to the axis. This is computerized axial tomography and does not apply to other means of performing tomography.

CT is much like magnetic resonance imaging (MRI) used in the medical field, but CT makes use of ionizing radiation and measures absorption, whereas MRI uses non-ionizing radio frequency radiation to detect the magnet resonance of the hydrogen molecules. A typical application of CT in industry is the detection of defects such as pores, cracks and particle analysis in materials. CT is used in metrology to measure the outer and inner dimensions of a part (de Chiffre *et al.*, 2014).

Figure 38 shows how the data is generated: the X-ray source sends rays through a sample whereby attenuation of the x-rays occur and the intensity of the beam is then measured by the detector on the opposite side of the sample. The position and intensity of each two-dimensional (2D) capture is then processed by the computer using sophisticated algorithms to form a 3D voxel model (a voxel is the 3D analogue of a pixel in 2D images) (Hellier, 2012; Maskery *et al.*, 2016; Kruth *et al.*, 2011).

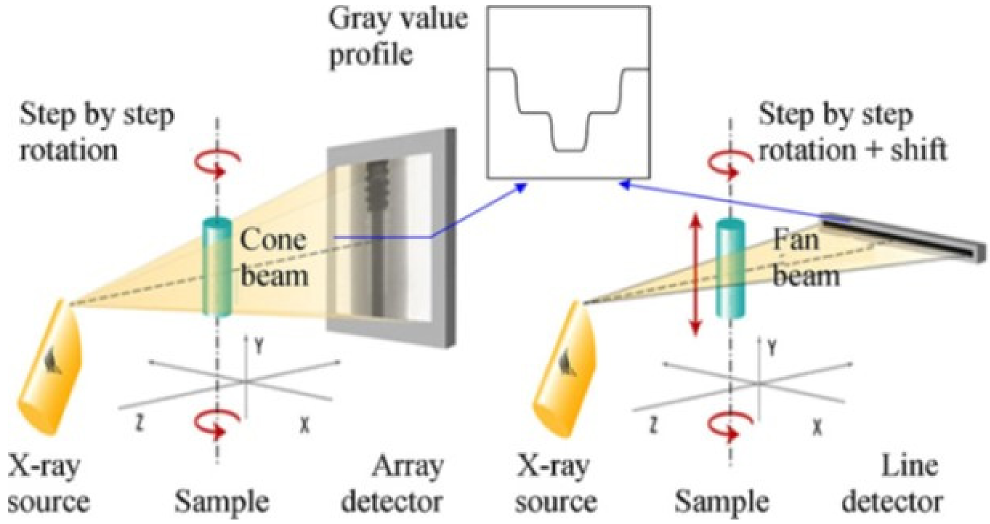

Figure 38: 2D flat panel detector with cone beam and 1D line detector with fan beam: a grey value profile along one pixel line is shown. (Kruth et al., 2011)

The amount of attenuation is determined by the distance travelled through the material. The absorption is proportional to the attenuation coefficient, which is a property dependent on the composition and density of the material. The most common factors that influence the amount of radiation that passes through material are:

- *Photoelectric effect.* The photon transfers its energy to an electron in some energy shell of the atom in the material. The photon could either move the electron from one shell to another. Or if the photon has energy above the required orbital energy level, it will eject the electron from the atom (Figure 39).

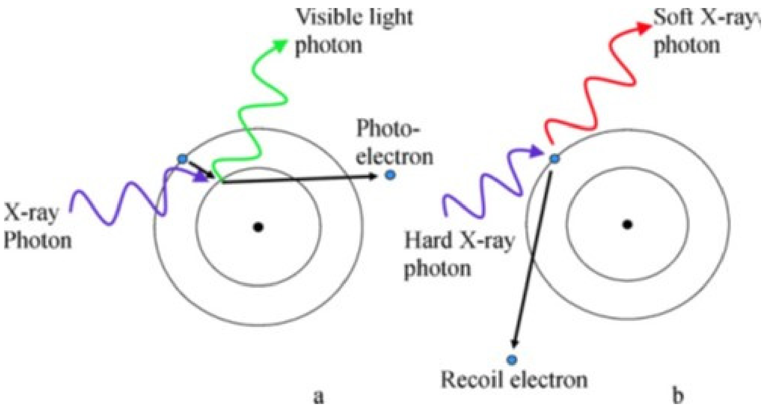
Visible light photon
Photo-electron
X-ray Photon
Soft X-ray photon
Hard X-ray photon
Recoil electron
a
b

Figure 39: Photoelectric absorption (a) and Compton scattering (b). (Kruth et al., 2011)

- *Rayleigh scattering,* also known as "coherent scattering and elastic scattering" occurs when a photon is deflected without reduction in energy by the electrons in the orbitals of the atom. It is estimated to account for 20% of the total attenuation.
- *Compton scattering* occurs between orbital electrons and photons within a 0.1–3.0 MeV energy range. The x-ray photon interacts with the free outer electron; the electron is then ejected from the atom and the x-ray photon scatters in a different direction with reduced energy and a lower wavelength. This phenomenon varies with the atomic number of the material and is roughly inversely proportional to the energy of the x-ray photon.
- *Pair production.* If photon energy is at or above an energy level of 1.02 MeV, the photon interacts with the electric field around the nucleus, it undergoes a change of state and is transformed into two particles; an electron and a positron (antimatter equivalent of the electron) essentially taking energy and creating matter (Figure 40). The electron and the two particles neutralize each other in a phenomenon known as annihilation radiation, emitting two 0.51 MeV photons in different directions which are then absorbed and scattered within the medium. Figure 41 shows the attenuation coefficient for aluminium, iron and polyethylene at different energy levels.

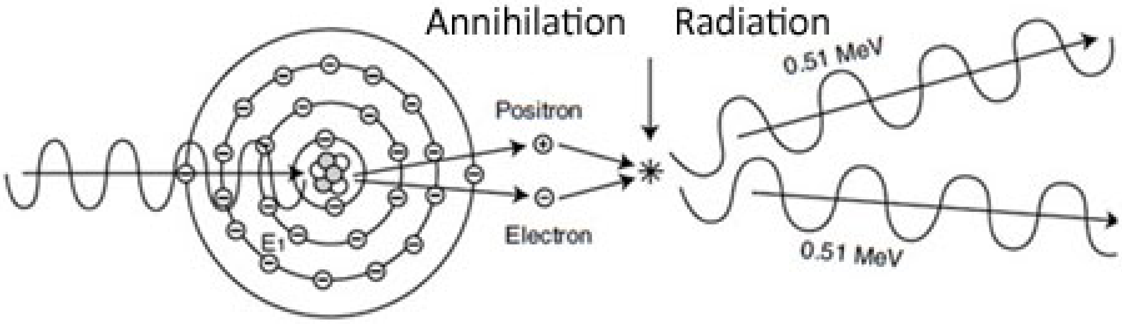
Annihilation
Radiation
0.51 MeV
Positron
Electron
E1
0.51 MeV

Figure 40: Pair production (Hellier, 2012)

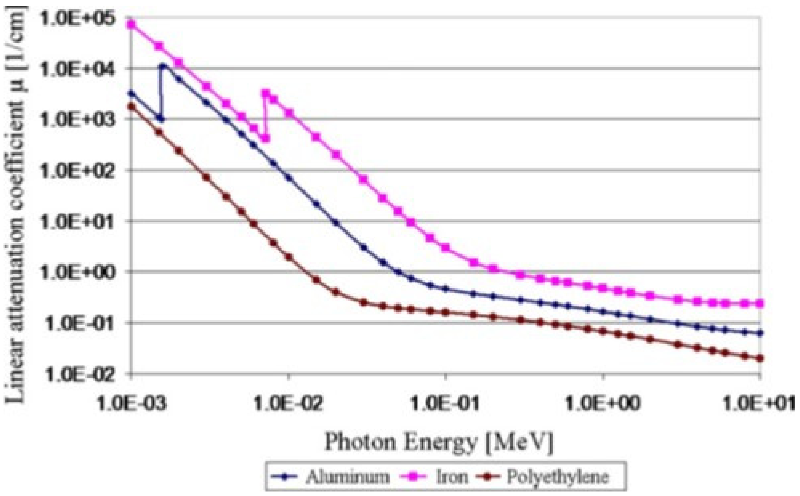

Figure 41: Linear attenuation coefficient for different photon energies. (Kruth et al., 2011)

Ionizing radiation is a concern as it could be harmful to the health of living tissue and change the electrical nature of matter (Hellier, 2012; Kruth *et al.*, 2011).

Technical systems

The five basic components of the X-ray CT process in order are:

- Source of X-ray radiation.
- Test specimen.
- X-ray detection.
- Processing.
- Interpretation.

X-ray source

X-rays are produced in a vacuum tube. High-speed electrons are attracted to the positive potential of the anode. When the electrons hit the target they decelerate very fast, turning ~99% of their energy into heat and ~1% into radiation. Therefore, the target should be able to withstand high temperatures and have the capability to dissipate the heat. There are various methods and techniques used (resonance-type transformer, betatrons, linear accelerators and Van de Graaff generators) with the basic underlying principle being: accelerate high voltage electrons to hit a target so that electrons can be expelled from the material; the electrons at higher orbitals within the material will then fall to a lower state orbital and release X-rays with precise energy, determined by the electron energy levels.

The X-ray energy determines the amount of penetration into the material, while the intensity determines the amount of energy flowing per unit time. The higher the current applied the higher the intensity of radiation. The applied voltage or kilo voltage (kV) of the anode determines the energy as it could increase and decrease the kinetic energy of the electrons. Energy of the radiation is a very important characteristic. The energy is directly related to the wavelength: the shorter the wavelength the higher the penetration (Hellier, 2012; Kruth *et al.*, 2011).

X-ray detectors

Figure 42 shows the three main methods of scanning: pencil beam, fan and cone beam (from left to right respectively). The pencil beam scans the part moving in one plane, the plane is then rotated by a small degree and the process is repeated. The fan beam method scans the entire part in a 2D horizontal plane around the part, the process is then repeated in y-direction increments until the whole part has been scanned, as shown in Figure 38, on the right hand side. Line detectors have higher energy which works well for thicker objects but at the expense of much longer scanning duration.

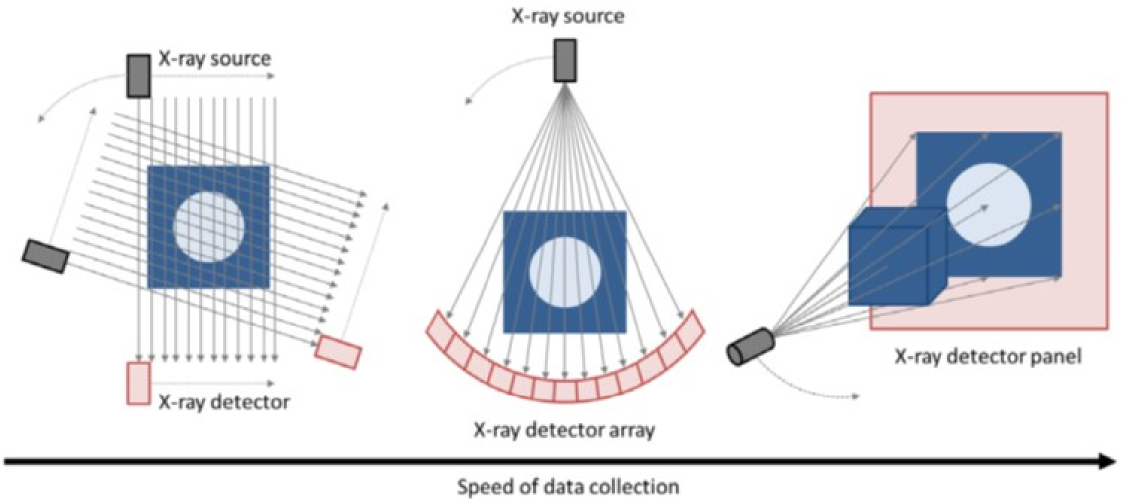

Figure 42: Schematics of pencil, fan and cone beam CT methods, respectively. In this diagram, the fan beam image depicts a curved detector while the cone beam image depicts a flat panel detector, it should be noted that curved and flat panel detector arrays can be used in each instance (Maskery et al., 2016)

A small X-ray spot is desirable because it will allow for sharp images; this can be done by making the target of the anode smaller, creating a small X-ray spot. Setting the distances between the source, sample and the detector determines the magnification, as shown in Figure 43.

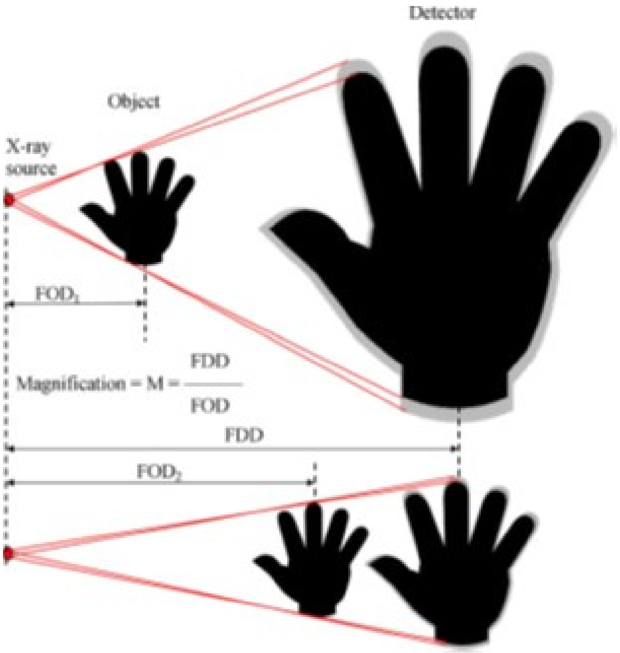

Figure 43: Image magnification and blurring by moving the object towards the source which has a finite X-ray spot (Kruth et al., 2011).

The quality of the image remains very important but there are always trade-offs that should be considered – an increase in the sample size would cause a decrease in the resolution, while an increase in magnification would give a higher resolution with blurred images. The resolution and contrast is a primary concern. The voxel size and physical resolution could, under normal circumstances, be accepted as interchangeable terms. However, this is not always the case as the magnification plays a crucial role in the calculation of the voxel size. In Figure 44, the influence of the voxel size and sample diameter of generic CT systems with a 2000 x 2000 pixel detector and geometric magnification, is shown (du Plessis *et al.*, 2016; Kruth *et al.*, 2011; Maskery *et al.*, 2016).

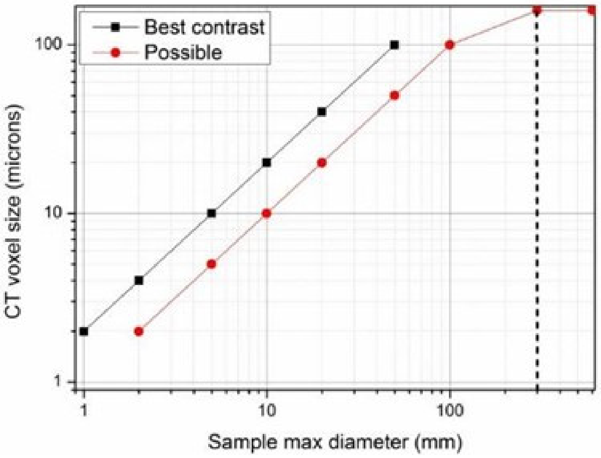

Figure 44: Effect of sample diameter on voxel size, when using a 2000 x 2000 pixel detector (Du Plessis et al., 2016)

Dense materials require longer exposure times to achieve reliable contrast due to decrease in penetration (Kruth *et al.*, 2011).

Software data processing

Scanning strategy is determined by the user and machine capabilities; a series of scanning guidelines were reported in Du Plessis *et al.,* (2017). Various strategies exist and are dependent on factors such as sample size and material composition. The most important consideration is the voxel size; typically the smaller the voxel size, the better the possibility of detecting small defects, but at increased scanning time. This is demonstrated in a series of scans of a DMLS component in du Plessis et *al*. (2016b).

If the X-ray moves through a space that has different materials or material properties, it will have varying attenuation coefficients at these areas. Reconstruction is done using the data of each linear 2D projection of the part. These projections from each slice is used to construct and form a digital 3D image of the object, as shown in Figure 45 in which only four increments are used to complete a full rotation. Kinematic machine components must have high accuracy as well as geometrical and thermal stability as these will directly influence the quality of reconstruction.

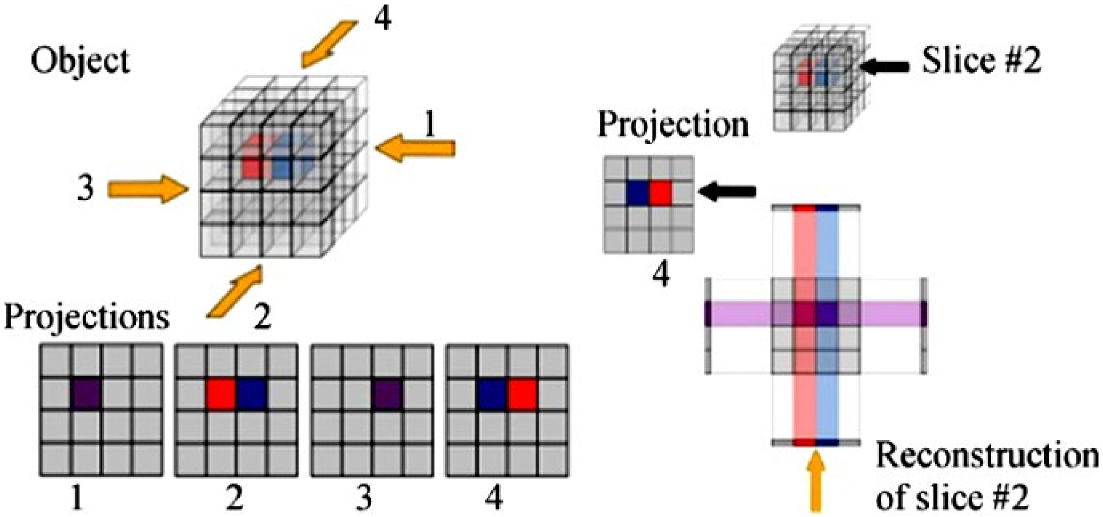

Figure 45: Example of back-projection reconstruction (Kruth et al., 2011)

An unwanted effect known as beam hardening; that often occurs is due to low energy photons (soft X-rays) that are attenuated much more than the high energy photons (hard x-rays). Soft photons will extinguish after travelling a short distance in the material and only hard X-rays will travel through the part (Figure 46). The intensity of the X-rays that do not pass through the part will be that of soft- and hard beams which increase the energy spectrum that reaches the detector. To avoid beam hardening, the soft beams are removed by inserting a filter in the front of the source, allowing only hard rays to travel through and past the part being inspected (Kruth *et al.*, 2011).

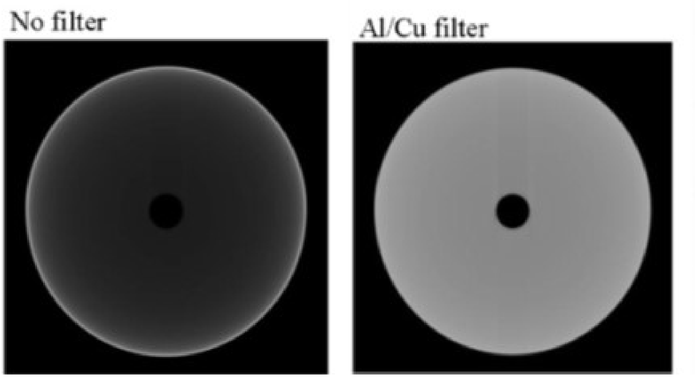

Figure 46: Effect of beam hardening without and with a physical filtering of the X-ray beam. Hollow cylinder: outer ø 6, inner ø 0.6 mm (Kruth et al., 2011)

The capability of CT scanning to identify the different grey values for each voxel allows the creation of a virtual image of materials with different densities. One such study was done by Ikram *et al.* (2015), where a virtual autopsy was done on a mummified bird to investigate the cause of death, as shown in Figure 47.

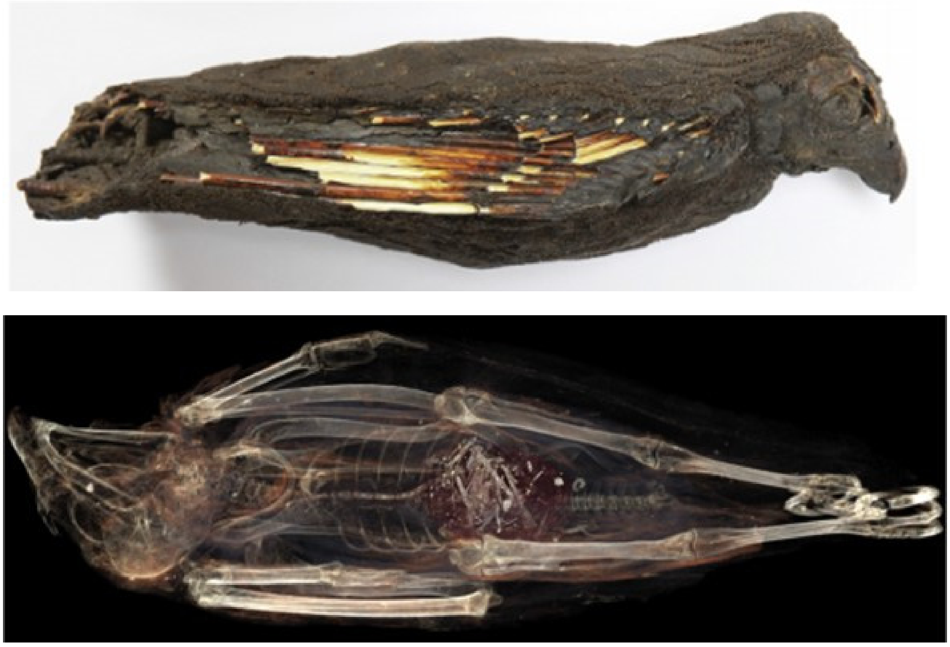

Figure 47: X-ray CT 'cause of death' investigation on a mummified bird (Ikram et al., 2015)

By applying X-ray CT for the examination of porosity, measurements of the sphericity of pores are often calculated to understand the shape of the pores that occur within a material. The calculations are shown below (Rezanezhad *et al.*, 2009; Ziółkowski *et al.*, 2014):

$$S = \frac{\pi^{\frac{1}{3}}(6V)^{\frac{2}{3}}}{A},$$

where: S=*pore* sphericity V=*pore* volume A=*pore* area

The shape factor will shift from zero to one; flat pores will be indicated by small fractions, with round pores approaching unity.

As indicated by du Plessis *et al.*, (2014): *"Using a full 3D CT scan of the calibration blocks, dimensional measurements can be done more accurately; but again this depends on various factors such as initial dimensional calibration, X-ray emission characteristics, data reconstruction parameter variations, choice of edge position in a gradient region (edge effect), and problems arising (such as beam hardening)"*.

2.5.4 Ultrasonic testing

The use of sound energy to evaluate the integrity of solid objects has probably been used since man was able to manufacture metal and pottery objects. Hellier (2012) suggests that English phrases such as "the ring of truth" and "sound as a bell" hint at the fact that these methods were used in earlier days. High frequency sound pulses from a transducer propagate through the test material, reflecting at interferences. Various techniques and equipment make this a very versatile solution.

In the 1870's, the first publication on the properties of sound waves in materials was done by Lord Rayleigh in his work "The Theory of Sound". Shortly after, the Curie brothers discovered piezoelectric crystals; they found that if pressure were to be applied to these crystals, an electric potential could be generated. The opposite was also found to be true; if electric potential was applied, the crystal would distort. The piezoelectric effect has many applications including the spark igniter in cigarette lighters, crystal microphones and of course, ultrasonic transducers. After the Titanic disaster in 1912, it was suggested that sound waves could be used to detect icebergs at sea. S. Y. Skolov suggested the use of ultrasonics to detect discontinuities in metal for the first time in 1929 (Hellier, 2012).

Ultrasonic testing (UT) can be used if sound transmission and surface finish are good and the shape is not complex. Table 6 shows the advantages and limitations of UT. A major innovation in UT is phased array inspection.

Ultrasonics is a branch of acoustics. The study of ultrasonics entails vibrational waves in solids, liquids and gasses that have a frequency above that of human hearing, which is 16 kHz – although a young person would be able to hear frequencies of up to 20 kHz. Various industries make use of ultrasound and some specialized areas have developed in scientific fields such as underwater acoustics (SONAR), sonochemistry, medical ultrasonics, etc. Figure 48 shows how different industries make use of ultrasonic principles (Ensminger and Bond, 2011).

Table 6: Advantages and limitations of UT

Advantages	Limitations
Provides precise results quickly	No permanent record (usually)
Thickness and depth information	Material attenuation, surface finish and contour
Type of flaw can be obtained from one side of the component	Requires couplant

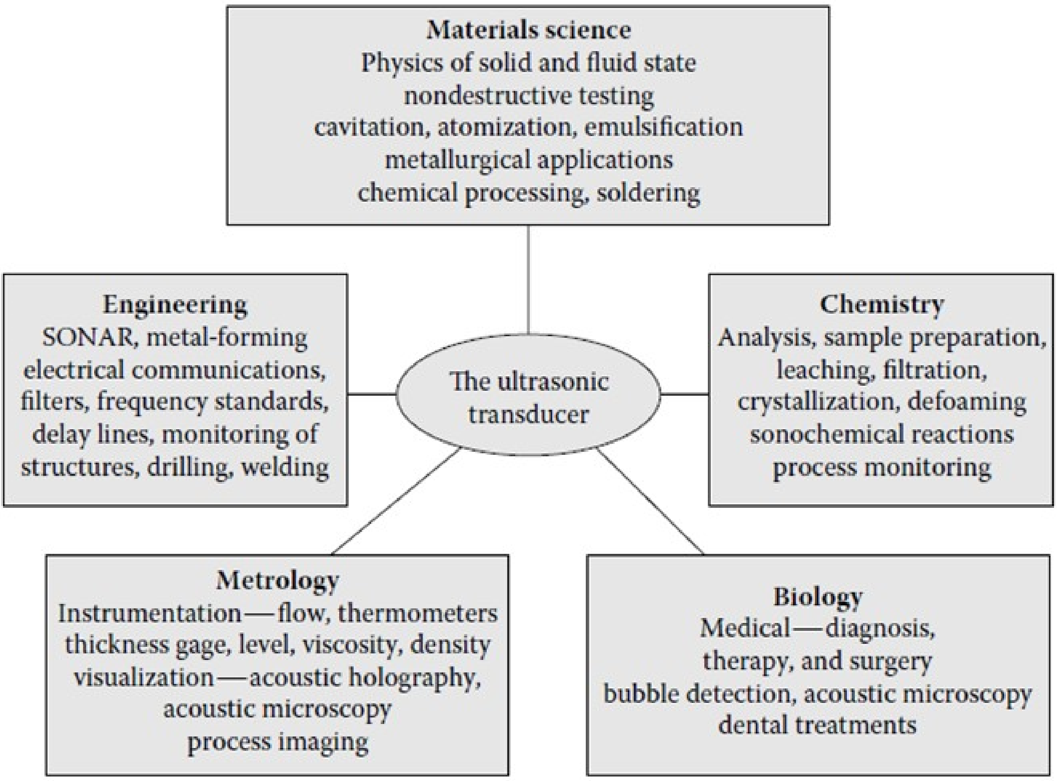
Materials science
Physics of solid and fluid state
nondestructive testing
cavitation, atomization, emulsification
metallurgical applications
chemical processing, soldering
Engineering
SONAR, metal-forming
electrical communications,
filters, frequency standards,
delay lines, monitoring of
structures, drilling, welding
The ultrasonic transducer
Chemistry
Analysis, sample preparation,
leaching, filtration,
crystallization, defoaming
sonochemical reactions
process monitoring
Metrology
Instrumentation—flow, thermometers
thickness gage, level, viscosity, density
visualization—acoustic holography,
acoustic microscopy
process imaging
Biology
Medical—diagnosis,
therapy, and surgery
bubble detection, acoustic microscopy
dental treatments

Figure 48: Ultrasonic industry application (Ensminger & Bond, 2011)

Since the 1970's, major advances have taken place, this is mainly due to technological advances in areas such as computer modelling and theoretical analysis of wave scattering and propagation.

2.5.4.1 Basic principles

The basic principle of UT NDT makes use of high frequency sound pulses from a transducer that propagates through the test material, reflecting at interferences. Various techniques and equipment make this a very versatile solution. Regarding the selection of these techniques, Hellier (2012) stated that "*the ways in which the sound waves propagate through the material and are attenuated, reflected or transmitted dictate the different ultrasonic methods or techniques used to detect the many types of discontinuities that can exist*." A basic UT technique "pulse-echo" is shown in Figure 44; a transducer sends a sound wave through the material and waits for the echo pulse to return. The time taken can then be converted into distance depending on the speed of sound of the measured material. If any defects are present, the sound waves would hit and bounce back from the defect (Ensminger and Bond, 2011; Hellier, 2012).

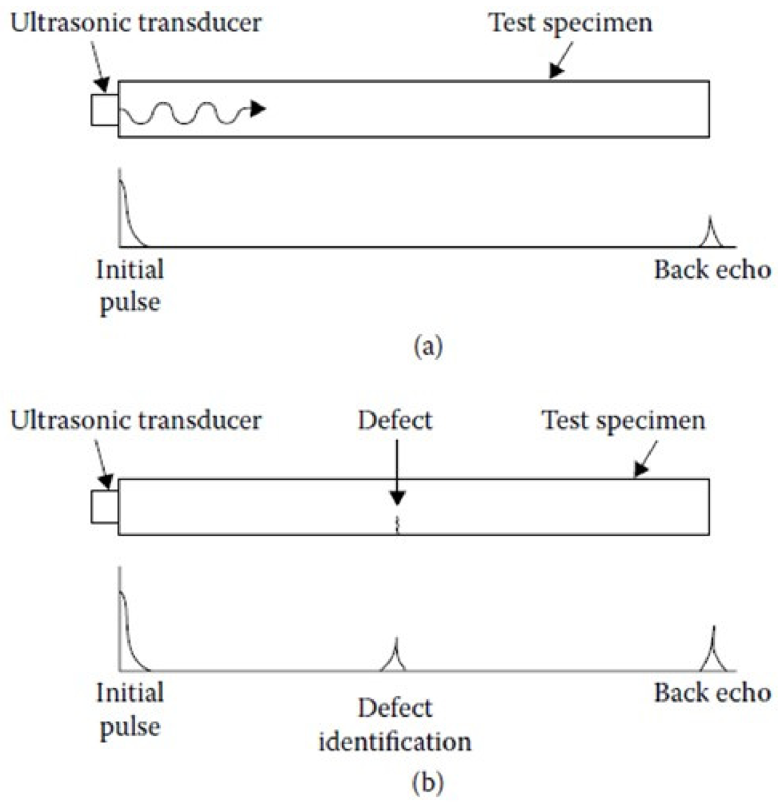
Ultrasonic transducer
Test specimen
Initial pulse
Back echo
(a)
Ultrasonic transducer
Defect
Test specimen
Initial pulse
Defect identification
Back echo
(b)

Figure 49: Pulse-echo principle of operation (Ensminger and Bond, 2011)

Wave propagation

In a substance, particles oscillate, without migrating, transferring energy to the adjacent particles and so the wave travels through a material, as seen in Figure 50. All materials experience these vibrations and resist the motion of particle movement; gases experience high and low pressures and in solids, the modulus of elasticity is the measure of the material’s resistance to compressive and tensile forces. Solids also have the ability to resist shear loads, and the rigidity of the material is given by the modulus of rigidity. The rigidity of a solid creates new wave modes to propagate through the material: shear, lamb and surface (Rayleigh) waves. In shear waves, the particles move up and down, perpendicular to the direction of propagation. If a shear wave is set up to skim the surface, it changes into a surface (Rayleigh) wave: this wave moves in an elliptical fashion, up and down and from side to side. Lamb waves are complex waves similar to surface waves but occur through the entire thickness of the material. Lamb waves can only occur if the test piece thickness is below a couple of wavelengths of the applied frequency (Hellier, 2012; NDT Resource Centre, 2016; Russell, 2001).

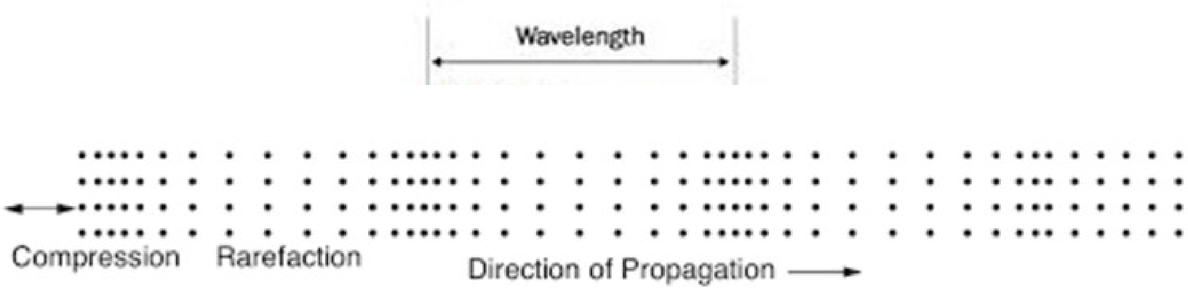

Figure 50: Longitudinal wave (Hellier, 2012)

The speed of sound in matter differs from the type of material and its state – sounds travel faster in solids than in liquids and, in turn, sound travels faster in liquids than in gases. The velocities of sound are mainly influenced by the elasticity and the density of the material. In solids, shear and longitudinal waves do not travel at the same velocities. The two velocity calculations are shown below:

$$V_L = \sqrt{\frac{E}{\rho} \cdot \frac{1 - v}{(1 + v)(1 - 2v)}}$$

$$V_S = \sqrt{\frac{E}{\rho} \cdot \frac{1}{2(1 + v)}}$$

$$or\ alternatively\ V_S = \sqrt{\frac{G}{\rho}}$$

Where:

V_L is velocity of longitudinal wave

V_S is velocity of shear wave

G is modulus of rigidity

ρ is material density

v is Poisson's ratio

E is elastic modulus

Velocity of all waves can be calculated but requires precise information about the material parameters. Factors such as heat treatment and the manufacturing process influence these results, and therefore calibration of equipment is often required.

In UT, detection of the smallest detectable flaw is dependent on the test frequency; the size of the detectable flaw would be half the wavelength:

$$\lambda = \frac{V}{f}$$

Where:

V is velocity of sound

λ is wavelength

f is frequency

The reflection of the sound wave is what makes this method able to detect defects; the reflection of a wave at an interface is dependent on the acoustic impedance of the materials. If a crack pore is present, it would contain air which has a different acoustic impedance value to the test material and this would cause some of the energy to be reflected and transmitted.

Reflection

The acoustic impedance (Z) is dependent on the material density and velocity of sound, as shown below:

$$Z = \rho \times V$$

Acoustic properties of some materials are given in Table 7. The ratio of the percentage reflected energy can be calculated by

$$Reflected\ energy = \left(\frac{Z_1 - Z_2}{Z_1 + Z_2}\right)^2$$

Where:

Z_1= acoustic impedance in medium 1

Z_2= acoustic impedance in medium 2

The reflected energy between a steel-to-water interface is ~88%, while a steel-to-air interface is at ~100%. Some UT methods make use of an immersed technique during NDT UT (Hellier, 2012).

Table 7: The acoustic properties of various mediums adapted from Hellier, (2012)

Material	Longitudinal wave velocity (mm/ µs)	Shear wave velocity (mm/ µs)	Impedance Z
Steel 4340	5.842	3.251	45.6
Ti6Al4V	6.172	3.302	27.3
Teflon	1.375	6.35	3.0
Water (20°C)	1.473	No shear component	1.48
Air (20°C)	0.356	No shear component	0.00041

When sound enters a medium at an angle, mode conversion and refraction takes place. The angle at which the sound enters the test piece is known as the angle of incidence. The angle of incidence will influence the amount of reflection and refraction, according to Snell's law, as shown in Figure 51:

$$\sin\frac{i°}{V_1} = \sin\frac{R°}{V_2}$$

Where:

$i°$ = angle of incidence

$R°$ = angle of refraction

V_1 = velocity in medium 1

V_2 = velocity in medium 2

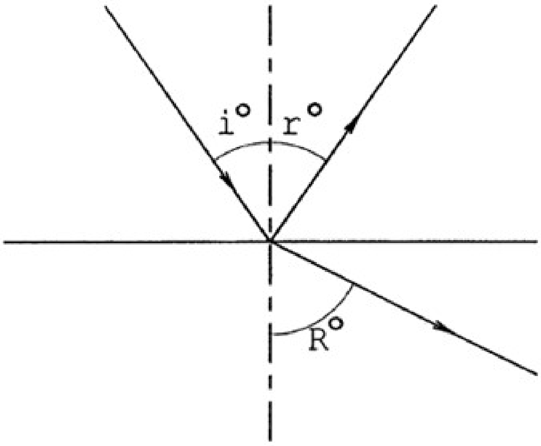

Figure 51: Depiction of Snell's law (Hellier, 2012)

Although the incident wave is a compression wave, a shear wave will start to develop, hence 'mode conversion'. The speed of the shear wave is different and therefore the two waves will refract at differing angles. Figure 52 shows how a compression wave undergoes mode conversion at a steel-air interface; the compression and shear wave is refracted according to their different velocities of sound. The amplitude of the shear wave could be ignored at small angles, but as the angle of incidence increases and so does the amplitude. Mode conversions can interfere with the results as unwanted reflections can be misinterpreted. These mode conversions can be set up due to various reasons such as the thickness of the sample, incident angle, the state of the material, etc. An in-depth study of the maths and physics of wave propagation is beyond the scope of this study (Hellier, 2012).

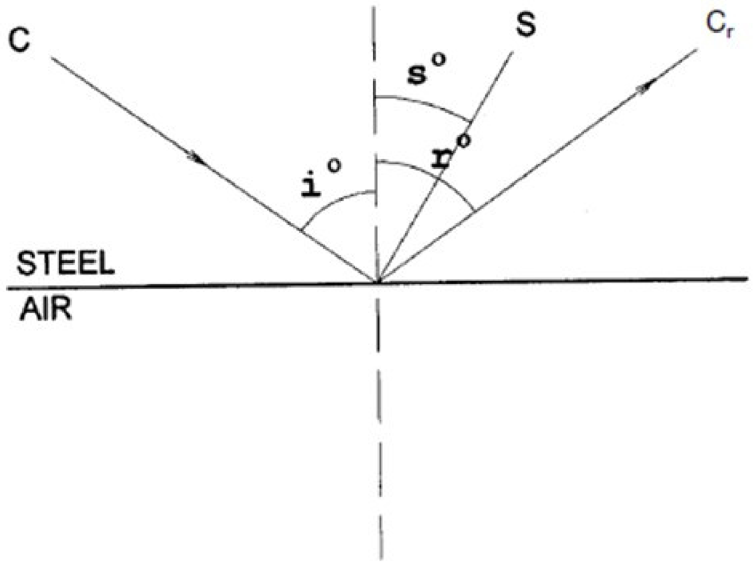

Figure 52: Mode conversion of compression wave at steel-to-air interface (Hellier, 2012)

The factors that cause loss of sound energy can be attributed to the following:

- Absorption
- Scatter
- Beam spread
- Interference and diffraction

Attenuation

The combined effect of scatter and absorption is known as attenuation. When a sound wave travels through a medium, its sound wave diminishes with distance, see Figure 53. This gradual loss of sound energy (attenuation) can be attributed to absorption and scatter.

The amplitude change of a decaying plane wave could be calculated by

$$A = A_0 e^{-\alpha z}$$

Where:

A_0 = amplitude at a location.

A = amplitude of the wave at a distance Z away from A_0.

α = attenuation coefficient of the material (nepers/length), neper is a dimensionless quantity. The attenuation coefficient could also be converted to decibels per unit length.

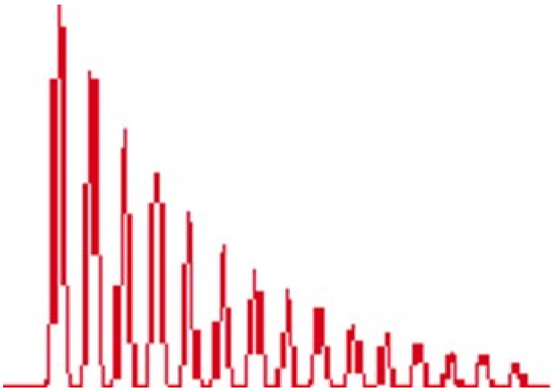

Figure 53: Decay of a propagating wave through material

Absorption, in its simplest form refers to the friction within the particles themselves. The friction is directly proportional to the frequency of the sound. Whereas scatter refers to the sound waves reflecting off the grain boundaries that are randomly orientated towards the direction of initial wave (Hellier, 2012; NDT Resource Centre, 2016).

Interference and diffraction

Constructive waves superimpose on each other and the amplitude at any point is equal to the sum of the amplitudes of each wave, whereas with destructive waves are not in phase so the amplitudes combine and cancel each other out. In Figure 54, constructive and destructive interferance of two sine waves that propagate from the same point can be seen.

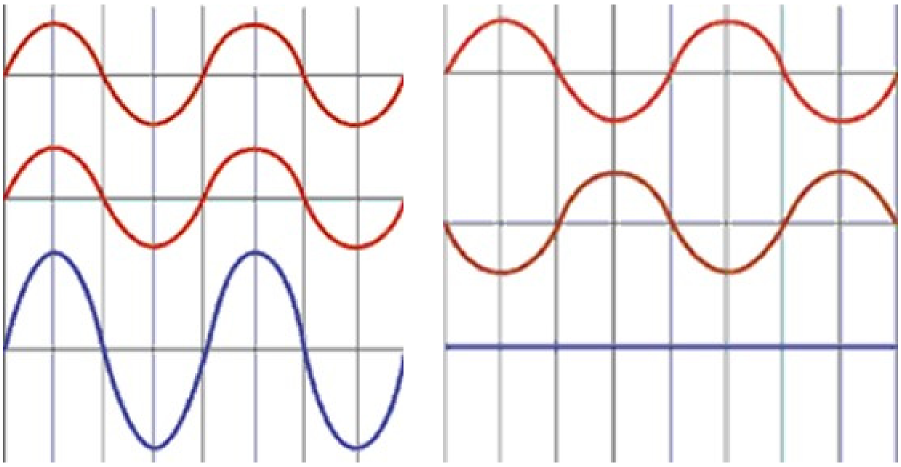

(a) (b)

Figure 54: 2 Dimensional illustrations of constructive (a) and destructive (b) interference (NDT Resource Centre, 2016)

UT makes use of a transducer to generate waves. These waves are generated at the surface of the transducer and propagate in a circular wave front. It is important to note that these waves are three-dimensional and that the transducer does not have a single point source as it has a diameter and surface: the waves originate on various points along the face of the transducer, known as a “finite source”. The points of constructive interference are known as nodes. Five points of origin are shown in Figure 55 below, where it can be seen that the sound field near the surface is very uneven. This area is known as the near-field (NF). The near-field can be calculated by

$$NF = \frac{D^2 \times f}{4 \times V}$$

Where:

D= transducer diameter

f= frequency

V= velocity

The sound field becomes more uniform as the beam spreads out from the centre of the transducer. Although the beam is not totally uniform, at some distance the beam becomes uniform and intense (Hellier, 2012; NDT Resource Centre, 2016).

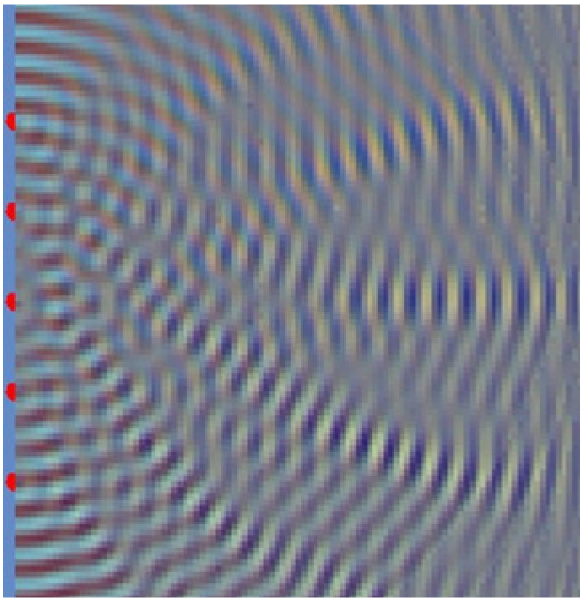

Figure 55: Multiple points of sound origination along the face of the transducer (NDT Resource Centre, 2016)

Beam spread

Beyond the near-field the beam spreads out like a cone, as shown in Figure 56. The angle of the cone can be calculated by

$$\sin\frac{\theta}{2} = \frac{1.22\lambda}{D}$$

Where:

θ= Angle of beam

λ= wavelength

D =transducer crystal diameter

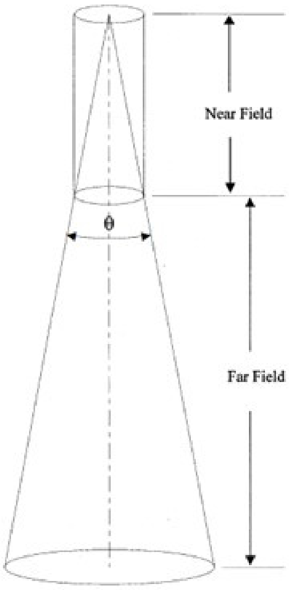

Figure 56: Beam spread of near- and far-field (Hellier, 2012)

Decibel

The unit used to express sound intensity is a decibel which is equal to one tenth of a bel, It is used to express the ratio of two sound signals. The difference between two signals is given by

$$dB = 20 \times Log\frac{A_1}{A_2}$$

Where:

A_1= Signal 1 amplitude

A_2= Signal 2 amplitude

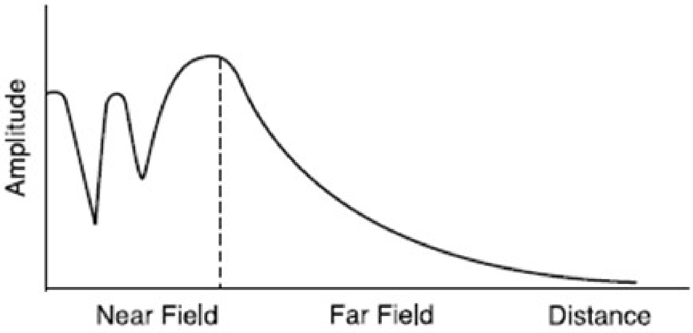

Figure 57: Amplitude over distance away from transducer (Hellier, 2012)

2.5.4.2 Equipment for UT

There are various systems and methods of measurement available, for example, some make use of water to submerge the test piece, which provides better acoustic transmission. However, all of them make use of the same basic principle; high frequency sound pulses from a transducer that propagates through the test material, reflecting at interferences. If the discontinuity is suitably orientated, detection of the defect is dependent on the size of the defect, the test frequency and gain used (Figure 58).

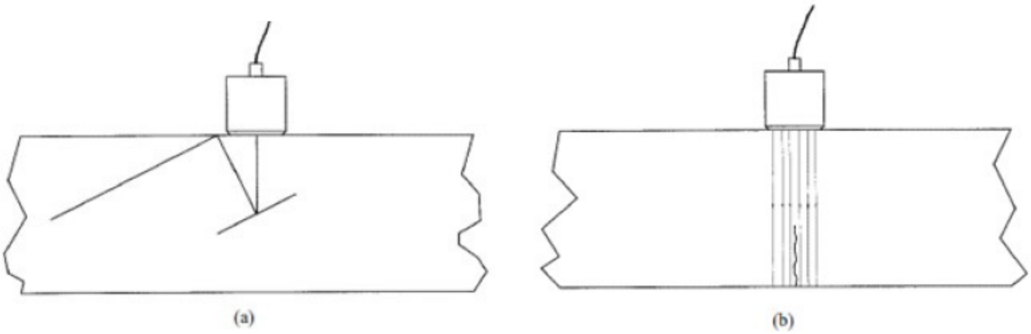

Figure 58: Unfavourable discontinuity orientation; reflecting away from the transducer (a) sound passing along crack (b) (Hellier, 2012)

The basic test equipment components are a transducer, pulser, receiver and display. In Figure 59, the simplified principle diagram is shown; the pulser creates a signal that goes to the transducer and receiver. The transducer converts the signal into sound energy which travels through the specimen and reflects back to the transducer where it is converted back into an electrical signal. The transducer signal is then sent to the receiver to be compared with the pulser signal on display.

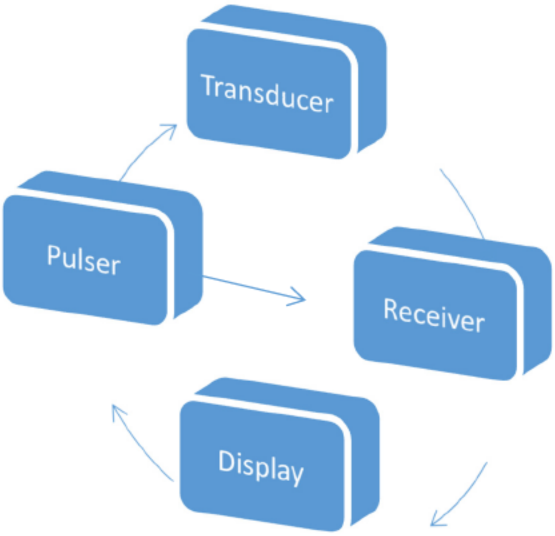

Figure 59: UT equipment principle diagram

Different methods of display are available, such as the A-, B-, C- and D-scan displays. A- and B-scan displays are shown in Figure 60, where IP is the initial pulse, BW the back wall, while A, B and C are the defects. The A-scan plots the amplitude of the incoming signals against time. The A-scan only shows the data at the current position below the probe although in the figure it shows how the A-scan differed along the scanning path. In the B-scan, the transducer moves across the sample (Figure 61). The B-scan creates a 2D sectional image of the entire specimen; that is if the transducer was moved over the entire part. It creates this image by recording the time of flight of the waves whilst the transducer is moved across the sample at a predetermined speed.

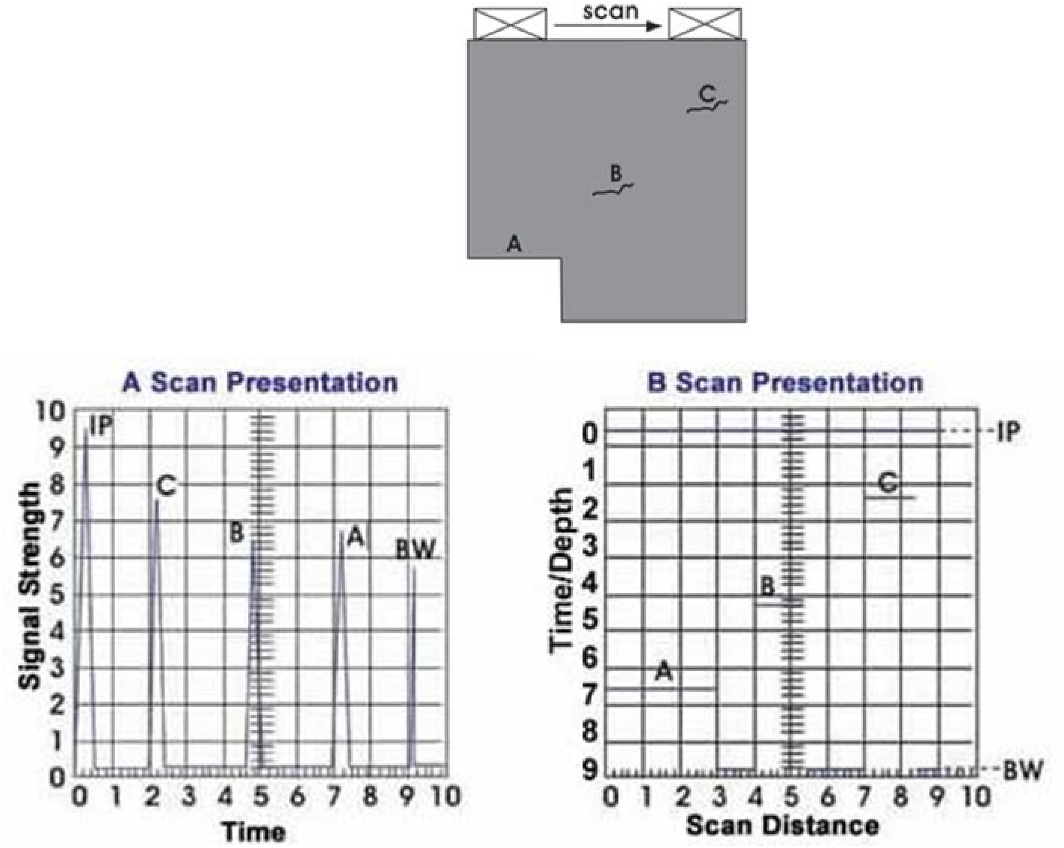

Figure 60: A- and B-scan of inspection block (NDT Resource Centre, 2016)

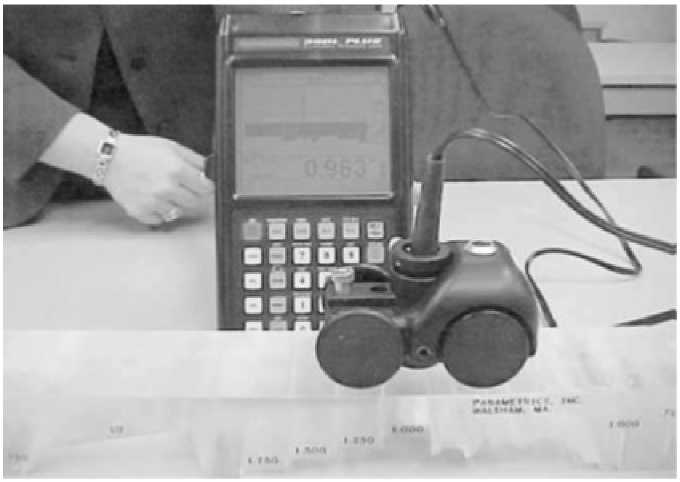

Figure 61: B-scan instrument (Hellier, 2012)

The C-scan is shown in Figure 62 and is similar to that of the B-scan but it moves across the specimen in the Y and X direction, creating a plane view parallel to the scanning.

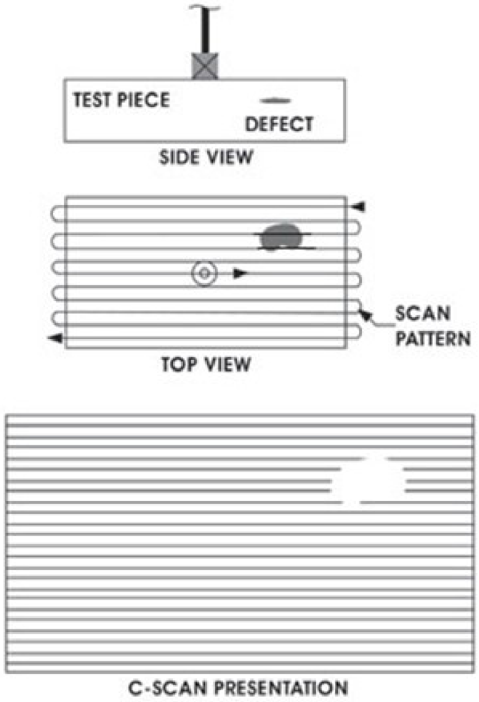

Figure 62: C-scan of test piece with defect (NDT Resource Centre, 2016)

Transducers

Various transducer configurations are available to form different types of beams for different applications. Two methods of wave generation are available:

Electromagnetic Acoustic Transducers (EMAT) induce a magnetic field within the electrically conductive part being inspected, setting up a Lorentz force which is transferred to the lattice structure of the material, producing an elastic wave.

Piezoelectric transducers make use of the piezoelectric effect to turn electrical pulses into mechanical vibrations and vice versa.

Both the EMAT and piezoelectric transducers have their advantages and disadvantages, for example, EMAT does not require couplant. Piezoelectric transducers are more common and are used in new developments such as phased array transducers. There are two groups of piezoelectric transducers: contact and immersion transducers. In Figure 63, a single transducer is shown (Innerspec Technologies, 2016) while the different types of immersion setups are shown in Figure 64.

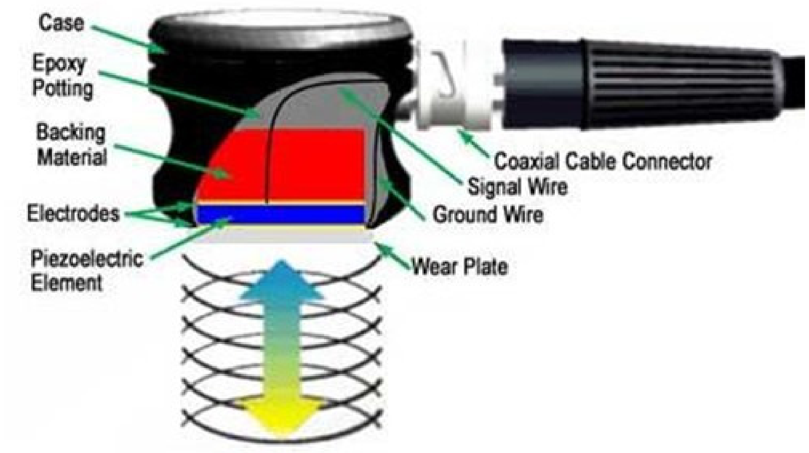
Case
Epoxy Potting
Backing Material
Electrodes
Piezoelectric Element
Coaxial Cable Connector
Signal Wire
Ground Wire
Wear Plate

Figure 63: Schematic of a single transducer (NDT Resource Centre, 2016)

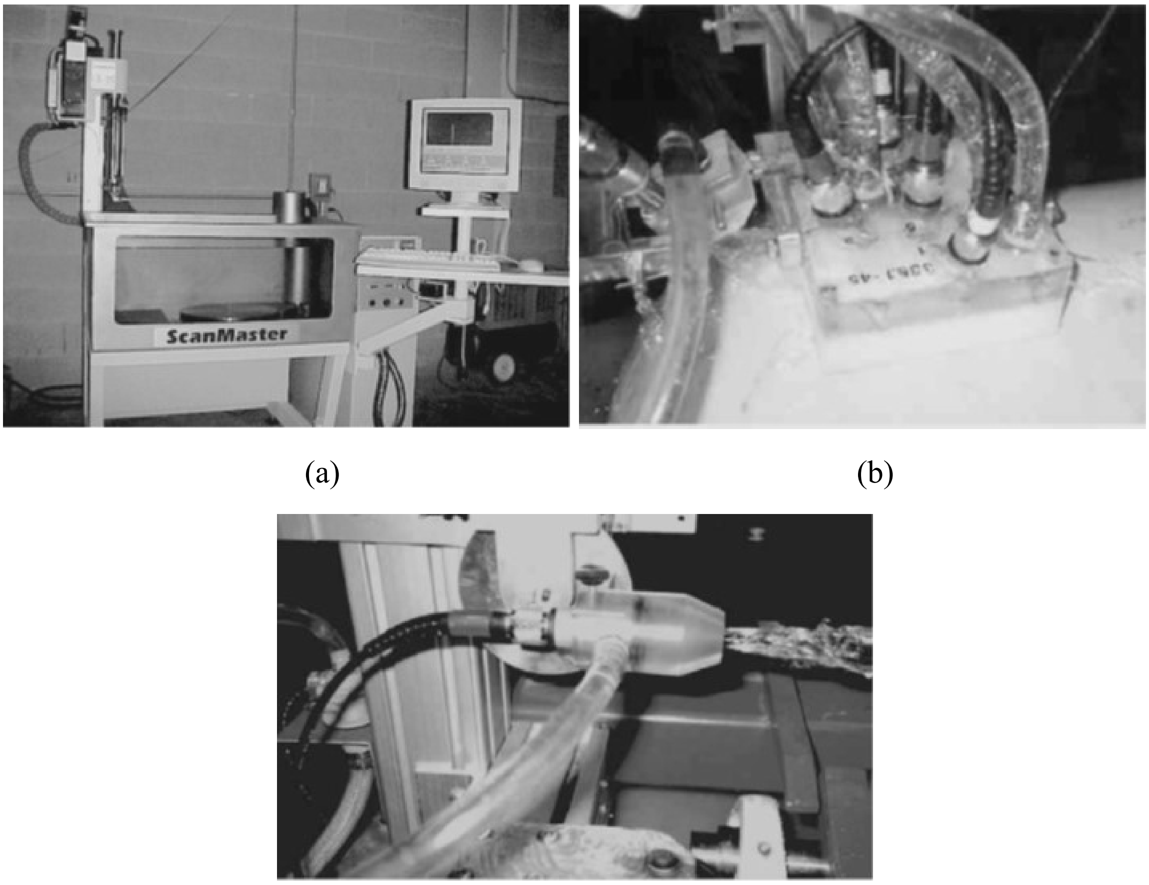
ScanMaster

(a) (b)

(c)

Figure 64: Immersion bath with (a) bubbler (b) and squirter systems (c) (Hellier, 2012)

The dead zone is one of the important characteristics of a transducer and refers to the area in front of the transducer in which the initial pulse that is being transmitted blinds the pulse that is being received.

For the transducer to properly transmit and receive waves from the specimen, proper contact is needed to minimize the reflections due to the acoustic impedance of the air between the contact surfaces. One method to ensure proper contact is the use of a couplant which displaces the air: most commonly a gel is placed between the transducer and the test piece. Other coupling methods, such as immersion, bubbler and squirting, make use of water. Examples are shown in Figure 64. The immersion method makes use of a tank filled with water: the specimen is placed inside the tank and the transducer is moved over the specimen and does not make contact with the specimen. A bubbler has a transducer within a small housing that is filled with water which is continually pumped through it to form a thin film of water between the transducer and the specimen. The squirter makes use of a jet of water that sprays onto the specimen: the transducer is placed behind the jet of water so as to transmit and receive sound waves by means of the jet. Therefore, systems are divided into two groups – contact and immersion methods.

Some of the different transducers available include the angle beam, dual transducer, focused transducer, focused wedge, dual transducer and phased array transducer. Each of these transducers are designed and used for specific applications. As the principles of optics apply to sound, the focused transducer focuses its energy in a small focal point. The dual transducer makes use of a single unit to transmit a sound wave and a single unit to receive the sound wave.

It is important to calibrate the transducer characteristics and equipment according to the standards that are available for each method. Different types of calibration equipment and methods are used including stepped wedges and distance/area-amplitude blocks. The IIW type reference block (IWW IIW type reference block an acronym for the International Institute of Welding) is commonly used in the US. In Figure 65, a standard IIW type calibration block is shown – note the featured small drilled holes representing flaws, used to test equipment.

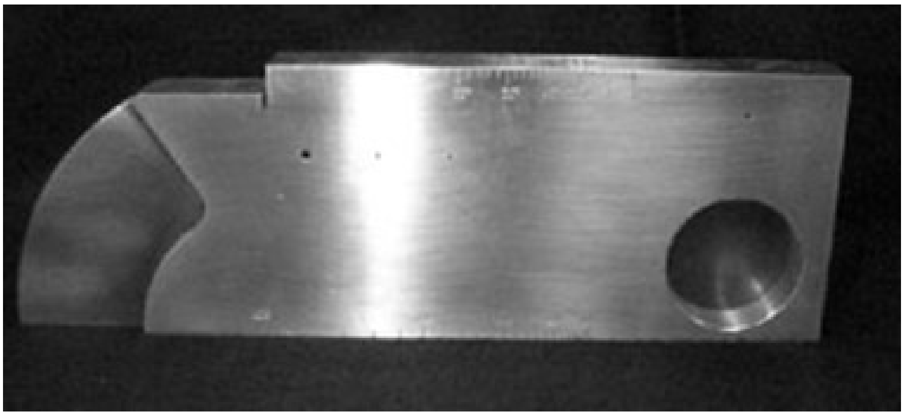

Figure 65:IIW type reference block (NDT Resource Centre, 2016)

Inspection techniques

Various techniques used for different applications include:

- Pulse-echo techniques

Contact scanning using compression waves; assessment is done by looking at the reflections from the back wall and discontinuities. It is important for the discontinuities to be orientated in such a manner where they do not reflect or reflect away from the transducer. Compression wave testing is often used for thickness gauging; the time taken between the initial pulse and the back wall echo is used to determine thickness.

- Angle beam shear waves

If orientation is unfavourable, the beam could be rotated to strike the discontinuity at an angle as close to perpendicular as possible. Compression waves can be used for angles below 10°, above 10° mode conversion makes the use of shear wave necessary. It then becomes necessary to move the beam beyond the first critical angle, leaving only shear waves present.

- Half skip and full skip

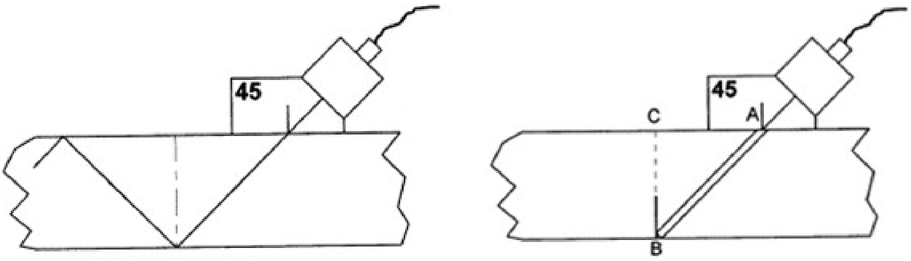

(a) (b)

Figure 66: Half skip method: no defect and no reflection (a); defect and reflection (b) (Hellier, 2012)

The angled transducer will transmit shear waves looking for surface breaking discontinuities. Half skip is referred to when the discontinuity is detected without reflecting off the back wall. If a defect is present on the top surface, the wave will first reflect on the back wall where after it will reflect from the discontinuity at the top and follow the same path back to the transducer.

- Beam path distance

For defects that are not on the top and bottom of a test piece, it is necessary to know the distance of the path. Pores and slag are some examples that are not sensitive to beam direction. The angle of the beam together with the speed of sound is used to plot the position of the defect.

- Rod and Pipe

An angled transducer is placed on the surface of a bar/pipe to measure for defects (Figure 67).

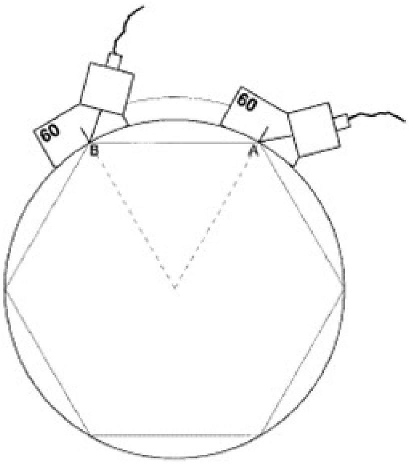

Figure 67: Angle beam on bar (Hellier, 2012)

- Multiple transducer techniques
  - Trough transmission

Two transducers are placed on opposite sides of the test piece facing each other.

  - Tandem

Two or more transducers are used on the same surface – the one transmits and the other receives. This is used to detect defects that do not break the top and bottom surface (Figure 68)

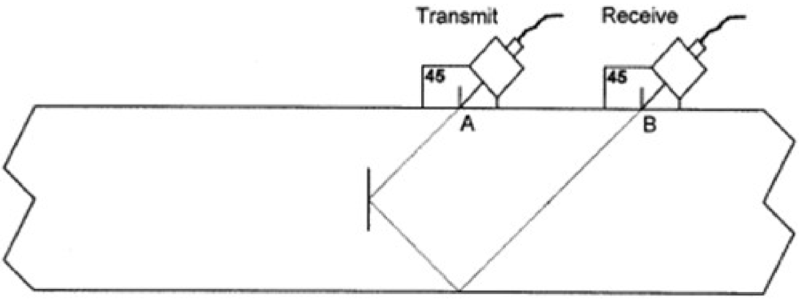

Figure 68: Tandem setup on a plate for defect in the centre of test piece (Hellier, 2012)

- Lamb wave

Lamb waves are used to detect defects. They can travel several metres in steel and therefore can be used to for rapid scanning application.

- Immersion

Immersion techniques are convenient for scanning large components – an example is shown in Figure 69. Most contact techniques can be applied to immersion testing, the advantages being consistent coupling, variable angles and focus, surface reflection ignored (gating), contour following and improved near-surface resolution.

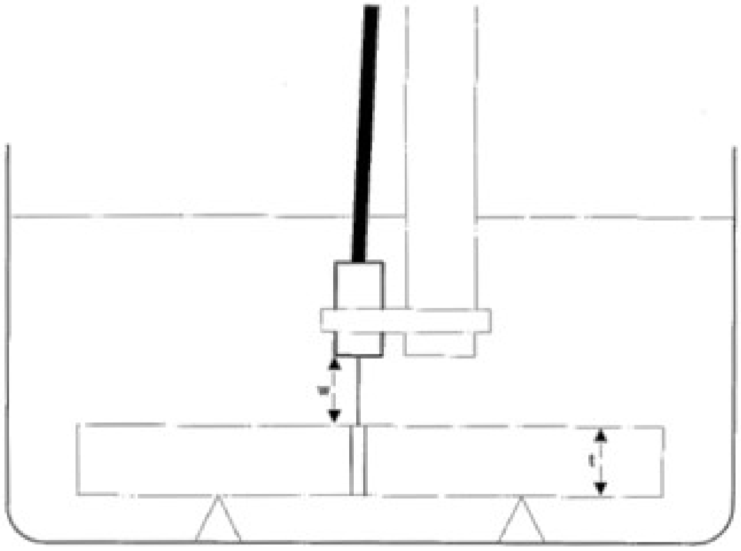

Figure 69: Immersion technique (Hellier, 2012)

- Maximum amplitude

Maximum amplitude system (MAS) works on the principle that as the transducer moves over a defect the shape of the defect will reflect at different amplitudes. The amplitude of the reflection will be displayed as a surface reflection from the defect. The sizing and location can then be done by moving the transducer across the defect and looking at the individual amplitudes: a rise would indicate that the surface of the defect is coming closer, whilst a decrease would indicate a surface that is moving away from the transducer.

- Tip diffraction
    - Standard angle beam

As the sound hits the tip of a reflector, the energy diffracts from the tip of the defect in a spherical form, as shown in Figure 70. This means that the diffracted beam would be spread out and is not directional. This addition signal is used to size the defect.

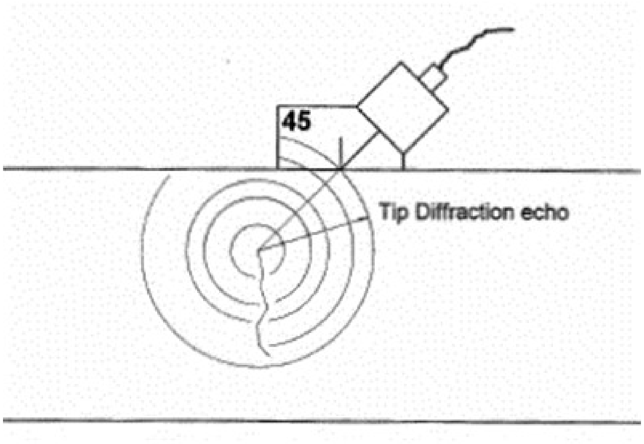

Figure 70: Tip diffraction echo (Hellier, 2012)

- Time of flight diffraction (TOFD)

Two angled compression wave transducers are used; one transmits while the other receives. TOFD uses tip diffraction to determine the top and bottom of a defect in one step. It makes use of an angled compression wave as its tip diffraction signal is stronger and a lateral wave is produced to determine the distance between the transmitter and receiver.

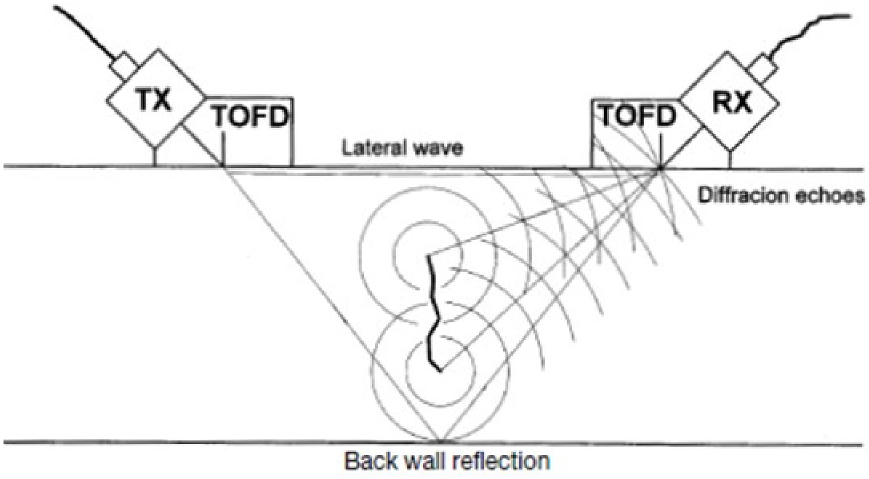

Figure 71: Time of flight diffraction (Hellier, 2012)

2.5.4.3 Influential variables

Ultrasonic examination can be influenced by various factors. It is shown that transducer frequency, angle and diameter have a great effect on the results. The practitioner needs to be aware of all the variables to be able to recognize defects and anomalies that could arise.

- *The temperature* of the material will influence the speed of sound, therefore it is important to note the temperature and calibrate equipment before each test. In metals, the change is small when compared to that of liquids. The speed of sound in water at 20°C is ~1480 m/s while at 30°C the speed is ~ 1570 m/s.

- *Attenuation* changes within a material due to temperature, material treatments (for example: hardening), micro porosity and grain size.
- Pulse length can affect the *resolution*.
- *Surface finish and coatings* affect the readings.
- *Contact –.* pressure and couplant will affect the amplitude of the signal. A dry surface would cause an air boundary.
- *Dendritic microstructure.* Branch-like grains occur in certain metals and are called dendrites. These dendrites grow in the direction of heat dissipation. These grains can redirect the energy of the wave.
- *Gain* can exaggerate insignificant indications.

2.5.4.4 Phased array UT

A major innovation in UT is phased array inspection. These transducers are made up of a set of single piezoelectric crystals to form an array that can steer and focus the energy. The elements are pulsed using a combination of elements and timing to excite and focus at the desired depth in the material. All basic principles of ultrasonic theory apply to phased array which is based on the constructive and destructive property of waves, as shown in Figure 72.

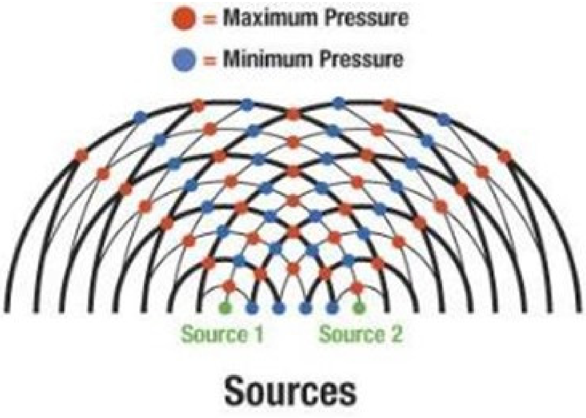

Figure 72: Two-point source interference pattern (Olympus, 2016)

The transducer receives signals that pulse the array elements in such a manner as to create a single beam travelling through the material in the desired direction; an example of a typical straight beam phased array transducer is shown in Figure 73. This ability to steer and shape the beam makes it possible to generate a vast number of beam profiles (Hellier, 2012; Olympus, 2016).

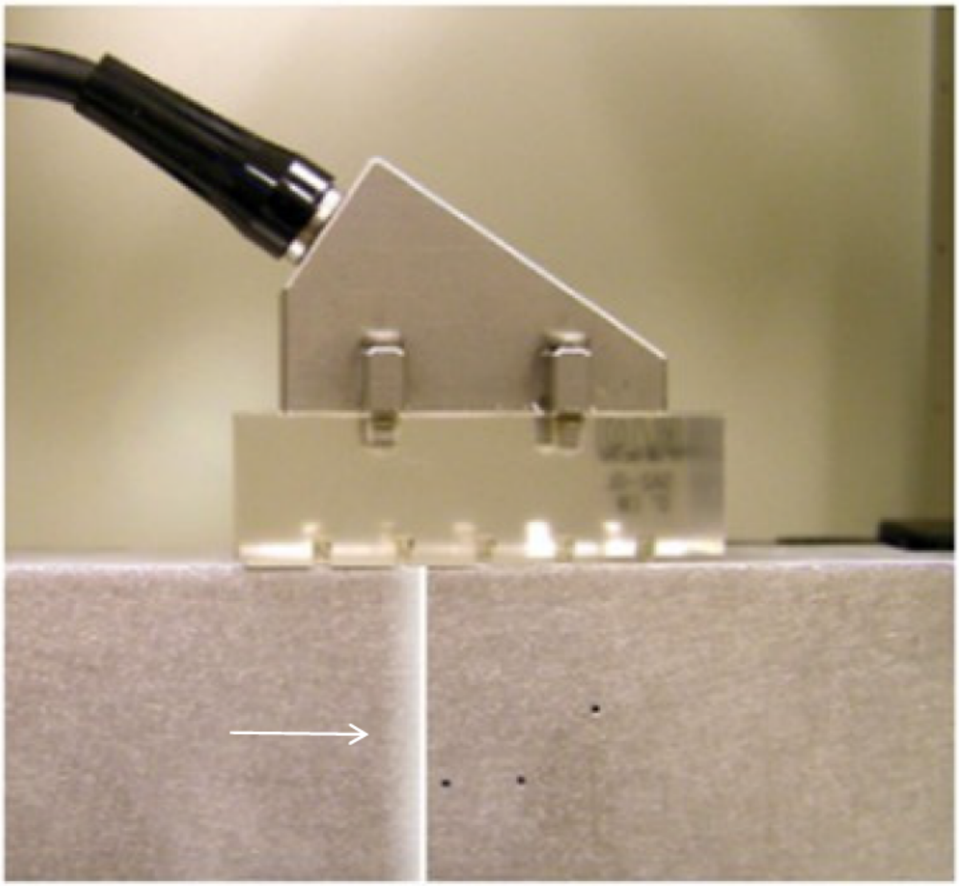

Figure 73: Linear straight beam scan from left to right using a phased array transducer (Olympus, 2016)

Phased array technology allows for the following:

- Control of beam angle, focal length and beam spot size.
- Inspection can be done at multiple angles; fixed or scanning.
- Greater flexibility for inspection of complex geometries.
- Stationary transducer can scan over an area with high speeds (Olympus, 2016).

Similar to conventional UT, phased array ultrasonic testing, or PAUT, makes use of certain parameters which influence the testing. The transducer is not only characterized by the type of beam and/or testing frequency, but also the number of elements and their geometry. In Figure 74, the parameters of a PAUT transducer are shown. The software will use this information to generate the desired beam. PAUT makes use of the constructive and destructive effects of wave phasing to control and steer the beam. In Figure 75, a focused beam is shown where the beam is created by triggering the outer elements numbered 1 followed by 2,3, etc., to 9. This causes a focused point along the depth of the test piece.

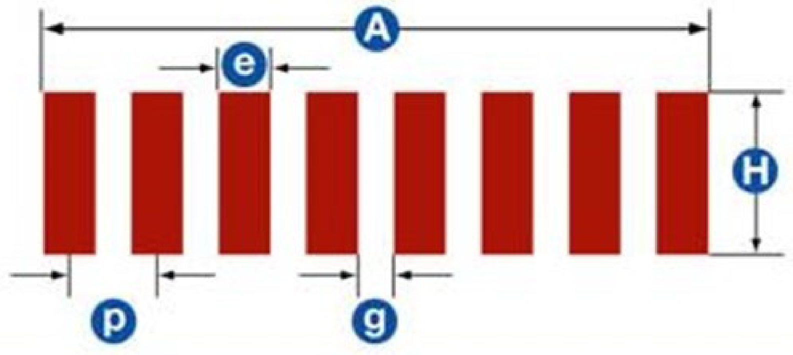

N = total number of elements in the array
A = total aperture in steering or active direction
H = element height or elevation. Since this dimension is fixed, it is often referred to as the passive plane.
p = pitch, or center-to-center distance between to successive elements
e = width of an individual element
g = spacing between active elements

Figure 74: Dimensional parameters of PAUT transducer (Olympus, 2016)

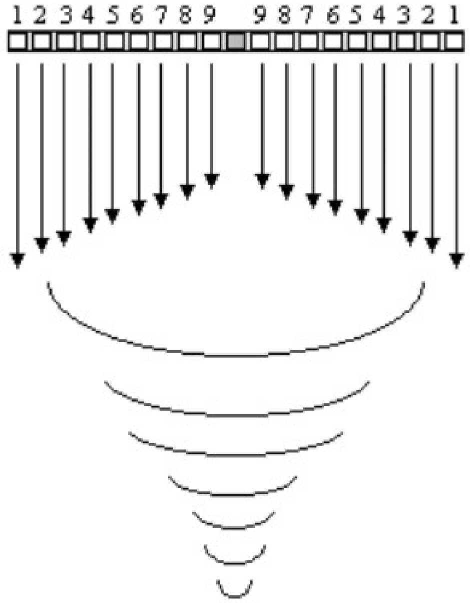

Figure 75: PAUT focused beam (Hellier, 2012)

The element size influences the beam-steering capabilities. As the element size decreases, the steering capability increases. However, if the element is too small (less than one wavelength-strong), side lobes would occur. Side lobes refer to sound energy that spreads out from the source at angles different to that of the primary beam. Generally, more elements are desirable as the only disadvantages are system cost and complexity, as the more elements the greater area coverage, improved sensitivity and steering capabilities. A small pitch and large aperture is desired. A large aperture means greater sensitivity, minimum unwanted beam spreading as well as better beam focusing. A small pitch allows for greater steering range. PAUT transducers commonly have 16, 32 and 64 element apertures.

In Figure 76, a PAUT test is carried out on a test block that has holes through it; the A-scan is shown on the right with defect echoes indicated by the coloured ellipses. The software gives feedback on the individual waveforms that are superimposed to form a representation of the block below the transducer. The software has the ability to identify the depth and location of defect with respect to the transducer. The software allows for investigation of the signal by dragging a cursor (blue in Figure 76) over the defect. The signal strength will then be indicated on the left by a peak which is used to indicate depth or distance of the defect.

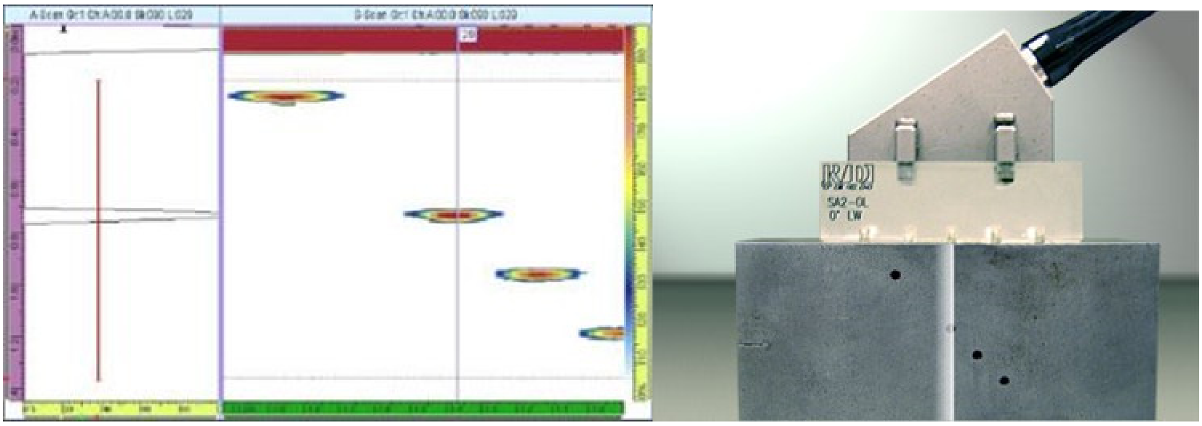

(a) (b)

Figure 76: PAUT A- and linear scan result (a) on a test piece with holes (b) (Olympus, 2016)

2.5.5 Acoustic testing

2.5.5.1 Acoustic emission testing

Acoustic emission testing (AE) is based on the principle that elastic stress waves are generated by the rapid release of energy in the material due to relaxation of the stress and strain fields. These waves are then measured by electric sensors and interpreted. Some of the sound wave theory from the previous section (2.5.4) should be kept in mind during this section. AE can be used in different stages; during manufacturing, after manufacturing and whilst in service. When AE is applied during manufacturing, it serves as a quality control method, whilst it can be applied as a NDT method post manufacturing. AE is used in on-line health monitoring of pipes and pressure vessels, leak detection, rotating equipment, production line components and structures subject to stress and loading. In the 1950s, the first extensive study acoustic emission testing was reported by Dr. Joseph Kaiser in Munich, Germany, in his Ph.D. thesis. Table 8 shows the advantages and limitations of AE (Hellier, 2012; Raj *et al.*, 2007).

Table 8: The AE advantages and limitations

Advantages	Limitations
Large components (pipes, etc.) can be monitored, less sensitive to geometry	Sensors often need contact with surface
Can possibly predict failure	Multiple sensors needed for flaw detection
Continuous monitoring(on-line)	Signal interpretation required

One of the AE methods that is used for NDT is based on the natural resonant frequency of a component. Resonant frequency of any component is dependent on the material properties, dimensions and densities. This resonant frequency is what gives different musical instruments their unique sound. For example, string instruments sound different when the tension in the string is changed; the same applies for different diameters of the string or when using metal compared to nylon. ASTM originally approved this general method in 1998. Various companies use different techniques. These include, amongst others, the resonant acoustic method (RFDA), the resonant inspection theory and the impulse excitation technique (IMCE) (Stultz *et al., 2005;* Bono *et al.*, 2010; IMCE, 2016; The Modal Shop, 2016).

These methods are used to look for defects on production lines of metal components. If the component being measured has a deviation from the known frequency of a faultless component, it indicates that there is a structural defect within the measured component e.g., a crack that reduces the stiffness causing the resonant frequency to drop. The degree of shift of the resonant frequency is proportional to the degree of the defect. The resonant frequency of an undamped object f_r is given by

$$f_r = \sqrt{\frac{k}{m}},$$

Where:

k=stiffness

m=mass

These variables are dependent on material properties and sample geometry. To illustrate this, consider the following: a single degree-of-freedom (SDOF) mass hanging from a spring and with this spring containing some damping, as illustrated in Figure 77.

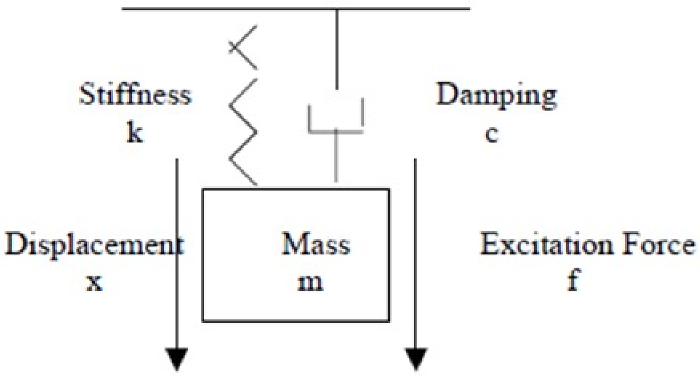

Figure 77: Single degree-of-freedom mass model (Schiefer and Sjoeberg., 2005)

The equation of motion is given by

$$m\ddot{x}(t) + c\dot{x}(t) + kx(t) = f(t)$$

Where:

f= excitation force
k=stiffness
c=damping coefficient
m=mass

The energy introduced into the system by the excitation force is transferred into the system as kinetic energy of the mass and potential energy of the spring, which is dissipated by the damping. These two equations describe a simple SDOF system, but the underlying principle remains the same for more complex systems. The mass of the material is dependent on the volume and density while the stiffness is dependent on the Young's modulus and cross-sectional geometry. Therefore, any defects that influence the mass or stiffness will cause a shift in the natural frequencies. For example, porosity reduces the mass, thus increasing the natural frequency. A crack would reduce the material stiffness in the region of the crack which reduces the natural frequency. These shifts are measurable if the defect is structurally significant with respect to the size and location within a specific resonance mode shape. Material damping refers to the capacity of the material to dissipate energy during mechanical vibration. Various works set out to determine the damping characteristic of materials with regard to factors such as stress, frequency, temperature microstructure and so forth. Most metals and alloys exhibit a low damping capacity. (NDT, 2016; Schiefer and Sjoeberg, 2005).

Table 9: The typical structural defects detectable by RAM-NDT (Bono et al., 2008)

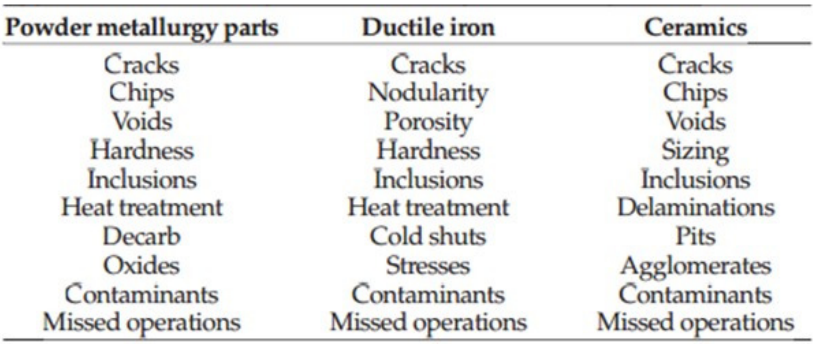

Powder metallurgy parts	Ductile iron	Ceramics
Cracks	Cracks	Cracks
Chips	Nodularity	Chips
Voids	Porosity	Voids
Hardness	Hardness	Sizing
Inclusions	Inclusions	Inclusions
Heat treatment	Heat treatment	Delaminations
Decarb	Cold shuts	Pits
Oxides	Stresses	Agglomerates
Contaminants	Contaminants	Contaminants
Missed operations	Missed operations	Missed operations

Schiefer and Sjoeberg (2005) describe the principle of resonant acoustic method testing (RAM-NDT) by "*Resonant inspection measures the structural response of a part and evaluates it against the statistical variation from a control set of good parts to screen defects*." Some objects that look rigid to the human eye also undergo deformation under loading. This implies that it also has the capability to vibrate. All structures have resonant frequencies; the structure will amplify certain frequencies when energy is introduced. Tuning forks vibrate at their natural frequencies for a long period of time when they are lightly tapped. The general flow of this process is indicated in Figure 78; the process makes use of an electromechanical hammer to induce a vibration. The sound waves are then measured via a microphone and sent to a digital controller which processes the information. This information is then used for the pass/fail criteria (Bono *et al.*, 2010).

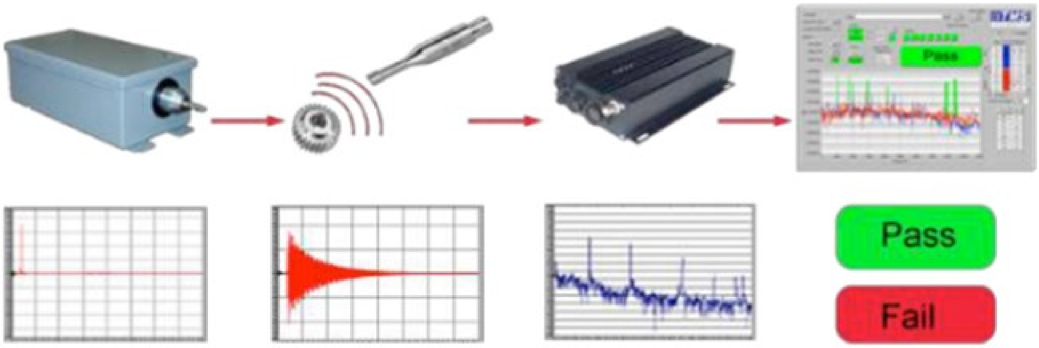

Figure 78: RAM-NDT equipment from the Modal Shop and their process flow (Bono et al., 2010)

Figure 79 shows how the processed signal peaks are measured and compared to be within range. Any shift would be recognized indicating a fault in that specific part.

RFDA Basic from IMCE makes use of the impulse excitation technique; this technology is also used to measure elastic properties of predefined shapes. This is done quickly and effectively by measuring the resonant frequencies and internal friction damping of the specimen. The RFDA Basic is designed for performing such tasks by tapping the component, creating an impulse that causes the component to vibrate at its own natural frequency. These frequencies are measured by a microphone and sent to the RFDA software where the resonant frequencies and internal damping is measured and the elastic properties can be calculated. Figures 80 and 81 illustrate the principle of the RFDA basic operation and how the values are obtained for the material properties of predefined shapes. In this case, a rectangular bar is placed on two support wires. The microphone is place above the midpoint of the bar to measure the sound waves propagating from the bar as the bar flexes up and down (vibrating) when tapped by the hammer (IMCE, 2016).

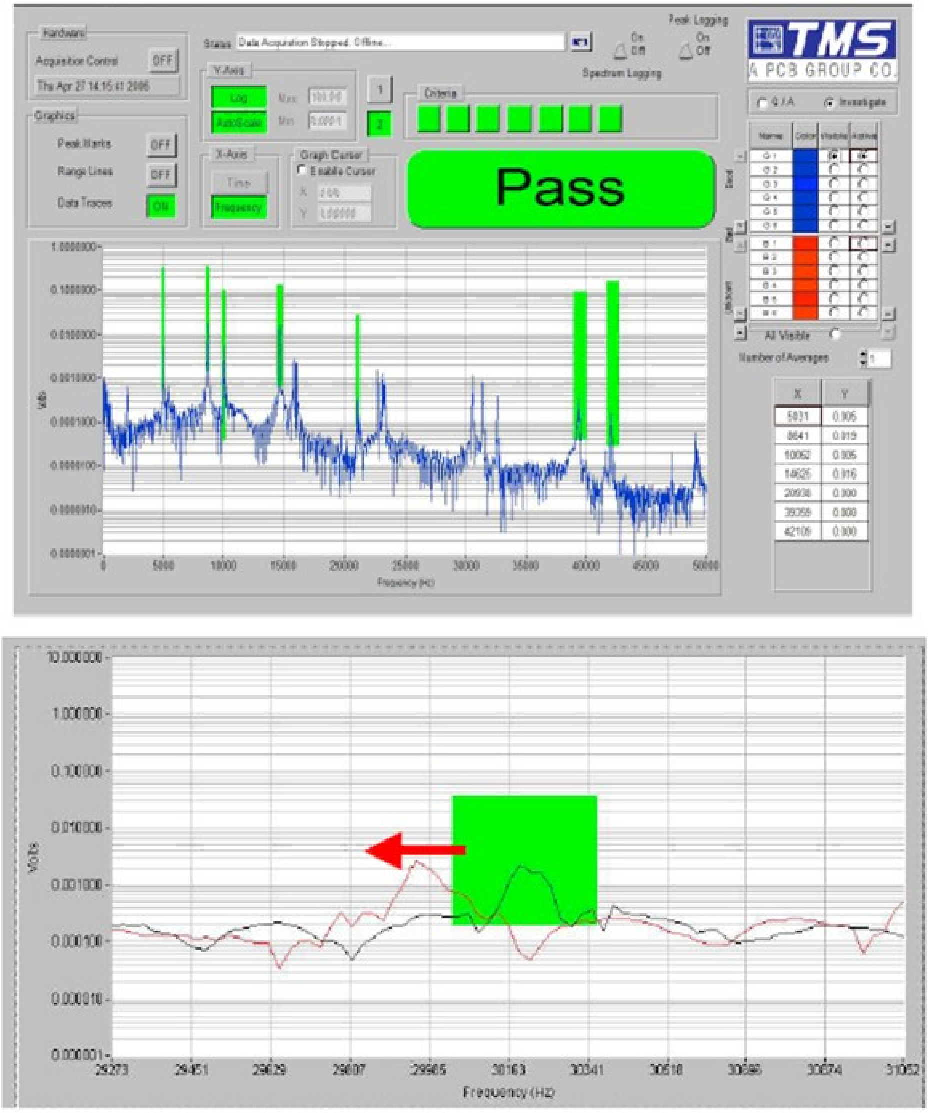

Status: Data Acquisition Stopped. Offline...

Thu Apr 27 14:15:41 2006

X	Y
5031	0.006
8641	0.019
10062	0.005
14625	0.016
20938	0.000
39059	0.000
42109	0.000

Hardware
Acquisition Control
OFF
Graphics
Peak Marks
OFF
Range Lines
OFF
Data Traces
ON
Y-Axis
Log
AutoScale
Max
Min
1
2
X-Axis
Time
Frequency
Graph Cursor
Enable Cursor
Criteria
Pass
Peak Logging
On
Off
Spectrum Logging
TMS
A PCB GROUP CO.
Q.I.A
Investigate
Good
Bad
Unknown
All Visible
Number of Averages
1.0000000
0.1000000
0.0100000
0.0010000
0.0001000
0.0000100
0.0000010
0.0000001
Volts
0
5000
10000
15000
20000
25000
30000
35000
40000
45000
50000
Frequency (Hz)
10.000000
1.000000
0.100000
0.010000
0.001000
0.000100
0.000010
0.000001
Volts
29273
29451
29629
29807
29985
30163
30341
30518
30696
30874
31052
Frequency (HZ)

Figure 79: RAM-NDT software interface after an acoustic measurement of a component (top). An indication of a typical peak frequency shift of a defective component (bottom) (Bono et al., 2010)

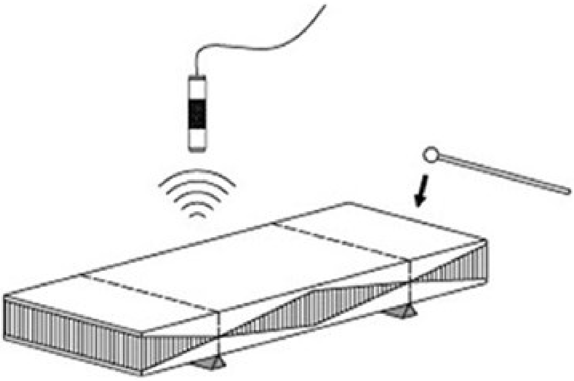

$$E = 0.9465 \left(\frac{m\, f_f^{\,2}}{w}\right)\left(\frac{L^3}{t^3}\right) T$$

with ***E*** *the Young's modulus*
f_f *the flexular frequency*
m *the mass*
L *the length*
w *the width*
t *the thickness*
T *the correction factor*

Figure 80: RFDA-basic modulus of elasticity calculation for rectangular bar (IMCE, 2016)

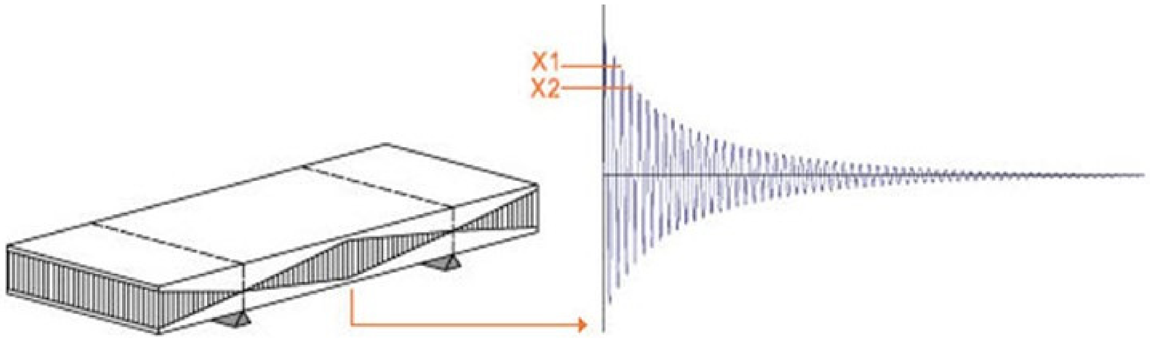

$$\text{Internal friction} = Q^{-1} = \frac{\text{energy dissipated as heat per unit volume over one cycle}}{\text{energy stored per unit volume}} = \frac{1}{\pi}\ln\left(\frac{X_1}{X_2}\right)$$

Figure 81: RFDA-basic internal friction calculation characterized by the material and defects (IMCE, 2016)

2.5.6 Summary

The physics behind each NDT process is based on basic laws; however, the equipment and software capabilities might be difficult to grasp as they are man-made. With the development of new technologies and the integration thereof, more complex systems arise. A good example of NDT is X-ray CT scans.

UT is versatile, easy to employ and has many different applications for specific needs.

AE has a high initial investment cost in time and money spent to be able to differentiate between defect-free and defective parts. Thereafter, AE is a quick and simple method to use as a quality control method.

2.6 NDT evaluation of AM objects

In AM, the variation in part quality and mechanical properties, due to presence of defects, surface roughness and residual stress, can limit its use in high-value or mission critical applications. Quality assurance and certification becomes all the more important in the production of safety related AM components e.g., the aeronautical-, automotive- and medical industries. Certification can be obtained by various means including the manufacturing of ancillary test specimens or NDT using computer tomography.

Another option is to monitor the process during building; the layerwise build-up process of additive manufacturing allows for detailed monitoring (Krauss *et al.*, 2012; Selfi *et al.*, 2016).

Khairallah *et al.* (2016) suggests that to reduce porosity in order to obtain engineering quality standards, instead of working on a trial and error principle, to rather use model and predictive simulation which can reduce time and cost.

A great challenge in AM is in the access and/or sharing of information regarding the machine setup parameters that prevent the user from overriding the machines present processing conditions, thereby preventing optimization of these conditions (Selfi *et al.*, 2016).

The National Institute of Standards and Technology (NIST) has developed a program to meet the need for qualification of AM processes. The objective of the *Qualification for Additive Manufacturing Materials, Processes, and Parts* program being "*Develop test methods and protocols, provide reference data, and establish requirements to reduce the cost and time to qualify AM materials, processes, and parts*" (NIST, 2016).

As stated by Waller *et al.* (2015), the factors that challenge NDT of AM products are

- Complex geometries.
- Rough surface finish.
- Variable and complex grain structure.
- Undefined defect types, sizes and shapes.
- Lack of effect-of-defect studies.
- Lack of physical reference standards.
- Lack of written inspection procedures for AM processes.
- Lack of probability of detection (PoD) information.
- Lack of mature in-process monitoring techniques.

Everton *et al.* (2016) describe various studies that focus on methods for on-line monitoring used in different metal AM processes. Most of these methods make use of closed-loop visual inspection techniques.

2.6.1 CT scans

Since the introduction of dimensional CT metrology, intricate components produced by AM can be inspected for geometrical and tolerance quality control which is not possible in any other way as there are no methods to measure internal geometries. Computed tomography is a very useful tool for accuracy measurements, especially for control of the inner walls and complex inner structures, their size and locations. CT combined with AM technology is often used in reverse engineering with applications in the medical, industrial, archaeological and historical fields (du Plessis *et al.*, 2016; Kruth *et al.*, 2011; Kim *et al.*, 2016; Maskery *et al.*, 2016).

Gapinski *et al.* (2016) applied a coordinate measuring machine (CMM) and CT scanner to a plastic ABS FDM part to determine the possibilities of CT in the AM process. It was found that the convergence of measurement with these two methods does exist. However, deviations of measurements arose mostly from CT as the scanner collects data representing the whole element with a much greater number of points, whereas CMM automatically filtered data which is implicated from the size of the measuring tip and the number of measurement points. It was found that the surface roughness influenced the results (Figure 82).

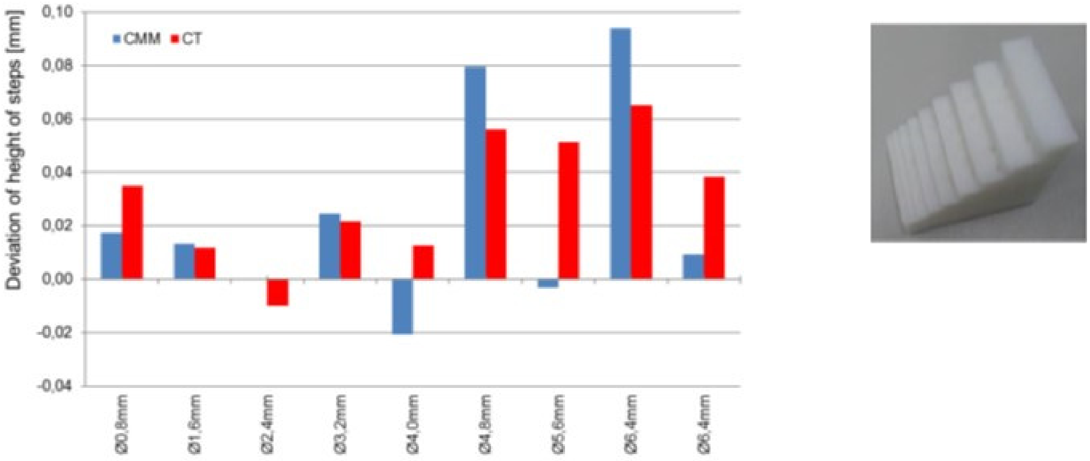

Figure 82: Deviation of height of steps measured on CMM and CT scans (Gapinski et al., 2016)

X-ray CT was used to confirm interlayer pores of a SLS nylon component that was glued together; the part was filled with blue ink, which in turn leaked out at one of the corners, as shown in Figure 83 (de Chiffre *et al.*, 2014).

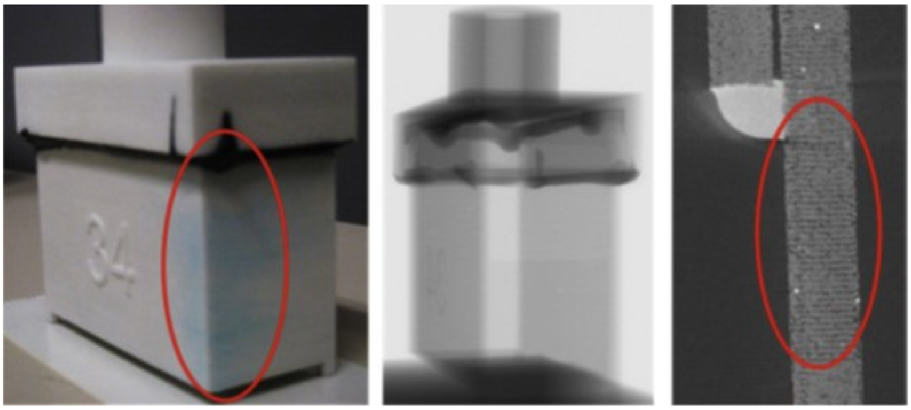

Figure 83: Nylon SLS components glued together; the right picture is a section through the CT model, showing the nylon parts (grey colour), interlayer porosity (dark spots), small particle inclusions and the glue in white (de Chiffre et al., 2014)

In CT scans, density calibration can be carried out using the grey values to determine the densities of different types of metals, similar to the way in which air in the pores are distinguished from metal. A widely used method used to carry out such calibrations is based on the differing densities of water and air in a glass container (water phantom) which would yield different grey values. Figure 84 shows a cross-section of the water phantom and how the grey value differs for these different materials (du Plessis *et al.*, 2014). For metals, less penetration will result, causing lower contrast and imaging quality (du Plessis *et al.*, 2014).

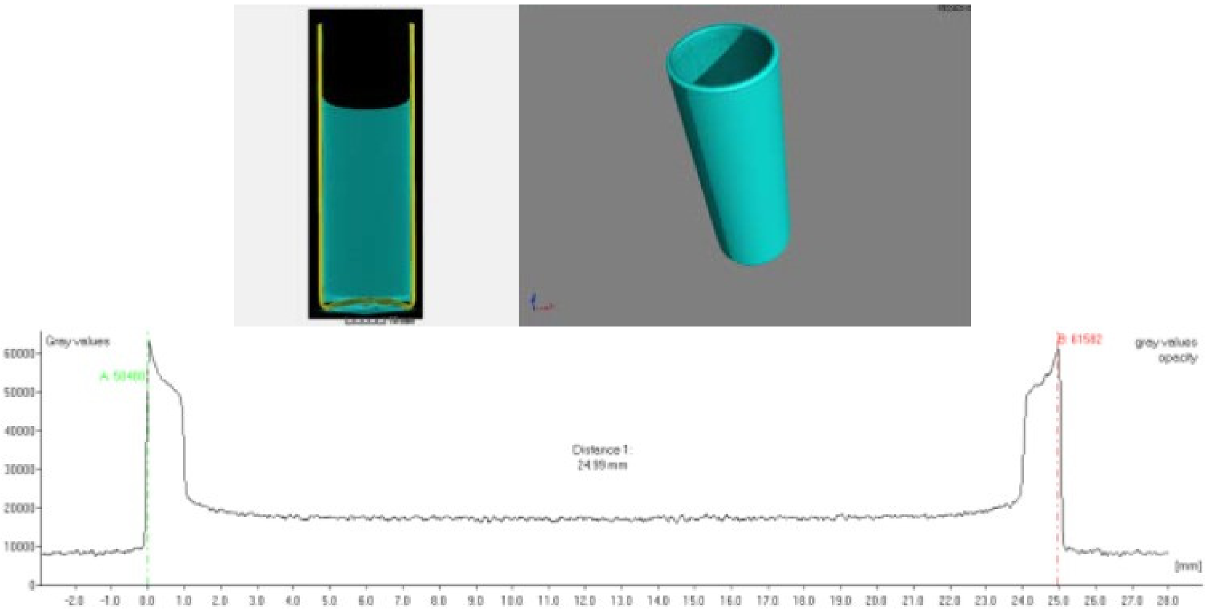

Figure 84: Water in a glass container surrounded with air atmosphere (above) grey value cross-section (below) (du Plessis et al., 2014)

Aloisi and Carmignato (2016) compared dimensional measurements of CT to that of tactile coordinate measuring machines (CCM). They produced three AM parts: one of metal produced using SLS and the other two were polymer FDM parts, as shown in Figure 85, with SLS on the left and FDM in the middle and right. The samples had an *Rz* surface roughness ranging between 30 and 125 µm. It was found that the CT external diameters were always smaller than CCM measurements by ~*Rz*/2 and the CT internal diameters were always greater than CCM by the same amount. It was confirmed that the results hold true for different test conditions when used in different CT systems, sized parts, manufacturing processes (roughness, material) and voxel sizes. The parts had similar Abbott-Firestone curves and it was suggested to investigate the influence thereof on the dimensional deviation. Figure 86 shows the deviation of the CT measurements compared to CMM measurements of the SLS sample with a *Rz* value of 125 µm external and 100 µm internal (Aloisi and Carmignato., 2016).

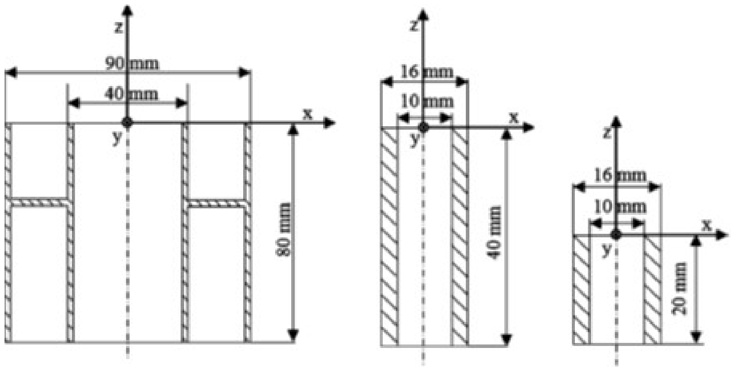

Figure 85: CAD dimensions of SLS and FDM dimensional samples Note: for better visibility, sample 1 is represented with a 1:2 scale, whereas samples 2 and 3 are represented with a 1:1 scale (Aloisi and Carmignato., 2016)

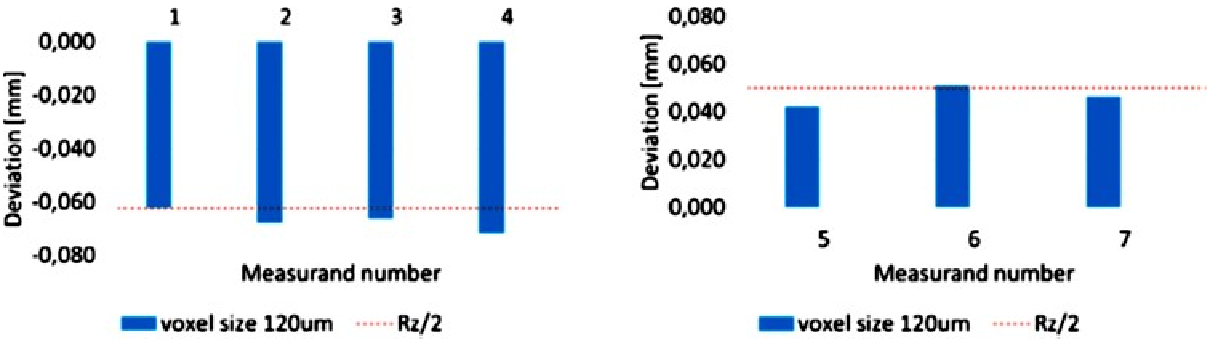

Figure 86: Deviations between CT and CMM measurements for external diameters of SLS l sample. Vertical columns represent the deviations for each measure,, while the horizontal axis represents the measure and number. The dashed line shows the value corresponding to Rz/2of the external surface. (Left) Deviations between CT and CMM measurements for the internal diameters of the same sample. Vertical columns represent the deviations for each measure , while the horizontal axis represents the measure and number. The dashed line shows the value corresponding to Rz/2of the internal surface. (Right) (Aloisi and Carmignato., 2016)

An X-ray CT surface analysis of DMLS AlSi10Mg was investigated by Townsend *et al.* (2016) where the results were compared to that found during focus variation (FV) scanning. Both the CT and FV STL data were imported to CloudCompare software for comparison. X-ray CT scanning was carried out using a Nikon XT H 22 microfocus CT with voxel size of 17 µm. FV measurements were taken using an Alcona G4 (10x objective lens, vertical resolution 0.2 µm with 2.3 µm sampling distance. The areal surface parameter data was computed according to ISO 25178-2 and filtering to ISO 25178-3. It was found that the surface roughness *Sa* and *Sq* values obtained by CT were 28% and 29% greater than that of FV. The two different surface maps of the sample are shown in Figure 87. To determine the validation of X-ray CT surface roughness of AM parts, comparisons between known roughness values of test plates (Rubert Microsurf 334 comparator) were made. The X-ray CT was set to a voxel size of 12.9 µm. The results are shown in Table 10. From this it was suggested that for areal surface roughness measurements, an initial guideline is that the voxel size should be below *Ra* and *Sa* to avoid errors.

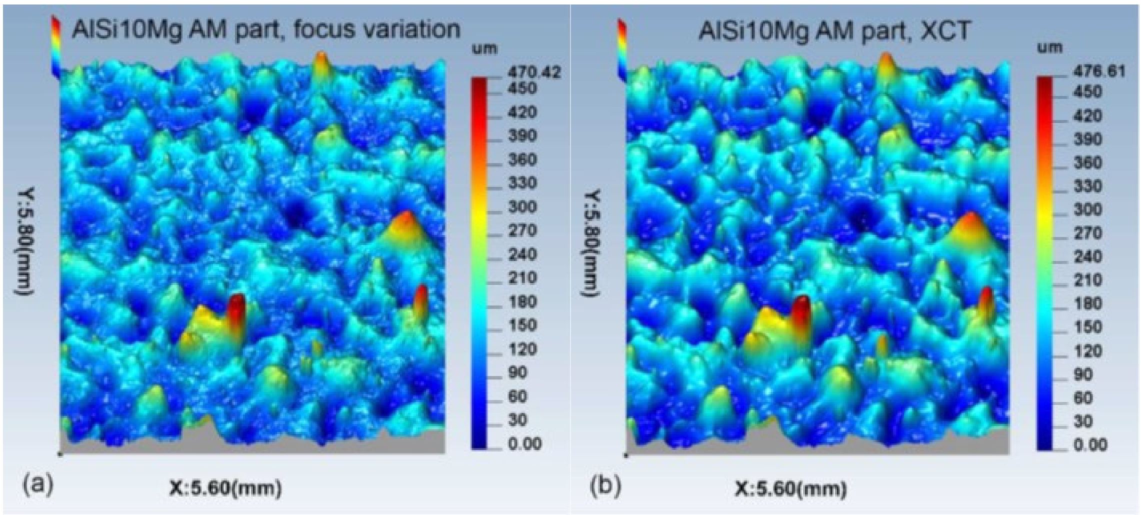

Figure 87: FV (a) and CT (b) height maps of the DMLS AlSi10Mg surface (Townsend et al., 2016)

Table 10: The *Ra* values of Rubert values compared to *Sa* values of CT and FV (Townsend *et al.*, 2016)

Nominal Rubert Plate *Ra* (µm)	Mean FV *Sa* (µm)	Mean XCT *Sa* (µm)	Difference between mean XCT and FV *Sa* (% of FV)
50	51.1	55.6	8.8 %
25	27.4	31.3	14.5 %
12.5	12.4	14.6	17.2 %
6.3	6.6	9.0	34.5 %
3.2	4.0	5.6	40.5 %
1.6	2.5	3.5	43.1 %
0.8	0.56	1.09	95 %

Probability of detection (PoD) refers to the ability of a NDT technique to detect flaws and in X-ray CT and AM there are aspects of PoD and minimum flaw size standards that are undetermined. One of the best ways to determine whether a NDT technique, including X-ray CT, is reliable is to test a component with an artificial defect. Kim *et al.* (2016) inspected the quality of DMLS Inconel 625 parts with internal features (EOS M270 with spot size 100 µm and default Inconel 625 settings, particle size between 15 and 65 µm), using X-ray CT and compared them with the CAD data (Figure 88). This revealed that the manufacturing process had deviations of up to 100 µm when compared to the CAD. It was suggested that ±50 µm tolerances are related to the AM process rather than measurement uncertainty (Kim *et al.*, 2016).

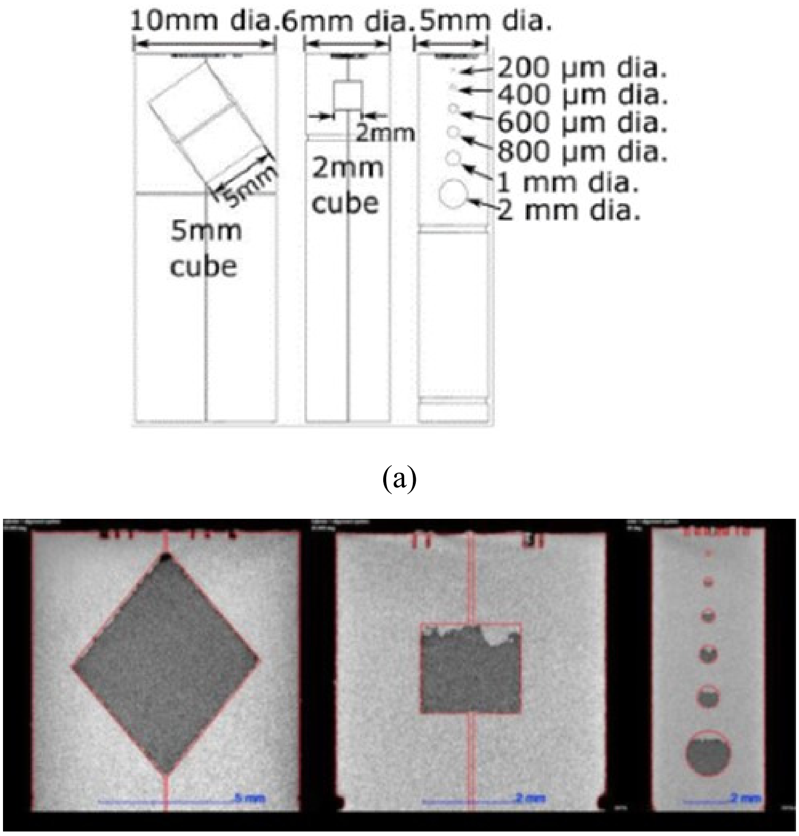

(b)

Figure 88: Design of internal features of samples (a) CT of internal features of samples (b) (Kim et al., 2016)

Karme *et al.* (2015) also investigated the possibility of using CT equipment as a quality control method for AM parts. The focus of the research was on a small tubular design and a specimen (Stainless Steel 316L) built using a research machine similar to that of EOS M series systems (200W at 1 m/s scanning speed, spot size 100 µm, layer thickness 20 µm), as shown in Figure 89. The scanning strategy made use of 5 mm stripes with a 90° rotation after each layer. CT scanning was done using copper filters and a custom machine which incorporates the high power, high resolution phoenix|x-ray Nanotom 180 NF (CMOS flat panel detector with 2304 x 2284 pixels of 50 µm x 50 µm size) and obtained 600-720 images in a full rotation, with exposure time of 5-15 s for each image. An effective pixel size of 6.8-8 µm was obtained. It was found that the slightly different scan settings as well as different density thresholds caused a variation between CT data (surface area, volume, porosity, etc.). The porosity of the specimen was measured at ~1% and distribution occurred in two patterns, as shown in Figures 90 and 91. The first type of porosity pattern occurred on the surface at 4° angles; this coincided with the intervals of the converted STL file that was set at an angular resolution tolerance setting of 4°. The second type occurred in the 5 mm squared edge line pattern with a 200 µm, which coincided with the stripe parameter rotated at 90° after each layer (Karme *et al.*, 2015).

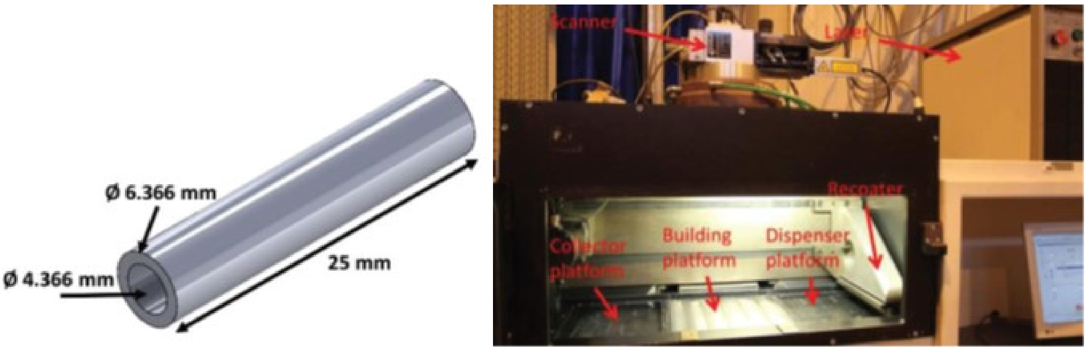
Ø 6.366 mm
Ø 4.366 mm
25 mm
Scanner
Laser
Recoater
Collector platform
Building platform
Dispenser platform

(a) (b)

Figure 89: Tubular sample (a) AM research equipment (b) used by Karme et al. (2015)

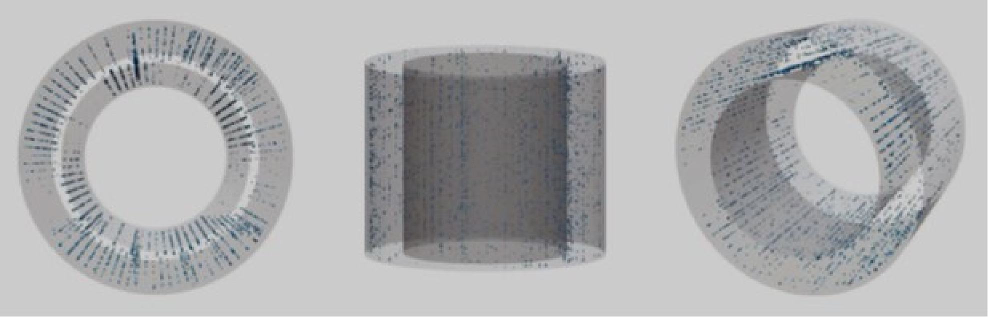

Figure 90: Porosity of tube specimen 3 (Karme et al., 2015)

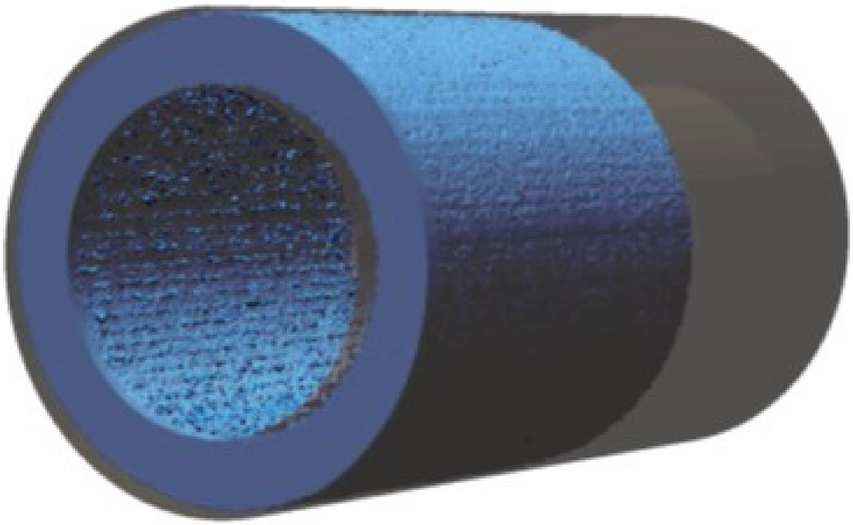

Figure 91: Surface reconstruction of specimen 3 overlaid with the CAD model pipe, showing volume decrease. Higher inner surface relief penetrated the original model in places where the polygon edges are located (4° intervals), otherwise the specimen surfaces are inside the model extents (Karme et al., 2015)

A comparison between confocal microscope image and X-ray CT image is shown in Ziółkowski *et al.* (2014). The 316L stainless steel specimen was manufactured with a Realiser II (MCP HEK GmbH) machine. The images show clearly how the edges of pores are better indicated with the confocal microscope, as shown in Figure 92. The work focuses on determining the pore formation in three building orientations; X-plane, Z-plane and at 45° to the X-, Y- and Z-plane.

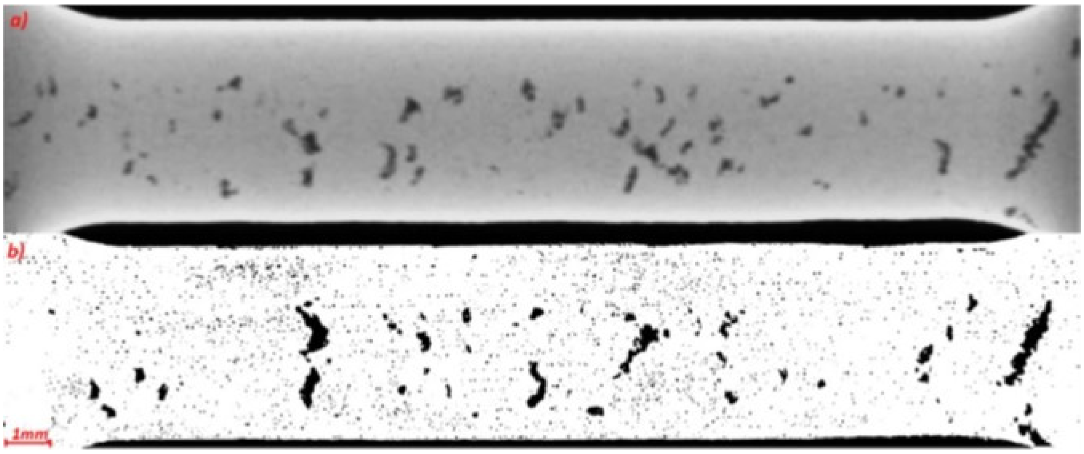

Figure 92: Cross-sectional comparison of specimen built in X-plane; (a) X-ray CT (b) Confocal Microscope (Ziółkowski et al., 2014)

The pore size distribution and sphericity of the pores in the specimens built in the three directions were calculated using X-ray CT and are indicated in Figures 93 and 94.

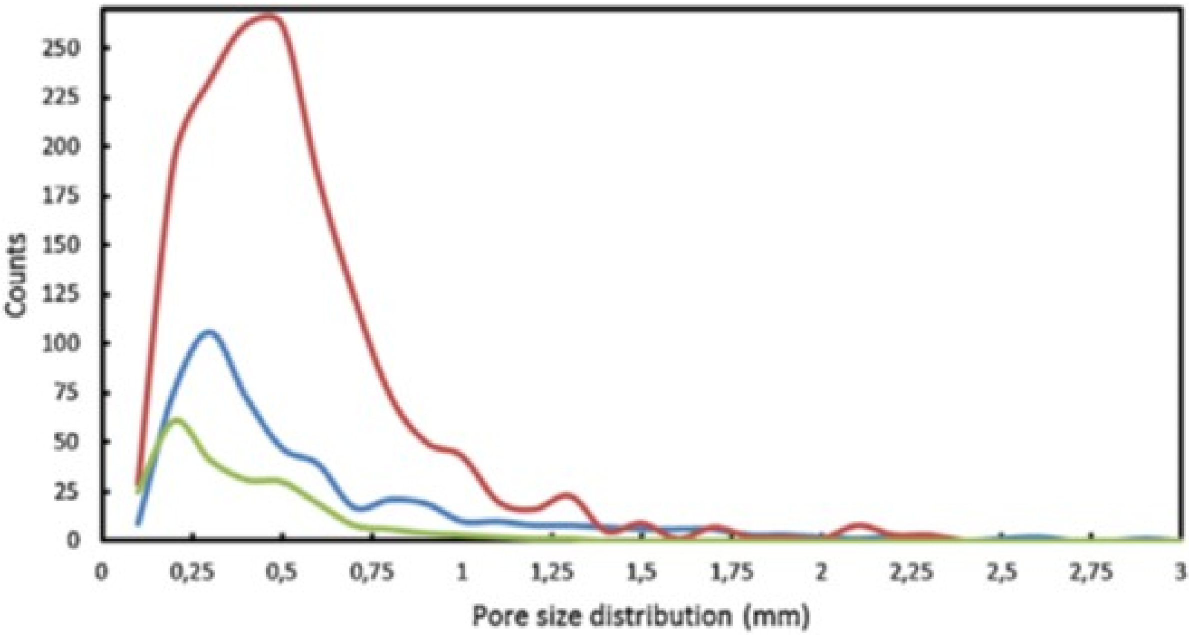

Figure 93: Histogram of pore size in X (RED), Y (BLUE) and 45 ° to X,Y and Z bono(GREEN) directions (Ziółkowski et al., 2014)

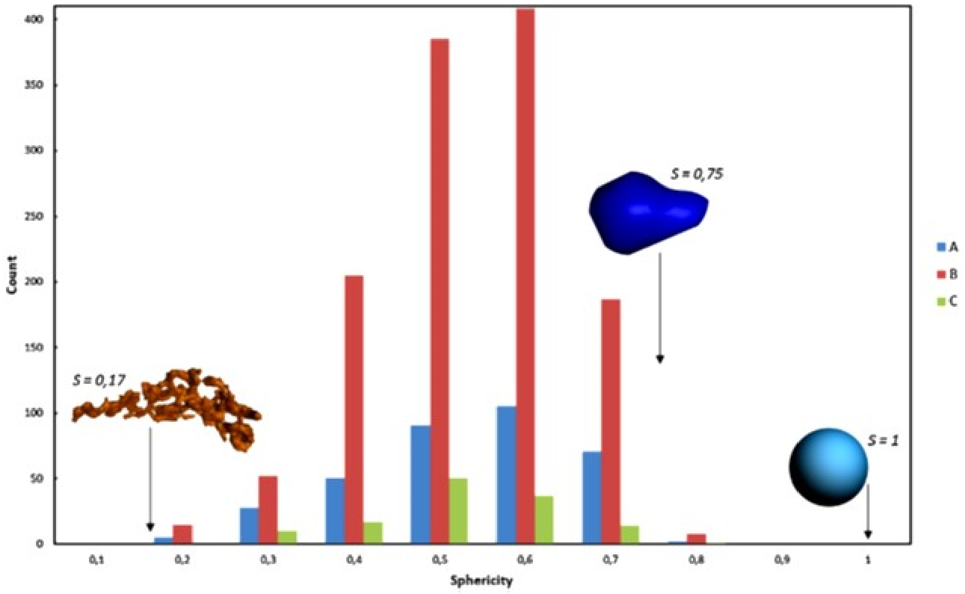

Figure 94: Sphericity distribution for specimens built in X (red), Y (blue) and 45 ° to X,Y and Z (green) directions (Ziółkowski et al., 2014)

Du Plessis *et al.* (2015) investigated a DMLS Ti6Al4V cylinder (30 mm in diameter and 60 mm high with build direction in the long axis) with relatively complex geometry (Figure 95). During the build process, supports from adjacent parts came loose interrupting the build. It was decided to continue the build and investigate whether the defects could be picked up by CT. CT scanning (48 µm resolution) was carried out before and after hot isostatic pressing (HIP) treatment. HIP treatment was done at a temperature of 920°C+/−10°C and pressure of 1000 bar for a dwell time of 120 minutes in an argon atmosphere. The layered defects, resulting from inhomogeneous powder deposition caused by the loose supports, could easily be detected using CT scanning as seen in Figure 96; the red volume indicated is large and flat. The average porosity dropped from 0.005% to 0.002% after HIP treatment (du Plessis *et al.*, 2015).

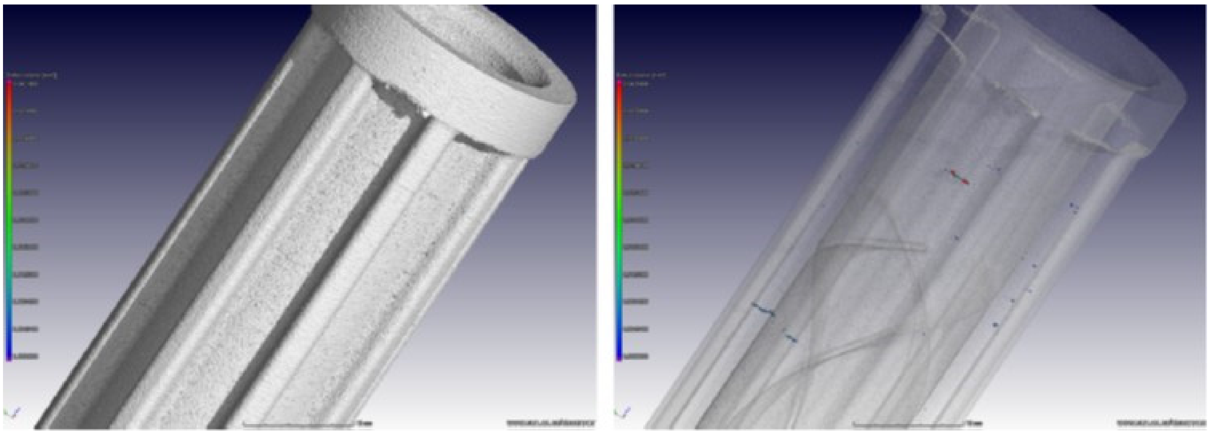

Figure 95: 3D view of Ti6Al4V DMLS sample showing the surface (left) and the internal defects (right) (du Plessis et al., 2015)

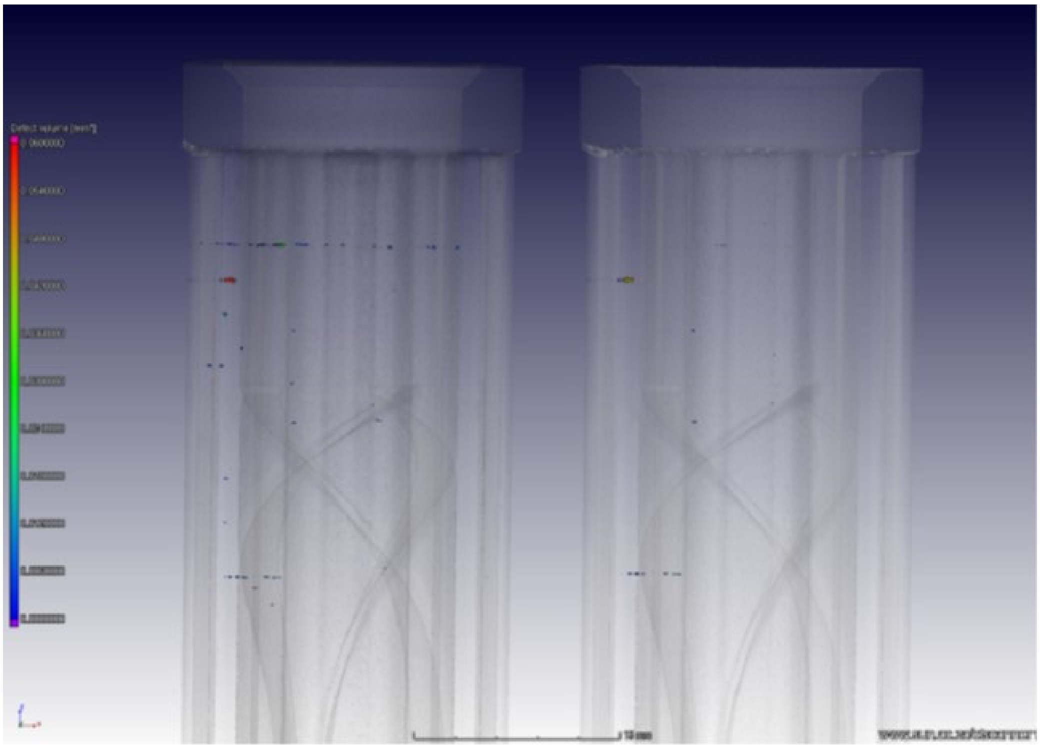

Figure 96: Transparent view of DMLS cylinders before (left) and after (right) HIP treatment (du Plessis et al., 2015)

Du Plessis *et al.* (2016b) analyzed a 100 mm part and a 20 mm part. It was concluded that they could not be directly compared, as the best possible resolution is limited by the size of the object, resulting in different defect detection capabilities. With reference to CT-scans, "*image quality and detail detectability can vary considerably between systems and even between different types of scans on the same system*".

Elaboration on the standard approach to CT scans of internal structure and pores for different AM materials is required. In turn, estimation of critical pore size which can have an effect on mechanical properties of DMLS sample is an important task.

2.6.2 Ultrasound Testing

Slotwinski *et al.* (2014) investigated the possibility of creating a UT sensor for in-situ monitoring of porosity formation during DMLS of cobalt-chrome (CoCr) with the hope that this would possibly lead to process validation and real-time adjustments to the parameters. An ultrasonic transducer was situated within the substrate facing upwards. Ultrasonic pulse-echo technique was applied to measure the speed of sound within the material. The speed should vary with a change in porosity within the material. The results showed a linear correlation between the percentage porosity (measured using X-ray CT) and the wave speed, as seen in Figure 97. The data showed no definite margins of the detectable percentage porosity at this stage.

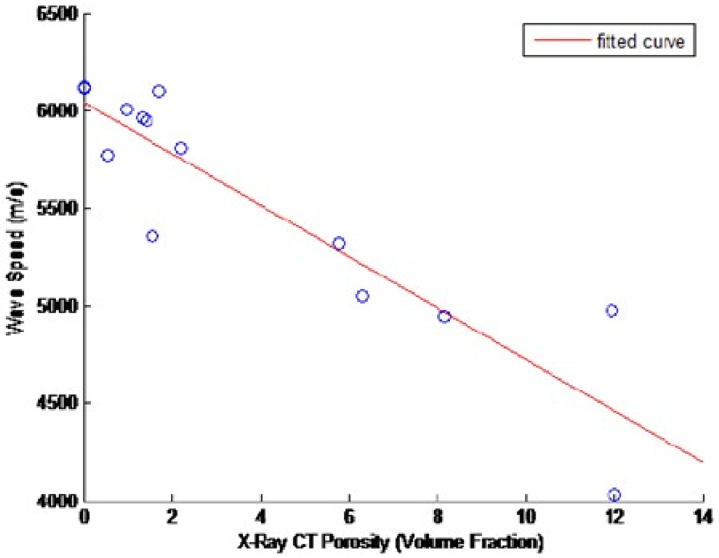

Figure 97: Ultrasonic wave speed vs. X-ray CT porosity (Slotwinski et al., 2014)

Laser-induced ultrasonic NDT on DMLS components was investigated. This method is somewhat more complex and the system used by Popovich *et al.* (2016) to carry out this work is depicted in Figure 98. The system makes use of a laser which hits the surface of an object to induce a thermo-optic excitation of ultrasonic pulses. Some waves are reflected while others first penetrate before returning to the surface and the receiver. These ultrasonic pulses are then measured by the receiver and used to determine wave characteristics such as velocity. It is found to be a feasible method to determine material properties, but no defect analysis was shown.

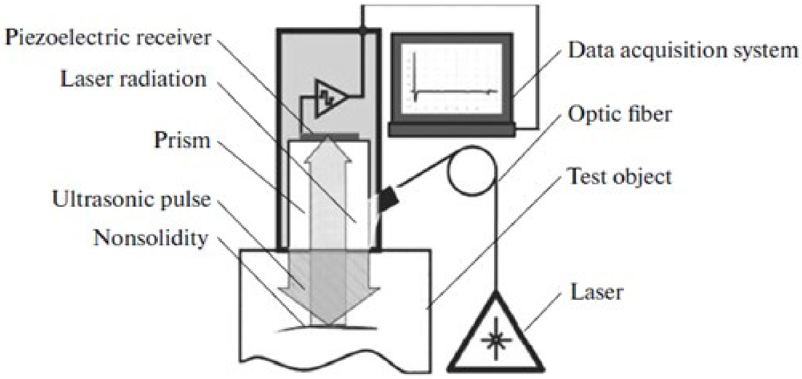
Piezoelectric receiver
Laser radiation
Prism
Ultrasonic pulse
Nonsolidity
Data acquisition system
Optic fiber
Test object
Laser

Figure 98: Laser-ultrasonic equipment (Popovich et al., 2016)

In a report by NASA, Waller *et al.* (2014) set out to strengthen NASA's inter-departmental NDT knowledge at the Johnson Space Centre. This NDT focused specifically on NDT methods for NASA's AM components. UT was applied to determine the voids in 2219 aluminium alloy parts produced by EBM. The information regarding this test was not included in the report. However, a photo of the scanned area and the resultant A- and B-scans were included (Figure 99).

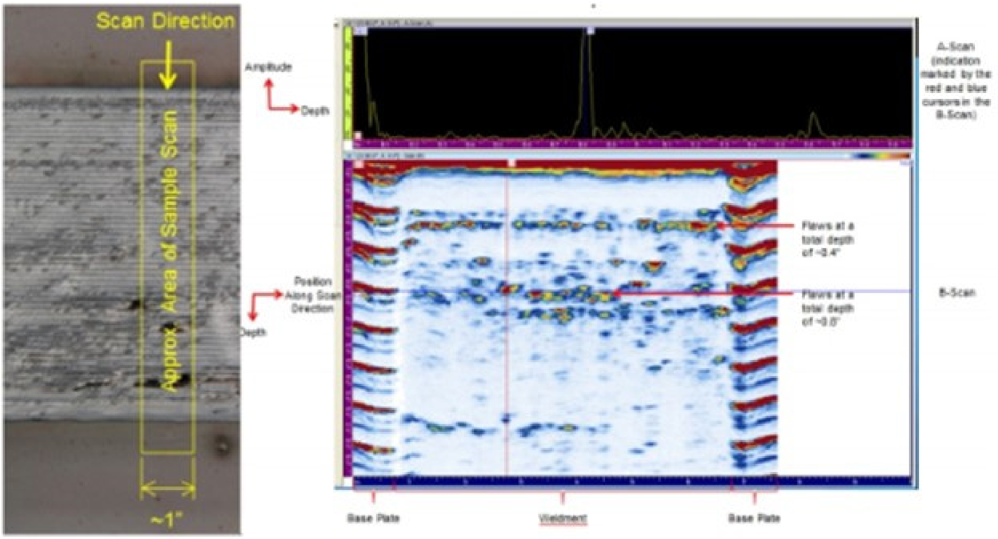

(a) (b)

Figure 99: EBM part scanned via ultrasonic; area (a)and A- and B- scans (b) (Waller et al., 2014)

Waller et al. (2014) also mentioned that although the geometry allows for Eddy current testing (ET), it cannot be applied to DMLS components due to the surface roughness and grain structure which cause background noise. The test was carried out on an Inconel baffle, as shown in Figure 100.

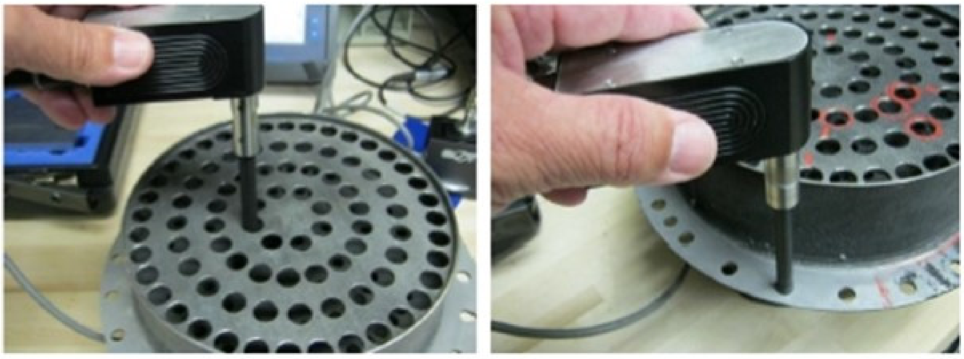

Figure 100: Eddy current testing of DMLS component (Waller et al., 2014)

2.6.3 Acoustic Emission

Acoustic emission (AE) testing is a versatile method as it can be developed and applied in various forms for each specific need. Various methods have been developed for specific applications and it is no different for the AM industry.

Wu *et al.* (2016) applied acoustic emission to an FDM machine as an on-line process monitoring system; an AE sensor was placed on the filament extruder and monitored the data using a data acquisition system and a personal computer (Figure 102). This was accomplished by making use of the relationship between the sounds emitted at certain machine operating conditions enabling recognition of five different extruder operating conditions in the equipment.

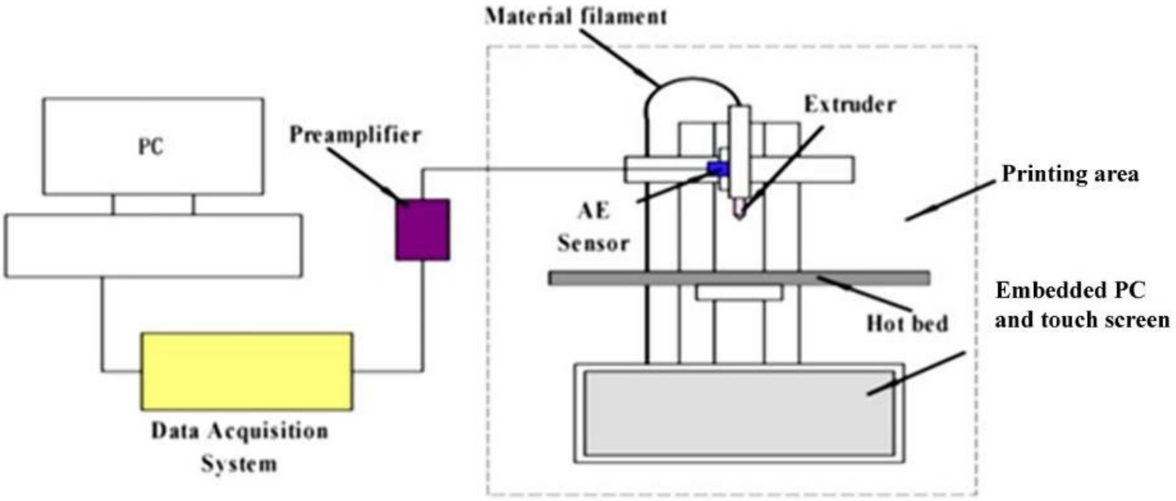

Figure 101: AE system for a FDM machine (Wu et al. 2016)

In a virtually similar application, Whiting (2015) in his thesis studied the application of AE during the LENS manufacturing as a process monitoring system in which the AE of the nozzle was measured to monitor the rate of powder flow through the nozzle. It was mentioned that this system will be implemented into the OptomecLENS 850-M machine.

Strantza *et al.* (2015) used a post manufacturing method that combines pressure and acoustic sensors to detect defects in AM parts. Internal cavities were placed within a component, which was then subjected to loading (Figure 102). The cavity's pressure was monitored as well as acoustic sensors were used to detect a flaw. All data were used to investigate certain phenomena to gather information about the flaw. These tests were carried out with DMLS parts undergoing fatigue testing and static loading. An important outcome to take note from the results is that there was no difference in the AM results compared to the conventional materials i.e. the AE can be applied to AM. Further information on this method of work can be found in Strantza *et al.* (2015).

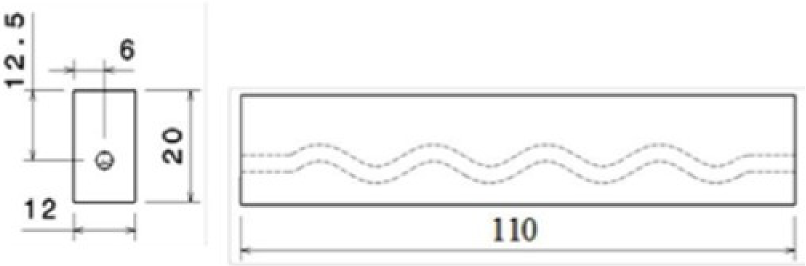

Figure 102:DMLS sample with internal sinusoidal cavity; tested with AE in combination with pressure sensors (Strantza et al., 2015)

Rong (2015) investigated the possibility of obtaining a relationship between AE signals and fracturing during tensile testing; however, this is outside the scope of this study. AE is also being applied during DMLS manufacturing as a laser weld monitoring system; again this study focuses on post-process- pre-service evaluation of AM parts. It was found that the cumulative AE hits tend to decrease with increasing porosity of AM samples.

AE NDT has not yet been implemented as a post manufacture quality control method on AM components. The Modal Shop in the PCB Electronics Group made available the following papers illustrating the capabilities of their RAM-NDT as a quick quality control option for companies with production lines “Fundamentals of resonant acoustic method NDT”, by Stultz *et al*., (2005); “Resonant inspection as an automated NDT method for sinter brazed powder metal components”, by Bono *et al.* (2007); “Resonant inspection to validate resonant frequency characteristics within brake components for improved NVH performance” by Bono *et al.* (2010) and “New methodology applying resonant inspection for quality testing of very small powder metal components” also by Bono *et al*. (2007). Although these papers are not focused on the AM industry, it could be of some value regarding the applicability of AE as an in-house NDT method for DMLS produced parts. The latter mentioned article provides an insight into to how this method has been applied to small powdered metal components produced by metal injection moulding (MIM). In DMLS, the production of small intricate metal components is often realized due to the advantages of the technology. The components used in the following case study are medical parts used for gripping. In Figure 103, It can be seen that these components are relatively small and complex in shape.

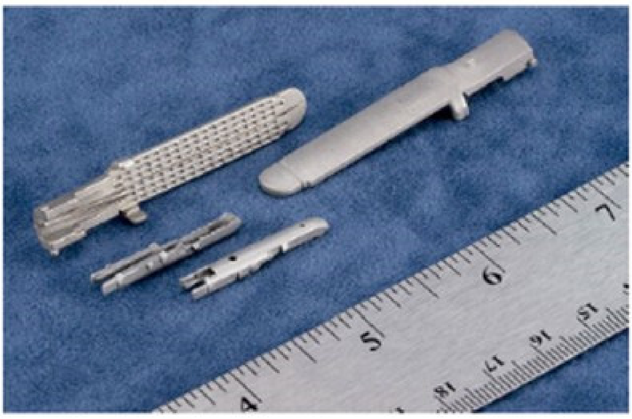

Figure 103: Small MIM parts used during AE case study by Bono et al., 2010

In this case, study components are dropped as opposed to previous methods which supported the component in some way while being impacted. The setup uses gravity to generate an impulse. The part is dropped through a directing tube and on exiting the tube, it hits a force transducer which triggers the resonant frequency measurement. After impact, whilst falling, the measurement is recorded before the component reaches the collector bin. The experimental setup is shown in Figure 104 – this specific setup includes an automatic sorting mechanism which moves the "passed" components to one bin and the "failed" components to the opposite bin.

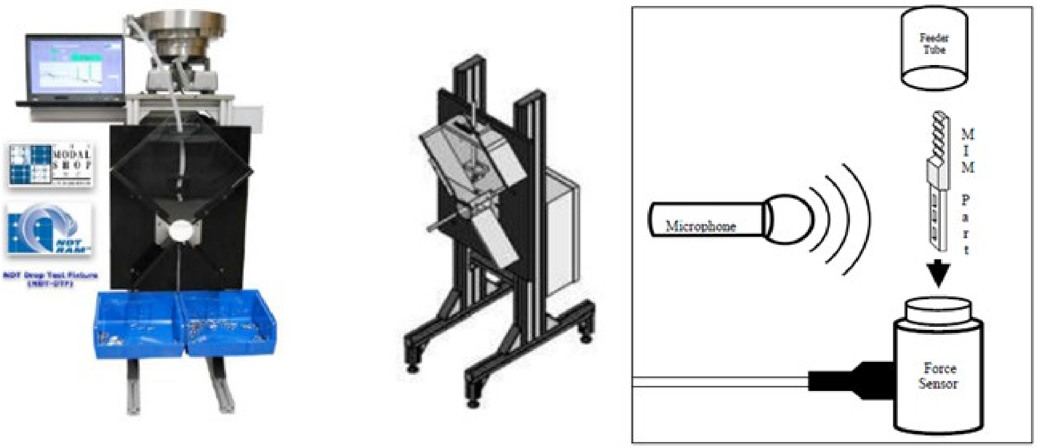

Figure 104: AE drop test equipment from Modal Shop (Bono et al., 2010)

A large number of components were tested and the maximum frequency and amplitude were clearly distinguishable in the components with defects compared to that of the defect-free components. The results are shown in Figure 105. It can be seen that there is a clear frequency shift with components that contain structural defects. This method was a more effective and time-efficient way to test small MIM components compared to the prior visual testing applied by the company.

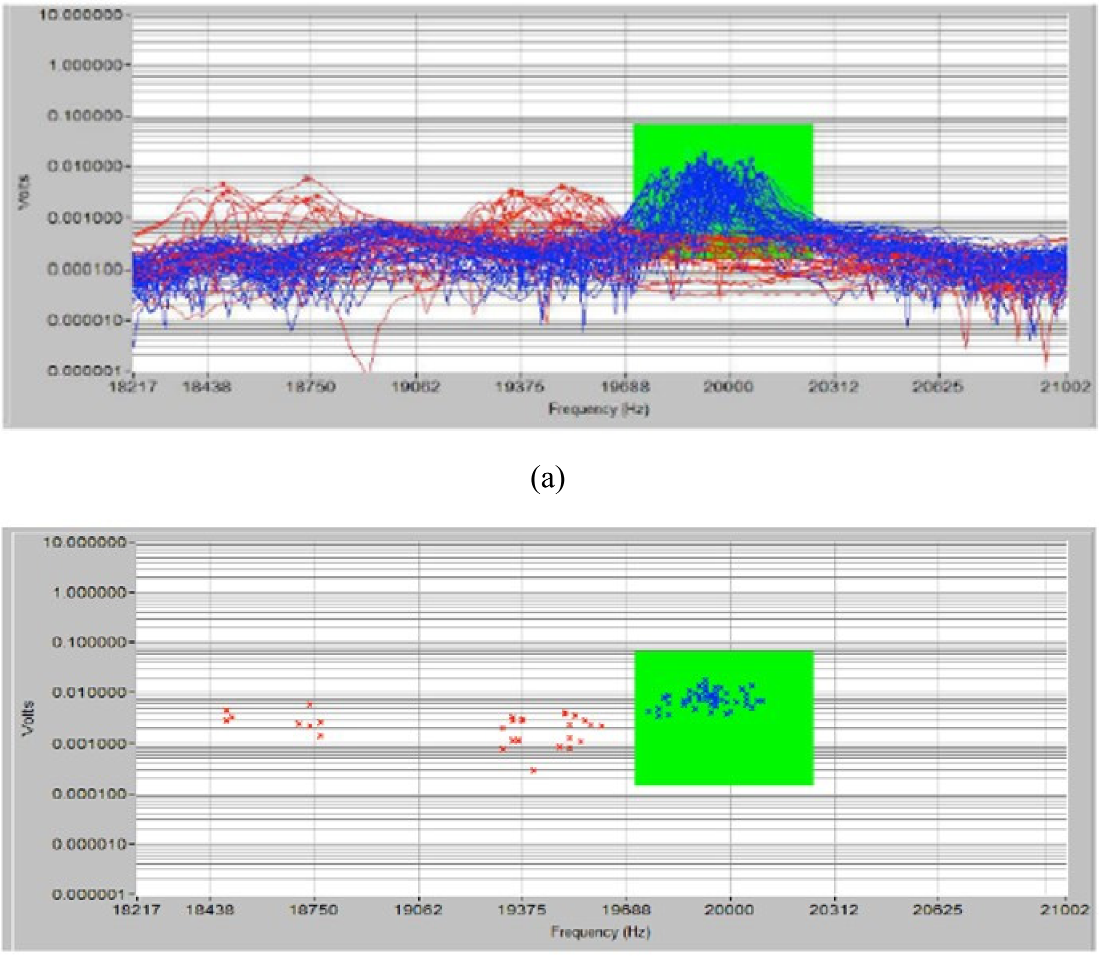

(a)

(b)

Figure 105: MIM AE drop test results with (a) and without (b) traces – red indicating failed parts (Bono et al., 2010.)

2.6.4 Summary

The factors that challenge NDT of AM mentioned in section 2.6 highlight the great challenge when evaluating DMLS components. The freedom of design and complex shapes make each test unique. A definitive parameter of various NDT methods is the difference in the size of detectable defects. To date, there are no known standards for minimum allowable defect sizes and it will still take some time before these would be in place.

To understand all the possibilities and limitations of using X-ray CT for AM requires an extensive study of all the factors which could influence the results: source current, source voltage, magnification, number of angular poses, exposure time, number of projection images per pose (image averaging), sensitivity of the detector, use of filter plate (material, thickness, position), CT strategy (measuring the whole object at once or in parts), combining measurements with different current/voltages/targets, etc. However, X-ray CT seems to be a promising method for AM parts. The capability of detecting small defects and obtaining detail with no restriction to complex geometry is of great value. One major drawback is the time and cost.

UT in AM may seem to be a viable option at first glance, but most AM components are complex in geometry. It is a general principle of UT that there must be a good coupling between the sensor surface and the component. Thus, complex geometries together with the size of the UT transducer are a great restriction on small intricate parts. The method seems to be a viable solution in all other respects.

AE testing has not been applied to AM as a post-manufacturing quality control method. Literature shows that this method has been successfully applied in various industries that manufacture complex and often small components. This could be the ideal solution for simple, affordable and time-effective in-house non-destructive screening.

Chapter 3: MATERIALS AND METHODS

3.1 EOSINT M280

All samples were manufactured from Ti6Al4V (ELI) powder using an EOSINT M280 DMLS machines (Table 11) at the CRPM facility in Central University of Technology, Free State. The M280 systems are optionally equipped with a 200- or 400 watt fibre laser. A fibre laser provides an exceptionally high beam quality and power stability which can be monitored during the build process using the Laser Power Monitoring (LPM) option. The system operates in both protective nitrogen and argon atmospheres, which allows for a wide range of materials to be processed – from light metals to super alloys. Ti6Al4V samples were manufactured in an argon atmosphere.

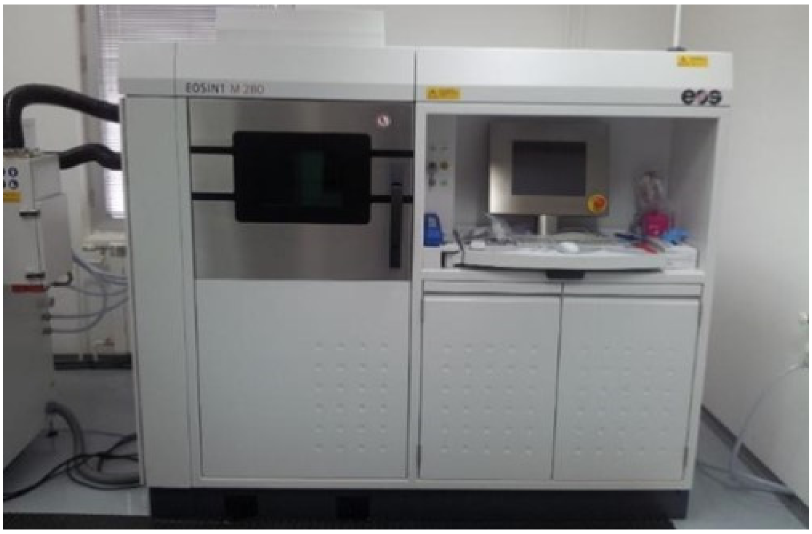

Figure 106: EOSINT M280 machine

Table 11: The EOS technical data for EOSINT M280 machine (EOS GmbH, 2016)

Building volume	250 mm x 250 mm x 325 mm
Laser type	Yb-fibre laser, 200 W
Laser wavelength	1075 nm
Precision optics	F-theta-lens, high-speed scanner
Scan speed	up to 7.0 m/s
Variable focus diameter	100 - 500 µm
Power supply	32 A
Power consumption	maximum 8.5 kW / typical 3.2 kW
Software	EOS RP Tools; EOSTATE Magics RP (Materialise
CAD interface	STL. Optional: converter for all standard formats

The M280 system is compatible with the following materials: Maraging Steel MS1, Co-Cr MP1, Stainless Steel GP1, Stainless Steel PH1, Stainless Steel 316L, Ti6Al4V and Ti6Al4V ELI, AlSi10Mg, Ni alloys IN718, IN625, HX (EOS GmbH, 2016).

3.2 DMLS Ti6Al4V (ELI) samples

Samples were manufactured using Ti6Al4V (ELI) powder – a pre-alloyed gas atomized powder. The chemical composition was as follows: Ti – balance, Al – 6,34%, V – 3,94%, O – 0,082%, N – 0.006%, H – 0,001%, Fe – 0,25%, C – 0.006% (weight %). The equivalent diameters (by volume) of the powder particles were $d_{10} = 12.03$ µm, $d_{50} = 21.38$ µm and $d_{90} = 31.15$ µm.

The parameters of the process were set to produce the best possible density. Samples were produced at standard process-parameters from EOS for Ti6Al4V at layer thickness of 30 µm; argon was used as the protective atmosphere. A back-and-forth (zigzag) scanning strategy in stripes with width of 5 mm and a hatch distance between tracks of 100 µm was applied for manufacturing the specimens.

3.2.1 Rectangular samples

Rectangular samples are shown in Figure 63. An artificial defect that mimicked a crack was inserted and produced in the centre of the block. The defect in the design thickness was set at a thickness of 90 µm. These samples were developed specifically for material property (modulus of elasticity) analysis using the RFDA Basic (Figure 117). Additionally, defects were introduced to investigate the influence of cracks on the AE results. The size and geometry of these samples made testing simple for initial results.

Table 12: The dimensions for the rectangular samples and the internal defect

Sample size, mm		Defect size, mm	
Length, l	*60*	l_1	*40*
Width, w	20	w_1	*10*
Thickness, t	7	t_1	*0.09*

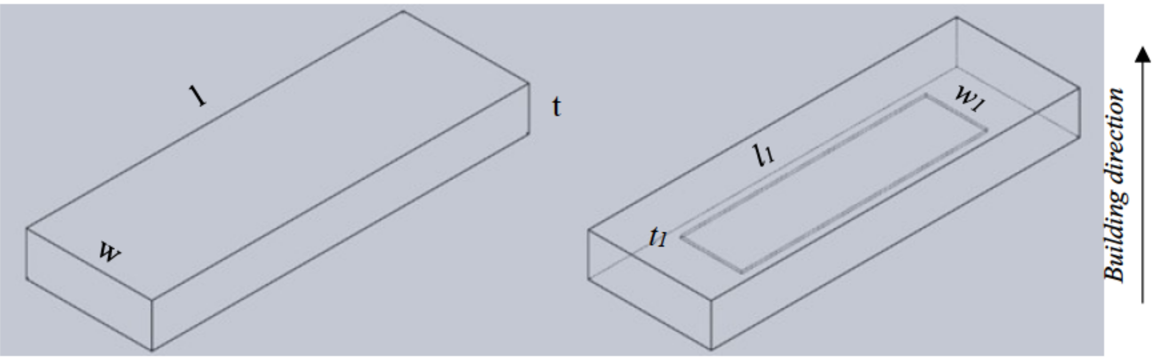

Figure 107: Outline of CAD drawing of samples without (left) and with defect (right)

Ten samples were manufactured, six without defects and four with artificial defects. The artificial defects were placed in the centre of the rectangle. Five samples were subjected to heat treatment for stress relieving. The remaining five were used in as-built conditions.

After the ten samples were produced, five samples were removed from the substrate and the remaining five was sent for heat treatment (Table 13). The two groups were divided into as-built and stress relieved, each consisting of two samples with defects and three without defects.

Heat treatment was carried out in an argon atmosphere for three hours at 650°C.

Table 13: The sample identification for rectangular blocks

Defects	AS-Built	Stress Relieved
	AB1	SR1
	AB2	SR2
	AB3	SR3
☒	AB4	SR4
☒	AB5	SR5

3.2.2 Samples with fine inner structure

To estimate the accuracy of detecting small defects in DMLS components, samples with fine inner structures were built and investigated. These samples contained the following specific vertical and horizontal defects:

- “Pins” with cubed cavities – to investigate accuracy and pore formation in *z*-direction (building direction).
- “Blocks with horizontal semi-cylinder channels” and “steps with horizontal cavities” – to investigate accuracy and pore formation in *xy*-direction; influence of varying powder thickness that causes insufficient penetration into the previous layer.

3.2.2.1 Pins with cubed cavities

Pins with small rectangular gaps (vertical built cavities) were manufactured. The prescribed CAD gap thicknesses were: 200; 160; 120; 80; 40; 30; 20; 15 and 7.5 µm (Figure 109). Identification of the samples is shown in Table 14.

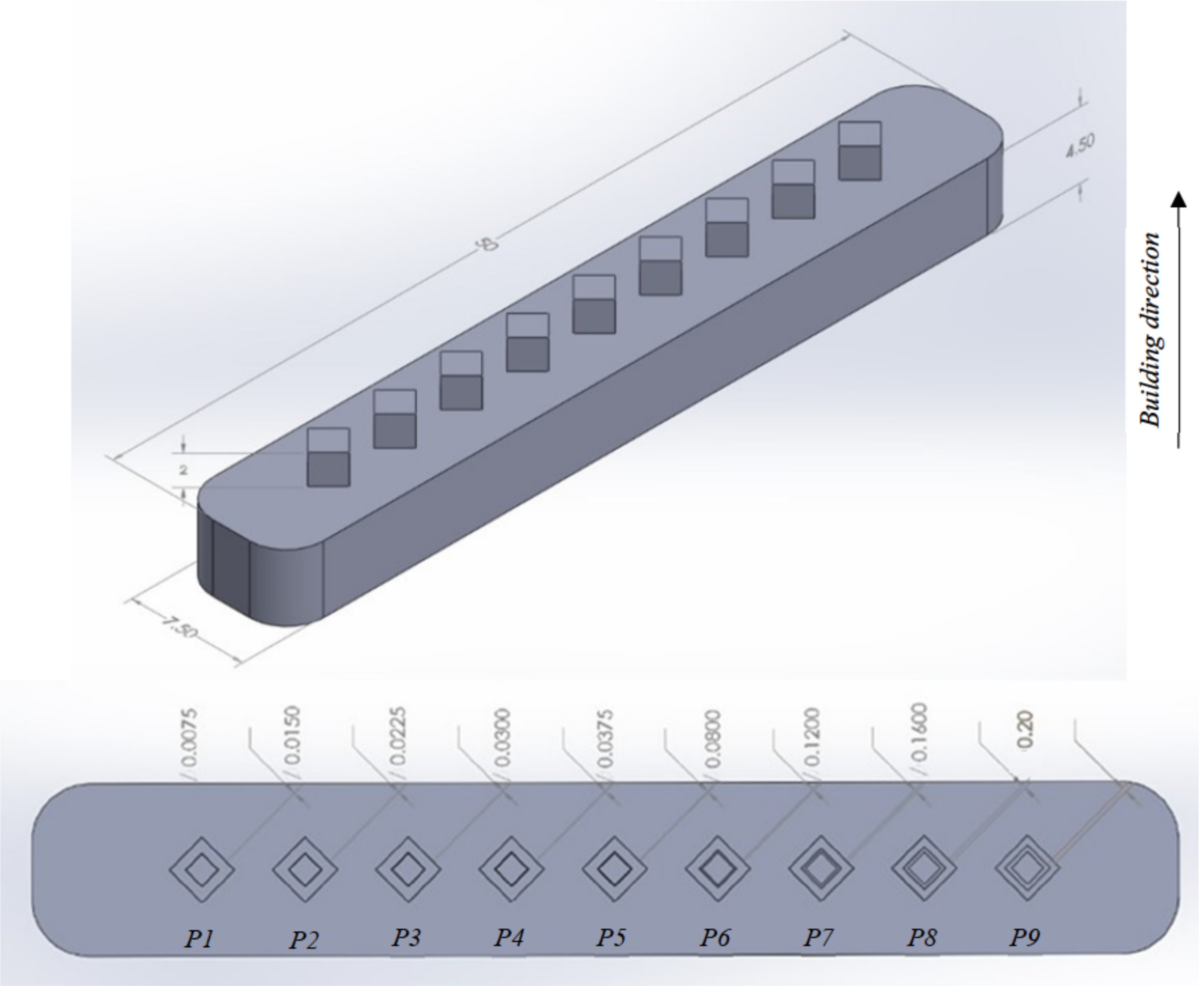
50
4.50
2
7.50
Building direction
0.0075
0.0150
0.0225
0.0300
0.0375
0.0800
0.1200
0.1600
0.20
P1
P2
P3
P4
P5
P6
P7
P8
P9

Figure 108: CAD model for pins with cubed built cavities

Table 14: Sample identification for pins with fine structure

Sample	Prescribed gap size, µm		Sample	Prescribed gap size, µm
P1	7.5		P6	80
P2	15		P7	120
P3	22.5		P8	160
P4	30		P9	200
P5	37.5			

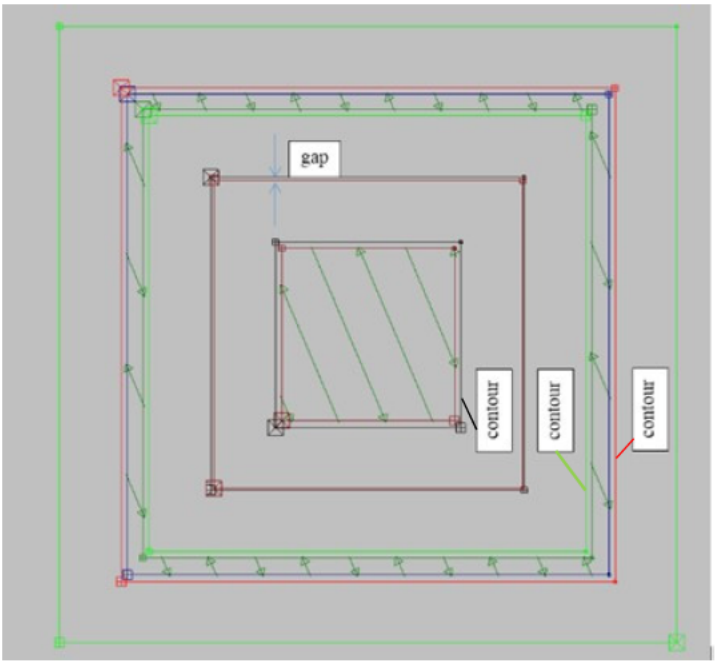
gap
contour
contour
contour

Figure 109: Schema for DMLS scanning parameters of the pins with gaps (top view)

3.2.2.2 Block with horizontal semi-cylinder channels

The next CAD model contained a block with horizontal semi-cylindrical cavities with different prescribed diameters: from 60 to 360 µm (samples C1–C6, Figure 110)

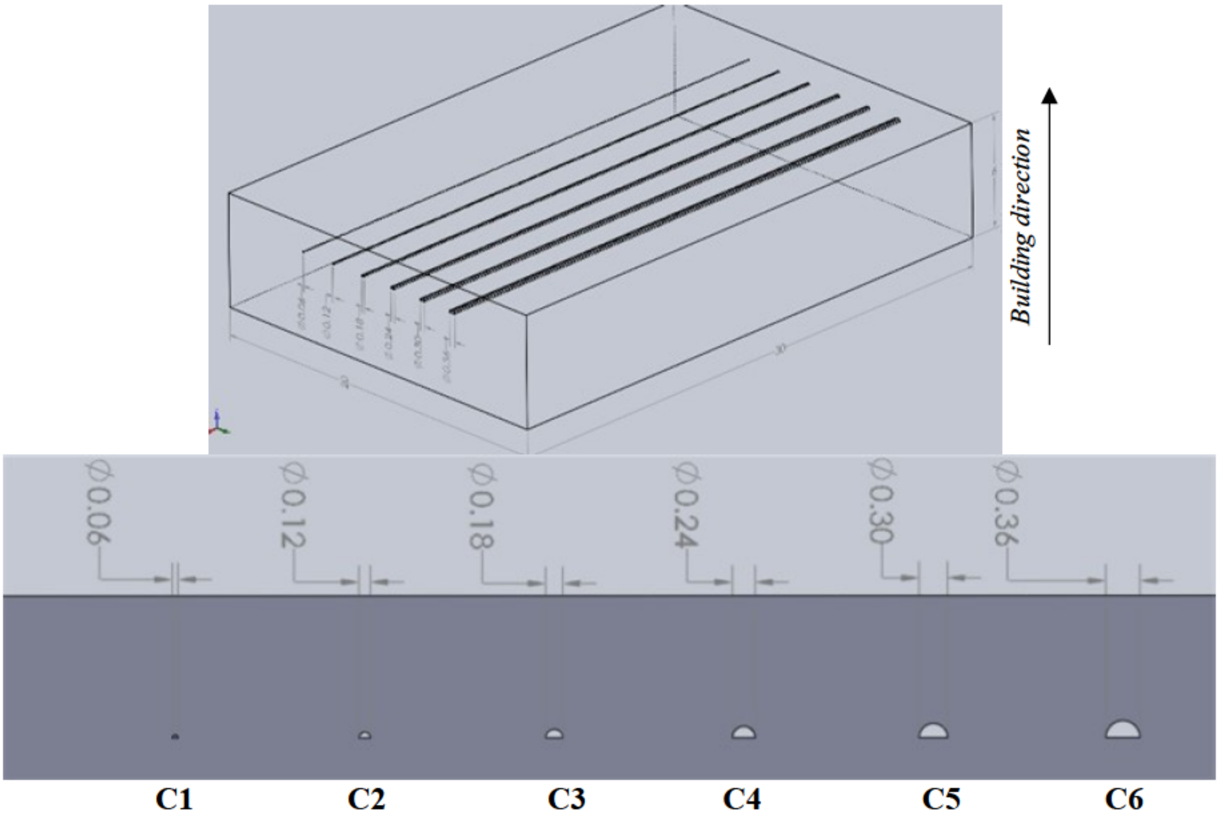
Building direction
∅0.06
∅0.12
∅0.18
∅0.24
∅0.30
∅0.36
C1
C2
C3
C4
C5
C6

Figure 110: CAD model for horizontal block with semi-cylinder channels

3.2.2.3 "Steps" with horizontal cavities

"Steps" samples with internal cavities were designed to contain rectangular defects in the plane perpendicular to the build – voids were created by not scanning a square area within each step. The thicknesses varied from (30 - 180) μm, as shown in Figure 111 and Table 15.

Table 15: The sample identification for steps with rectangular defects

Sample	Gap size, μm	Sample	Gap size, μm
S1	-	S5	120
S2	30	S6	150
S3	60	S7	180
S4	90		

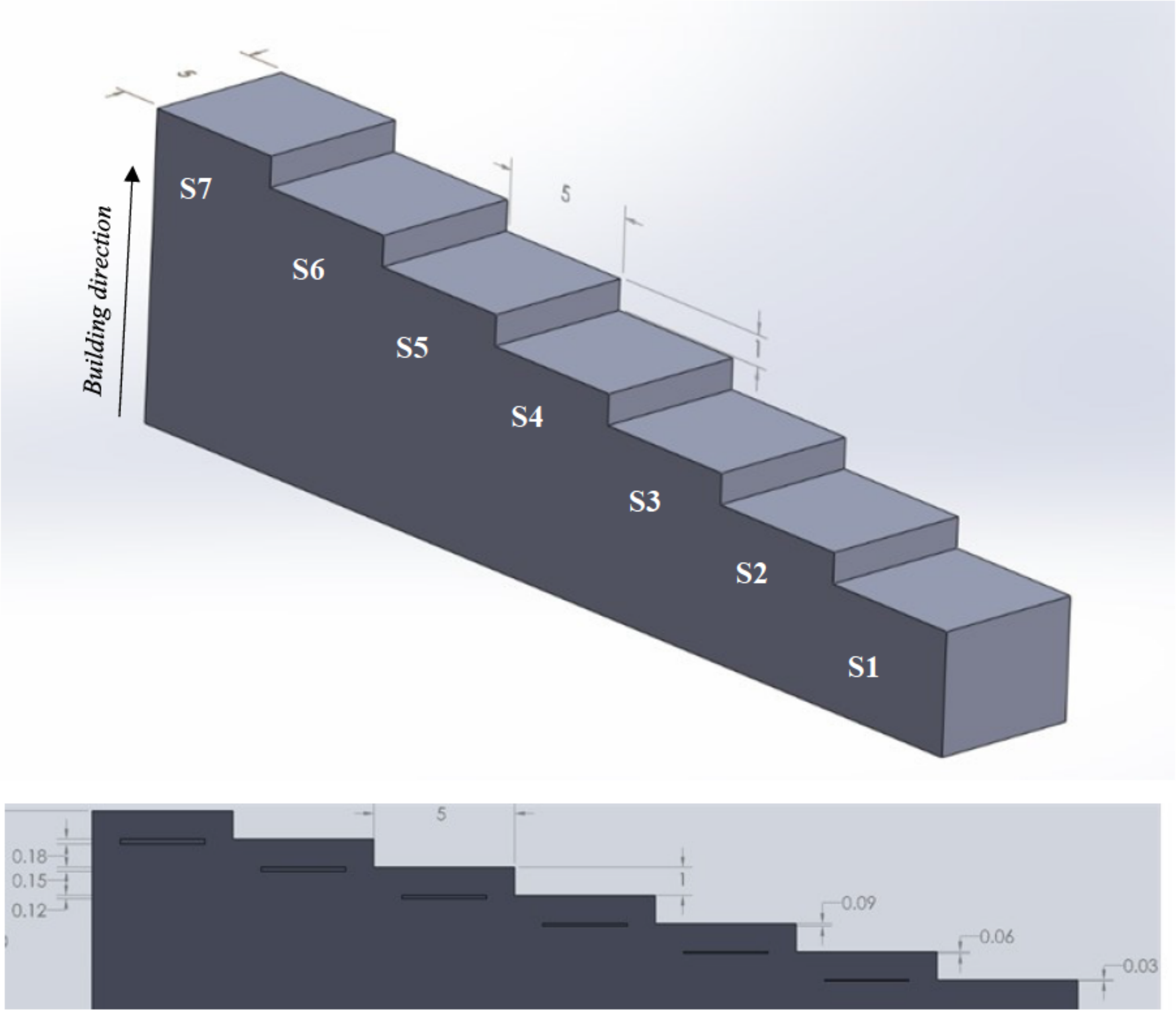
5
S7
S6
S5
S4
S3
S2
S1
5
1
Building direction
0.18
0.15
0.12
5
1
0.09
0.06
0.03

Figure 111: CAD of step samples with cavities

Summary

Two different types of samples were produced. One set was used to investigate the probability of detection and the second to recognize the size and shape of internal defects. DMLS samples were built with/without internal cavities.

3.3 Methods

3.3.1 Visual testing

Surface and cross-section analysis was done using a scanning electron microscope (SEM) and optical microscopes. Optical and SEM tests provide detailed, in-depth visual analyses of components. SEM was carried out with a NeoScope JCM 5000 (Figure 112), operated at (10-15) kV. The optical microscopes used were a Smartzoom 5 and an Scope A1, both from Zeiss.

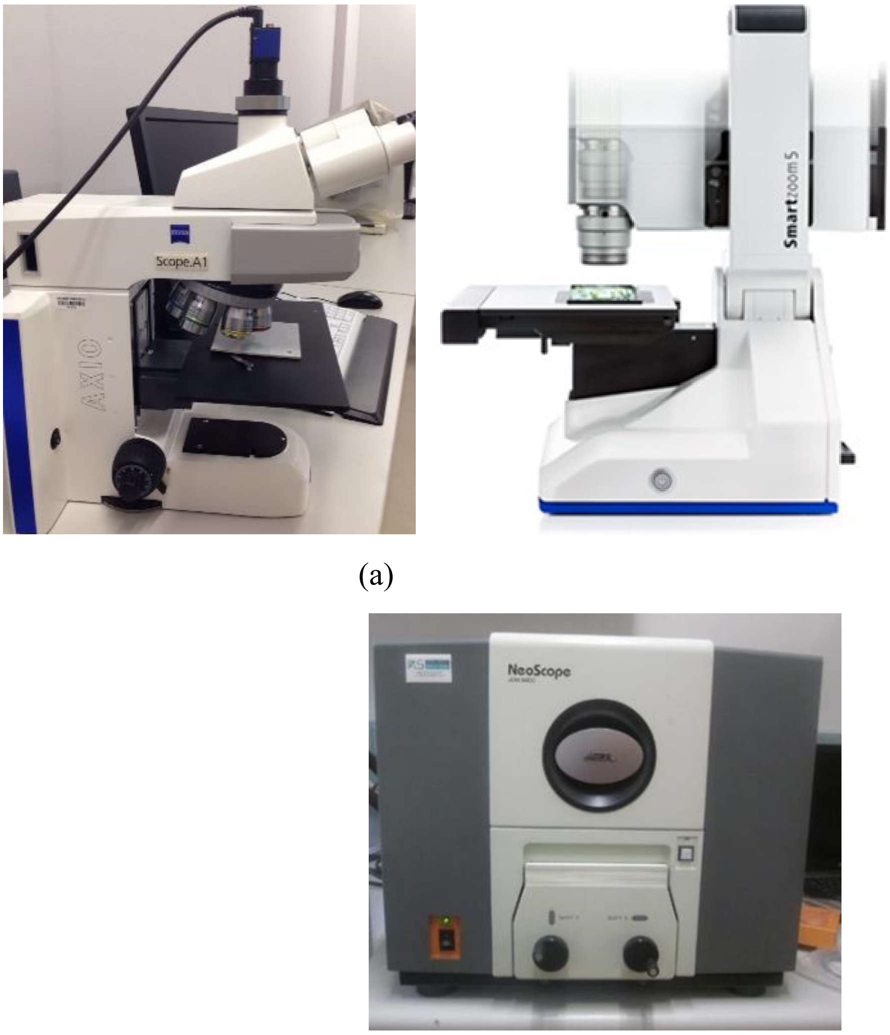

(a) (b)

(c)

Figure 112: SmartZoom5 (a) and Scope A1 (b) optical microscopes; NeoScope JCM 5000 scanning electron microscope (c)

For pore analysis and analysis of the cavities' sizes and shapes, samples were cut with an electrical discharge machine (EDM). The small templates were incorporated into MultiFast resin by CitoPress (Figure 113a). Samples were polished with a Tegramine-25 system (Figure 113b), as recommended by Taylor & Weidmann (2009), and etched with Kroll's reagent. An optical microscope was used for metallographic analysis.

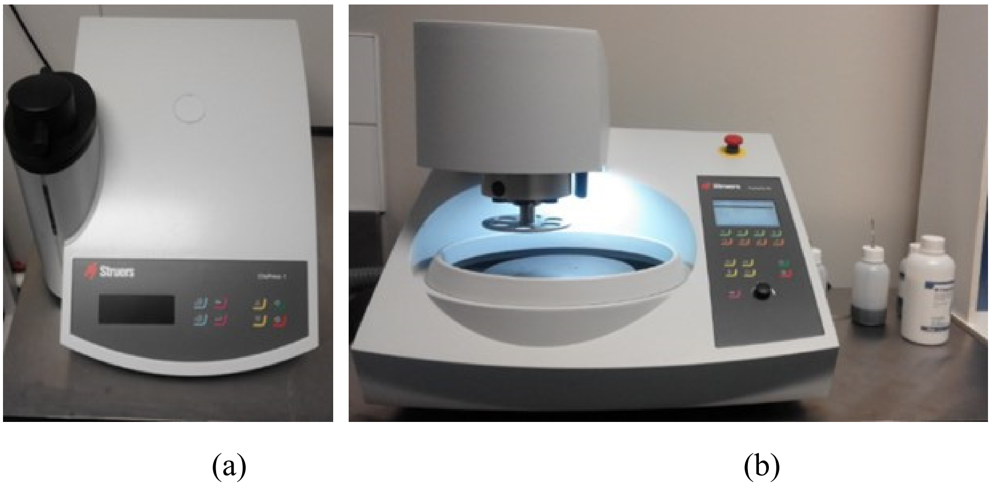

(a) (b)

Figure 113: CitoPress 1 (a) and polishing machine Tegramin-25 (b)

3.3.2 Micro computed tomography

General Electric phoenix v|tome|x L240/NF180

X-ray micro computed tomography (microCT) was used in this study. The phoenix v|tome|xL240 is a walk-in cabinet micro-CT scanner manufactured by General Electric (Wunstorff, Germany). It contains two X-ray tubes; one with a reflection-type target and the other with transmission-type target, with a diamond window which increases X-ray emission. This system incorporates a continuous scanning option compared to others that have stepwise rotation (Figure 114).

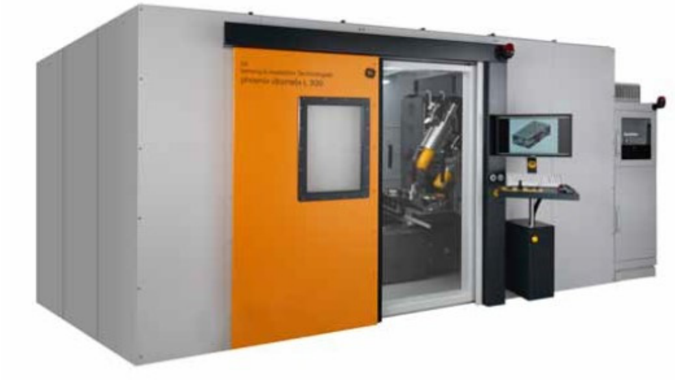

Figure 114: phoenix v|tome|x L 240 X-ray CT scanner (GE Oil & Gas, 2016)

A General Electric phoenix v|tome|x L240/NF180 installed in the Central Analytical Facility at Stellenbosch University was used. X-ray settings were 150 kV and 150 µA with 2000 images acquired in a full rotation at an image acquisition time of 500 ms per image, with averaging set to two images and one image skip per rotation. Detector shift was activated to minimize ring artefacts. Background calibration was performed and the scan time was approximately 40 minutes per scan at 40 µm voxel size. A 1 mm copper beam filter was used to filter out the low energy X-rays to reduce beam hardening. Reconstruction was done with system-supplied Datos reconstruction software. Analysis was performed with Volume Graphics VGStudio Max 2.1 or Visualization Sciences Group Avizo Fire 8.0 commercial 3D analysis software packages.

3.3.3 Phased array ultrasonic testing

The Gekko is manufactured by M2M and is a phased array flaw detector (Figure 115). This machine is very versatile as it offers the ability to carry out conventional UT, PAUT, TOFD as well as the Total Focusing Method (TFM). The Gekko is a user-friendly, portable device. It is fitted with 64 parallel channels and conventional UT channels and complies with international standards - ASME, AWS, API, ASTM, ISO-EN (M2M, 2016).

Figure 115: M2M Gekko phased array flaw detector (M2M, 2016)

The TFM was chosen for the test using longitudinal waves without mode conversion and a 10 MHz array, comprising of 16 elements set to pulse-echo. The wedge was a 4.4 degree angled custom Rexolite wedge, giving a diffraction angle of 11.73 degrees. The sound velocities were set according to known values of Ti6Al4V as: 6.172 m/s and 3.302 m/s for the longitudinal and shear wave velocity respectively. The PAUT test procedure is shown in Figure 116.

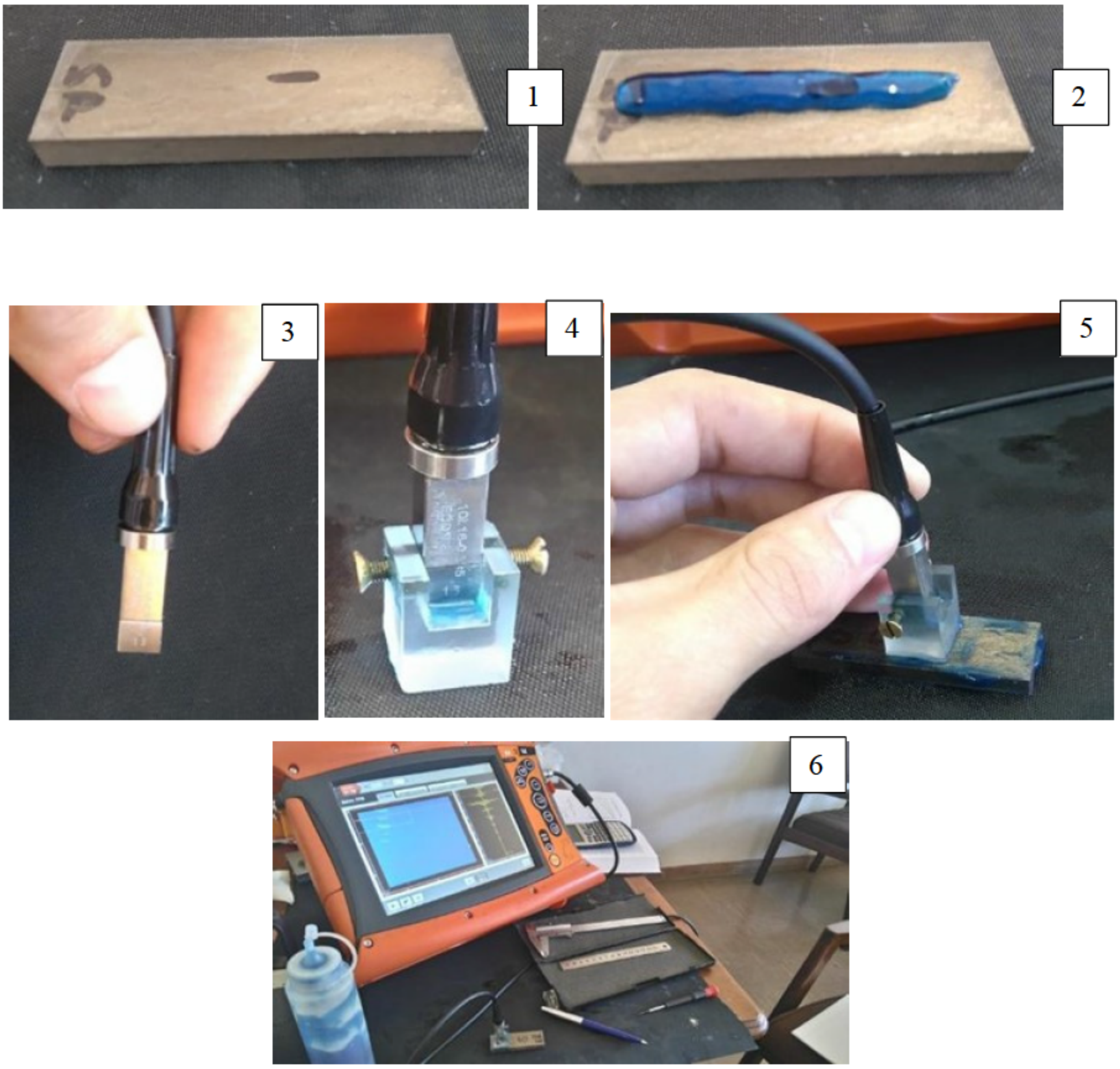

Figure 116: PAUT test procedure: 1– sample, 2–couplant on surface, 3- PAUT transducer, 4- transducer and wedge, 5- PAUT scanning on block, 6- experimental setup/equipment

3.3.4 Acoustic emission

The RFDA from IMCE (IMCE-RFDA, 2017) has the capability to measure the resonant frequency and damping at room temperature. The samples are tapped manually to create a vibration that is measured by a USB-microphone (Figure 117). The software can then calculate the material properties of predefined shapes based on the frequency and damping characteristics.

To determine the resonant frequencies, impulse excitation measurements were made with the RFDA Basic in an air atmosphere at room temperature. Modulus of elasticity, shear modulus and Poisson's ratio were recorded.

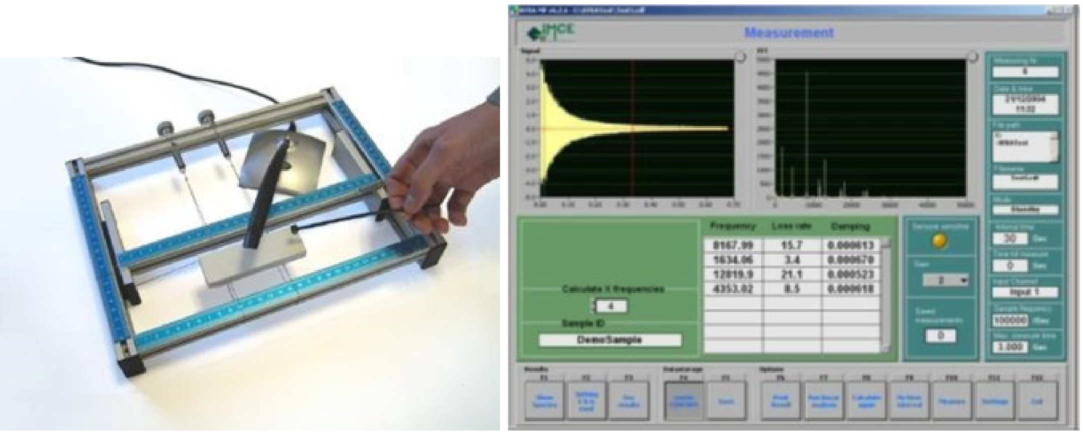

Frequency	Loss rate	Damping
8167.99	15.7	0.000613
1634.06	3.4	0.000670
12019.9	21.1	0.000523
4353.02	8.5	0.000618

Calculate X frequencies: 4
Sample ID: DemoSample

(a) (b)

Figure 117: RFDA Basic: testing equipment (a) and software (b)

3.3.5 Surface roughness testing

The surface roughness of the specimens was measured with the Surftest SJ-210 portable surface roughness tester from Mitutoyo Corp. (Figure 118); measurements were taken in different directions of both as-built and stress-relieved samples. Surface roughness was measured in accordance with ISO1997, λ_c=2.5 mm.

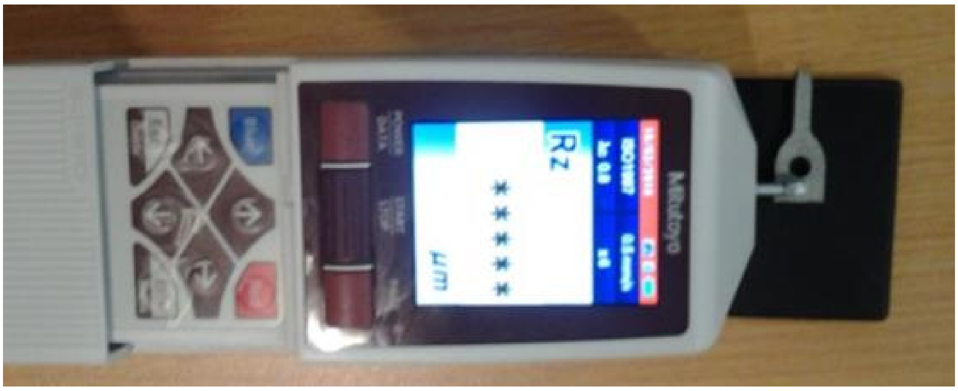

Figure 118 Surface roughness tester Surftest SJ-210 measuring the flat specimen

Summary

In this chapter, the material, methods and apparatus were described. Ti6Al4V ELI test samples were produced by the EOSINT M280 system. The CAD design of specimens was made with SolidWorks; samples were placed in a simulated chamber via the Magics interface (communicating directly with the M280 machine) and were produced by DMLS via the EOSINT M280 machine. Four methods were selected: Visual testing-optical microscope and SEM, micro computed tomography, phased array ultrasonic testing-TFM and the acoustic emission-resonant acoustic method.

Chapter 4: RESULTS AND DISCUSSION

The DMLS process is sensitive to various process-parameters. The literature showed that a small change in a single parameter such as: laser power, layer thickness, etc., could cause major defects. The properties of parts produced by this technology depend on: the geometrical characteristics of each single track, the morphology of each layer, and the cohesion of tracks and layers. Changing only one process parameter or powder property (for example, particle size distribution or chemical composition) may cause porosity or cracks to form in the 3D object (Yadroitsava *et al.*, 2015a). This sensitivity to parameters is ascribed to the nature of the process and the fact that this technology incorporates various other fields such as lasers, optics and metallurgy.

Referring to the many different NDT methods, Hellier (2012) mentions that from the 1950's to the present, NDT has grown considerably due to innovation and development of new materials and instrumentation. NDT covers a wide range of methods of analysis used to evaluate the properties of a material and these are now widely used for various industrial applications. At the commencement of the research, with no prior knowledge of NDT, it was found that part of the results would be to gain some knowledge of the different methods available. NDT proved to be a very broad field with a vast number of different methods, technologies and applications. With this in mind, part of the investigation and selection of the methods could be seen as results.

4.1 Testing the samples with fine internal structure

4.1.1 Pins with cubed cavities

To compare prescribed CAD sizes with the actual size of the cavities in the DMLS Ti6Al4V pins (Figure 119), cross-sectional images of the pins were studied with an optical microscope.

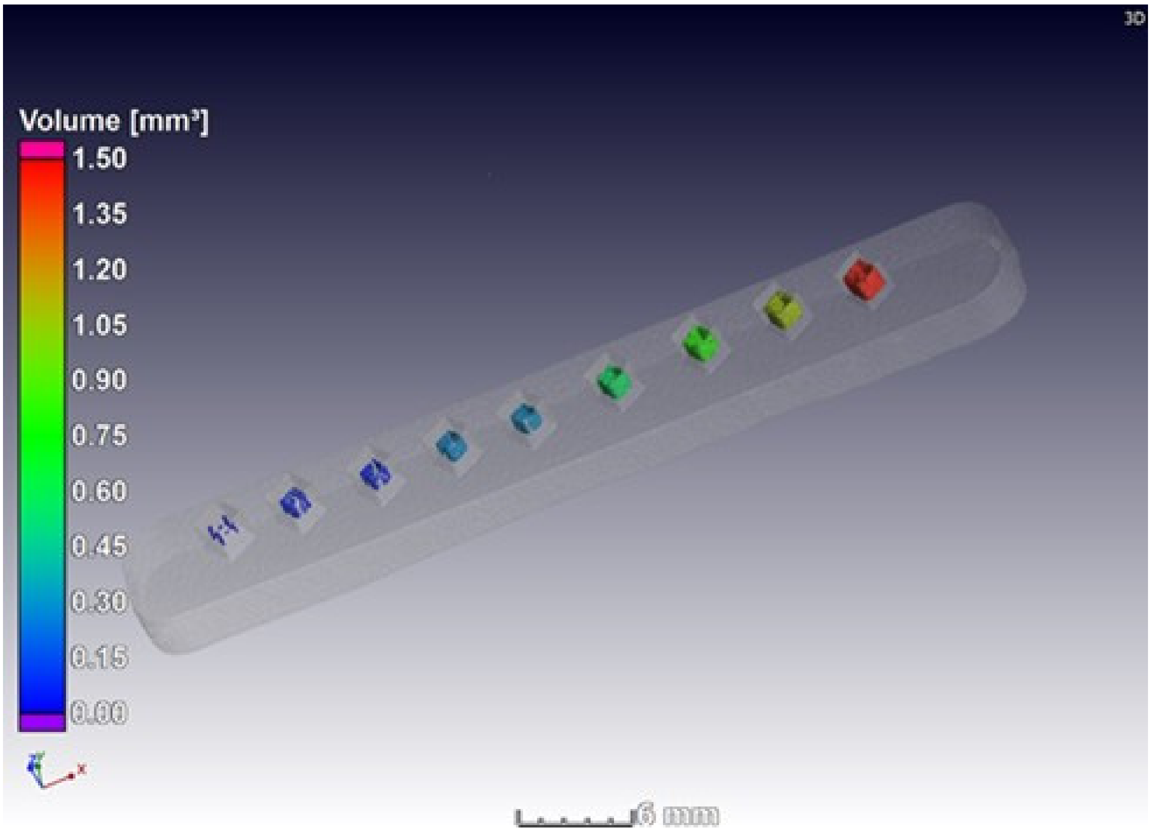

Figure 119: Transparent 3D image of pins and cubed defect pore volumes from CT reconstruction

A continuous gap was only achieved in prescribed sizes greater than 160 µm (samples P8–P9, Figure 120). In the smaller-sized gaps, powder attached to the samples resulted in voids closing and forming porosity. It should be noted that the straight shape of the square, which was developed in the CAD model, changed during the DMLS manufacturing. As indicated, 90% of the powder particles size distribution was less than 31 µm, therefore any gap size smaller than 30 µm (pin P4) showed major irregularities in the intended edges. Powder particle size distribution, laser beam spot size (80 µm in the experiments) and energy input influences track geometry, continuous edges were only present in the squares when the CAD cavity width was greater than the single track width (about 100 µm at selected process-parameters), as seen in Figure 121.

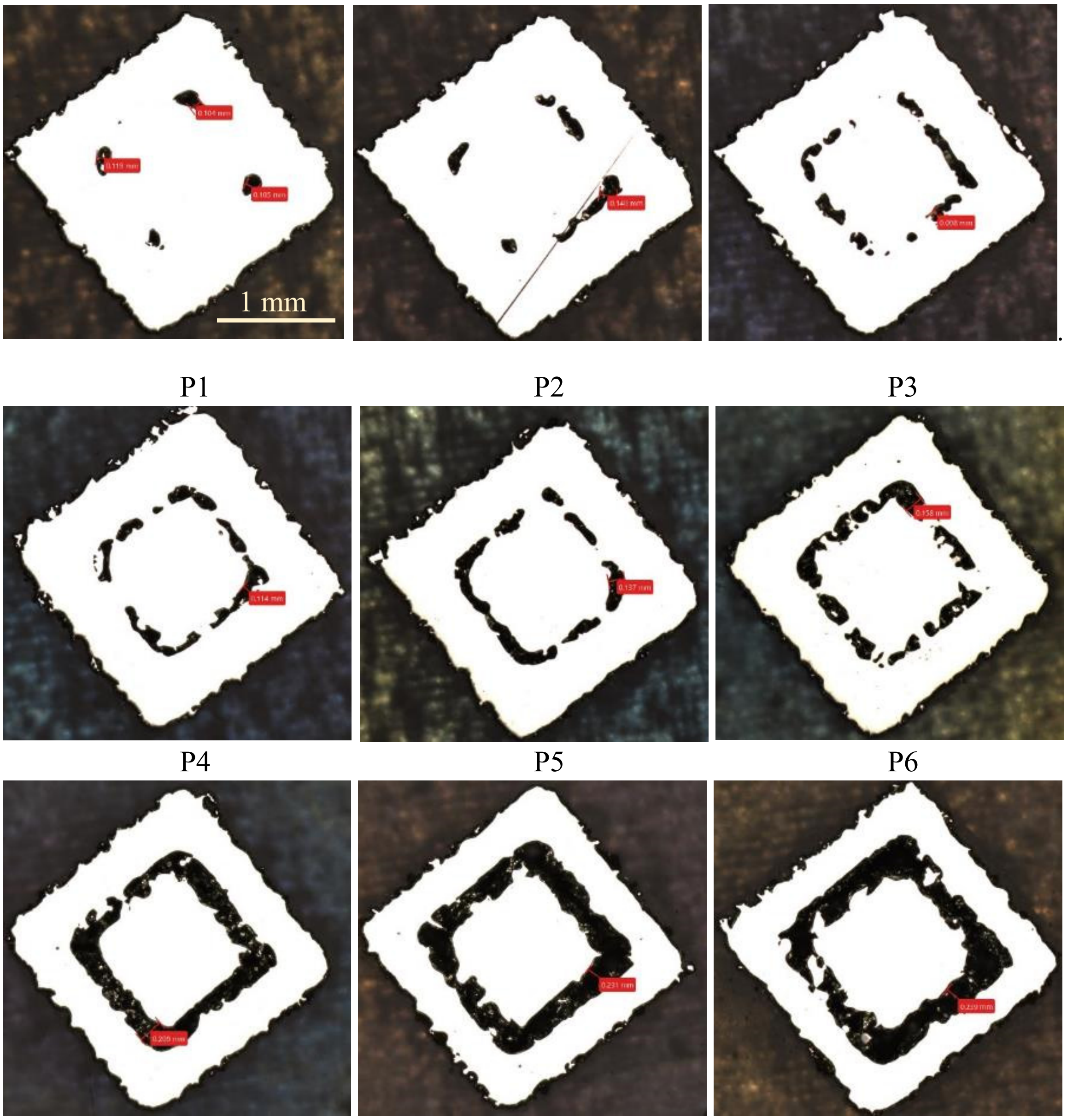
0.104 mm
0.119 mm
0.105 mm
1 mm
0.141 mm
0.008 mm
0.114 mm
0.137 mm
0.158 mm
0.209 mm
0.231 mm
0.229 mm

P1 P2 P3

P4 P5 P6

P7 P8 P9

Figure 120: Cross-sections of internal cavities in pins

Thus, selected process-parameters, scanning strategy, laser spot size and powder particle size distribution limited the manufacturing of straight vertical channels of 7.5–120 µm in size. Powder particles attached to the parts and irregularities in the tracks' geometry, resulted in high roughness and low accuracy of the straight edges.

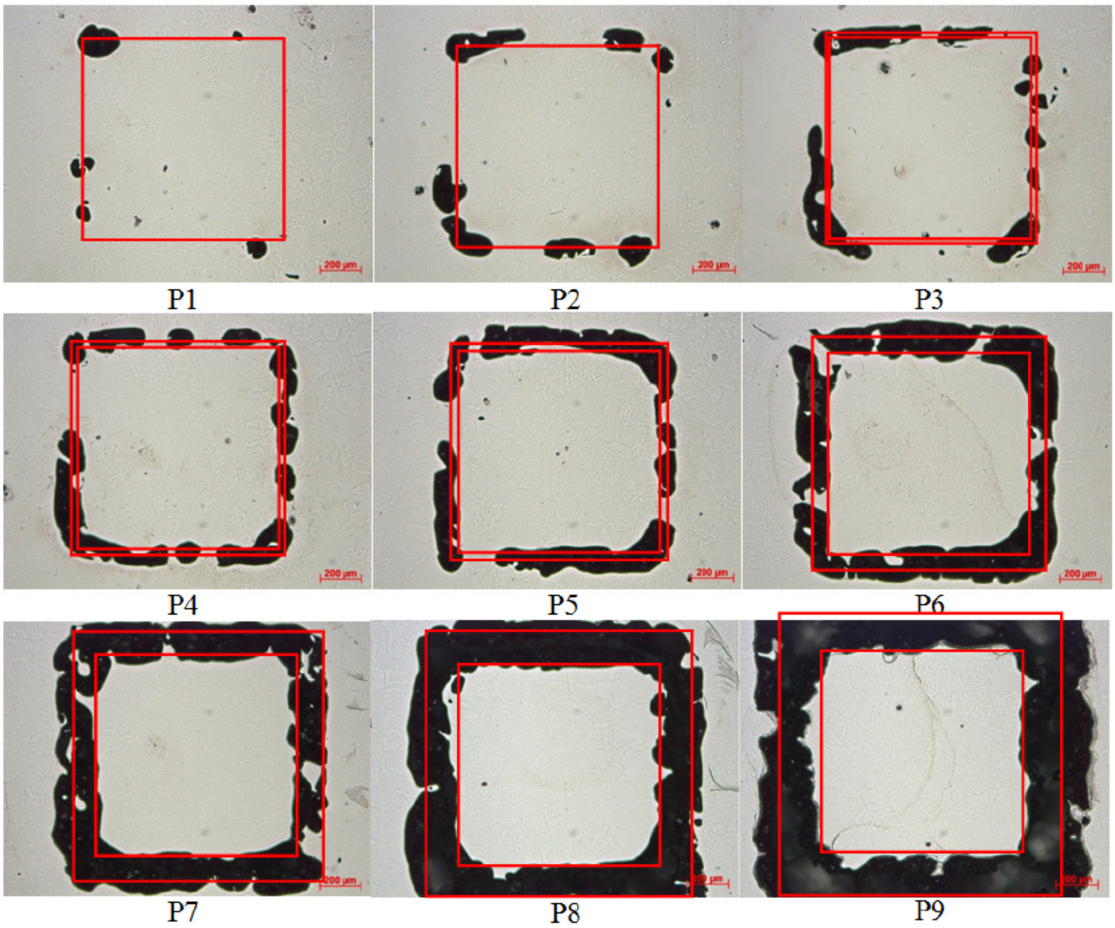

P1 P2 P3

P4 P5 P6

P7 P8 P9

Figure 121: Cross-sections of internal cavities in pins at higher magnification with intended CAD design (red squares)

CT scans were able to detect all vertical cavities (7.5–200 µm gap) introduced in the pin samples (Figure 122). Du Plessis *et al.* (2016) showed that the cavities with sizes ranging between (90–200) µm could clearly be recognized by CT scans in the DMLS pins with vertical cavities. As the CT scans indicated, the cube-shaped defects had vertical cavity walls with varying thicknesses, parallel to the build direction. The 7.5 µm thick cavity wall was clearly seen and the cavity was estimated as 70 µm. This value was obtained from cross-sectional analysis and had a maximal actual size of about 105 µm, which is close to the estimated value from the CT scans.

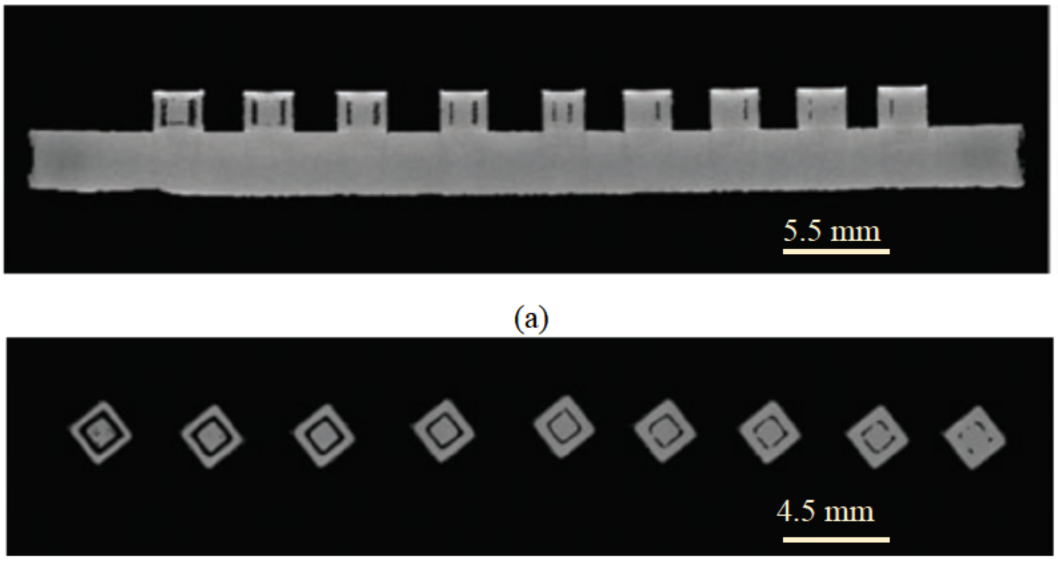

(a)

(b)

Figure 122: The pin samples with induced cubed defects. CT slice images from side (a) and top (b) views (du Plessis et al., 2016)

The difference between the prescribed CAD cavities in the DMLS pins P1–P9 (Figure 123), and the cavities estimated by CT scans is shown in Table 16. The difference in pore volume was 60-70% in the small prescribed cavities with sizes 7.5–80 µm (Figure 124). The largest manufactured straight vertical channels with sizes of 120–200 µm showed a difference of about 50% between that measured by CT scan and the prescribed CAD model. However, images of cross-sections showed that certain open channels could only be produced from 160 µm gap thickness at the selected process-parameters and scanning strategy. This value is governed by the track's width and satellites that, in turn, are limited by powder particle size distribution.

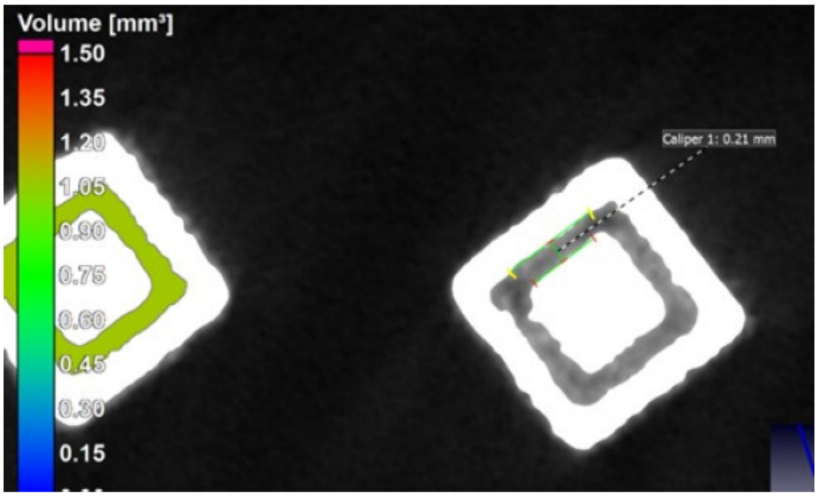

Figure 123: CT image of cavity-P9.

Table 16: The pore volume of pins with cubed cavities. CAD vs. Micro CT

Sample	CAD gap size, µm	Micro CT pore volume (mm^3)	CAD pore volume (mm^3)	Difference in pore volume (mm^3)
P1	7.5	0.07	0.022669	0.04733
P2	15.0	0.16	0.045678	0.11432
P3	22.5	0.19	0.069030	0.12097
P4	30	0.27	0.092727	0.17727
P5	37.5	0.29	0.116771	0.17323
P6	80	0.57	0.259712	0.31029
P7	120	0.81	0.404928	0.40507
P8	160	1.08	0.560896	0.51910
P9	200	1.47	0.728000	0.74200

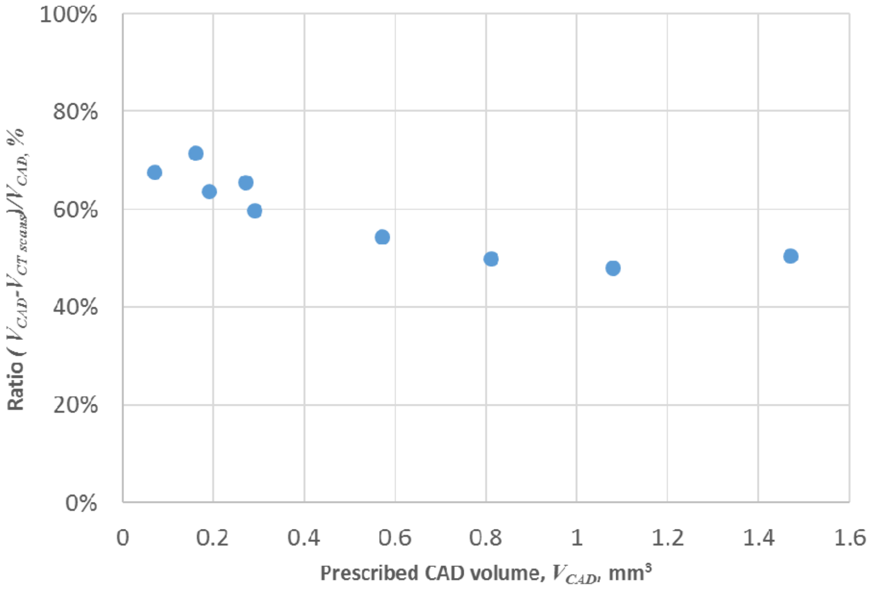

Figure 124: Difference between prescribed CAD cavities and cavities estimated by CT scans in DMLS pins P1–P9

4.1.2 Blocks with horizontal semi-cylinder channels

The blocks containing horizontal semi-cylinder channels, 60–360 µm in diameter, were CT-scanned (Figure 125) then cross-sectioned (Figure 126) to estimate the actual shape of the channels. The intended diameters of the CAD were drawn on top of each hemisphere to make comparisons with the prescribed sizes. The manufactured DMLS channels differed from the semi-spherical channels: they were irregular and had different sizes and shapes compared to the prescribed CAD model.

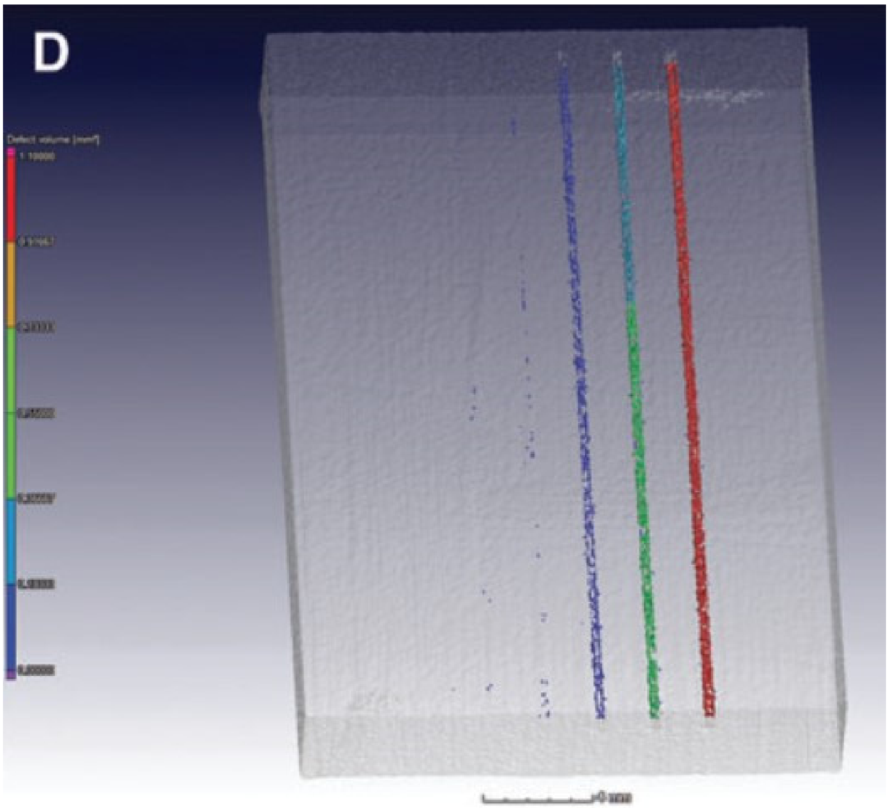

Figure 125: A transparent CT defect analysis view of CT reconstruction of the rectangular sample with induced line/track defects of varying thicknesses perpendicular to the build direction (du Plessis et al., 2016)

The cause of these irregularities could be easily explained when looking at the effects of building direction. Since these channels were built in a horizontal direction, layer thickness as well as “up and down skin” (Figure 21) plays a great role in small detail. Layer thickness, in this case, was set to 30 µm for recoating, resulting in an actual 45-60 µm powder layer due to densification of previous scanned layers and roughness of the single layer. Looking at C1, it had an intended diameter of 60 µm, which consequently has a radius that is less than the layer thickness 45 µm – therefore it is physically impossible to create a circular shape with only the first layer (Figure 127). For diameters that are greater than the layer thickness, the edges of the semi-cylinder cannot be created in the building direction, as shown in Figure 128; the blue lines indicates the point at which the laser scanning should stop. This problem is only applicable for small diameter/overhangs, but as they become larger, another problem arises. This problem is due to the loose powder and the inability of the molten pool to penetrate into any solid part of the component being built. Therefore, irregular surfaces below the upper edges are expected.

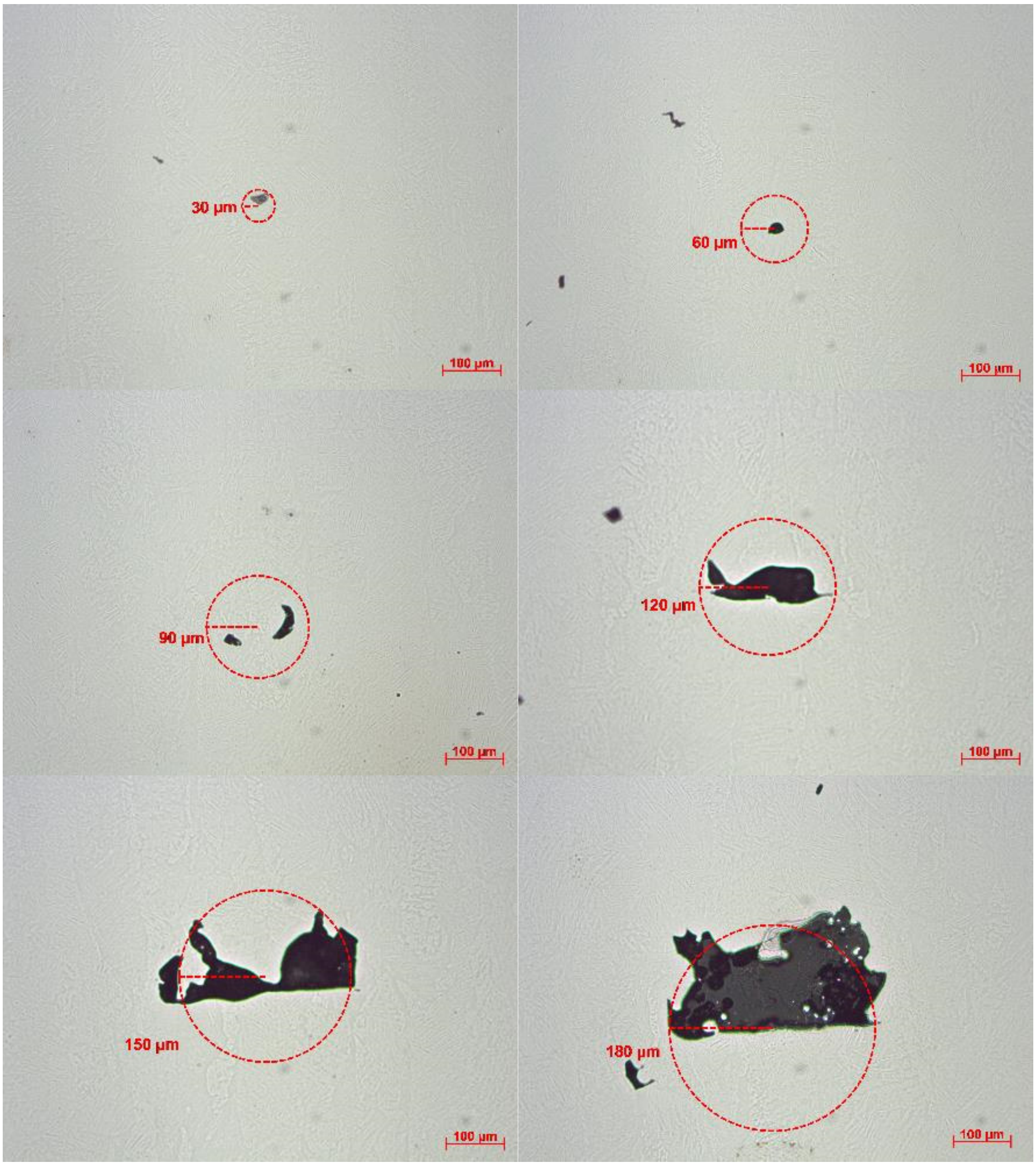
30 µm
60 µm
90 µm
120 µm
150 µm
180 µm
100 µm

Figure 126: Cross-sections of Ti6Al4V ELI rectangular block with semi-cylinders with prescribed CAD radius indicated

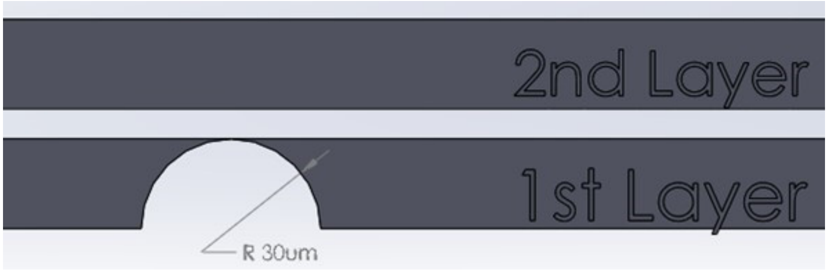
2nd Layer
1st Layer
R 30um

Figure 127: Illustration of semi-cylinder-C1 build limitations

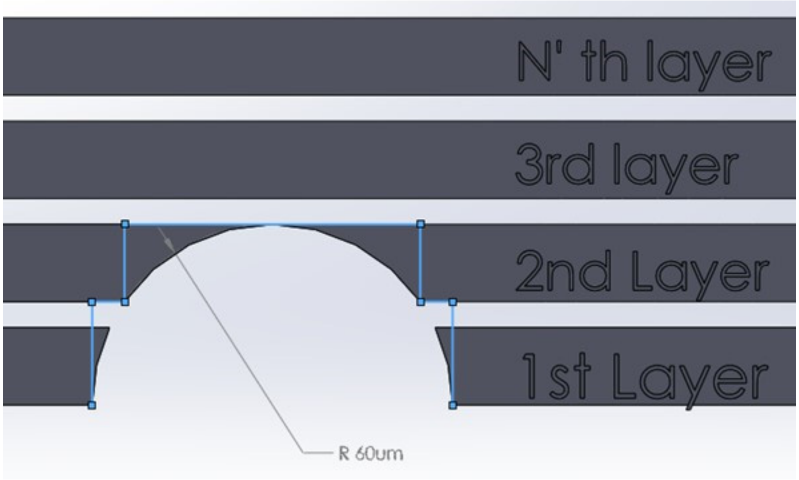

Figure 128: Illustration of semi-cylinder-C2 build limitations

Looking at the isolated 3D Micro CT image of channel C3 in Figure 129, it can be seen that the track is not only irregular in the length, but in all directions. Surface roughness of the straight, horizontal top edge of the hemisphere could be a contributing factor. Micro CT gives an accurate indication of each channel.

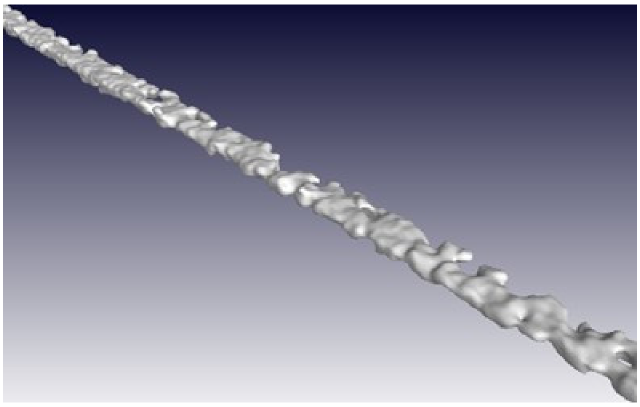

Figure 129: CT reconstruction of semi-cylinder horizontal pore C3 with prescribed CAD diameter of 180 µm

The semi-cylindrical horizontal pore C3 of 180 µm diameter was only marginally detectable by CT scans, whereas channel C2 of 120 µm in size was recognized as isolated pores. The pore of 60 µm (C1) was not seen at all (du Plessis *et al.*, 2016). Defects with sizes of 90–200 µm were clearly recognized by CT scans, but the top edges of each channel were not at the same height and not fully a pore space, that is, they were partially solid. The semi-spherical CAD shape of the pore in the actual DMLS part changed to an irregular shape. This is not only due to the penetrating molten pool from the upper layer, but also due to the particles attached on the inside edges (Figure 130).

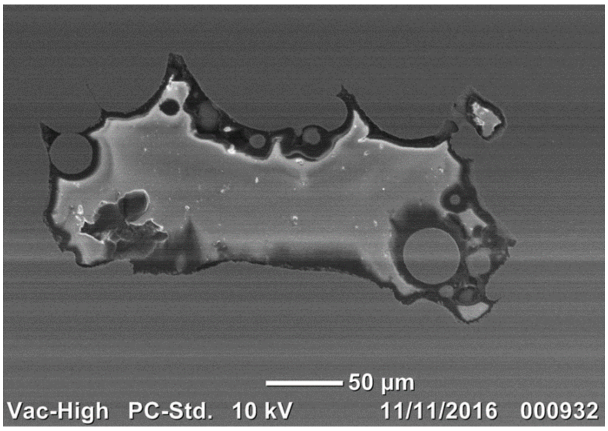

Figure 130: SEM image of cross-sections of prescribed semi-spherical cylinders with intended diameter of 150 µm

4.1.2 Step samples with horizontal cavities

The cause of the rectangular horizontal pores found in these step samples, is not much different to that of the horizontal hemispherical channels. It was found that although CT scanning gives a clear indication of small pores (depending on CT parameters) as seen in Figures Figure 131 and Figure 132, slight definition was lacking when compared to physical microscopy (Figure 133). However, physical microscopy does not have the ability to investigate at any section of the sample and when used, sample destruction and preparation is needed.

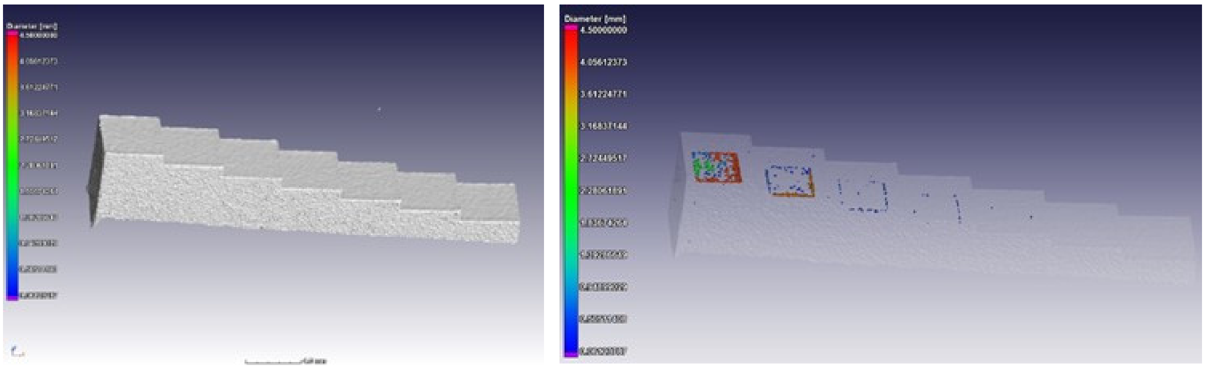

(a) (b)

Figure 131: 3D image of step samples with horizontal pore volumes from CT reconstruction (a) and transparent image with pores (b)

Cross-sectioning showed that in DMLS parts, internal cavities had irregular shapes and the melt of the upper layers closed the spaces. Only from cavity S4 (90 µm gap) did artificial porosity begin to form. However, even at S7 which is six layers thick (6×30 µm = 180 µm), an open cavity could not be produced at the selected scanning parameters. Powder particles attached to the sample and the penetrated molten pool was clearly visible by SEM (Figure 134).

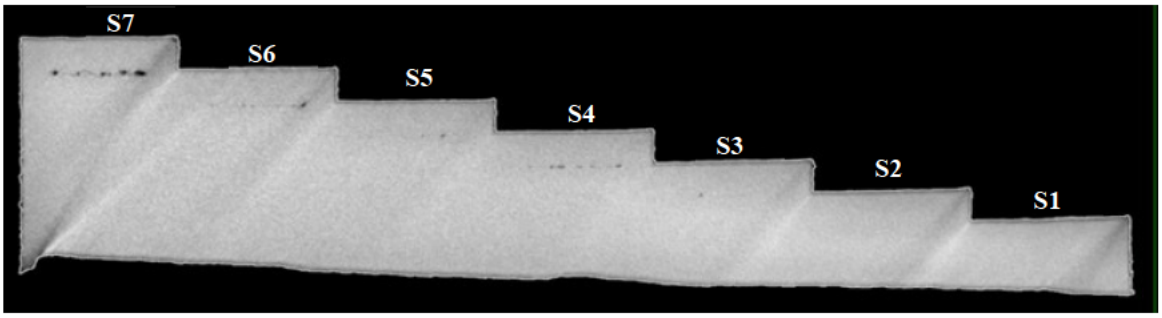
S7
S6
S5
S4
S3
S2
S1

Figure 132: The stepped sample with defects. CT slice images from side view

S2 and S1 samples

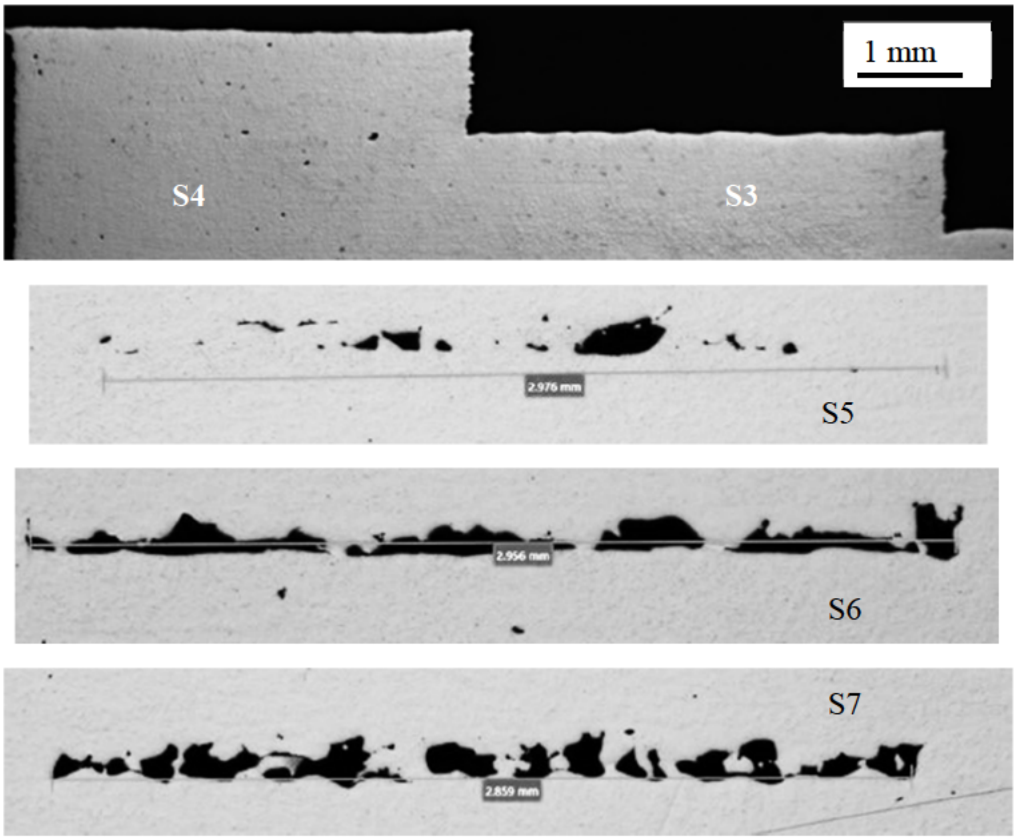
1 mm
S4
S3
2.976 mm
S5
2.956 mm
S6
S7
2.859 mm

Figure 133: Optical microscope photos of cross-sections of step samples

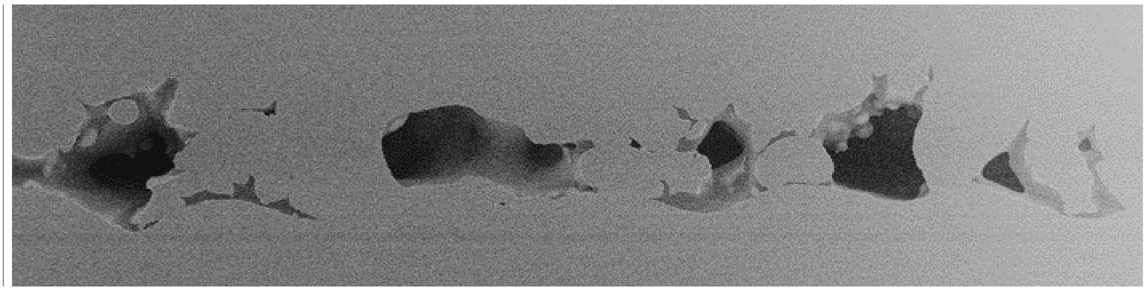

Figure 134: SEM image of S7 sample

In the manufactured samples, the prescribed rectangular cavities were solid, but with irregular porous edges, visible in CT scans and cross-sectioning (Figure 131 and Figure 133). It must be noted that EOSINT uses different laser input process-parameters for the contour to that of the core of the sintered object. Therefore, process-parameter settings affected the geometrical characteristics of the molten pool which led to varying shapes seen in the inner structure.

4.2 Testing of artificial porosity in large rectangular samples

Visual inspection of the manufactured Ti6Al4V (ELI) rectangular samples did not reveal any visible defects and cracks on the surfaces (Figure 135). Surface roughness influences the results in various ways. For example, in UT when the transducer is placed on the surface, any irregularity would influence beam conduction. In CT scans, surface roughness influences part dimensions. In visual testing, pores and micro cracks could be hidden below rough and irregular surfaces because it could be masked by attached powder particles on the side surface of DMLS components. The surface roughness of the DMLS specimen will vary with the direction in which the probe moves with regard to the building direction or the scanning strategy used for the specimen. For example, when checking surface roughness of the top surface of the specimen, if the probe moves perpendicular to the tracks, it will have a greater roughness than when it is running on a track in the same direction of the scanning. Roughness measurements were made 12 times on each surface, each time rotating the block by 30 °. The top surface roughness was recorded as Rz=34.5 µm, Ra=5.9 µm average with 12.97 µm and 1.79 µm standard deviation respectively. The side surface roughness was recorded as Rz=89.9 µm, Ra=14.5 µm average with 17.93 µm and 3.19 µm standard deviation respectively. The large standard deviation can be attributed to the above-mentioned factors. There was less probability that defects, such as micro cracks, be detected on the side surface with Rz=89.9 µm, compared to the top surface (Rz=34.5 µm).

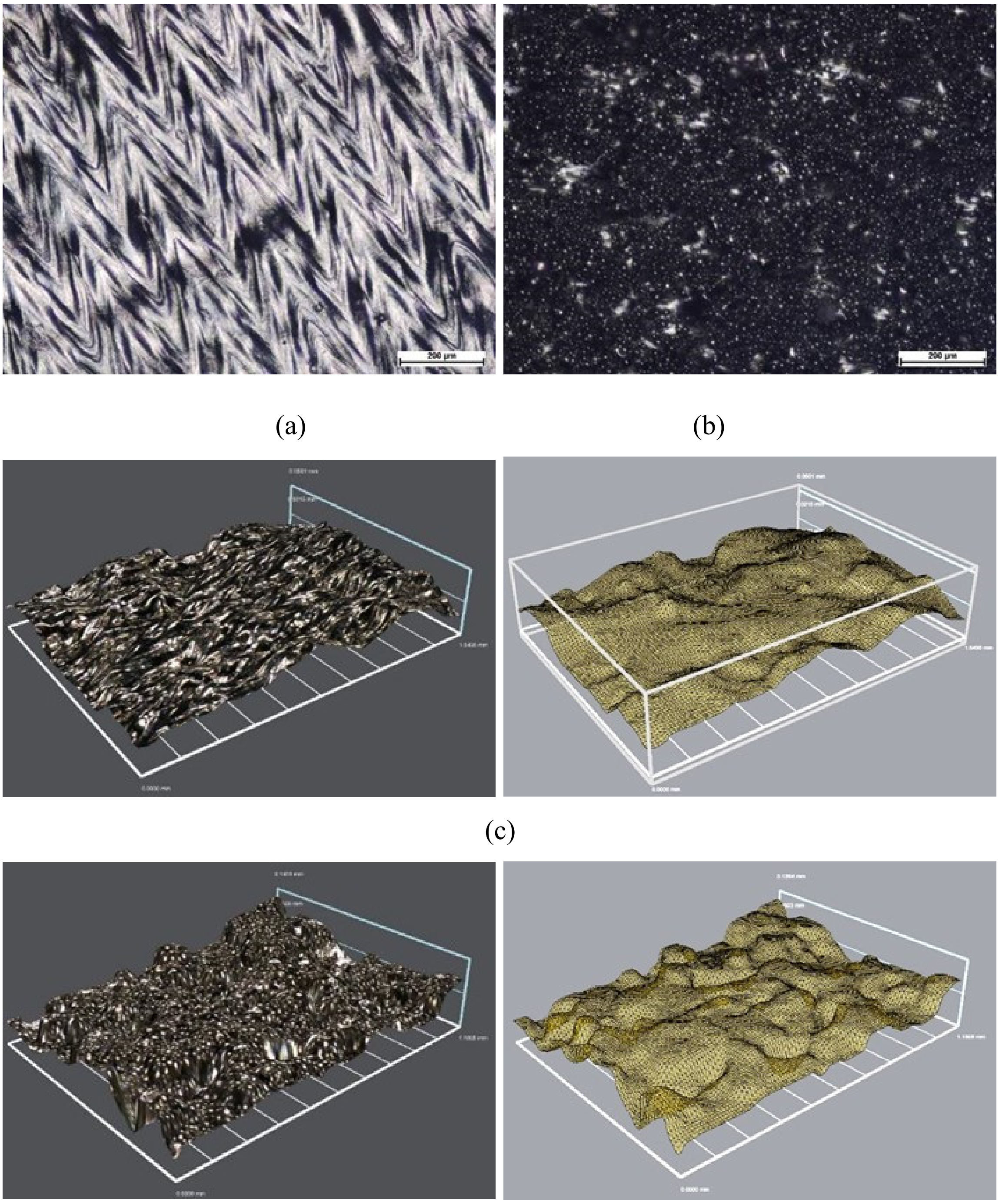

(a) (b)

(c)

(d)

Figure 135 Optical images of top (a) and side surface (b) and 3D reconstruction of top (c) and side surface (d) of DMLS Ti6Al4V sample

Micro CT scans showed that the control group of samples, AB 1-3 and SR 1-3, had no defects, only some random small pores. The samples AB4 and SR4 had a very fine defect layer, while samples AB5 and SR5 had a more pronounced defect layer, but it was not continuous, as shown in Figure 136. For the rectangular samples; both AB–SR, the volume and shape of the designed defects varied from (0–36) mm^3, that was 0.4% of the total prescribed porosity. The planned porosity of the samples with artificial defects was 0–0.5%, but in reality the estimate from the CT scans' porosity of the samples were much lower: 0%, 0.06% and 0.11% for AB1, AB4 and AB5 shown in Figure 136(a) and 0%, 0.03% and 0.31% for SR1, SR4 and SR5 shown in Figure 136(b). The partial re-melting of the powder in the inner area of the sample (artificial defect) can cause porosity reduction. Some of the unmelted powder, which remains in the inner cavities, can mask the pores when using microCT.

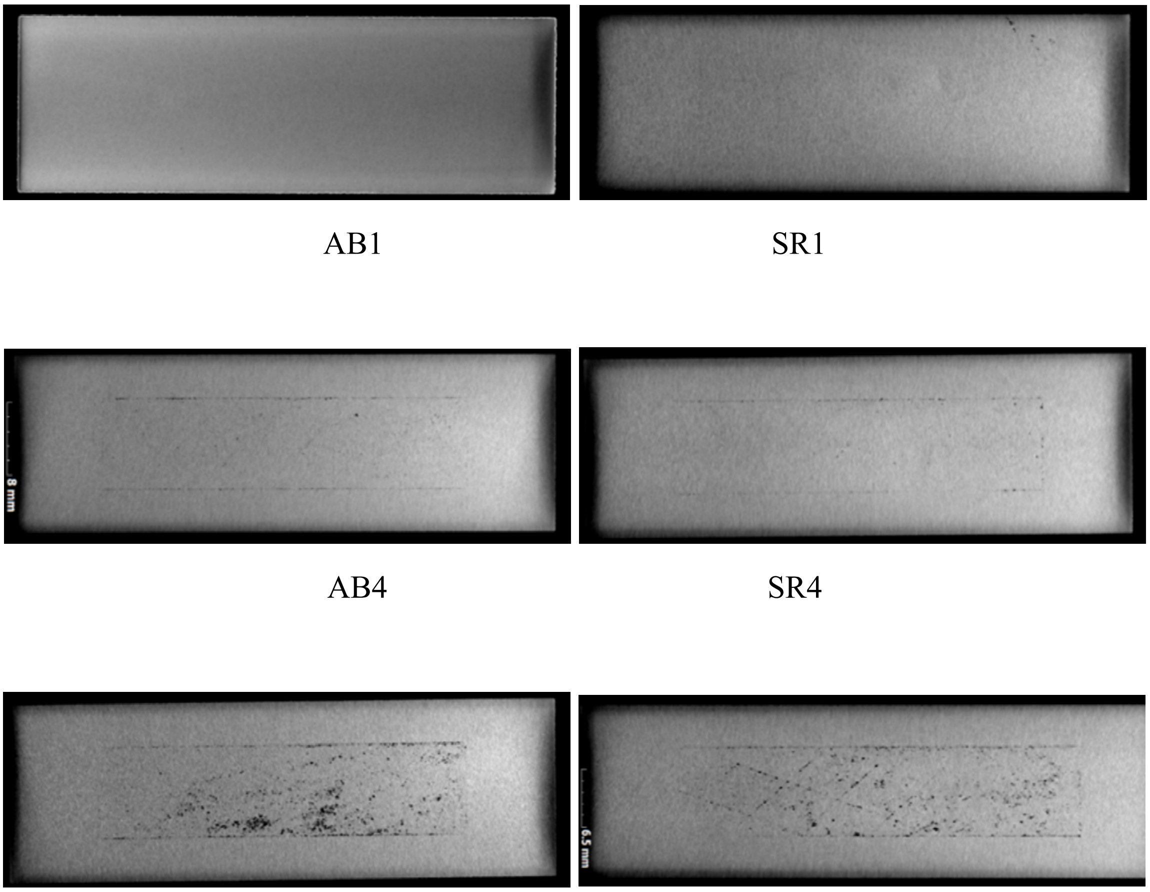

AB1 SR1

AB4 SR4

AB5 SR5

Figure 136: DMLS samples without defects and with artificial defects upon micro CT inspection (top view)

The 3D distribution of the pores in the sub-volume near defects, from a close-up 15 μm resolution at micro CT inspection of samples with defects AB5 and SR5 is shown in Figure 137. Ultrasonic testing was able to identify some defects under certain conditions – in two samples (AB 5 and SR 5) areas with relatively large voids could be detected when scanning on the top surface (Figure 138 – Figure 140).

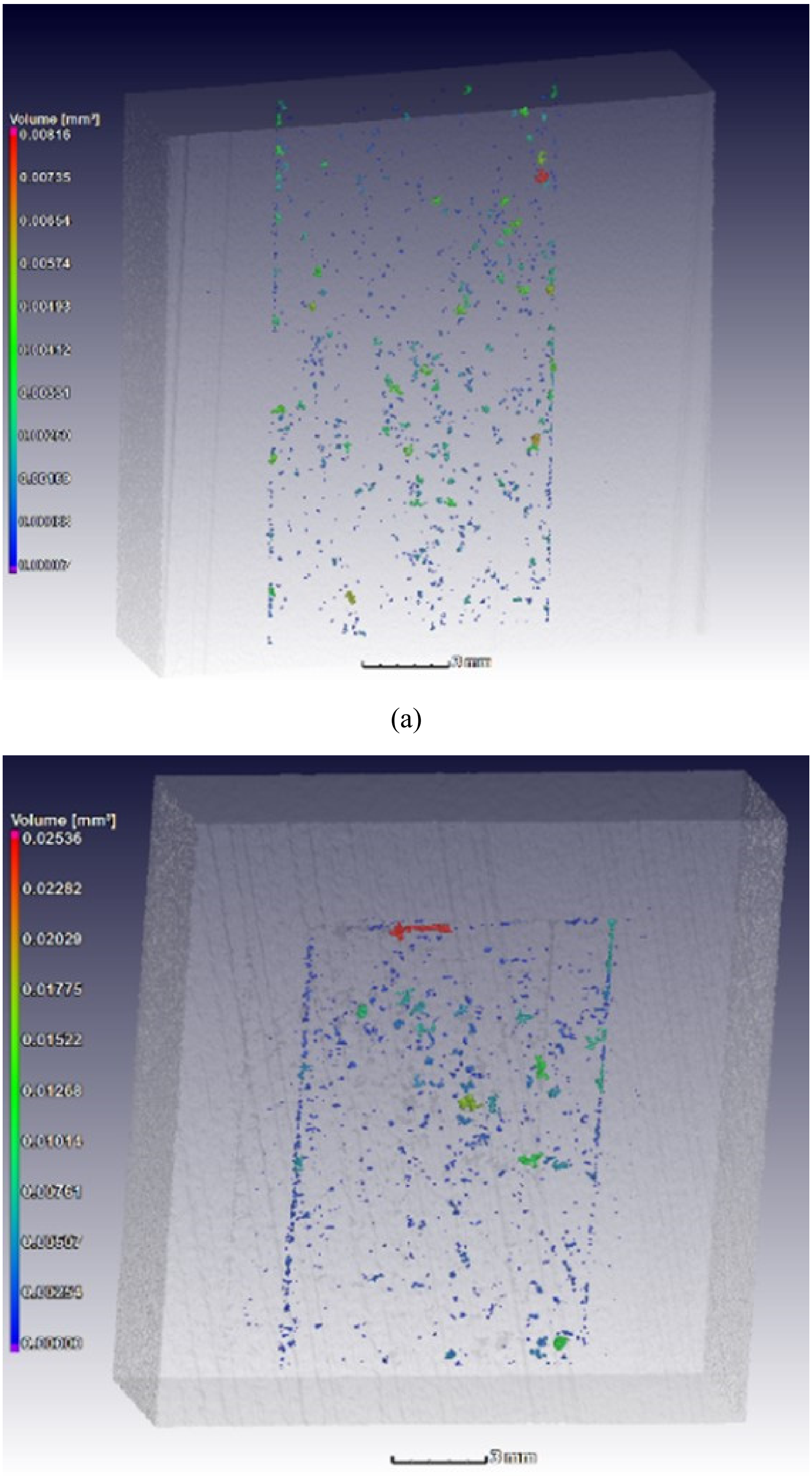
Volume [mm³]
0.00816
0.00735
0.00654
0.00574
0.00493
0.00412
0.00331
0.00250
0.00169
0.00088
0.00007
3 mm
Volume [mm³]
0.02536
0.02282
0.02029
0.01775
0.01522
0.01268
0.01014
0.00761
0.00507
0.00254
0.00000
3 mm

(a)

(b)

Figure 137: 3D distribution of the pores in the sub-volume near defects from a close-up 15 µm resolution at micro CT inspection: AB5 (a) and SR5 (b) samples

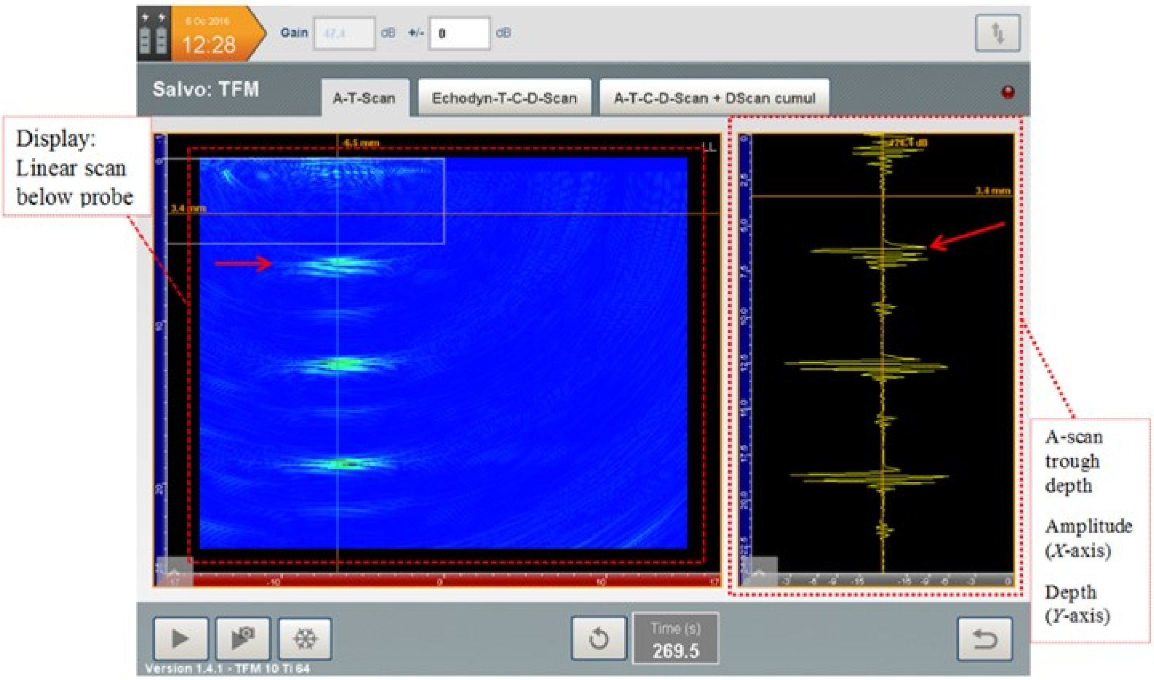
12:28
Gain
dB
+/-
0
dB
Salvo: TFM
A-T-Scan
Echodyn-T-C-D-Scan
A-T-C-D-Scan + DScan cumul
6.5 mm
3.4 mm
3.4 mm
Time (s)
269.5
Version 1.4.1 - TFM 10 Ti 64
Display:
Linear scan
below probe
A-scan
trough
depth
Amplitude
(X-axis)
Depth
(Y-axis)

Figure 138: TFM result of AB 2;screen shot with descriptions: red arrows indicate the first back wall echo, thereafter the echo repeats, horizontal orange line/cursor could be set to investigate at certain depths; in this case 3.4mm

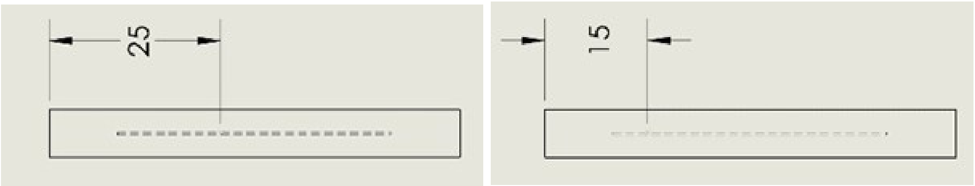

Figure 139: Detected defect position of samples AB5 (left) and SR5 (right) as indicated in Figure 140; measurements taken were made from edge to the centre of the wedge

The samples AB4 and SR4 showed no defects – to some degree this is true, though the CT scanning (Figure 136) revealed that these samples contained fewer and smaller pores than AB5 and SR5. Although the results of AB5 and SR5 indicated that defects were present, some concerns arise regarding the applicability of this testing method on DMLS-manufactured samples. The entire layered defect could not be identified – only some areas were identified. Some factors that made it possible to detect the defect during this test are:

- a smooth- and flat surface for the transducer's surface to move across with proper contact,
- the size of the transducer was smaller than the surface to be inspected,
- the orientation of defect. The operator has to have access to the surface for the transducer to make proper contact on the areas that have to be scanned, the orientation of this defect needs to be parallel to the surface.

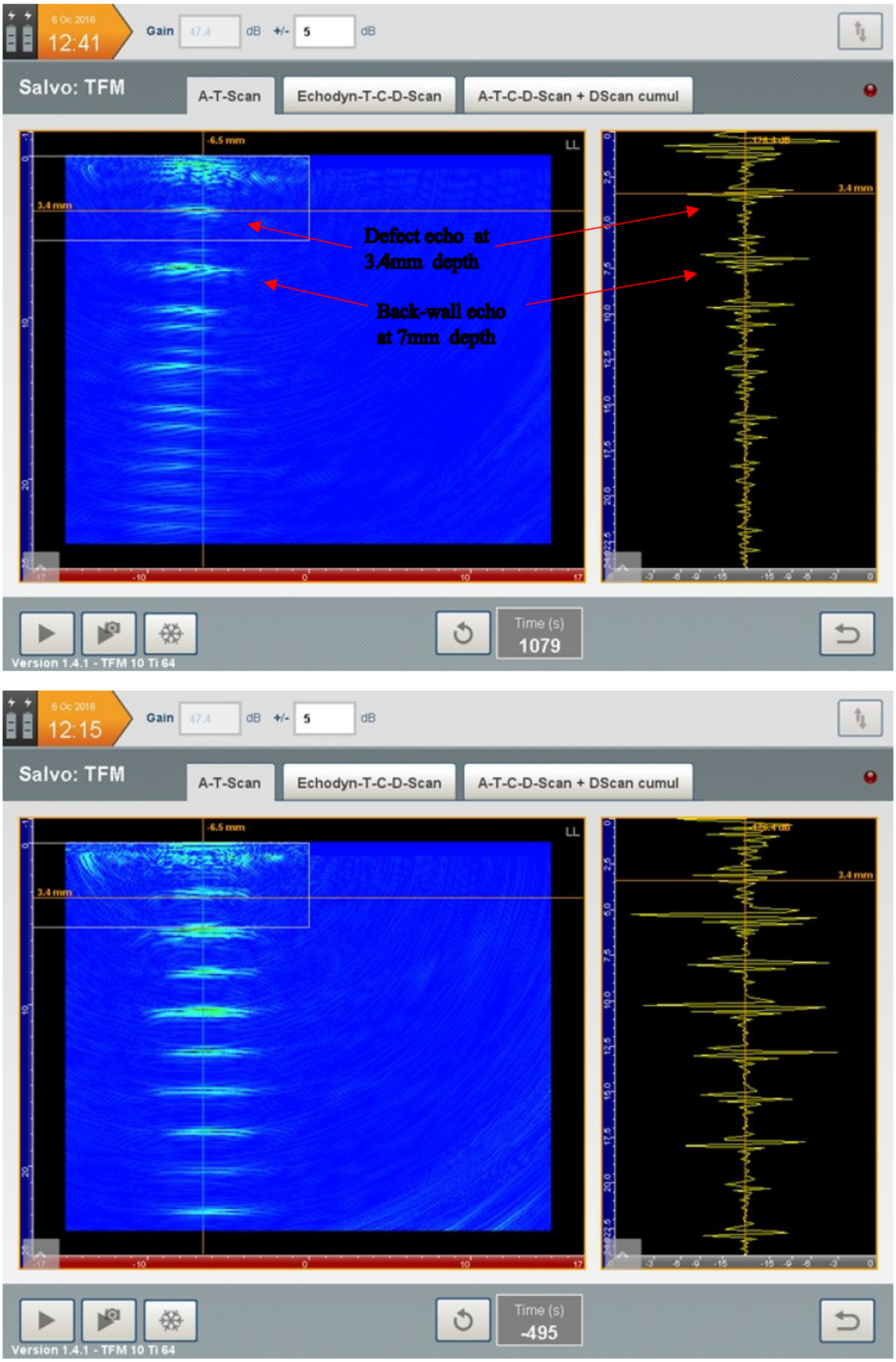

Defect echo at 3.4mm depth

Back-wall echo at 7mm depth

6 Oc 2016
12:41
Gain
47.4
dB
+/-
5
dB
Salvo: TFM
A-T-Scan
Echodyn-T-C-D-Scan
A-T-C-D-Scan + DScan cumul
-6.5 mm
3.4 mm
3.4 mm
Time (s)
1079
Version 1.4.1 - TFM 10 Ti 64
6 Oc 2016
12:15
Gain
47.4
dB
+/-
5
dB
Salvo: TFM
A-T-Scan
Echodyn-T-C-D-Scan
A-T-C-D-Scan + DScan cumul
-6.5 mm
3.4 mm
3.4 mm
Time (s)
-495
Version 1.4.1 - TFM 10 Ti 64

Figure 140: TFM results of AB 5(top) and SR 5(bottom)

AE testing proved that there were reliable differences in the data for the DMLS samples with different mass and thickness (Table 17, Figure 141). Some noticeable differences in the frequencies were found between as-built and stress-relieved samples without defects – flexural and torsion frequencies were higher for stress-relieved samples with similar mass.

Table 17: The acoustic emission testing data, sizes and mass of the samples

Sample	*E-modulus, GPa	*Flexural frequency, Hz	*Torsion frequency, Hz	Length, mm	Width, mm	Thickness, mm	Mass, g
AB 1	106.55±0.022	8399.9±0.82	13649.9±0.39	60.15	19.93	6.15	31.64
AB 2	107.14±0.005	8390.0±0.20	13648.3±0.16	60.16	19.93	6.13	31.58
AB 3	106.95±0.009	8392.8±0.34	13643.5±0.05	60.18	19.95	6.14	31.65
AB 4	107.80±0.004	8487.0±0.19	13789.6±0.11	60.18	19.93	6.19	31.90
AB 5	106.86±0.318	8460.5±0.09	13791.3±0.13	60.18	19.93	6.19	31.83
All as-built	107±0.4						
SR 1	112.17±0.004	8244.2±0.19	13546.8±0.43	60.39	19.93	5.91	30.50
SR 2	112.85±0.005	8745.3±0.12	14240.0±0.05	60.19	19.92	6.23	32.01
SR 3	113.20±0.004	8644.4±0.08	14085.5±0.08	60.19	19.94	6.15	31.70
SR 4	111.12±0.008	7208.3±0.20	12014.8±0.15	60.45	19.93	5.15	26.47
SR 5	110.28±0.013	7090.4±0.45	11835.5±0.15	60.50	19.93	5.08	26.03
All stress-relieved	112±1.1						

* Average value ± standard deviation

The modulus of elasticity values obtained from AE are shown in Table 17. These values coincide with known values for DMLS Ti6Al4V. Moletsane *et al.* (2016) reported that the modulus of elasticity obtained from tensile testing of DMLS Ti6Al4V as-built and stress-relieved horizontal samples were 112±2.1 GPa and 117±2.2GPa respectively.

The present study revealed that even a relatively simple method such as RFDA Basic could identify the defective samples (Figure 141), with low porosity (less than 0.5 per cent), from the defect-free samples, if the samples have the same geometry. Differences between as-built- and stress-relieved samples could be detected. The RFDA Basic can potentially determine a "fingerprint" of frequencies and their damping for complex DMLS parts. This study has a perspective in developing a simple and effective method of determining defective DMLS samples, as micro CT is quite expensive and a time-consuming method.

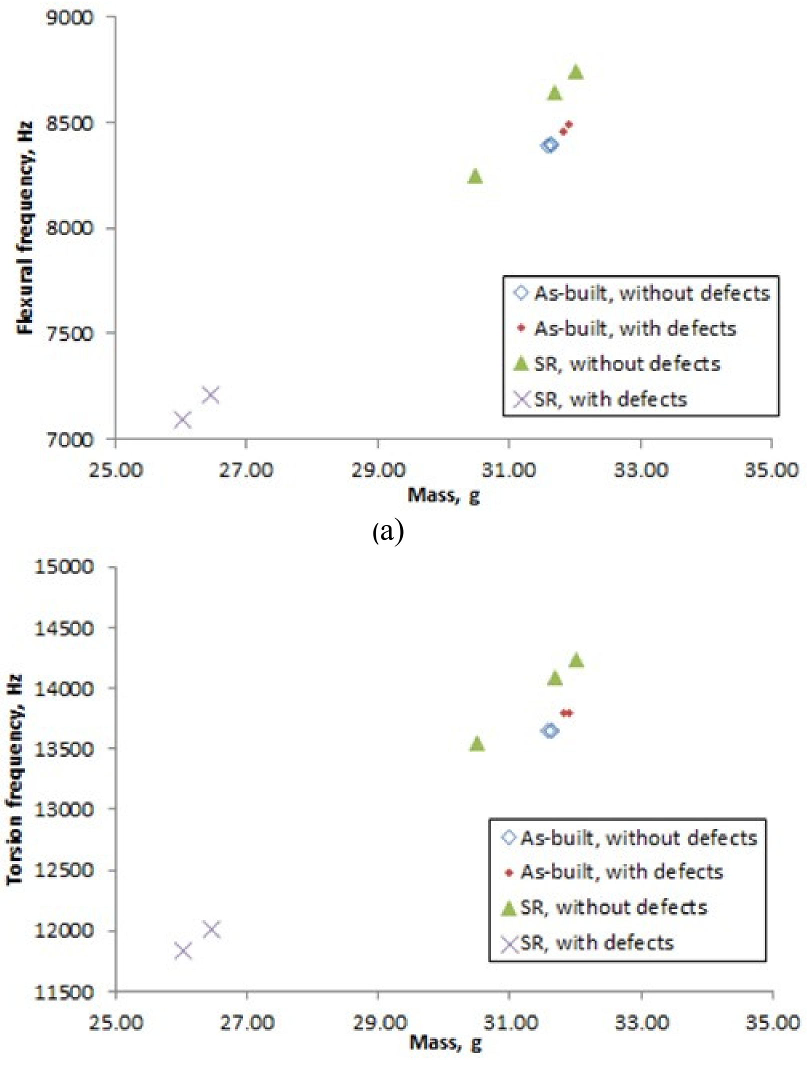

(a)

(b)

Figure 141: Flexural (a) and torsional (b) frequencies of the different specimens versus the mass

4.3 Non-destructive testing DMLS components using AE

The possibility of detecting defects in-house with the use of acoustic emission was investigated, due to its low cost and simplicity. As already discussed, AE is based on the natural vibrating frequency of a component; any defect will change the stiffness and/or mass resulting in a change in frequency measured. Samples free of artificial defects are compared to that of blocks containing defects. The flow diagram of the process (Figure 142) is similar to RAM shown in Figure 78 on page 77.

Personal development of AE equipment and software interface is in progress and forms part of the planned project. Experiments were carried out with a DIY microphone circuit testing setup and a microphone with integrated electronics. The experimental setup is shown in Figure 143.

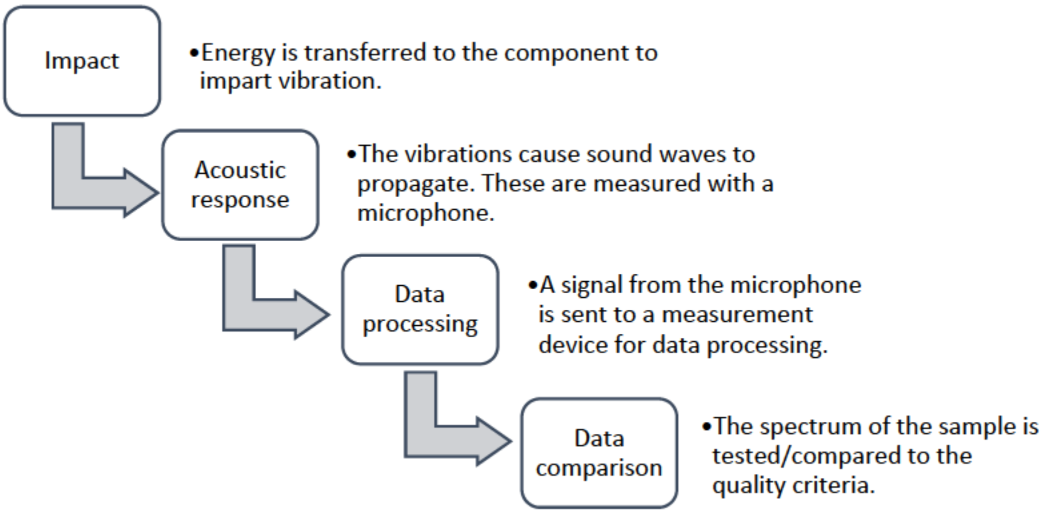
Impact
Acoustic response
Data processing
Data comparison

- Energy is transferred to the component to impart vibration.
- The vibrations cause sound waves to propagate. These are measured with a microphone.
- A signal from the microphone is sent to a measurement device for data processing.
- The spectrum of the sample is tested/compared to the quality criteria.

Figure 142: Flow diagram of post manufacturing AE NDT

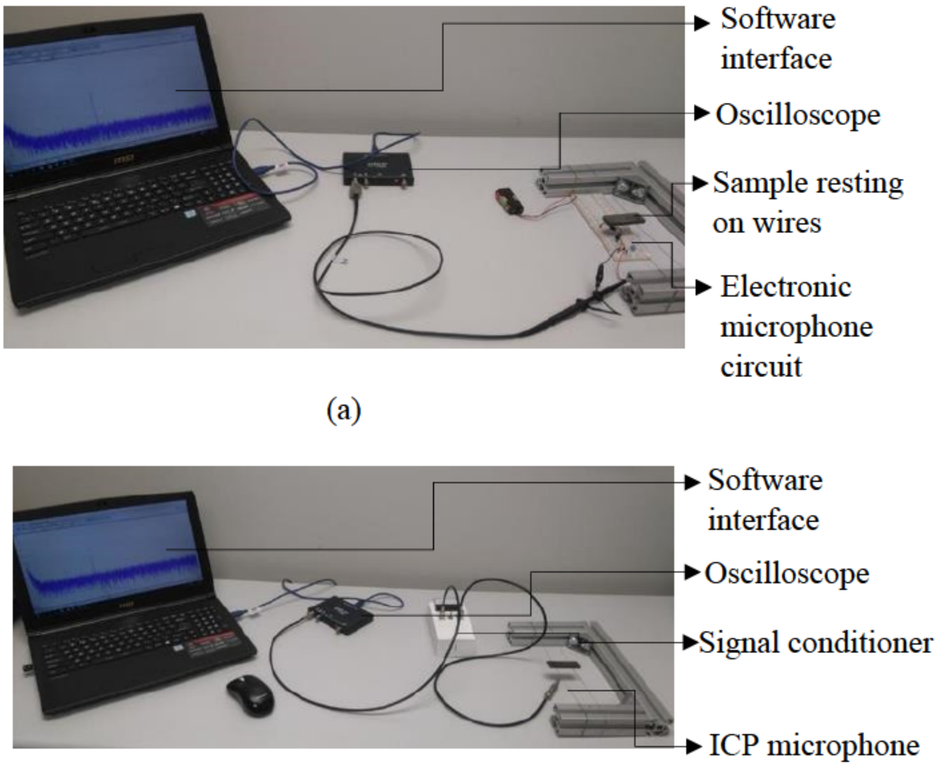
Software interface
Oscilloscope
Sample resting on wires
Electronic microphone circuit
Software interface
Oscilloscope
Signal conditioner
ICP microphone

(a)

(b)

Figure 143: AE testing setup with DIY electret microphone (a) and ICP microphone method (b)

In these AE methods, energy is transferred to the component via a small hammer to impart vibration (Figure 143b). Acoustic response is then measured with a 10 mm electret condenser microphone and amplifier circuit. An oscilloscope and PC software interface to carry out spectrum analysis. A PicoScope 2207B oscilloscope was used for the tests, while the function of the software was to record a sample and carry out spectrum analysis. The peak frequency was measured manually from the software and recorded. (Figure 144). The acoustic response, using the ICP method, was measured with a quarter inch ICP microphone from PCB electronics (model number is 130E20). These microphones need an external charge to operate, therefore, a signal conditioner was required. These are available from PCB Electronics, but it was decided to develop a signal conditioner for this purpose as it is not a very complex component. Data processing was done with the oscilloscope and PC software interface to carry out spectrum analysis, similar to the previous method.

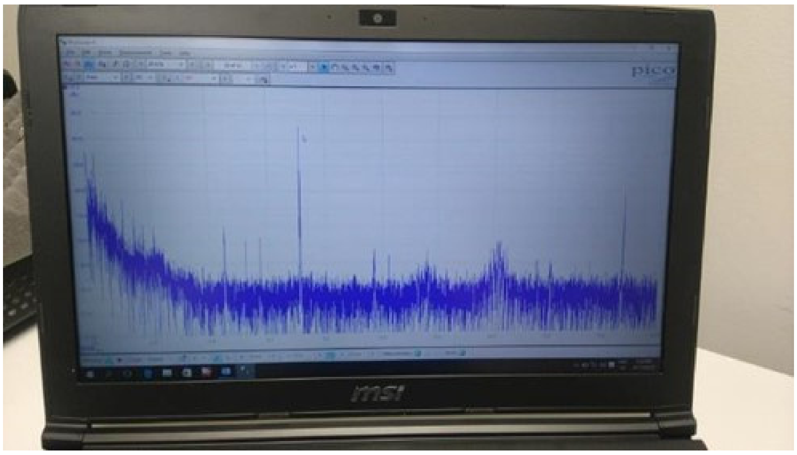

Figure 144: PicoScope software interface on a personal computer. Fast FourierTransform(FFT) is shown with the cursor pointing towards peak frequency.

4.3.1 AE testing of the rectangular blocks with artificial porosity

The flexural frequencies were reported for the samples with artificial defects as shown in Table 17 on page 126.

Table 18: The comparison of flexural frequencies (Hz) between RFDA and the DIY –ICP microphone methods for as-built and stress-relieved blocks

Sample	RFDA	DIY Microphone		ICP Microphone	
	Flexural frequency	Flexural frequency	Difference in comparison with RFDA	Flexural frequency	Difference in comparison with RFDA
AB 1	8399.88	8406.208	6.328	8404.566	5.686
SR 5	7090.39	7100.883	10.493	7100.973	10.583

As shown in Table 18, the test results for the two methods were very similar, which might indicate that either the test method or surroundings had an influence on the results.

4.3.2 AE testing of the blocks with pins

To determine the probability of using AE as a defect detection method, four blocks with pins were manufactured; one was built as designed with cavities and the remaining three were without cavities i.e. solid pins. The blocks with solid pins were then used as a control to indicate the frequencies of a "good part". The block with porous pins was used as a defective sample. The samples were manufactured on supports in order to control sample mass more effectively when removing them from the substrate. The mass of each of these samples was 7.5 g.

The samples were dropped onto a horizontal pin to excite the sample and cause vibration. These vibrations were measured with a half inch ICP microphone and amplifier combination from PCB Electronics. Each sample was dropped three times. The recording settings were as follows: 10 000 measurements, 100 kHz sampling rate and 50 kHz low pass filter. Signal data (only first 8192 points) were fed into Mathcad 2001 for spectrum analysis using discrete Fourier transforms.

Three samples without artificial pores were used as a control to indicate the frequencies of a "good part". The fourth sample was used as a defective sample. The resultant plot of each sample's average is shown in Figure 145. Peak resonating frequencies are clearly seen at approximately 10 000, 15 000 and 19 000 Hz.

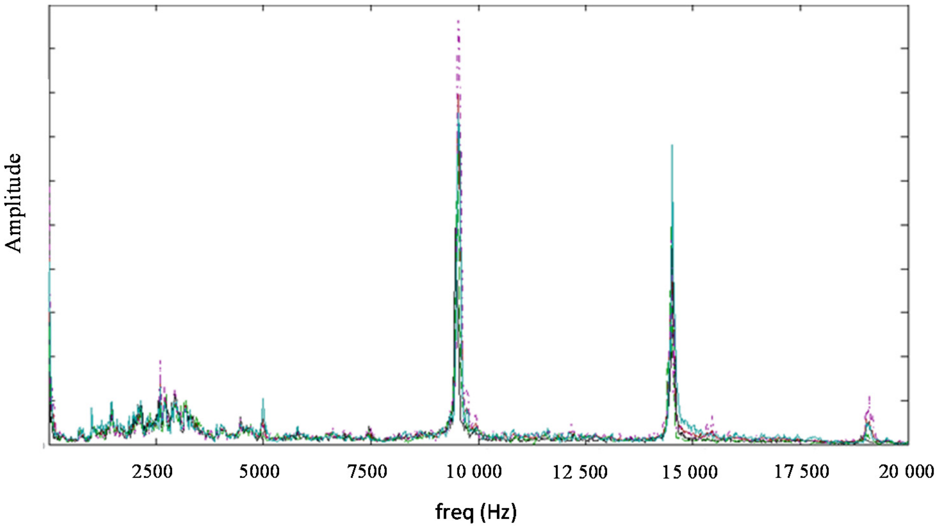

Figure 145: Discrete Fourier transform of all four sample traces overlaid

These three peaks were investigated in more detail and it was found that there was very little distinguishable difference between the samples at the 15 000 and 19 000 Hz peaks. Sample 1, 2 and 3 had an identical peak frequency of 9522Hz. Sample 4 shifted to a lower frequency 9448 Hz, as shown in Figure 146.

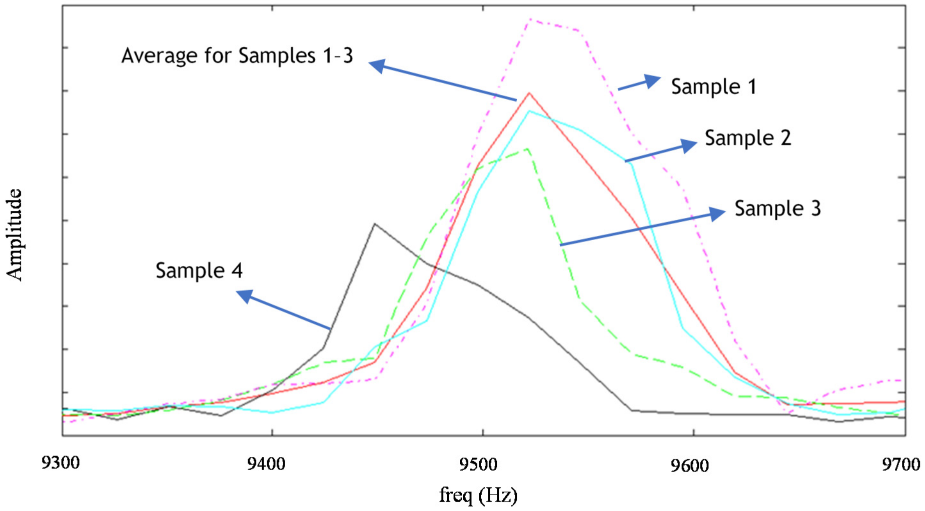

Figure 146: Amplitude of AE signals versus frequency for solid (samples 1–3) and “defect” block

From the CT scan, the volume of cavities inside this block was measured at 2.3 mm^3. Taking into account the total volume of the solid block with pin, the method applied recognized 0.13% of the porosity. Although the results seemed to be promising, as a clear difference was found, the question at hand is; is the shift due to the artificial porosity or are there some other influences such as surface roughness, etc. Therefore, future work entails duplicating the results before attributing the shift to porosity.

4.3.4 Planned work

The next steps are to understand the limitations and applicability of AE testing for AM. These steps entail the development of software and its user interface along with selecting and developing testing equipment. These steps will allow a detailed understanding of each variable and its influence on the results obtained.

A dropping rig will be designed for testing and a sound-insulated box will be built to minimize noise. It is planned to use LabVIEW software. These possibilities have been investigated and the project is in progress. PicoScope has a software development kit (SDK) available that is compatible with LabVIEW. The spectrum analysis will take place within this program.

Parallel to the post process testing, and investigation on whether online monitoring via AE can be used as a quality control method similar to the method in which AE is used during conventional welding. This entails placing a microphone inside the building chamber and recording sounds of defective processing so as to later recognize faults during a build.

Chapter 5: CONCLUSIONS

Manufacturing components for industries where quality is absolutely crucial requires that the parts be tested before being commissioned into service. Failure to do so could cause death or loss of expensive equipment and time. When new manufacturing technologies such as DMLS enter the market, the question is always: "*How does the quality compare to that of conventional manufacturing methods?*" Standard testing procedures are in place for conventional technologies and these standards give the end-user the assurance and peace of mind that the purchased product does comply with a set of minimum requirements. For example, the metal cable used in elevators should not only comply with a set of known material properties, but the cable should also be tested for defects before service. Thus, when new technologies emerge, formal issued standards always lag behind, which hinder technology growth.

DMLS offers many advantages in certain niche areas due to the freedom and complexity of design. Medical implants and aerospace components manufactured using DMLS technology need to be tested in-house for defects before service. To test these complex and often intricate parts is somewhat difficult.

As the part is tested before being used, it is necessary to test the component without compromising the structural integrity of the part – hence the term non-destructive testing. Many NDT methods are available, each having its unique advantages, disadvantages and applications. Therefore, a suitable testing method is required – a method capable of detecting the specific defects that arise from the DMLS manufacturing process. As with all business, the testing should be quick and affordable. An understanding of the DMLS process and how defects arise are a prerequisite for selection of an appropriate testing method. Once it is understood what defects must be identified, the selection of the testing method can commence. For the selection of the testing method, a basic understanding of the operational physics and equipment is necessary in order to make an informative decision on the applicability of the method.

The focus of study is on metal components but more specifically on Ti6Al4V components as they are more often used in life-threatening applications. Ti6Al4V exhibits residual stress and consequently, cracks and changes in material properties are a concern. As with metal castings, so also in DMLS components, pores remain a concern as they directly affect the material strength. Therefore, samples with artificial defects were produced and investigated with the chosen NDT methods.

The DMLS process creates parts from fine powdered material by melting small single tracks, layer by layer, which makes it highly sensitive to manufacturing process-parameters. Literature shows that for each material there are numerous researchers investigating the parameters, such as laser power, scanning speed and layer thickness. Research to find the optimum parameters is required to reduce defects and residual stresses. Parallel to these parameters and building strategies that are being developed, companies are investigating new methods and machinery to produce better quality parts. One such method makes use of substrate heating to increase the temperature of the material so as to reduce residual stress within the component.

It was found that not only are there numerous NDT methods, but also within a certain principle of operation, various subcategories exist. For example, UT has many different techniques and equipment, ranging from complicated automatic scanning of submerged parts to a simple handheld depth gauge. This makes finding and selecting the right equipment difficult. During the initial stages of this research, it became apparent that there was a vast amount of information available on the capabilities of the different techniques. However, it had to be borne in mind that NDT has become a specialized field of study and it was necessary to limit the depth of the research on this topic. It is of great importance that the operator of the machine is well-trained and has a clear understanding of the equipment, input settings and how to interpret the information generated by the test equipment.

The advantages of X-ray CT outweigh any other method when considering the vast amount of information generated, not only as an NDT method, but it is possible to see and interpret features below the surface of the component. This is mainly due to the capability to view the component and defects in three dimensions on a computer screen. Although it is generally accepted as a valuable testing method across industries, sadly, it is expensive and time-consuming. Often it is only used for more specific areas such as research and product development. The capability of CT scanning to create a virtual image of materials with different densities is of great value and in this study, X-ray CT scanning was able to detect the artificial defects that were created within the samples. The shape and defect location was clearly identified as well as the percentage porosity was given.

UT TFM was able to indicate that some defects were present. The shape and size of the artificial defects could not be determined. Therefore, this method is not a solution for testing complex medical or aerospace components. However, it is not to say that it is not a viable method for DMLS components, as it will definitely work on components that are not small and complex.

Acoustic emission with the RFDA method was able to accurately determine the material properties of Ti6Al4V processed by DMLS. A clear difference between the resonant frequencies was shown between samples with and without defects. Although this appears to be a promising method, the shape, size and location could not be indicated from the data. For AE to be used in industry, certain preparatory steps need to be taken before testing. This entails initial testing (screening control) of parts with and without defects in order to gather the signature frequency data. Thereafter, testing can be carried out quickly and the results could indicate some aspects of the nature of the defect. The use of X-ray CT scanning for DMLS parts was proven to be accurate, although this is not an in-house solution. The possibility of using AE as an in-house testing method for certain predefined parts seems to be a promising solution. There is a particular need for testing production parts that are manufactured using DMLS because these parts cannot be produced using other production methods. The major drawback of selecting AE as a NDT testing method is that preparatory work must be done to validate a part, and this would not be possible to test a component that is only produced once. For example: a patient-specific medical implant would only be produced for one person, which means that the cost and time needed to develop AE for that specific implant would exceed that of using X-ray CT. Not only that – the implant is often required for a patient in life-threatening circumstances which requires immediate attention.

Possible future endeavours include investigating the use of AE on the production parts; determining whether it would accurately indicate defects on complex and relatively small components. The probability of detection of the type and size of defect would need to be determined. A better understanding of the acoustic principals and equipment would lead to the development of equipment to investigate the DMLS process while building (on-line monitoring).

References

3D Printing Industry, 2016. *Carbon Finally Unveils First Commercial CLIP 3D Printer* (Online) Available from: http://3dprintingindustry.com/news/carbon3d-finally-unveils-first-commercial-clip-3d-printer-75675/ (Accessed on 1 August, 2016).

3DPrint.Com, 2016. *HP's Multi Jet Fusion 3D Printer Unveiled* (Online) Available from: https://3dprint.com/133713/hp-mjf-3d-printer-unveiled/ (Accessed on 1 August, 2016).

Aloisi, V. and Carmignato, S., 2016. Influence of surface roughness on X-ray computed tomography dimensional measurements of additive manufactured parts. *Case Studies in Nondestructive Testing and Evaluation*, 6 (B), pp. 104–110.

ASTM F2792-12a, *Standard Terminology for Additive Manufacturing Technologies*, (Withdrawn 2015), ASTM International, West Conshohocken, PA, 2012.

Bikas, H., Stavropoulos, P. and Chryssolouris, G., 2016. Additive manufacturing methods and modelling approaches: a critical review. *The International Journal of Advanced Manufacturing Technology*, 83(1-4), pp.389-405.

Bono, R. and Sorensen, S., 2008. Resonant acoustic method delivers defect-free parts. *Advanced materials & processes*, 166(7), pp.25-28.

Bono, R.W. and Stultz, G., 2010. *Automated resonant inspection to validate resonant frequency characteristics within brake components for improved NVH Performance* (No. 2010-01-1699). SAE Technical Paper.

Bono, R.W., Schiefer, M.I. and Stultz, G.R., 2007. *Resonant inspection as an automated NDT method for sinter brazed powder metal components*, SAE International, 2007.

Bono, R.W., Sorensen, S.A. and Stultz, G.R., 2010. New methodology applying resonant inspection for quality testing of very small powder metal components. *International Conference on Powder Metallurgy & Particulate Materials*, June 27-30, 2010, Hollywood, Florida.

Boyer, R., Welsch, G., Collings, E.W., 2007. *Materials Properties Handbook. Titanium alloys*. 4th ed. ASM International.

Broderick, T.F., Jackson, A.G., Jones, H. and Froes, F.H., 1985. The effect of cooling conditions on the microstructure of rapidly solidified Ti-6Al-4V. *Metallurgical Transactions* A, 16(11), pp.1951-1959.

Carino, N.J., 2013. Training: Often the missing link in using NDT methods. *Construction and Building Materials*, 38, pp.1316-1329.

Chen, X., 2014. *Computational and experimental approach for non-destructive testing by laser shearography* (Doctoral dissertation, University of Zaragoza, Spain).

Chua, C.K. and Leong, K.F., 2003. *Rapid prototyping: principles and applications* (Vol. 1). World Scientific.

CSIR, 2016. *The basics of laser physics* (Online) Available from: http://www.csir.co.za/lasers/basics_of_lasers.html (Accessed on 16 August, 2016).

De Chiffre, L., Carmignato, S., Kruth, J.P., Schmitt, R. and Weckenmann, A., 2014. Industrial applications of computed tomography. *CIRP Annals-Manufacturing Technology*, 63(2), pp.655-677.

Donachie, M.J., 2000. *Titanium: a technical guide*. ASM international.

Du Plessis, A., Broeckhoven, C., Guelpa, A. and Le Roux, S.G., 2017. Laboratory X-ray micro-computed tomography: a user guideline for biological samples. *GigaScience*, 6(6), pp.1-11.

Du Plessis, A., Le Roux, S.G. and Guelpa, A., 2016. The CT Scanner Facility at Stellenbosch University: An open access X-ray computed tomography laboratory. Nuclear Instruments and Methods in Physics Research Section B: Beam Interactions with Materials and Atoms, 384, pp.42-49.

Du Plessis, A., Le Roux, S.G., Booysen, G. and Els, J., 2016a. Directionality of Cavities and Porosity Formation in Powder-Bed Laser Additive Manufacturing of Metal Components Investigated using X-Ray Tomography. *3D Printing and Additive Manufacturing*, 3(1), pp.48-55.

Du Plessis, A., Le Roux, S.G., Booysen, G., Els, J., 2016b. Quality Control of a Laser Additive Manufactured Medical Implant by X-Ray Tomography. *3D Printing and Additive Manufacturing* 3 (3), 175-182.

Du Plessis, A., Le Roux, S.G., Els, J., Booysen, G. and Blaine, D.C., 2015. Application of microCT to the non-destructive testing of an additive manufactured titanium component. *Case Studies in Nondestructive Testing and Evaluation*, 4, pp.1-7.

Du Plessis, A., Seifert, T., Booysen, G. and Els, J., 2014. Microfocus X-ray computed tomography (CT) analysis of laser sintered parts. *The South African Journal of Industrial Engineering*, 25(1), pp.39-49.

Ensminger, D. and Bond, L.J., 2011. *Ultrasonics: fundamentals, technologies, and applications*. 3rd ed., CRC press, Taylor & Francis group, 765 p.

EOS GmbH, 2016. *Additive Manufacturing* (Online) Available from: http://www.eos.info/ (Accessed on 24 June, 2016).

EOS Training Manual, 2012. *Basic Training EOSINT M280*, Edition: 04.12, Article number: 9229-3501.

Everton, S.K., Hirsch, M., Stravroulakis, P., Leach, R.K. and Clare, A.T., 2016. Review of in-situ process monitoring and in-situ metrology for metal additive manufacturing. *Materials & Design*, 95, pp.431-445.

Fogagnolo, J.B., Sallica-Leva, E., Lopes, E., Jardini, A.L., Caram, R., 2012. The effect of the laser process-parameters in the microstructure and mechanical properties of Ti-6Al-4V produced by selective laser sintering/melting, *Proceedings of METAL 2012*, Brno, Czech Republic, 23-25 May, 2012.

Gapinski, B., Janicki, P., Marciniak-Podsadna, L. and Jakubowicz, M., 2016. Application of the Computed Tomography to control parts made on Additive Manufacturing process. *Procedia Engineering*, 149, pp.105-121.

GE Oil & *Gas, phoenix v|tome|x L300*, (Online) Available From: https://www.gemeasurement.com/inspection-ndt/radiography-and-computed-tomography/phoenix-vtomex-l-300 (Accessed 9 September, 2016).

Ginzel, E., 2002. *Computerized tomography* (CT), (Online) Available From: http://www.ndt.net/ndtaz/ndtaz.php (Accessed 1 September, 2016).

Hauk, V. ed., 1997. *Structural and residual stress analysis by nondestructive methods: Evaluation-Application-Assessment*. Elsevier.

Hecht, J. 2012. Fiber lasers: The state of the art. *Laser Focus World*, 48, (4) (04), pp. 57-60 Available from: http://www.laserfocusworld.com/articles/print/volume-48/issue-04/features/the-state-of-the-art.html (Accessed on 16 August, 2016).

Hecht, J., 2010. Short history of laser development. *Optical Engineering*, 49(9), pp.091002-091002.

Hellier, C. J., 2012. Handbook of nondestructive evaluation, 2nd ed., Mcgraw-Hill, USA.

Ikram, S., Slabbert, R., Cornelius, I., Du Plessis, A., Swanepoel, L.C. and Weber, H., 2015. Fatal force-feeding or Gluttonous Gagging? The death of Kestrel SACHM 2575. Journal of *Archaeological Science*, 63, pp.72-77.

IMCE, 2016 (Online) Available from: Imce http://Www.Imce.eu (Accessed July 8, 2016).

Innerspec Technologies, *EMAT Technology*, (Online) Available from: http://innerspec.com/knowledge/emat-technology (Accessed 28 November, 2016).

Karme, A., Kallonen, A., Matilainen, V.P., Piili, H. and Salminen, A., 2015. Possibilities of CT scanning as analysis method in laser additive manufacturing. *Physics Procedia*, 78, pp.347-356.

Khairallah, S.A., Anderson, A.T., Rubenchik, A. and King, W.E., 2016. Laser powder-bed fusion additive manufacturing: Physics of complex melt flow and formation mechanisms of pores, spatter, and denudation zones. *Acta Materialia*, 108, pp.36-45.

Kim, F.H., Moylan, S.P. and Villarraga-Gómez, H., 2016. Inspection of embedded internal features in additively manufactured metal parts using metrological x-ray computed tomography. 2016 *Summer Topical Meeting: Dimensional Accuracy and Surface Finish in Additive Manufacturing*, 27-30 June, 2016, Raleigh, NC.

Krakhmalev, P., Fredriksson, G., Yadroitsava, I., Kazantseva, N., Du Plessis, A. and Yadroitsev, I., 2016. Deformation behavior and microstructure of Ti6Al4V manufactured by SLM. *Physics Procedia*, 83, pp.778-788.

Krauss, H., Eschey, C. and Zaeh, M., 2012. Thermography for monitoring the selective laser melting process. *Solid Freeform Fabrication Symposium*, Texas, Austin, 6-8 August, 2012.

Kruth, J.P., Badrossamay, M., Yasa, E., Deckers, J., Thijs, L. and Van Humbeeck, J., 2010. Part and material properties in selective laser melting of metals. *16th international symposium on electromachining* (ISEM XVI) edition:16, Shanghai, China, 19-23 April 2010.

Kruth, J.P., Bartscher, M., Carmignato, S., Schmitt, R., De Chiffre, L. and Weckenmann, A., 2011. Computed tomography for dimensional metrology. C*IRP Annals-Manufacturing Technology*, 60(2), pp.821-842.

Kruth, J.P., Froyen, L., Van Vaerenbergh, J., Mercelis, P., Rombouts, M. and Lauwers, B., 2004. Selective laser melting of iron-based powder. *Journal of Materials Processing Technology*, 149(1), pp.616-622.

Leuders, S., Thöne, M., Riemer, A., Niendorf, T., Tröster, T., Richard, H.A. and Maier, H.J., 2013. On the mechanical behaviour of titanium alloy TiAl6V4 manufactured by selective laser melting: Fatigue resistance and crack growth performance. *International Journal of Fatigue*, 48, pp.300-307.

Lewandowski, J.J. and Seifi, M., 2016. Metal Additive Manufacturing: A Review of Mechanical Properties. *Annu. Rev. Mater. Res*, 46, pp.14-1.

M2M, 2016. *Gekko* (Online) Available from: https://www.m2m-ndt.com/products/Gekko.htm (Accessed on 15 December, 2016).

Manfredi, D., Calignano, F., Krishnan, M., Canali, R., Ambrosio, E.P., Biamino, S., Ugues, D., Pavese, M. and Fino, P., 2014. Additive manufacturing of Al alloys and aluminium matrix composites (AMCs). WA Monteiro (Edr.), *Light Metal Alloys Applications*, InTech.

Maskery, I., Leach, R.K. and Thompson, A., 2016. X-ray computed tomography for additive manufacturing: a review. *Measurement Science and Technology*, 27(7), pp.72001-72017.

Materialise, 2015. *How to Choose the Perfect File Resolution*. Available at: https://i.materialise.com/blog/how-to-choose-the-perfect-file-resolution-when-turning-your-3d-model-into-a-3d-print/ (Accessed on 15 September, 2016).

Moletsane, M.G., Krakhmalev, P., Kazantseva, N., Du Plessis, A., Yadroitsava, I. and Yadroitsev, I., 2016. Tensile properties and microstructure of direct metal laser-sintered TI6AL4V (ELI) Alloy. *South African Journal of Industrial Engineering*, 27(3), pp.110-121.

Nanoscribe, 2016. *Nanoscribe is Winner of World Technology Award 2015* (Online) Available from: http://www.nanoscribe.de/en/media-press/press-releases/nanoscribe-winner-world-technology-award-2015/ (Accessed on 1 August, 2016).

NDT 2016, (Online) Available from: https://www.nde-ed.org (Accessed 24 September, 2016).

Nickels, L., 2016. Additive manufacturing: A user's guide. *Metal Powder Report*, 71(2), pp.100-105.

NIST, 2016. *Qualification for Additive Manufacturing materials, processes and parts* (Online) Available from: https://www.nist.gov/programs-projects/qualification-additive-manufacturing-materials-processes-and-parts (Accessed on 19 September, 2016).

Olympus, 2016. *Phased Array Tutorial*, (Online) Available from: http://www.olympus-ims.com/en/ndt-tutorials/phased-array/ (Accessed 5 December, 2016).

OptoSigma, 2016. *fθ Lenses for CO_2 Lasers* (Online) Available from: http: https://www.global-optosigma.com/en_us/Catalogs/gno/?from=page&pnoname=f-theta-10600&ccode=W3203&dcode=&gnoname=f%CE%B8-75-10600 (Accessed on 17 August, 2016).

Organovo, 2016. *Press Releases* (Online) Available from: http://phx.corporate-ir.net/phoenix.zhtml?c=254194&p=irol-newsArticle&ID=2186698 (Accessed on 29 June, 2016).

Popovich, A.A., Masaylo, D.V., Sufiiarov, V.S., Borisov, E.V., Polozov, I.A., Bychenok, V.A., Kinzhagulov, I.Y., Berkutov, I.V., Ashikhin, D.S. and Il'inskii, A.V., 2016. A laser ultrasonic technique for studying the properties of products manufactured by additive technologies. *Russian Journal of Nondestructive Testing*, 52(6), pp.303-309.

PRNewswire, 2007. *Objet Announces New Rubber-Like Flexible Material* (Online) Available from http://www.prnewswire.co.uk/news-releases/objet-announces-new-rubber-like-flexible-material-tangoplus-offering-unmatched-218-elongation-at-break-153774255.html (Accessed on 28 June, 2016).

Raj, B., Jayakumar, T. and Thavasimuthu, M., 2007. *Practical non-destructive testing.* Woodhead Publishing. 3rd ed, Alpha Science, India.

Rezanezhad, F., Quinton, W.L., Price, J.S., Elrick, D., Elliot, T.R. and Heck, R.J., 2009. Examining the effect of pore size distribution and shape on flow through unsaturated peat using computer tomography. *Hydrology and Earth System Sciences*, 13, pp. 1993–2002.

Rong, Y., 2015. *Acoustic Emission Evaluation and Mechanical Property Characterization of Stainless Steel Specimens Manufactured by Powder Based 3-D Printer*. MSc dissertation, University of Pittsburgh, 55 p.

Russell, D., 2001. Acoustics and vibration animations. *A Tutorial IEEE, Frequency Control Reference and Tutorial Information website*, (Online) Available from: http://www.acs.psu.edu/drussell/demos.html (Accessed 24 September, 2016).

Schiefer, M.I. and Sjoeberg, L., 2005. Physical basis of the Resonant Acoustic Method for flaw detection. *Advances in powder metallurgy and particulate materials*, 3, pp. 87–97.

Seifi, M., Salem, A., Beuth, J., Harrysson, O. and Lewandowski, J.J., 2016. Overview of materials qualification needs for metal additive manufacturing. *JOM*, 68(3), pp.747-764.

Slotwinski, J.A., Garboczi, E.J. and Hebenstreit, K.M., 2014. Porosity measurements and analysis for metal additive manufacturing process control. *Journal of research of the National Institute of Standards and Technology*, 119, p.494.

SolidWorks, 2015. *Preparing SOLIDWORKS Models for 3D Printing*. Available at: http://blogs.solidworks.com/tech/2015/05/preparing-solidworks-models-3d-printing.html (Accessed 15 September, 2016).

Strantza, M., Aggelis, D.G., de Baere, D., Guillaume, P. and Van Hemelrijck, D., 2015. Evaluation of SHM System Produced by Additive Manufacturing via Acoustic Emission and Other NDT Methods. *Sensors*, 15(10), pp.26709-26725.

Stratasys, 2010. *New Model Support Style Reduces Material Cost and Build Time* (Online) Available from: http://investors.stratasys.com/releasedetail.cfm?ReleaseID=599538 (Accessed on 1 August, 2016).

Stratasys, 2015. Getting the Most out of Metal 3D Printing: Understanding Design & Process Controls for DMLS. *Metal 3d Printing White Paper*, 14 p. https://www.stratasysdirect.com/content/white.../DMLS_White_Paper_201509_v3.pdf (Accessed on 4 January, 2017).

Stultz, G.R., Bono, R.W. and Schiefer, M.I., 2005. Fundamentals of Resonant Acoustic Method NDT. *Advances in Powder Metallurgy and Particulate Materials*, 3, p.11.

Taylor, B., Weidmann, *Application Notes–Metallographic Preparation of Titanium*, Struers, Ballerup, Denmark, pp. 1-6.

The Modal Shop, Inc, 2016. *Resonant Acoustic Method*, (Online) Available from: http://www.modalshop.com/ndt/Resonant-Acoustic-Method?ID=73 (Accessed 21 July, 2016).

Townsend, A., Blunt, L. and Bills, P.J., 2016. Investigating the capability of microfocus x-ray computed tomography for areal surface analysis of additively manufactured parts. In: *American Society for Precision Engineering Summer Topical Meeting: Dimensional Accuracy and Surface Finish in Additive Manufacturing*, 27th - 30th June 2016, Raleigh, NC, USA.

Van Zyl, I., Yadroitsava, I. and Yadroitsev, I., 2016. Residual stress in Ti6Al4V objects produced by Direct Metal Laser Sintering. *South African Journal of Industrial Engineering*, 27(4), pp.134-141.

Vrancken, B., Buls, S., Kruth, J.P. and Van Humbeeck, J., 2015. Influence of preheating and oxygen content on Selective Laser Melting of Ti6Al4V. *16th RAPDASA Conference*, Pretoria, South Africa, 4-6 November 2015.

Waller, J., Parker, B., Hodges, K., Walker, J., Wells, D., Burke, E., Generazio, E., Todorov, E., Price, A., James, S. and Dutton, B., 2015. Qualification of products fabricated via additive manufacturing using nondestructive evaluation. *Trilateral Safety & Mission Assurance Conference* (TRISMAC 2015) Virtual Meeting ESA-ESRIN; 21-22 May 2015, Frascati, Italy.

Waller, J.M., Parker, B.H., Hodges, K.L., Burke, E.R. and Walker, J.L., 2014. *Nondestructive evaluation of additive manufacturing state-of-the-discipline report*. NASA White Sands Test Facility; NM, US, 47 p.

Whiting, J., 2015. *Acoustic emission monitoring of multi-phase fluid flow in laser-engineered net shaping process (LENS)*, MSc dissertation, Northern Illinois University.

Wohlers, T. and Caffrey, T., 2014. Wohlers Report 2014: 3D printing and additive manufacturing state of the industry. *Annual worldwide progress report*, Fort Collins, Wohlers Associates.

Wohlers, T. Wohlers Report 2015: 3D Printing and Additive Manufacturing State of the Industry. *Annual Worldwide Progress Report*, Fort Collins, Wohlers Associates.

Wu, H., Wang, Y. and Yu, Z., 2016. In situ monitoring of FDM machine condition via acoustic emission. *The International Journal of Advanced Manufacturing Technology*, 84(5-8), pp.1483-1495.

Xu, W., Brandt, M., Sun, S., Elambasseril, J., Liu, Q., Latham, K., Xia, K., Qian M., 2015. Additive manufacturing of strong and ductile Ti–6Al–4V by selective laser melting via *in situ* martensite decomposition. *Acta Materialia*, 85, pp. 74–84.

Yadroitsava, I., Els, J., Booysen, G. and Yadroitsev, I., 2015a. Peculiarities of single track formation from TI6AL4V alloy at different laser power densities by selective laser melting. *South African Journal of Industrial Engineering*, 26(3), pp.86-95.

Yadroitsava, I., Grewar, S., Hattingh, D. and Yadroitsev, I., 2015b. Residual Stress in SLM Ti6Al4V Alloy Specimens. *Materials Science Forum*, 828, pp. 305-310).

Yadroitsava I. and Yadroitsev I., 2015. Residual stress in metal specimens produced by Direct Metal Laser Sintering. *International Solid Freeform Fabrication Symposium*, August 10-12, 2015, University of Texas at Austin, USA.

Yadroitsev, I. and Smurov, I., 2011. Surface morphology in selective laser melting of metal powders. *Physics Procedia*, 12, pp.264-270.

Yadroitsev, I. and Yadroitsava, I., 2015. Evaluation of residual stress in stainless steel 316L and Ti6Al4V samples produced by selective laser melting. *Virtual and Physical Prototyping*, 10(2), pp.67-76.

Yadroitsev, I., 2009. Selective laser melting: *Direct manufacturing of 3D-objects by selective laser melting of metal powders*. LAP Lambert Publishing, 307 p.

Yadroitsev, I., Gusarov, A., Yadroitsava, I. and Smurov, I., 2010. Single track formation in selective laser melting of metal powders. *Journal of Materials Processing Technology*, 210(12), pp.1624-1631.

Yadroitsev, I., Krakhmalev, P. and Yadroitsava, I., 2014. Selective laser melting of Ti6Al4V alloy for biomedical applications: Temperature monitoring and microstructural evolution. *Journal of Alloys and Compounds*, 583, pp.404-409.

Yadroitsev, I., Krakhmalev, P. and Yadroitsava, I., 2015. Hierarchical design principles of selective laser melting for high quality metallic objects. *Additive Manufacturing*, 7, pp.45-56.

Ziółkowski, G., Chlebus, E., Szymczyk, P. and Kurzac, J., 2014. Application of X-ray CT method for discontinuity and porosity detection in 316L stainless steel parts produced with SLM technology. *Archives of Civil and Mechanical Engineering*, 14(4), pp.608-614.

APPENDIX 1: Brief history of AM

Only some of the main events of AM have been recorded. There have been great developments and many companies have contributed to the development of AM. For a more detailed history, see reference (Wohlers, 2014).

In the 1960's the *Battelle Institute* attempted to create a solid object using photopolymers with two intersecting lasers at different wavelengths. They used *DuPont*'s photopolymer that was invented in 1950. In 1967, Wyn K. Swainson from Denmark applied for a patent for a Holography method similar to that of *Battelle* called "Method of Producing a 3D Figure by Holography". Swaison formed *Formigraphic Engine Co*. and in 1994 they still did not have a commercially available system. In 1974, *Formagraphic* demonstrated with the aid of a very basic system that a 3D part can be generated. *Formigraphic* became *Omtec Replication*. *Battelle* developed similar techniques with aid from DARPA funding. In the late 1970's, *Dynell Electronics Corp*. gained a series of patents on Solid Photography. This method involved cutting cross-sections by computer and stacking them to form a 3D object.

3D Systems launched the SLA-1 – they were the first in the world to launch a commercially available AM machine and did so in 1987. SLA-1 generated polymer parts from a process called stereolithography (SLA) (Wohlers, 2014).

In 1991, three other AM technologies that did not make use of SLA came into existence, they were: Fused Deposition Modeling (FDM) from *Stratays*, Solid Ground Curing (SGC) from *Cubital* and Laminated Object Manufacturing (LOM) from *Helisys*. (Wohlers, 2014).

In 1992, Selective Laser Sintering (SLS) from *DTM* (now part of 3D Systems) became available.

In 1993, *Soliegn* commercialized direct shell production (DSPC) specifically for investment casting; *Massachusetts Institute of Technology* (MIT) invented and patented DSPC that *Soliegn* used. *3D Systems* and *Ciba* introduced QuickCast build style that is still used to date.

In 1994, *EOS* commercialized their first laser sintering machine, EOSINT. *Solidscape* introduced the first machine that could deposit wax materials, called ModelMaker.

In 1996, low-cost 3D printers were introduced. A semi-automated paper lamination system for under $ 10 000 was sold by *Schroff Development*.

AeroMet was founded in 1997 and developed Laser Additive Manufacturing (LAM) specifically aimed at the aerospace industry.

In February 1999, *3D Systems* started selling the SLA 700 system for $ 800,000 making it the most expensive plastic-base machine at that time. In April of the same year, *ExtrudeHone* (now Exone) installed an AM machine - the ProMetal RTS-300 at Motorola for building metal parts. *Fockele and Schwarze* of Germany introduced its steel powder-based selective laser-melting system that was developed with the *Fraunhofer Institute of Laser Technology*. *Röders* began to sell its Control Metal Buildup (CMB) machine that was based on *Fraunhofer Institute for Production Technology*'s developments.

In 2000, *Buss Modeling Technology* announced that it would manufacture and sell a colour 3D printer. *Precision Optical Manufacturing* (POM) announced a process used to build and repair metal parts called Direct Metal Deposition (DMD). Sales started two years later and the company is active to this day. *Z Corp* introduced the first commercially available colour 3D printer.

In 2001, *Solido,* at that time known as *Solidimension,* introduced a new AM desktop technology that uses laminated sheets of PVC plastic. In February, 3D systems acquired a French company; *OptoForm*, that developed a stereolithography method that uses different material pastes that harden. These pastes included ceramics and metals. In May, *Solidica* disclosed technical details on its ultrasonic consolidation process. *Generis GmbH* commercialized its GS1500 that is used to produce sand cores and moulds for metal castings. *EOS* introduced its DirectSteel 20-V1 product, a steel-based powder consisting of particles 20 microns in size. In the same year, the rapid solidification process was developed by *RSP Tooling LLC*, which makes use of a metal spray technique.

In 2002, the first machines to produce structures from biomaterials for tissue engineering, called the Bioplotter, were sold by *Envisiontec GmbH*.

At the end of 2005, *MTS* said in an announcement that making titanium parts for the aerospace industry is not a profitable business model (Wohlers, 2014).

In 2006, *Speed Part* (now Sintermask GmbH) shipped their first system, although they were founded in 2000. They developed a new technology that made use of a masked infrared light to sinter an entire powder layer at a time. (Chua and Leong, 2003; Wohlers, 2014).

In the second quarter of 2006, *EOS* introduced stainless steel and cobalt-chrome materials. In May, *Desktop Factory* announced they were developing a device that used an inexpensive halogen light and drum-printing technology that would cost around $5000 to $ 7000.

In January 2007, *3D Systems* announced, the V-Flash stereolithography machine that used a film transfer method that built parts upside down. Later that year, *Objet Geometries* introduced a rubber-like material called TangoPlus and claimed a 218% elongation at break point (PRNewswire, 2007). *EOS* were the first to commercialize Ti6Al4V for DMLS (EOS GMBH-HIS, 2016). *Objet Geometries* debuted their multi-material machine (PolyJet) capable of printing in two different materials at once – called the Connex500. *SinterMask* showed their new system in 2007 at EuroMold, the Pollux 32, that could sinter entire layers at once (Chua and Leong, 2003).

In 2008, *EOS* introduced a high temperature machine capable of 385°C. This led the AM industry into a new range of thermoplastics that could be applied. *Nuvatronics* announced the PolyStrata, a micro fabrication technology for very small electronic devices. *Huntsman Advanced Materi*als announced a new technology that uses microshutters and UV light to cure a photopolymer, claiming to be faster and more accurate than stereolithography.

In January 2009, the ASTM committee for AM technologies was created to set standards on testing, processes, materials, design and terminology. In February, *EOS* and *Victrex* announced PEEK HP3, a new PEEK material for the EOSINT P800. In March that year, *Realizer GmbH* introduced the SLM 50 the first selective laser melting machine for a desktop. In April, *Bits from Bytes* released the RapMan 3D printer kit for only $750.

In 2010, two support software programs were developed – Smart Supports from *Stratasys,* that was used to reduce the support material of FDM (Stratasys, 2010). The second software was from *Materialise* and was called Magics Metal SG, which is used to generate support for metal AM.

In 2010, AM was adopted as the manufacturing method for in-the-ear hearing aids, while the AM dental industry was experiencing growth. A key FDM patent expired and inexpensive open-source kits became available and ever since, FDM has experienced enormous growth. In July, *Delta Micro* introduced a machine that sold for less than $3000. It contained a single spool system with the best part quality in its class. In October, *3D systems* bought *Bits from Bytes* that offered inexpensive FDM kits, this gave them a foothold in the hobbyist and educational markets.

In February 2011, *CRP Technology* introduced a carbon-fibre-filled material for SLS. At the annual RAPID conference in Minneapolis, Wilfried Vancraen (founder and CEO of Materialise) received an Industry Achievement Award for his extensive contributions to AM. *Optomec* released a new wide-area Aerosol Jet print head for use in 3D printing and conformal electronics. The DARPA, Mesoscopic Integrated Conformal Electronics (MICE) program was the origin of aerosol jet printing. The MICE program is used for development of 3D printing of solar cells, displays and electronics. In August, *Kelyniam Global* announced that it was shipping skull implants made from PEEK. The ASTM and ISO AM committee F42 and 261 respectively made a cooperative agreement to reduce duplication of effort. In November, *EOS* announced that it had installed 1000 laser sintering machines.

In January 2012, *MakerBot* released the MakerBotReplicator for only $1749, while *3D Systems* announced a consumer-orientated 3D printer for below $1300. In March, *BumpyPhoto* launched a 3D printer for photos, generating 3D models from digital photos. *Solidoodle* announced its second-generation machine that would be sold for $499. *3DMTP* announced a cloud-based service that can manipulate architectural models for 3D printing. In September, *Sigma Labs* released PrintRite3D, a system that is used to qualify the process and certify metal AM aerospace parts. *Materialise* launched its new software for metal AM Magics 17. In December, *Oragonvo Holding* and *Autodesk* announced collaboration to create the first 3D bioprinting software.

In January 2013, *Optomec* released a high-resolution thermal imaging device, used to monitor the melt pool of their LENS equipment. In March that year, *Materialise* announced their HeartPrint service that could print patient-specific cardiovascular models for medical use (Wohlers 2014).

In August 2014, *Oxford Performance Materials* received the first FDA 510(k) approval for their OsteoFab 3D printed patient-specific implant. At IMTS, a 3D printed car was produced over six days by *Local Motors*; they produced the chassis and body using 3D printing. In October, *HP* announced their new technology, HP Multi Jet Fusion that uses a binding agent to fuse the material. They reported that “In 11 hours — during which time an FDM system could produce 50 parts or an SLS system 250 — MJF can print 2500 parts per build unit”. In November, *Mazak* released a machine called INTEGGRX i-400AM that combined direct energy deposition with 5-axis machining (Wohlers, 2015; 3DPrint.Com., 2016).

In January 2015, *Voxel8* released a machine capable of combining FDM with embedded electronic circuits. *Rolls Royce* announced that they were planning to test the largest ever 3D printed engine part – a titanium front bearing housing, with a load-bearing part of 1.5m in diameter. In March, *ExOne* announced Exerial, a machine with multiple stations that is used for continuous production lines. *Graphene 3D* Lab released their nano-carbon-filled electrical conductive graphene FDM filament. *Carbon 3D* unveiled their new technology called Continuous Liquid Interface Production (CLIP) (Wohlers, 2015). At the end of 2015, *Nanoscribe* won the World Technology Award in New York; they manufactured the world's most precise 3D printer. *Nanoscribe* makes use of a non-linear two-photon absorption process to fabricate micro- and nanostructures (Nanoscribe, 2016).

In 2016, *Orgonovo* announced they had signed their first customer orders to study the effects of drug exposure on the kidney proximal tubule (Organovo, 2016). At RAPID 2016, *HP* unveiled its new HP Multi Jet Fusion 3D printing technology with two machines: the HP Jet Fusion 3D 3200 and the HP Jet Fusion 3D 4200 (3DPrint.Com., 2016). In April, *Carbon3D* launched its first commercially available CLIP-based 3D printer. Carbon3D's approach has been said to be up to 100 times, faster with higher resolution and better mechanical properties, than other traditional 3D printers. In June, *Vader Systems* launched their first commercial system, the MK1, based on MagnetoJet technology. Their technology is based on the principle of using magnetism to deliver molten metal to produce a dense part. *RepRap*'s X150 3D won the Best of Industry Award for 2016 (3D Printing Industry, 2016).